UNIVERSIDAD POLITÉCNICA DE MADRID
Escuela Técnica Superior de Ingenieros de Caminos, Canales y Puertos

Fire-safe lithium-ion batteries: material, assessment, and mechanism

DOCTORAL THESIS

Submitted for the degree of Doctor by:

Mingyang Zhang
Ingeniero de Materiales

Madrid, 2025

UNIVERSIDAD POLITÉCNICA DE MADRID
Escuela Técnica Superior de Ingenieros de Caminos, Canales y Puertos

Doctoral Degree in Engineering of Structures, Foundations and Materials

Fire-safe lithium-ion batteries: material, assessment, and mechanism

DOCTORAL THESIS

Submitted for the degree of Doctor by:

Mingyang Zhang
Ingeniero de Materiales

Under the supervision of:
Dr. De-Yi Wang

Madrid, 2025

Title: Fire-safe lithium-ion batteries: material, assessment, and mechanism

Author: Mingyang Zhang

Doctoral Programme: Engineering of Structures, Foundations and Materials

Thesis Supervision:

Dr. De-Yi Wang, Senior Researcher, IMDEA Materials Institute, Madrid, Spain

External Reviewers:

Thesis Defense Committee:

Thesis Defense Date:

💞 *Yi He*

Acknowledgement

Time flies, and now it's my turn to say goodbye. As I reach this moment, I would like to take the opportunity to express my deep gratitude to many people.

First and foremost, I would like to sincerely thank my supervisor, Prof. Wang. He gave me the invaluable opportunity to study in Spain and has imparted not only a wealth of academic knowledge but also life lessons that I will carry with me. I am especially grateful for his unwavering support, whenever I encountered difficulties, he guided me through them with patience and wisdom. From him, I have learned so much, not only about research but also about perseverance, life philosophy, and interpersonal skills. Most importantly, he helped me realize that I am the one in control of my work, my emotions, and my life.

Secondly, I would like to extend my sincere thanks to all my colleagues at the IMDEA Materials Institute for creating such a friendly and supportive working environment. I am especially grateful to the technicians: Jinema, Manuel, Javier, Rafael, Juan Pedro, Vanesa, and Amalia for their thorough training and kind guidance during the experimental work. My sincere thanks go to all the HPPN group members for their help and companionship during my time here. I am particularly thankful to Abdul, Junchen, Xiang Ao, Wei Tang, Arnab, Jose Hobson, Afshin, and Elena for their contributions to my research work. I also want to express my appreciation to Xiaolu, Meihui, Guangzhong, Monsur, Yunhuan, Raquel, Sunan, Juan, Yanyan, Wei Cai, Ruofan, Xiaowei, Qiong Tan, Qi Chen, Jalal, Chunxiang, Shuanglan, Sree, Biaobiao, and many others. We supported each other and shared unforgettable moments both at work and in life. Meanwhile, I would like to thank Prof. Jean-François Gohy from Université catholique de Louvain for offering me the important opportunity to exchange ideas and gain new knowledge. I'm also grateful to the group members at UCLouvain's lab for their warm welcome and genuine kindness, especially Yinghui, Zhenni, Hao Wang, and Carla.

Last but certainly not least, I want to express my deepest gratitude to my family: my parents, my older sister, my parents-in-law, and Yi's grandmother. To my parents: thank you for raising me with love and care, for teaching me countless life lessons, and for providing a warm and harmonious environment in which I could grow. To my sister: thank you for being my closest ally throughout my whole life. Most of all, I want to extend my heartfelt thanks to my husband, Yi He. Before meeting him, I never imagined how deeply one person's presence could fill another with such happiness. He understands me completely, supports every decision I make, and works tirelessly for the life we're building together. His constant companionship has been the strongest source of faith and motivation throughout my PhD journey. I also sincerely thank my motherland, China, for the financial support that made this journey possible.

Earning a doctorate marks the end of one journey and the beginning of another. I am truly grateful for everything I have experienced and learned along the way, and I will carry these lessons with me as I prepare for the many journeys ahead. I am my best self!

Mingyang

June 2025

Abstract

Electrochemical energy storage plays a vital role in enabling the integration of renewable energy and supporting the development of smart grids. Among various technologies, lithium-ion batteries have emerged as the most promising solution due to their high energy density, fast charging capability, long cycle life, and overall reliability. However, despite these advantages, lithium-ion batteries face significant safety concerns, with thermal runaway being the most critical. The use of flammable organic solvents in conventional electrolytes is a major contributor to triggering thermal runaway by fuelling exothermic reactions under abuse conditions. The development of flame-retardant or self-extinguishing electrolyte systems is essential to mitigate thermal risks and ensure the safe deployment of lithium-ion batteries in future energy infrastructures.

Aside from material design, the evaluation of electrolyte flammability is equally important for advancing battery safety. Although various tests are employed to assess the flammability of electrolytes, the most widely used self-extinguishing time test remains unstandardized, which is often conducted under inconsistent conditions, resulting in limited reproducibility and poor comparability across different studies. Furthermore, existing assessments tend to focus on individual components (such as electrolytes) without confirming whether these improved components enhance the overall safety of the battery. The correlation between material-level safety improvements and full-cell combustion behavior remains insufficiently explored. This disconnect not only limits accurate prediction of battery thermal safety but also impedes the rational design of next-generation fire-safe materials.

This thesis aims to advance the development of fire-safe batteries through a comprehensive approach that integrates innovative component design, standardized evaluation methods, and mechanistic understanding. It seeks to establish more rigorous and systematic protocols for electrolyte flammability assessment, elucidate the underlying working mechanisms of flame retardants within the electrolyte, and reveal the correlations between safety evaluations at the electrolyte and single-cell levels. Based on these objectives, the research focus of this thesis is outlined as follows:

(i) In Chapter 3, a novel composite solid-state electrolyte with the “ceramic in polymer - polymer in ceramic” hierarchical structure is introduced, which exhibits enhanced mechanical properties, good fire resistance, and better electrochemical performance compared to conventional polyethylene oxide solid-polymer electrolytes.

(ii) In Chapter 4, the key parameters of the self-extinguishing time test are systematically summarized and thoroughly investigated. Based on repeatability and reliability, burning a glassfiber separator (diameter:16 mm) with absorption of 0.1 g liquid electrolyte can be

proposed as a unified method. The concept of self-extinguishing efficiency is further proposed with a new evaluation criterion. The feasibility of the new protocol is verified, and the working mechanism of flame retardants in electrolytes is elucidated.

(iii) In Chapter 5, an in-depth fire safety evaluation of pouch cells containing three representative flame-retardant electrolytes is conducted using cone calorimetry. Flame retardants that exhibit excellent performance in electrolytes fail to deliver meaningful improvements in the battery's fire safety. Finite element simulations reveal discrepancies in combustion behavior between electrolytes and full-cell levels, indicating an indirect correlation between the intrinsic flame retardancy of the electrolytes and the overall fire resistance of the batteries.

Resumen

El almacenamiento electroquímico de energía es clave para integrar energías renovables y desarrollar redes inteligentes. Las baterías de iones de litio destacan por su alta densidad energética, carga rápida, larga vida útil y fiabilidad, pero enfrentan serios riesgos de seguridad, siendo la fuga térmica el más crítico. Los disolventes orgánicos inflamables en electrolitos convencionales alimentan reacciones exotérmicas bajo condiciones de abuso, provocando esta fuga. Por ello, desarrollar electrolitos ignífugos o autoextinguibles es fundamental para reducir riesgos térmicos y asegurar su uso seguro en futuras infraestructuras energéticas.

Además del diseño de materiales, la evaluación de la inflamabilidad de los electrolitos es igualmente crucial para el avance de la seguridad en baterías. Aunque se emplean diversas pruebas para evaluar la inflamabilidad de los electrolitos, la prueba de tiempo de autoextinción, que es la más utilizada, carece de estandarización y con frecuencia se realiza bajo condiciones inconsistentes, lo que conduce a una reproducibilidad limitada y a una comparabilidad deficiente entre diferentes estudios. Asimismo, la mayoría de las evaluaciones existentes tienden a centrarse en componentes individuales (como los electrolitos) sin verificar si las mejoras a nivel de componente se traducen en un aumento real de la seguridad global de la batería. La relación entre las mejoras en la seguridad a nivel material y el comportamiento de combustión a nivel de celda completa sigue siendo insuficientemente comprendida. Esta desconexión no solo limita la precisión en la predicción de la seguridad térmica de las baterías, sino que también dificulta el diseño racional de materiales ignífugos de próxima generación.

Esta tesis tiene como objetivo avanzar en el desarrollo de baterías seguras contra incendios mediante un enfoque integral que integra el diseño innovador de componentes, métodos de evaluación estandarizados y una comprensión mecanicista. Busca establecer protocolos más rigurosos y sistemáticos para la evaluación de la inflamabilidad de electrolitos, esclarecer los mecanismos de funcionamiento subyacentes de los retardantes de llama dentro del electrolito y revelar las correlaciones entre las evaluaciones de seguridad a nivel de electrolito y de celda individual. Basándose en estos objetivos, el enfoque de investigación de esta tesis se detalla a continuación:

(i) En el Capítulo 3, se presenta un nuevo electrolito sólido compuesto con una estructura jerárquica de “cerámica en polímero - polímero en cerámica”, que exhibe propiedades mecánicas mejoradas, buena resistencia al fuego y un mejor desempeño electroquímico en comparación con los electrolitos poliméricos sólidos convencionales de óxido de polietileno.

(ii) En el Capítulo 4, se resumen e investigan los parámetros clave de la prueba de tiempo de autoextinción. Basándose en la repetibilidad y confiabilidad, se propone como método unificado la combustión de un separador de fibra de vidrio (diámetro: 16 mm) impregnado con

0.1 g de electrolito líquido. Además, se introduce el concepto de eficiencia de autoextinción con un nuevo criterio de evaluación. Se verifica la factibilidad del nuevo protocolo y se esclarece el mecanismo de acción de los retardantes de llama en los electrolitos.

(iii) En el Capítulo 5, se evalúa la seguridad contra incendios de celdas pouch con tres electrolitos retardantes de llama mediante calorimetría de cono. Aunque los retardantes muestran buen rendimiento en electrolitos, no mejoran significativamente la seguridad de las baterías. Simulaciones por elementos finitos revelan discrepancias en la combustión entre electrolitos y celdas completas, indicando una correlación indirecta entre la inflamabilidad intrínseca del electrolito y la resistencia al fuego de la batería.

Table of Contents

List of Figures

List of Tables

Abbreviations and Acronyms

AC	Alternating Current
AGG	Aggregate
ASSLB	All-Solid-State Lithium Battery
ARC	Accelerating Rate Calorimeter
BC	Battery Case
BLE	Blank Liquid Electrolyte
BMS	Battery Management System
CCT	Cone Calorimeter Test
CDP	Cresyl Diphenyl Phosphate
CEI	Cathode-Electrolyte Interphase
CIP	Contact Ion Pair
CIP	Ceramic in Polymer
CSSE	Composite Solid-State Electrolyte
CV	Cyclic Voltammetry
CW	Cotton Wick
DEC	Diethyl Carbonate
DEEP	Diethyl Ethylphosphonate
DEMEMPA	Bis(N,N-Diethyl)(2-Methoxyethoxy) Methylphosphonamidate
DFEA	2,2-Difluoroethyl Acetate
DMA	Dynamic Mechanical Analyzer
DMC	Dimethyl Carbonate
DMMP	Dimethyl Methylphosphonate
DN	Donor Number
DOPO	9,10-Dihydro-9-Oxa-10-Phosphaphenanthrene-10-Oxide
DPMB	1-Diphenylphosphoryloxy-4-Methylbenzene
DPOF	2-Ethylhexyl Diphenyl Phosphate
DSC	Differential Scanning Calorimetry
DTA	Differential Thermal Analysis
EC	Ethylene Carbonate
EDS	Energy Dispersive X-Ray Spectroscopy

EIS	Electrochemical Impedance Spectroscopy
EMC	Ethyl Methyl Carbonate
ESI-HRMS	Electrospray Ionization High-Resolution Mass Spectrometry
EV	Electric Vehicle
ESW	Electrochemical Stability Window
FEM	Finite Element Method
FPPN	Hexafluorocyclotriphosphazene
FR	Flame Retardant
FTIR	Fourier Transform Infrared Spectroscopy
FWHM	Full Width at Half Maximum
GCD	Galvanostatic Charge-Discharge
GC-MS	Gas Chromatography-Mass Spectrometry
GFS	Glassfiber Separator
GPE	Gel Polymer Electrolyte
HCE	Highly Concentrated Electrolyte
HEV	Hybrid Electric Vehicles
HFPN	Hexafluorocyclotriphosphazene
HP	Hyperparameter
HRC	Heat Release Capacity
HRR	Heat Release Rate
HTR	Heat-Temperature-Reaction
IP	Insulfrax Paper
ISC	Internal Short Circuit
LCO	Lithium Cobalt Oxide
LE	Liquid Electrolyte
LFL	Lower Flammable Limit
LFP	Lithium Iron Phosphate
LIB	Lithium-Ion Battery
LiTFSI	Lithium Bis(Trifluoromethanesulfonyl)Imide
LMB	Lithium-Metal Battery
LSV	Linear Sweep Voltammetry
MCC	Macroscale Cone Colorimeter
ML	Machine Learning

MOF	Metal-Organic Framework
NMC	Lithium Nickel Manganese Cobalt Oxide
NMP	N-1-Methyl-2-Pyrrolidone
PAN	Polyacrylonitrile
PC	Propylene Carbonate
PE	Polyethylene
PEO	Polyethylene Oxide
PFPN	Ethoxy(Pentafluoro)Cyclotriphosphazene
pHRR	Peak Heat Release Rate
PIC	Polymer in Ceramic
PMMA	Polymethyl Methacrylate
PP	Polypropylene
PVC	Polyvinyl Chloride
PVDF	Polyvinylidene Fluoride
PVDF-HFP	Poly(Vinylidene Fluoride-co-Hexafluoropropylene)
RF	Random Forest
SEE	Self-Extinguishing Efficiency
SEI	Solid Electrolyte Interphase
SEM	Scanning Electron Microscopy
SET	Self-Extinguishing Time
SIE	Solid Inorganic Electrolyte
SLP	Single-Layer Pouch Cell
SOC	State of Charge
SPE	Solid Polymer Electrolyte
SS	Stainless Steel
SSE	Solid-State Electrolyte
SSIP	Solvent-Separated Ion Pair
TBP	Tributyl Phosphate
TEM	Transmission Electron Microscopy
TEP	Triethyl Phosphate
TEPi	Triethyl Phosphite
TFMP	Bis(2,2,2-Trifluoroethyl) Methylphosphonate
TGA	Thermogravimetric Analysis

THR	Total Heat Release
TMP	Trimethyl Phosphate
TMPi	Trimethyl Phosphite
TMPPi	Tris(4-Methoxyphenyl)Phosphine
TOF-SIMS	Time-of-Flight Secondary Ion Mass Spectrometry
TOP	Trioctyl Phosphate
TPP	Triphenyl Phosphate
TPPi	Triphenyl Phosphite
TSP	Total Smoke Production
TTFP	Tris(2.2.2-Trifluoroethyl)Phosphate
TTFPi	Tris(2,2,2-Trifluoroethyl) Phosphite
TTI	Time-to-Ignition
XRD	X-Ray Diffraction

1. Introduction

1.1. Lithium-ion batteries

The extensive reliance on limited fossil fuels for heating, power generation, and transportation has led to severe challenges in current energy development. In particular, the harmful emissions associated with fossil fuel combustion not only contribute to global climate change and acid rain but also cause long-term degradation of fragile ecosystems, ultimately posing a serious threat to human survival. Addressing this urgent issue requires a transition from conventional energy sources to green and sustainable alternatives such as solar, wind, and other renewable energies. However, these renewable energy sources are inherently intermittent and variable, making their integration into existing power systems a significant technical challenge.[1-4] The fluctuating nature of renewable energy generation imposes a burden on grid operators, who must rely on conventional fossil-fuelled power plants to maintain stability and ensure a continuous power supply. Consequently, mitigating the intermittency of renewable sources has become a critical task in the context of energy system transformation. To effectively manage these fluctuations, the development and deployment of cost-effective electrochemical energy storage technologies are essential. Electrochemical energy storage is widely regarded as a key enabler of the smart grid, which aims to accommodate a high penetration of renewable energy while simultaneously supplying electricity to electric vehicle (EV) and hybrid electric vehicle (HEV).[2, 5, 6] Among various secondary battery technologies, lithium-ion batteries (LIBs) stand out due to their high practical energy density, fast charging capability, minimal memory effect, long cycle life, and relatively low environmental impact. In recent years, LIBs have emerged as the leading energy storage solution in applications ranging from EVs to large-scale grid storage, playing a pivotal role in the ongoing transition away from fossil fuels.[7, 8]

Since the first commercial LIB was developed by the Sony company in 1991, continuous scientific and technological endeavours have been put forward to improve the overall performance of LIBs, including higher energy density and safer stability.[9] A LIB typically consists of four main components: cathode, anode, separator, and electrolyte. Its operating principle is illustrated in Figure 1.1. During charging, lithium ions (Li^+) are released from the cathode and migrate through the electrolyte to be stored in the anode. During discharge, the process is reversed as Li^+ moves back to the cathode, generating electrical energy. The electrolyte acts as an ionic conductor, enabling smooth Li^+ transport between the electrodes, while the separator - a thin, microporous polymer membrane - physically isolates the cathode and anode to prevent short circuits, yet allows Li^+ to pass freely. Due to the repeated shuttling

of Li^+ between the electrodes during charge and discharge, LIBs are often referred to as "rocking-chair batteries".[10]

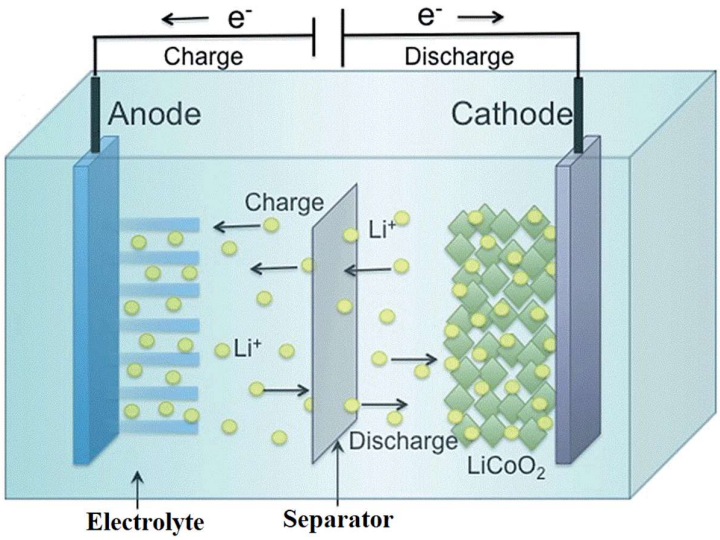

Figure 1.1 The working mechanism of rechargeable LIBs is based on the reversible intercalation and deintercalation of Li^+ between electrodes through the electrolyte.[11]

The electrodes in LIBs are composed of porous materials designed to facilitate ion transport and electron conduction. As presented in Figure 1.2a, the cathode is usually composed of lithium metal oxides, such as lithium cobalt oxide ($LiCoO_2$), lithium iron phosphate ($LiFePO_4$, LFP), or lithium nickel manganese cobalt oxide (NMC), each offering distinct advantages in terms of energy density, thermal stability, and cycle life.[12, 13] On the other hand, the anode is most commonly made of graphite, a form of carbon known for its layered structure that allows for efficient Li^+ intercalation. Despite the remarkable progress achieved in LIB technology - resulting in its widespread adoption in consumer electronics, EVs, and grid-scale energy storage - significant challenges remain that must be addressed to meet the growing performance demands of next-generation applications.[14, 15] One of the primary limitations lies in the cathode, where the key challenge is to further enhance the energy density without compromising structural stability or safety. This requires the development of new high-capacity materials or strategies to optimize the utilization of existing materials, such as increasing voltage windows or improving Li^+ diffusion kinetics. On the anode side, the anode has evolved from conventional graphite toward high-capacity materials such as silicon and lithium metal (Figure 1.2b). However, the main hurdle involves mitigating the substantial volume expansion that occurs in high-capacity materials like silicon during lithium insertion and extraction.[16-18] This mechanical stress can lead to particle pulverization, loss of electrical contact, and continuous formation of unstable solid electrolyte interphase (SEI), which collectively degrade battery performance. Therefore, developing novel electrode materials and structural designs is essential for enhancing cycle stability and prolonging battery life.[19]

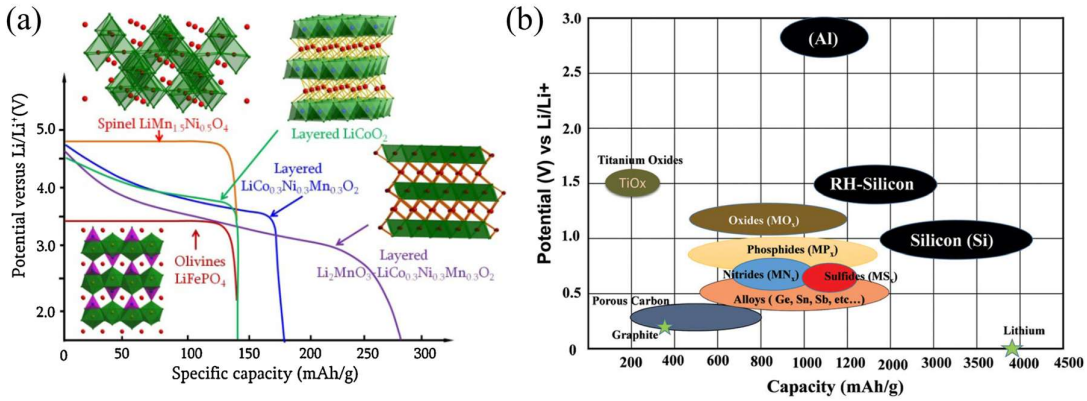

Figure 1.2 (a) The formulae, structure, and potential profile differences among typical cathode materials in LIBs.[20, 21] (b) The potential and specific capacity comparison of different anode materials.[22, 23]

As the blood enables smooth ion conduction in LIBs, liquid electrolyte (LE) plays an important role in overall performance, including energy density, cycle stability, and safety. To achieve both high dielectric constant and low viscosity, current commercial electrolytes employ a combination of lithium salts and solvents composed of cyclic carbonates (e.g., ethylene carbonate (EC) and propylene carbonate (PC)) alongside linear carbonates (e.g., ethyl methyl carbonate (EMC), diethyl carbonate (DEC), and dimethyl carbonate (DMC)).[24, 25] While these formulations deliver exceptional electrochemical performance, the volatile and flammable nature of organic solvents poses a huge challenge to the fire safety of the whole battery system. As presented in Table 1.1, when linear carbonates exhibit low viscosities that can enhance molecular freedom, their low flash points pose stability concerns, particularly when exposed to the air or in the presence of Li salt.[26]

Table 1.1 Commonly used organic solvents for commercial electrolytes.

Abbr.	Full name	Structure	ε[a)]	Vis[b)]	BP[c)]	MP[d)]	FP[e)]
EC	Ethylene Carbonate	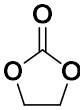	90.0	1.86	248	39	160
PC	Propylene Carbonate	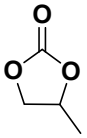	66.3 (20°C)	1.91 (40°C)	242	-49	135
EMC	Ethyl Methyl Carbonate	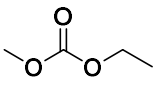	3.0	0.65	109	-55	23
DEC	Diethyl Carbonate	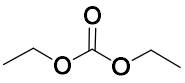	2.8	0.62 (40°C)	127	-43	31
DMC	Dimethyl Carbonate	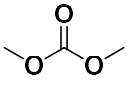	3.1	0.59	90	5	18

Abbr.	Full name	Structure	ε[a)]	Vis[b)]	BP[c)]	MP[d)]	FP[e)]
FEC	Fluoroethylene carbonate	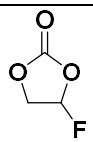	100.3	4.10	212	18	102
VC	Vinylene carbonate	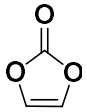	126.0	-	162	19-22	73
GBL	γ-Butyrolactone	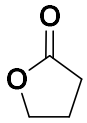	42.0	1.70	204	-44	101

[a)]: dielectric constant at 25ºC; [b)]: viscosity at 25ºC; [c)]: boiling point; [d)]: melting point; [e)]: flash point

1.2. Thermal runaway

Among the constraints discussed, safety is the primary barrier to the commercial adoption of LIBs. Despite their satisfying electrochemical performance, inherent safety risks continue to hinder broader application across various scenarios.[3, 27-30] Numerous incidents involving fires and explosions associated with LIBs have been reported worldwide, spanning from consumer electronics such as cell phones and laptops to EVs and even aircraft.[31, 32] These catastrophic events not only result in equipment damage and substantial economic losses but also pose serious threats to human safety, thereby impeding the widespread commercialization and adoption of LIBs in transportation systems and large-scale energy storage infrastructures. As depicted in Figure 1.3, thermal runaway represents one of the most hazardous failure modes in LIBs. It refers to a self-accelerating and uncontrollable process in which an excessive amount of heat is rapidly generated and accumulates within the cell when the battery is subjected to various abuse conditions, such as mechanical abuse,[33] electrical abuse,[34] and thermal abuse.[35] This process is further exacerbated by a positive feedback loop known as the "heat-temperature-reaction" (HTR) mechanism, ultimately leading to cell overheating, fire, and explosions.[36, 37]

As depicted in Figure 1.4, the battery will undergo a series of complicated exothermic reactions during the thermal runaway process, including the decomposition of the SEI layer, reactions between the electrolyte and the anode, separator melting, decomposition of the cathode and electrolyte, binder degradation, combustion of the electrolyte, etc. Among these, the decomposition of SEI is widely recognized as the initial trigger for the subsequent exothermic chain reactions leading to thermal runaway.[38, 39] The decomposition temperature of the SEI varies depending on the specific battery chemistry, typically ranging from 70ºC to 90ºC. As the SEI decomposes, the electrode material becomes re-exposed to the electrolyte. Under the drive

from electrode potential, Li^+ will react with the electrolyte to form a new interface, which continuously undergoes decomposition and regeneration and generates heat.

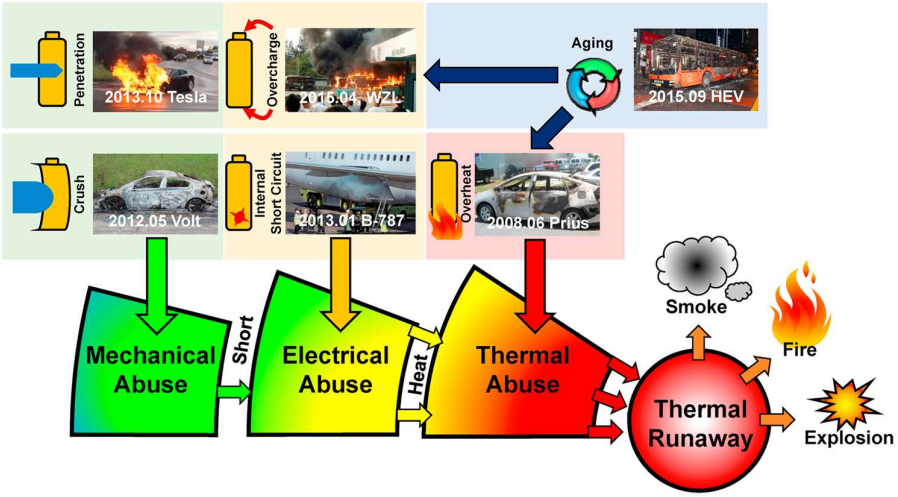

Figure 1.3 Accidents related to thermal runaway of LIBs caused by mechanical abuse, electrical abuse, and thermal abuse.[37]

As the battery's temperature approaches the melting point of the separator, typically around 130°C for polyethylene (PE) and 160°C for polypropylene (PP), the separator begins to shrink and deform locally.[40, 41] This mechanical failure can lead to direct contact between the cathode and anode, causing an internal short circuit (ISC) and a rapid increase in the rate of heat generation. Excessive heat accumulation subsequently leads to the volatilization and decomposition of the organic carbonate-based electrolyte, releasing flammable gases. Simultaneously, the commonly used binder polyvinylidene fluoride (PVDF) can react with lithium to produce hydrogen gas, further increasing the internal pressure of batteries.[42, 43] This stage is also marked by multiple exothermic processes, including the decomposition of lithium salts and cathode materials, as well as chemical crosstalk between the electrodes. Lithium hexafluorophosphate ($LiPF_6$), a commonly used lithium salt, decomposes at elevated temperatures into lithium fluoride (LiF) and the Lewis acid phosphorus pentafluoride (PF_5). PF_5 can further react violently with the electrolyte solvent, releasing toxic hydrofluoric acid (HF) gas. The thermal decomposition temperatures of cathodes vary, and the oxygen release mechanisms of commonly used cathodes such as lithium cobalt oxide ($LiCoO_2$, LCO), $Li(Ni_{0.33}Co_{0.33}Mn_{0.33})O_2$ (NCM111), and $Li(Ni_{0.8}Co_{0.15}Al_{0.15})O_2$ (NCA) have been widely reported.[44-48] The released oxygen, due to its high reactivity, may react with the anode and the electrolyte, further fuelling combustion reactions. As these exothermic reactions proceed in a positive feedback loop, the battery temperature rises more rapidly. Once the internal pressure exceeds the threshold of the pressure relief valve, a large volume of flammable gas is rapidly expelled, exacerbating the propagation of thermal runaway and potentially resulting in explosion.

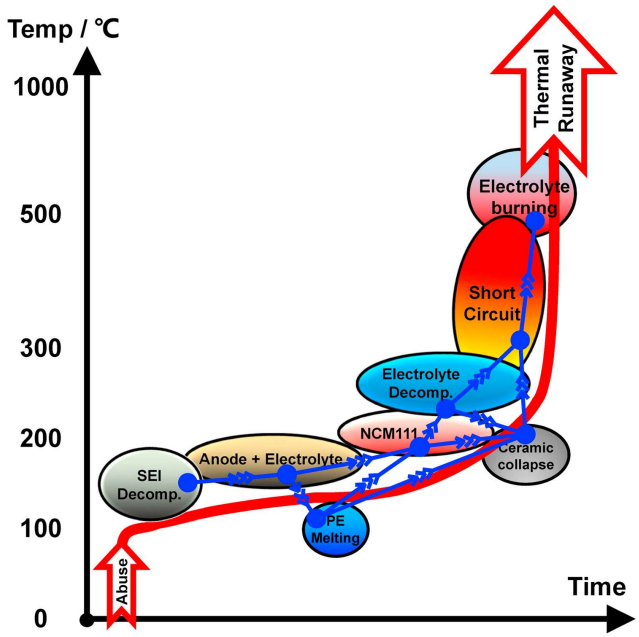

Figure 1.4 Schematic illustration of the thermal runaway mechanism of a LIB consisting of a NCM111 cathode, a graphite anode, and a PE-based ceramic-coated separator.[37]

1.3. Strategy to improve electrolyte safety

To mitigate safety risks, various strategies have been developed, including physical and chemical modifications of battery components and enhancements to battery management systems (BMS).[49, 50] Among these, improving the intrinsic flame retardancy of LEs is considered the most critical and effective approach, particularly considering the mechanisms underlying thermal runaway. Several methods have demonstrated the potential to enhance the intrinsic safety of electrolytes, such as the incorporation of flame retardants (FRs), the solidification of electrolytes, the application of high-concentration electrolytes, and the adoption of thermally stable lithium salts.

1.3.1. Using flame retardants as additives

The combustion of electrolytes is driven by a chain reaction, which can be interrupted by adding suitable FRs to reduce their flammability. According to their flame-retardant mechanisms and elemental composition, the most commonly used FRs in electrolytes are phosphorus-based, fluorine-based, and phosphorus- and fluorine-containing compounds.[51-53] Although these additives can terminate the combustion chain reaction by scavenging reactive radicals such as hydrogen radicals (H·) and hydroxyl radical (HO·), it remains challenging to achieve inherent non-flammability, as the effectiveness of FRs is limited when used in small amounts (typically less than 40%). Moreover, most additives are electrochemically incompatible, which can severely degrade battery performance by increasing electrolyte viscosity and decreasing ionic conductivity.

1.3.1.1. Phosphorus-based flame retardants

Organophosphorus FRs are the most extensively studied additives due to their structural diversity, low toxicity, low cost, and high flame-retardant efficiency. As shown in Figure 1.5, phosphorus-based FRs commonly used in LIB electrolytes can be classified into pentavalent P(V) and trivalent P(III) compounds based on the oxidation state of the phosphorus atom.[54-61] P(V) FRs include (i) Phosphate (e.g., trimethyl phosphate (TMP), triethyl phosphate (TEP), tributyl phosphate (TBP), and triphenyl phosphate (TPP)); (ii) Phosphonate (e.g., dimethyl methylphosphonate (DMMP), diethyl ethylphosphonate (DEEP)); (iii) Phosphinate (e.g., 1-diphenylphosphoryloxy-4-methylbenzene (DPMB), 9,10-dihydro-9-oxa-10-phosphaphenanthrene-10-oxide (DOPO)), and (iv) multi-elemental FRs, such as phosphine oxide-based compounds (e.g., bis(N, N-diethyl)(2-methoxyethoxy) methylphosphonamidate (DEMEMPA)) and cyclotriphosphazene-based compounds (e.g., hexafluorocyclotriphosphazene (HFPN), ethoxy(pentafluoro)cyclotriphosphazene (PFPN)). P(III) FRs are represented by trimethyl phosphite (TMPi), triethyl phosphite (TEPi), triphenyl phosphite (TPPi), etc.

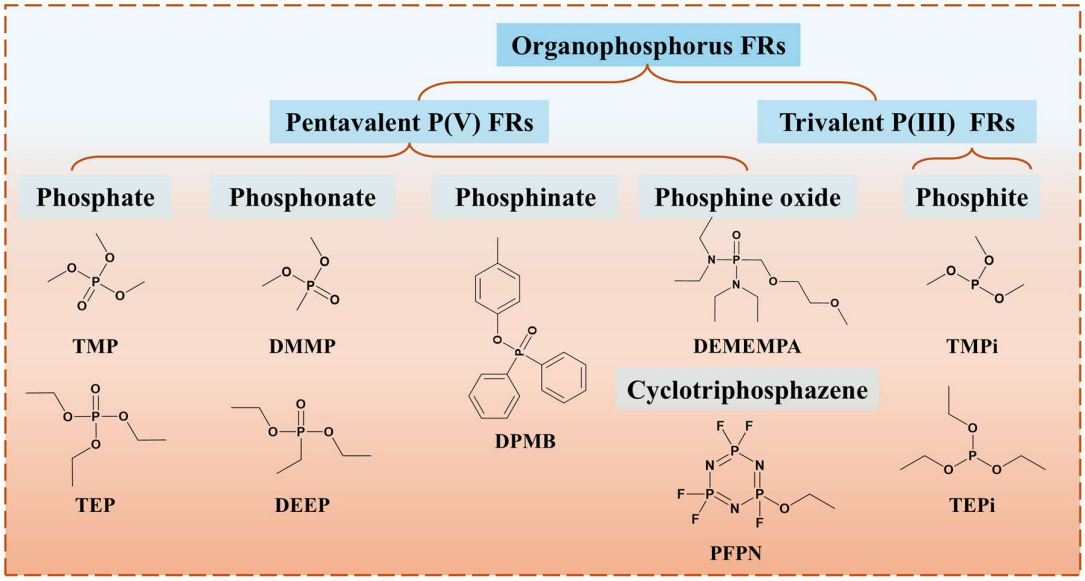

Figure 1.5 Structural demonstration of typical organophosphorus FRs applied to improve flame retardancy of LIB electrolytes.

As demonstrated in Figure 1.6, phosphorus-based FRs exhibit excellent flame-retardant performance through three primary mechanisms.[54, 62, 63] (i) Commonly used alkyl carbonate solvents will produce hydrogen radicals (H·) when heated. The generated H· will further react with oxygen to generate oxygen radicals (O·) and continue to trigger the formation of more free radicals. Organic phosphorus FRs are good free radical scavengers as they can decompose into phosphoric acid (H_3PO_4) at high temperatures, which subsequently converts into phosphorus oxygen radicals (PO·) to disrupt the propagation of free radical reactions. (ii) H_3PO_4 undergoes an endothermic dehydration reaction at elevated temperatures to yield phosphorus pentoxide

(P_2O_5) and water (H_2O), as described in Eq 1.1. This reaction absorbs heat from the combustion zone, lowers the local temperature, and thus suppresses flame propagation. (iii) The solid P_2O_5 can act as a non-combustible barrier by creating a protective layer on the fuel surface, thereby reducing the oxygen concentration and physically isolating the fuel from oxygen. Additionally, some phosphorus FRs can promote carbonization and facilitate the formation of carbon layers that further insulate the fuel and inhibit oxygen access.

$$2H_3PO_4 \rightarrow P_2O_5 + 3H_2O \qquad \text{Eq 1.1}$$

Phosphorus-based FRs exhibit excellent thermal stability and battery performance at both room and elevated temperatures, making them promising additives for reducing the risk of electrolyte. Several studies have reported that the incorporation of phosphates can effectively suppress undesirable chemical reactions within the battery.[64] However, despite these advantages, phosphorus-based FRs often show high viscosity and limited compatibility with carbon-based anodes, which will reduce the electrolyte ionic conductivity and greatly shorten the battery's cycle life.

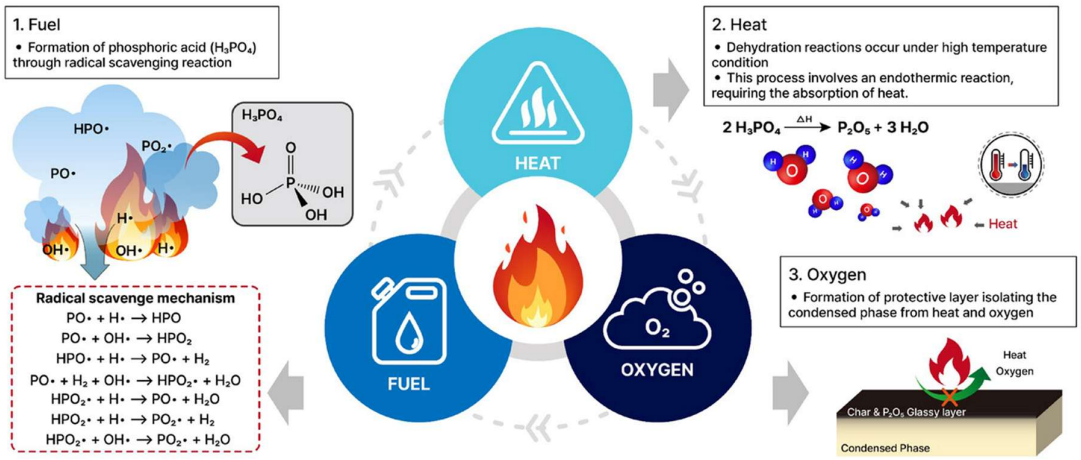

Figure 1.6 Combustion suppression pathway of phosphorus-based FRs targeting fuel, heat, and oxygen availability.[54]

1.3.1.2. Fluorine-based flame retardants

Unlike organophosphorus FRs, halogen-based FRs typically exhibit higher flash points and good thermal stability. Among them, fluorinated additives stand out due to their low viscosity and superior performance at low temperatures. Owing to their high flame-retardant efficiency and exceptional electrochemical compatibility, they are regarded as one of the most promising candidates for constructing non-flammable solvent systems.[65] Figure 1.7 presents several representative fluorides used as electrolyte solvents in LIBs.

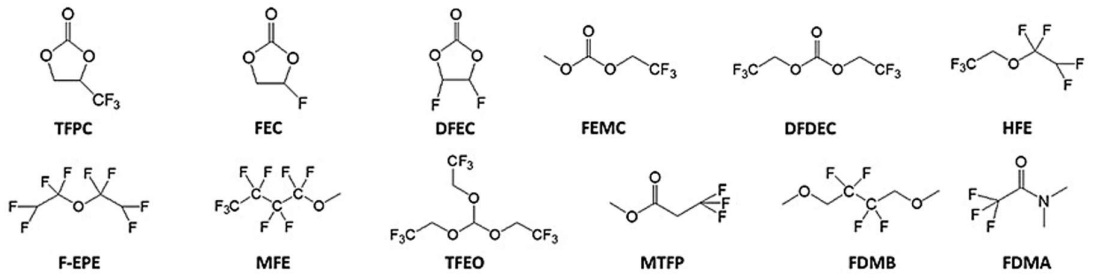

Figure 1.7 Structures of some fluorides used in LEs for Li batteries.[66]

Fluorinated FRs generally present favorable electrochemical properties and effective flame-retardant performance. Their low viscosity reduces intermolecular interactions among solvent molecules, thereby enhancing ionic conductivity. Additionally, the incorporation of fluorine can improve the composition and morphology of the SEI layer, helping to mitigate capacity fade associated with the use of high-concentration electrolyte additives. However, fluorine-based FRs often show limited compatibility with $LiPF_6$-based electrolytes. Furthermore, due to the need for specialized equipment and rigorous synthesis procedures, their high cost remains a major barrier to large-scale application. The generation of HF gas during decomposition also poses significant environmental and health risks.[67, 68]

1.3.1.3. Phosphorus- and fluorine-containing flame retardants

The incorporation of a single-element FR often presents a dilemma between flame retardancy and electrochemical compatibility. Achieving both excellent electrochemical performance and non-flammability is typically contradictory. To address this challenge, a multi-elemental flame-retardant strategy has been proposed.[69-71] By harnessing the synergistic effects of multiple functional elements, phosphorus- and fluorine-containing FRs offer notable advantages over single additives in electrolytes. This approach allows for a reduced additive concentration without compromising effectiveness, thereby minimizing undesirable side reactions and preserving overall battery performance. Additionally, it helps maintain low viscosity and high ionic conductivity, stabilizes the SEI, and mitigates capacity degradation under high-temperature conditions.

Several fluorinated phosphate-based FRs have been successively developed, with studies demonstrating that fluorination of phosphate can simultaneously enhance capacity retention and reduce combustion duration.[67, 68] When cyclotriphosphazene-based FRs such as PFPN and hexafluorocyclotriphosphazene (FPPN) are added at concentrations of 5%, the electrolyte exhibits self-extinguishing behavior. As shown in Figure 1.8, Yusuf et al. employed time-of-flight secondary ion mass spectrometry (TOF-SIMS) and transmission electron microscopy (TEM) to reveal that PFPN-based electrolytes can form a FR-derived cathode-electrolyte interphase (CEI) layer on the surface of the LFP.[72] This CEI layer, enriched with phosphorus and nitrogen elements, effectively suppresses the formation of a thick parasitic lithium fluoride (LiF) layer, thereby improving the electrochemical integrity of the battery. As a result,

developing new types of multi-elemental FRs that work effectively in electrolytes is an insightful approach to improving battery safety.

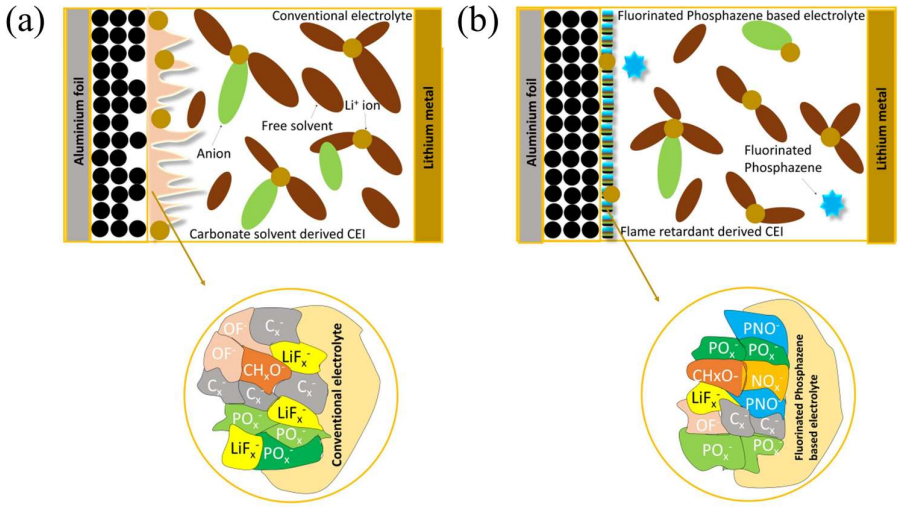

Figure 1.8 Schematic diagram of the CEI layer and fragment mosaic generated on the LFP electrode surface by (a) commercial electrolyte and (b) PFPN-based electrolyte.[72]

1.3.2. Solidification of liquid electrolytes

Replacing traditional LEs with solid-state alternatives offers an attractive option to the long-standing conflict between safety and electrochemical performance. Solid-state electrolytes (SSEs) are increasingly viewed as strong candidates to replace conventional organic LEs due to their inherent non-flammability and enhanced thermal stability.[73, 74] These electrolytes can be broadly categorized into three main types: solid inorganic electrolytes (SIEs), solid polymer electrolytes (SPEs), and composite solid-state electrolytes (CSSEs). Each class presents unique advantages and challenges in terms of ionic conductivity, interfacial compatibility, and mechanical strength. The transition toward SSEs not only addresses safety concerns but also lays the foundation for the development of next-generation high-energy-density batteries.[75]

1.3.2.1. Solid inorganic electrolytes

In comparison with conventional LEs, as presented in Figure 1.9, SIEs such as oxides, sulfides, and halides have attracted significant attention for the development of high-performance SSEs due to their solid nature, broader operating temperature ranges, and superior mechanical robustness.[76] Among them, crystalline oxide-based electrolytes stand out for their excellent air and thermal stability, as well as relatively low fabrication costs. Representative systems include garnet-type (e.g., $Li_{6.4}La_3Zr_{1.4}Ta_{0.6}O_{12}$, LLZTO), perovskite-type (e.g., $Li_{3x}La_{2/3-x}TiO_3$, LLTO), and NASICON-type materials (e.g., $Li_{1+x}Al_xGe_{2-x}(PO_4)_3$, LAGP) and $Li_{1+x}Al_xTi_{2-x}(PO_4)_3$, LATP). On the other hand, sulfide-based electrolytes, such as $Li_{10}GeP_2S_{12}$ (LGPS), exhibit significantly higher ionic conductivities and reduced grain boundary resistance compared to their oxide counterparts, making them highly promising for high-rate battery applications.

Despite these advances, a critical bottleneck remains: the formation of a stable and efficient solid-solid interface between the electrolyte and electrodes. High interfacial impedance and poor interfacial contact often hinder Li^+ transport and compromise overall electrochemical performance.[77, 78] Addressing these interfacial challenges is essential for realizing the full potential of SIEs in next-generation all-solid-state batteries.

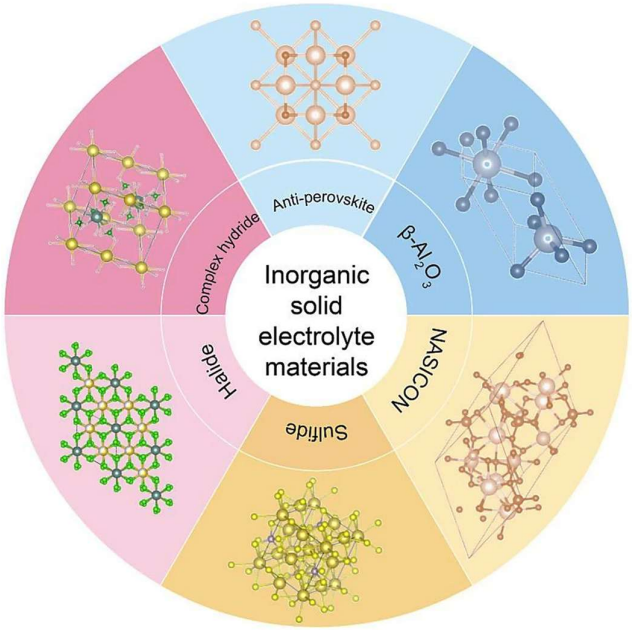

Figure 1.9 Main categories of inorganic solid electrolytes.[79]

1.3.2.2. Solid polymer electrolytes

Since the pioneering work by Fenton et al. in 1973, which demonstrated ionic conductivity in salt-doped polyethylene oxide (PEO), SPEs have garnered increasing attention due to their high flexibility, ease of processing, and enhanced safety compared to LEs. Unlike liquid systems, SPEs offer increased safety, reduced leakage risk, and improved mechanical integrity, making them attractive for safer lithium battery applications.[80]

PEO-based electrolytes are among the most extensively studied SPEs, largely due to their ability to solvate lithium salts through coordination with their ether oxygen atoms, which leads to the formation of relatively stable ion-conducting complexes. The Li^+ transport in SPEs relies on hopping between coordination sites provided by polar functional groups (e.g., ether oxygen or carbonyl groups) and the segmental motion of the polymer chains, as illustrated in Figure 1.10. On a molecular level, Li^+ migrates along the same polymer chain by hopping between adjacent coordinating sites, a process facilitated by local chain motion and flexibility. In addition, interchain transport plays a crucial role, wherein Li^+ transfer from one polymer chain to another through transient coordination exchanges, enabling long-range ion conduction across the bulk material. This dual-pathway transport is strongly dependent on the polymer's morphology and thermal dynamics.[81, 82] However, PEO is semicrystalline at room temperature,

and its crystalline domains restrict chain mobility, resulting in low ionic conductivity in ambient conditions (typically < 10^{-6} S cm^{-1}). The conductivity improves significantly above its melting point (~60°C), where the polymer transitions to an amorphous state, but elevated temperatures may not be suitable for all battery applications. Therefore, enhancing ionic conductivity can be achieved through strategies such as facilitating lithium salt dissociation, lowering the polymer's glass transition temperature (T_g), and reducing crystallinity to increase the proportion of amorphous phases.[83-85] These modifications increase the density and mobility of coordination sites, thereby optimizing both intrachain hopping and interchain transfer pathways essential for efficient ion transport in SPEs.

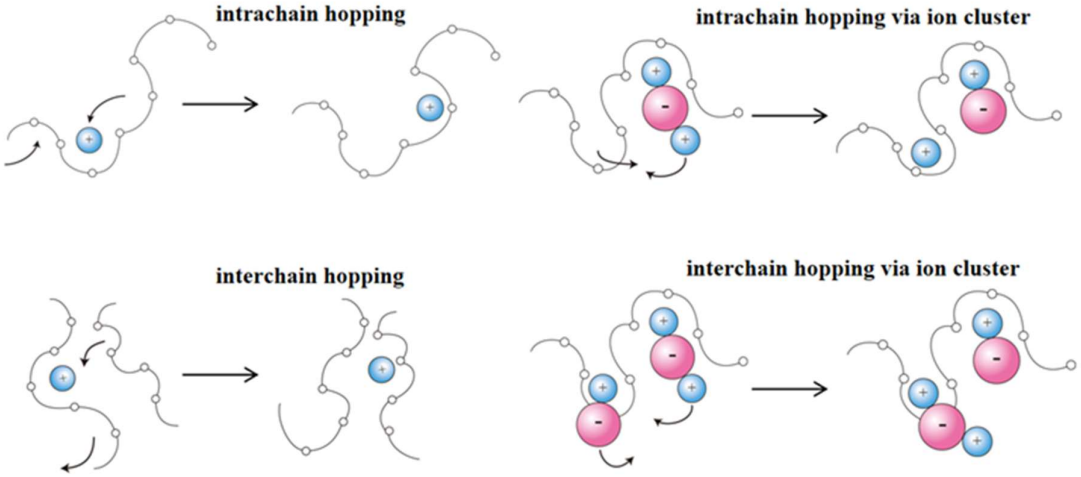

Figure 1.10 Li^+ transport occurs through a combination of intrachain and interchain hopping between coordination sites in the PEO chains.[81]

Nowadays, various polymer matrices have been extensively investigated for SPE development, including polyacrylonitrile (PAN), polymethyl methacrylate (PMMA), polyvinyl chloride (PVC), polyvinylidene fluoride (PVDF), and its copolymer poly(vinylidene fluoride-co-hexafluoropropylene) (PVDF-HFP).[84, 86-88] These polymers exhibit distinct chemical structures and polarities, enabling different functionalities such as lithium salt dissolution, ionic mobility regulation, and mechanical reinforcement. For instance, PAN offers strong polarity to facilitate lithium salt dissociation, while PVDF and PVDF-HFP provide excellent chemical stability and high dielectric constants, making them ideal for enhancing interfacial compatibility and overall electrolyte stability.

Despite these advantages, SPEs still face significant barriers to widespread application. The segmental mobility of polymer chains is significantly restricted at lower temperatures, leading to sluggish ion transport and poor performance in high-energy-density batteries. In addition to conductivity issues, SPEs face other challenges, including unstable electrode interfaces, trade-offs between mechanical strength and ionic mobility, and limited thermal stability.

1.3.2.3. Composite solid-state electrolytes

The drive to overcome the limitations of SPEs has sparked growing interest in CSSEs, which incorporate inorganic fillers or adopt gel-polymer frameworks to achieve a balance of high ionic conductivity, interfacial stability, and mechanical robustness. This multifunctional design approach is facilitating the transition of SPEs toward practical use in next-generation all-solid-state lithium batteries (ASSLBs).[89, 90] Rather than relying on single-phase polymers, CSSEs leverage the complementary properties of tailored host matrices and dispersed components to enhance both performance and durability. Their development is now considered a key direction for advancing ASSLB technologies.[91]

As illustrated in Figure 1.11a, recent progress in structural engineering and materials integration has enabled the classification of CSSEs into several representative types.[92] The first configuration (Figure 1.11b) incorporates dispersed inorganic fillers, including zero-dimensional (0D) nanoparticles, one-dimensional (1D) nanowires, and two-dimensional (2D) nanosheets, uniformly distributed within a polymer matrix. These fillers not only reduce the crystallinity of the polymer to facilitate Li^+ transport but also introduce complementary conduction pathways. The second type (Figure 1.11c) is a heterogeneous multilayer structure, in which layers with distinct functionalities, such as ion-conducting and mechanically supportive components, are sequentially assembled to achieve a balanced enhancement in electrochemical and mechanical performance. The third structural (Figure 1.11d) form involves three-dimensional (3D) interconnected inorganic frameworks infused with polymer electrolytes. This architecture offers both continuous Li^+ conduction networks and superior structural integrity, making it especially attractive for high-performance solid-state battery applications.

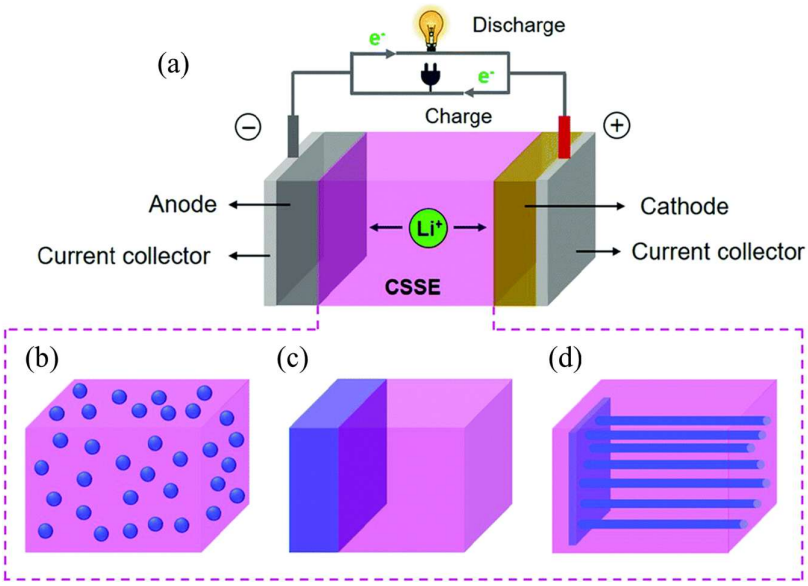

Figure 1.11 (a) Schematic of an ASSLB based on CSSEs and their structural types: (b) nanoparticle-filled matrix, (c) heterogeneous layered structure, and (d) 3D inorganic framework with polymer infiltration.[92]

With more and more attempts, various hosts and dispersed phases are combined into potential CSSEs, which not only enable a high ionic conductivity but also give good stability. Despite the widely held belief that SSEs offer superior safety compared to liquid systems, especially in lithium-metal batteries (LMBs), such claims remain insufficiently substantiated. Key challenges such as interfacial instability, moisture sensitivity, heat accumulation, and the risk of thermal runaway remain significant barriers to progress.[93]

1.3.3. Concentrated electrolytes

Although SSEs offer advantages in safety, their high interfacial resistance and low ionic conductivity have driven researchers to explore more practical alternatives, such as concentrated electrolytes.[94-96] Increasing the salt concentration in an electrolyte enhances interactions between cations, anions, and solvent molecules, while significantly reducing the amount of free solvent. Once the salt concentration surpasses a threshold (typically ~3-5 M), free solvent molecules are nearly eliminated, giving rise to a new class of highly concentrated electrolytes (HCEs) with unique solvation structures and superior electrochemical properties.

As illustrated in Figure 1.12, the high salt content fundamentally alters the solvation environment, resulting in the near absence of free solvent molecules.[97] This suppresses side reactions involving the solvent and significantly improves the overall electrochemical stability. Moreover, such a solvation structure promotes the formation of an anion-rich SEI enriched with inorganic species (e.g., LiF, Li_2O), which is chemically stable and structurally dense, thereby extending the battery's cycle life.

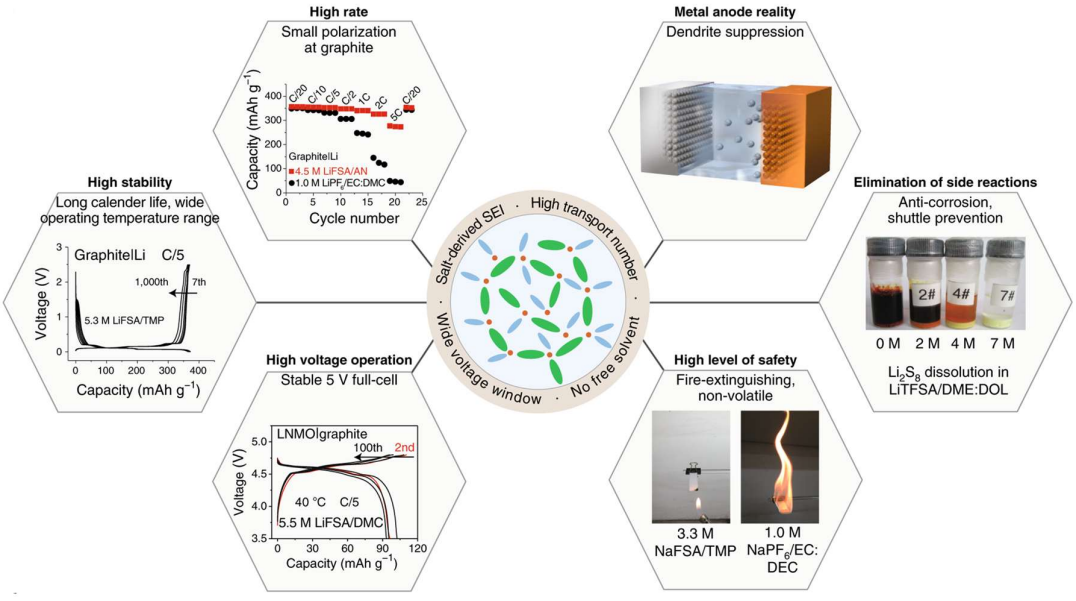

Figure 1.12 Schematic illustration of the electrochemical and thermal properties of HCEs.[97]

HCEs also exhibit a higher lithium transference number, which helps reduce polarization and enhances rate performance. In addition, the broadened electrochemical stability window allows

compatibility with high-voltage cathode materials. Beyond electrochemical advantages, HCEs also improve safety from a thermal standpoint.[98] The suppression of volatile free solvents leads to reduced flammability and mitigates the risk of thermal runaway, making them inherently safer under abuse conditions compared to conventional dilute electrolytes. From a practical perspective, HCEs are relatively easy to prepare and compatible with existing LE manufacturing infrastructure, which lowers production costs. Collectively, these characteristics make concentrated electrolytes a promising solution for enhancing the safety, energy density, and cycle life of next-generation lithium batteries.[99]

The highly concentrated nature of HCEs leads to a unique solvation structure, fundamentally governed by the competitive coordination between Li^+, solvent molecules, and anions. By tuning these interactions, the electrolyte's physicochemical and interfacial properties can be significantly optimized. Depending on the mode of coordination around Li^+, three primary solvation structures are typically observed: solvent-separated ion pairs (SSIP), contact ion pairs (CIP), and aggregates (AGG).[100] As illustrated in Figure 1.13, in dilute electrolytes, Li ions are primarily coordinated by solvent molecules, forming SSIPs, which tend to produce SEI layers rich in organic components at the electrode surface. With increasing salt concentration, the amount of free solvent decreases, and anions increasingly participate in the Li^+ coordination environment, leading to the formation of CIPs and AGGs. These structures promote the development of more stable SEIs that are enriched with inorganic species. The ability of a solvent to coordinate with Li^+ depends strongly on its dielectric constant and donor number (DN).[101] A high dielectric constant weakens the electrostatic interactions between ions, facilitating salt dissociation, while a high DN indicates stronger coordination ability with Li^+. In HCEs, the near elimination of free solvent molecules results in a densely cross-linked network dominated by AGG structures. This solvation regime is key to achieving high interfacial stability and robust electrochemical performance.[102, 103]

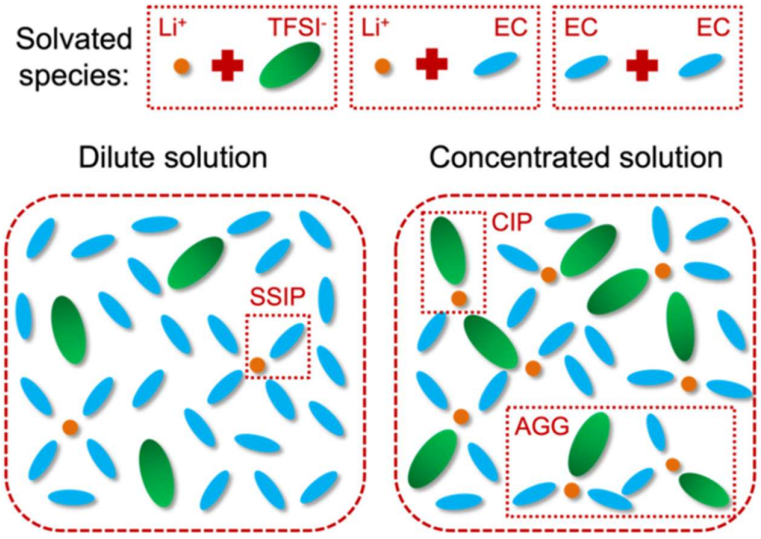

Figure 1.13 Comparison of Li^+ coordination environments in conventional LEs and HCEs.[100, 102]

1.4. Safety evaluation of lithium-ion batteries

Besides material optimization, it is requisite to perform comprehensive and systematic fire and explosion hazard assessments to circumvent potential risks at the earliest possible stage. In response to the dilemma, various safety assessment methods have been proposed over time, which can be briefly categorized into laboratory and industrial levels according to the scales of implementation. For instance, most laboratory research is concentrated on individual battery components, such as electrodes, electrolytes, separators, and SEI, with LEs being the most extensively studied due to their commercial maturity and notorious thermal instability.[54, 104-106] Beyond component-level analysis, the single-cell level has also gained increasing attention, particularly with the use of adiabatic calorimetry techniques such as the accelerating rate calorimeter (ARC), which enables direct quantification of a battery cell's thermal runaway behavior under near-adiabatic conditions, offering critical parameters such as self-heating rates, onset temperatures, and total heat release,[107] which are invaluable for understanding thermal stability and for designing safer battery chemistries and management systems.

1.4.1. Electrolyte flammability evaluation

The first work regarding flammability evaluation of LE was conducted by Wang et al.,[55] where glassy filters were adopted to immerse LE, and the samples were ignited vertically on an iron stand to record the burning time regarding the test procedure of plastic materials. After that, Xu et al. proposed a concept of "self-extinguishing time (SET)" in 2002, which is defined by normalizing the burning time against the mass of LE as Eq 1.2 shows:[108]

$$\mathrm{SET} = \frac{Burning\ time}{Mass\ of\ LE} \qquad \text{Eq 1.2}$$

where burning time and mass of LE correspond to the time from ignition to extinguishment and the mass of LE. Three different classes have been categorized as follows: (i) nonflammable: SET≤6 s g^{-1}; (ii) flame-retarded: 6<SET<20 s g^{-1}; (iii) flammable: SET≥20 s g^{-1}. Figure 1.14 illustrates an experiment evaluating the flammability of electrolytes using SET as an indicator.[109] The baseline electrolyte is highly flammable, with a SET value of 80 s g^{-1}, whereas the electrolyte modified with 2,2-difluoroethyl acetate (DFEA) is non-flammable, exhibiting a SET value of 0 s g^{-1}.

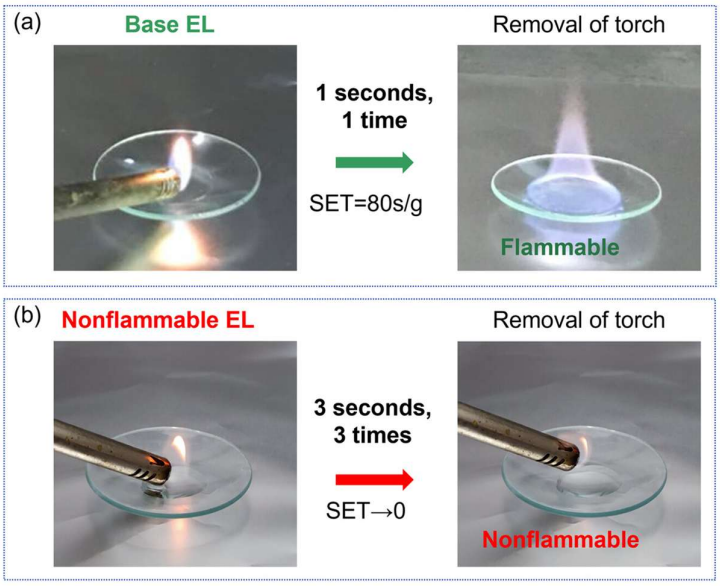

Figure 1.14 Flammability assessment of (a) the baseline electrolyte and (b) the experimental electrolyte using SET.[109]

In addition to SET, similar descriptive features were also put forward, including propagation rate and relative rate of SET, as illustrated by Eq 1.3 and Eq 1.4, respectively:

$$Propagation\ rate = \frac{Damaged\ length}{Propagation\ time} \quad \text{Eq 1.3}$$

where a glassfiber wick with ~140 mm length, absorbing ~5 g of LE samples, is set horizontally and ignited to allow the flame to spread for ~100 mm to record the propagation time.[51]

$$Relative\ rate = \frac{SET_0 - SE}{SET_0} \quad \text{Eq 1.4}$$

where SET_0 is obtained from the LE sample without additives, and SET is the value of modified LE.[110] Among these methods, SET has been widely recognized and extensively applied as an indispensable descriptor for LE safety. Subsequently, not only for LE, SET has also been adopted to evaluate the combustion behaviors of separators and gel polymer electrolytes (GPEs).[111, 112]

Except for the ignition test, differential scanning calorimetry (DSC) and thermogravimetric analysis (TGA) are powerful techniques exploited in the battery field to evaluate thermal stability and decomposition behavior of single components.[113, 114] DSC is a thermal analysis technique that measures the change in heat flow of substances during the temperature change. By recording the heat flow difference between the sample and the reference, DSC can be used to study the thermal properties of materials, such as melting point (T_m), T_g, and phase transitions. In the evaluation of electrolytes, DSC plays a key role in assessing thermal stability, phase behavior, and compatibility with electrodes, providing insights into their overall thermal response. It also enables the identification of decomposition onset temperatures. When mixed

with electrodes, DSC can reveal potential exothermic reactions, indicating thermal runaway risks. TGA complements DSC by providing the thermal decomposition behavior and volatility characteristics in electrolyte evaluations.[115, 116] By monitoring the mass change of samples during the heating process, TGA can determine the initial decomposition temperature, decomposition rate, and residue content of the electrolyte, thereby evaluating its thermal stability and thermal safety. For electrolytes containing highly volatile or easily degradable components, TGA is particularly suitable for analyzing their mass loss process and can be further used to compare the effects of different formulations on thermal stability.[113] However, both DSC and TGA results are highly sensitive to experimental parameters such as heating rate, sample quality, atmosphere type and flow rate. Therefore, strict control and consistency of test conditions are essential to ensure data reliability, reproducibility, and comparability across different samples and studies.

1.4.2. Single-cell safety assessment

To evaluate the thermal runaway behavior of individual cells, various thermal analysis techniques have been employed to investigate thermal stability and runaway characteristics from different perspectives. Typical methods include C80 microcalorimetry, cone calorimetry, ARC, and DSC, each focusing on different scales and thermal response processes. Among them, ARC is the most widely used, as it provides a near-adiabatic testing environment, unlike conventional measurements conducted under ambient conditions.[107, 117] In ARC tests, heat cannot dissipate to the surroundings but is instead entirely retain within the system, allowing the released reaction energy to directly contribute to the self-heating of LIBs. This setup effectively eliminates the influence of heat exchange with the environment, enabling a more accurate representation of the cell's intrinsic thermal behavior.

Based on extensive experimental analysis, researchers have identified four key temperature parameters to quantify and characterize the thermal runaway process of LIBs, as illustrated in Figure 1.15: the onset temperature of abnormal heat generation (T_1), the trigger temperature (T_2), the maximum temperature (T_3), and the maximum temperature rise rate ($(dT/dt)_{max}$).[118] T_1 reflects the overall thermal stability of the battery, T_2 corresponds to the inflection point where the temperature rise rate increases sharply, T_3 indicates the final stage of thermal runaway, and $(dT/dt)_{max}$ is generally positively correlated with the energy density of cells. Based on these characteristic temperatures and actual operating conditions, the thermal runaway process can be divided into four stages. In the first stage ($T < T_1$, typically below ~90°C), the battery remains relatively stable, with minor exothermic reactions such as the decomposition of SEI, and the temperature rise rate is low. The second stage, or thermal accumulation stage, involves exothermic reactions between the anode and the electrolyte, leading to heat buildup and shrinkage or melting of the separator. This causes ISC, marking the onset of thermal runaway, and the temperature rise rate increases rapidly.[119] In the third stage, as the temperature reaches

T_2, intense exothermic reactions occur, including electrolyte decomposition and chemical interactions between electrodes, releasing a large amount of heat and pushing the temperature rise rate to its maximum. Finally, in the fourth stage, when the temperature approaches T_3, the battery undergoes violent reactions accompanied by rapid gas release. The resulting pressure buildup can rupture the cell casing, causing ejection of materials, fire, or even explosion, which occur within a very short time.[117, 120]

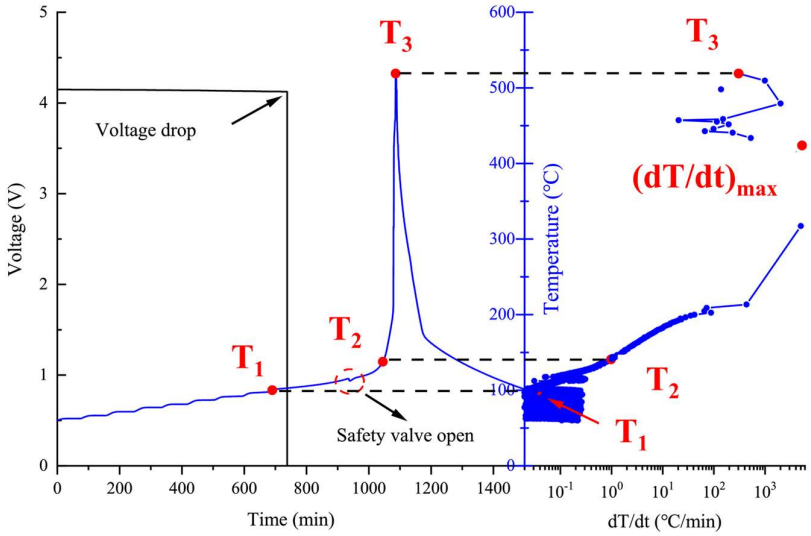

Figure 1.15 The temperature, voltage, and temperature increase rate of a commercial NCM811- Si_x/C cylinder LIB with a typical capacity of 4.5 Ah during the ARC test.[118]

1.4.3. Industrial battery safety evaluation

In contrast to the above electrolyte and single-cell assessments, safety evaluations at the industrial level focus primarily on modules, packs, and complete systems, as these more accurately reflect real-world application scenarios. Such assessments typically follow standardized testing protocols set by authoritative international bodies. To date, several safety standards have been introduced for LIBs, including IEC 62660-3 (International, 2022) for cell-level assessments, ISO 6469-1 (International, 2019) for pack and module levels, and GB/T 36276 (China, 2018) for system-level evaluations.[121-123]

Despite ongoing advancements and refinements in industrial battery evaluations, many risks and challenges persist. For instance, during the safety evaluation of a 50 Ah LFP/graphite battery pack consisting of five 10 Ah cells, Ping et al. encountered two or three jet flames, which presented significant safety threats to both the operator and the surrounding environment.[124] This is even more concerning when the test object is an EV battery that can support 400 kilometers of driving (Tesla MODEL S has a capacity of more than 80 kWh) or a container-type LIB energy storage station.[125] Furthermore, large-scale battery hazard analysis requires significant investment in experimental resources and infrastructure, which makes

existing standards-primarily designed for industrial applications-difficult to implement in standard laboratory environments.[126]

1.5. Motivation and objectives

Enhancing the fire safety of LIBs demands both the rational design of thermally stable electrolytes and the establishment of a standardized, quantitative evaluation framework.

Conventional approaches, such as incorporating FRs into electrolytes, offer simplicity but often suffer from an inherent trade-off between flame resistance and electrochemical performance. HCEs have shown potential in balancing these conflicting properties, yet their practical implementation is constrained by high production costs. SSEs, widely recognized for their non-flammable nature, represent a promising alternative. Among SSEs, CSSE, which addresses the poor interfacial compatibility of SIEs and the insufficient ionic conductivity of SPEs, has emerged as a leading strategy to simultaneously achieve high ionic conductivity and favorable interfacial contact. The ideal CSSE should combine advanced material design with enhanced nonflammability and superior electrochemical performance to meet the demands of next-generation energy storage systems.

Beyond material innovation, the safety assessment of LIBs at multiple scales is of critical importance. In component-level assessments, LE has been the most extensively investigated, as it plays a key role in the self-accelerating thermal runaway process under abuse conditions. However, as the most widely used descriptor to evaluate the flammability of LEs, the SET test is often performed under inconsistent conditions, leading to poor reproducibility and limited comparability across studies. The absence of standardized protocols for evaluating electrolyte flammability remains a critical barrier to the advancement of battery safety investigation. Apart from flammability evaluations of isolated components, fire-safety assessments at the cell level can offer more valuable insights for the development of advanced battery components. Nevertheless, most current safety evaluations focus on isolated components (typically the electrolyte) while largely overlooking the correlation between material-level safety enhancements and the actual fire behavior of full cells. Whether flame-retardant electrolytes can truly translate into improved thermal safety at the cell level remains to be verified. Overall, the development of fire-safe LIBs faces three key challenges:

i) The development of innovative CSSEs with enhanced nonflammability and improved electrochemical performance is essential.

ii) A unified SET methodology is urgently needed to enable rigorous and comparable assessment of flame-retardant performance for LEs.

iii) It is essential to figure out the relationship between electrolyte flammability and battery combustion behavior under abuse conditions.

Against the above challenges, the objectives of this thesis include the following three aspects:

i) Design and fabrication of advanced composite electrolytes through the integration of novel FRs and ceramic fillers, aiming to simultaneously improve interfacial compatibility and intrinsic fire resistance.

ii) Develop a standardized SET evaluation method to ensure reproducible and quantitative comparisons of flame-retardant efficacy, and to clarify the flame suppression mechanisms of FRs in electrolytes.

iii) Systematically investigate the combustion behavior of full cells with FR-modified electrolytes and correlate it with electrolyte flammability to clarify the link between material-level and cell-level fire safety.

2. Materials and Characterization

2.1. Materials

To prepare the solid electrolytes in Chapter 3, lithium bis(trifluoromethanesulfonyl)imide (LiTFSI, 99.8%), PEO (M_w = 600,000), N-1-methyl-2-pyrrolidone (NMP), and acetonitrile (99.5%) were purchased from Sigma-Aldrich Chemical Co. Lithium foils, $LiFePO_4$ (LFP), PVDF, and carbon black (Super-P) were supplied by MTI Chemical Regent Company. $Li_{6.4}La_3Zr_{1.4}Ta_{0.6}O_{12}$ (LLZTO, D_{50} = 450-550 nm) was bought from Shenzhen Huaqing New Material Technology Co., Ltd (China). $[Cu_3(BTC)_2(H_2O)_3]$·Guest (HKUST-1) was synthesized and activated as reported before.[127]

To establish a unified method to access the flammability of LEs in Chapter 4, lithium hexafluorophosphate solution in ethylene carbonate and diethyl carbonate, 1.0 M $LiPF_6$ in EC/DEC=1/1 (v/v); lithium hexafluorophosphate solution in ethylene carbonate and dimethyl carbonate, 1.0 M $LiPF_6$ in EC/DMC=1/1 (v/v); lithium hexafluorophosphate solution in ethylene carbonate and ethyl methyl carbonate, and 1.0 M $LiPF_6$ in EC/EMC=1/1 (v/v) were purchased from Sigma-Aldrich and stored in glove box once received. As absorbent materials, Whatman® glass microfiber Grade GF/A (GFS) separator was ordered from Sigma-Aldrich. Cotton wicks (CW) of different diameters (Φ2, 4, 6, 8 mm), ceramic fiber paper biosoluble insulfrax paper (IP), battery case (BC), and glass watch (GW, Φ40, 60 mm) were purchased from markets, GFS, CW, and IP were cut in different size for purposes.

To check the feasibility of the unified method, 15 additives were chosen and bought. Among them, triethyl phosphate (TEP), trimethyl phosphate (TMP), trimethyl phosphite (TMPi), trioctyl phosphate (TOP), dimethyl methylphosphonate (DMMP), triphenyl phosphate (TPP), triphenyl Phosphite (TPPi), bis(2,2,2-trifluoroethyl) methylphosphonate (TFMP), tris(2,2,2-trifluoroethyl)phosphate (TTFP), ethoxy(pentafluoro)cyclotriphosphazene (PFPN), and pentafluoro(phenoxy)cyclotriphosphazene (FPPN) were ordered from Sigma-Aldrich. Tris(4-methoxyphenyl)phosphine (TMPPi), 2-ethylhexyl diphenyl phosphate (DPOF), cresyl diphenyl phosphate (CDP), and tris(2,2,2-trifluoroethyl) phosphite (TTFPi) were acquired from TCI Chemicals.

To evaluate the influence of flame-retardant electrolytes on pouch cell safety in Chapter 5, electrodes were purchased from Canrd Technology Co., Ltd, China. LFP cathode with an active material content of 91.5% is coated on an aluminum foil with a thickness of 14 μm, providing an areal capacity of 1.69 mAh cm^{-2} and an areal density of 12.3 mg cm^{-2}. Graphite anode with an active material content of 95.7% is coated on a copper foil with a thickness of 8 μm, offering an areal capacity of 1.97 mAh cm^{-2} and an areal density of 5.8 mg cm^{-2}. These electrodes were

stored in a drying container after receiving them and cut into dimensions of 4.3 cm × 5.6 cm for the LFP cathode and 4.5 cm × 5.8 cm for the graphite anode. Nickel (Ni) and aluminum (Al) tabs (width: 4 mm) with adhesive polymer tape were acquired from Nanografi Nano technology and used as negative and positive terminals, respectively, which were connected to electrodes before transferring. All tab-connected electrodes were transferred to the glove box after drying under a dynamic vacuum oven at 100°C overnight.

Battery grade commercial electrolytes (BLE): lithium hexafluorophosphate solution in ethylene carbonate and ethyl methyl carbonate, 1.0 M $LiPF_6$ in EC/EMC = 1/1 (v/v), were purchased from Sigma-Aldrich and stored in the glove box once received. Trimethyl phosphite (TMPi), dimethyl methylphosphonate (DMMP), and cresyl diphenyl phosphate (CDP) were acquired from TCI Chemicals. The modified electrolytes were prepared by stirring the mixture of 80 wt% BLE and 20 wt% additives in vials in the glove box overnight. 25 μm microporous polyolefin membrane (2400) was provided by Celgard, LLC, which was cut into a size of 6 cm × 6 cm and used as the separator after vacuum treatment at room temperature overnight. Aluminum laminated film was obtained from Dai Nippon Printing Co., Ltd, and cut into the specific size of 10 cm × 10 cm, two sides of which were pre-sealed outside the glove box, and the remaining two ends were used for current collector sealing and electrolyte injection in the glove box. The thickness of assembled pouch cells is 0.4 mm.

2.2. Characterization

Fourier transform infrared spectroscopy (FTIR)

FTIR spectroscopy was employed to gain molecular-level insights into the chemical structure and functional groups of CSSEs and FRs, enabling the identification of characteristic bonds and molecular interactions. Spectra were acquired in ATR mode with the ThermoFisher Nicolet 5700 spectrometer, ranging from 4000 to 400 cm^{-1}.

Scanning electron microscopy (SEM) and energy dispersive X-ray spectroscopy (EDS)

Morphological analysis of the electrolytes and char residues was conducted using a field emission scanning electron microscope (Apreo 2S, Thermo Fisher Scientific) operated at 5 or 15 kV. Before imaging, the samples were sputter-coated with gold for 120 seconds at a current of 40 mA. EDS was employed to analyze the elemental distribution, using an Ultim® Max detector (Oxford Instruments, UK) integrated into the SEM system.

X-ray diffraction (XRD)

XRD is widely employed in battery research to characterize the structural properties of electrolytes and electrodes, such as analyzing the crystallinity of polymer electrolytes and evaluating the phase structure of graphite anodes. In this thesis, XRD patterns were collected

using a PANalytical Empyrean diffractometer with Cu Kα radiation (λ = 1.5406 Å) at room temperature. The instrument was operated at 45 kV and 40 mA, and data were acquired over a 2θ range of 10° to 90°.

Differential scanning calorimetry (DSC)

DSC is a crucial technique for determining key thermal properties of polymers, such as the glass transition temperature (T_g), melting point (T_m), and crystallinity (χ_c), which affect Li^+ conduction, electrolyte fabrication processes, battery operating temperatures, etc. DSC was employed on TA Q200 with a ramp of 10°C min^{-1} in a nitrogen atmosphere within the temperature range of -90 to 150°C. Only the second heating round was collected to remove the thermal history. The χ_c of polymer electrolytes was calculated regarding enthalpies (ΔH_m) of PEO perfect crystals as Eq 2.1:

$$\chi_c = \frac{\Delta H_m}{\Delta H_{PEO} * f_{PEO}} \quad \text{Eq 2.1}$$

where ΔH_m and ΔH_{PEO} are the melting enthalpies of polymer electrolytes and PEO perfect crystals (213.7 J g^{-1}) respectively, while f_{PEO} is the weight fraction of PEO in CSSEs[128].

Thermogravimetric analysis (TGA) and FTIR-coupled TGA (TGA-FTIR)

TGA is essential for evaluating the thermal stability of battery components and FRs, while coupling TGA-FTIR enables the elucidation of decomposition mechanisms of FRs within the electrolyte matrix. The TGA curves under nitrogen atmosphere were measured by using TA Q50 with a heating rate of 10°C min^{-1} from ambient temperature to 800°C. TGA-FTIR measurement was carried out on a TA Q50 coupled with a Thermofisher Nicolet 5700 spectrophotometer. About 10 mg of each sample was heated from room temperature to 500°C with a heating rate of 10°C min^{-1} under nitrogen.

Dynamic mechanical analysis (DMA)

DMA was conducted using a TA Q800 in multifrequency strain mode to evaluate the mechanical characteristics of electrolytes, applying an initial static force of 1 mN and a ramp force of 0.1 N min^{-1}. Young's modulus is defined as the ratio of stress (σ) to strain (ε).

$$E = \frac{\Delta\sigma}{\Delta\varepsilon} \quad \text{Eq 2.2}$$

where $\Delta\varepsilon$ and $\Delta\sigma$ are axial strain (proportional deformation) and tensile stress (force per unit area) in the linear elastic region of stress-strain curves. Storage modulus (E'), loss modulus (E"), and damping factor (tan δ) were recorded at temperatures ranging from -80 to 60°C, with a heating rate of 3°C min^{-1} under a frequency of 1 Hz and a preload of 0.1 N; the dimension of sample was 30 × 5 mm^2, and make sure the sample length clamped by machine as close as possible during testing.

Macroscale cone colorimeter (MCC)

MCC was employed to quantitatively evaluate the combustion characteristics of the electrolyte membranes, providing insight into their heat release behavior at the microgram level. The samples (~5 mg) were heated from 100 to 700°C in the pyrolysis zone with a heating rate of 1°C s^{-1}, all experiments were done in quadruplicate. The heat release rate (HRR) was obtained from the oxygen depletion measurements in W g^{-1}.

Cone calorimeter test (CCT)

As shown in Figure 2.1, CCT is a standard method for evaluating the flammability and heat release characteristics of materials under controlled heat flux. It can provide crucial parameters such as heat release rate, total heat release, ignition time, and smoke production, offering comprehensive insights into combustion characteristics and fire hazards. The test was conducted using a dual cone calorimeter (Fire Testing Technology Inc.), with calibration performed following ISO 5660-1 standards before experimentation.

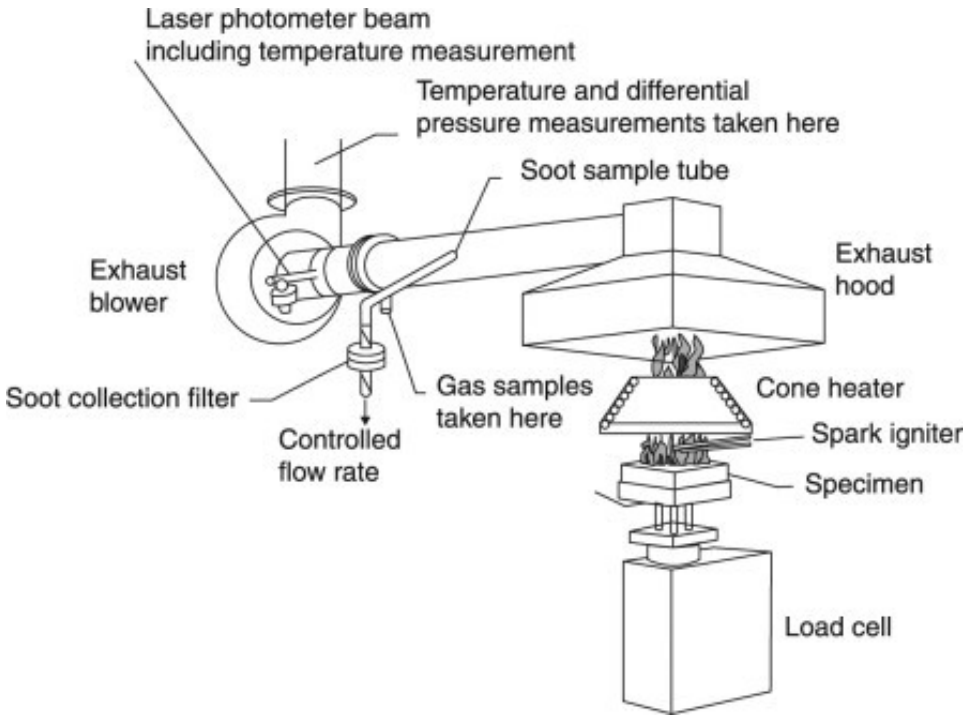

Figure 2.1 Schematic diagram of the main components of a cone calorimeter.[129]

Direct ignition test

Direct combustion tests offer a straightforward means to visually observe and roughly evaluate the burning phenomenon of electrolyte membranes. Samples of the same size (10 × 10 mm^2) were cut from electrolyte membranes and ignited with a portable gas lighter in a UL-test chamber. Once it caught fire, the ignitor was removed immediately, and the burning phenomenon was recorded by photos.

Linear sweep voltammetry (LSV)

LSV is a fundamental electrochemical technique employed to determine the electrochemical stability window (ESW) of electrolytes, which reflects their resistance to oxidative and reductive decomposition. By linearly sweeping the potential of an inert working electrode (SS), LSV identifies the onset potentials of electrolyte decomposition, offering crucial information about the anodic and cathodic limits.

Electrochemical impedance spectroscopy (EIS)

EIS was used to analyze the frequency-dependent response of electrolytes. By applying a small alternating current (AC) perturbation over a range of frequencies, EIS provides detailed information on charge transfer resistance, ion diffusion, and interfacial phenomena within electrolytes and electrode materials. As illustrated in Figure 2.2, the EIS spectrum can be divided into three main regions: the high-frequency (ohmic) region, the mid-frequency region, and the low-frequency region. The high-frequency region corresponds to the internal resistance of the battery, including the electrolyte and contact resistances. The mid-frequency region reflects the charge transfer processes occurring at the electrode/electrolyte interface and within the electrode's active material; this region typically appears as one or two semicircles, depending on the battery's composition and chemical properties. The low-frequency region is attributed to diffusion-related processes, such as ion diffusion within the electrode materials.

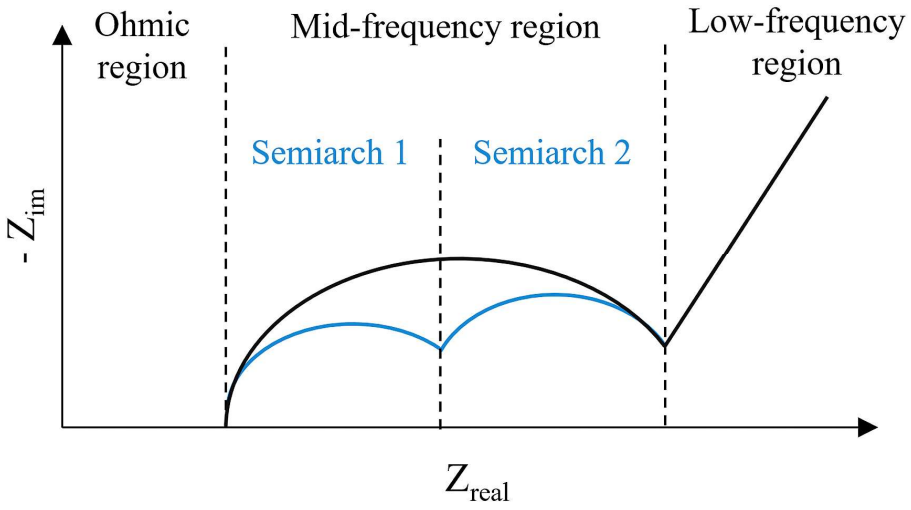

Figure 2.2 A representative Nyquist plot of LIB.[130]

Cyclic voltammetry (CV)

CV is an electrochemical technique used to study redox processes, reaction kinetics, and electrochemical properties of materials. During the CV test, the potential of a working electrode is cyclically swept between two voltages while measuring the resulting current, producing characteristic voltammograms. These voltammograms reveal information about oxidation and reduction potentials, electron transfer rates, and reversibility of electrochemical reactions.

Galvanostatic charge-discharge (GCD)

The GCD test is commonly employed to simulate the practical operation of batteries by applying a galvanostatic current while cycling the cell between predetermined voltage limits. It enables the evaluation of key performance metrics such as specific capacity, Coulombic efficiency, and cycling stability. In addition, rate capability testing is conducted under various current densities (C-rates) to assess the battery's ability to retain capacity during fast charge and discharge.

3. Design and Construction of Hierarchical Composite Solid Electrolytes

3.1. Introduction

To mitigate the flammability of both liquid and solid electrolytes, the incorporation of appropriate FRs was initially proposed.[14, 131-133] The employment of novel FRs has emerged as a key research direction in the design of advanced safer electrolytes. Among emerging candidates, metal-organic frameworks (MOFs) such as HKUST-1, ZIF-67, and UiO-66 have attracted considerable attention due to their tunable porosity, thermal stability, and demonstrated ability to suppress combustion.[134-136] At the same time, various crystalline oxides have been explored as SIEs due to their superior ionic conductivity and thermal stability, including garnet-type (LLZTO), perovskite-type (LLTO), and sodium superionic conductor NaSICON-type (LAGP and LATP).[137-139] Nevertheless, the key ongoing challenge is forming a stable solid-solid interface that minimizes interfacial impedance and enables efficient Li^+ transport.[140] To break out the limitation associated with the single polymer or inorganic solid electrolyte, CSSEs were defined and applied in numerous studies as they integrate the excellent flexibility of polymers and dendrite suppression capability of ceramics.[141-145] In previous work, Chen et al fabricated PEO/LLZTO CSSEs by adjusting the composite composition to achieve structure from “polymer in ceramic, PIC” to “ceramic in polymer, CIP”, where a high ionic conductivity of ~10^{-4} S cm^{-1} at 55°C was obtained;[146] Huo et al designed a sandwich CSSE structure referred to as “CIP-PIC-CIP” by leveraging the size effect, which enabled stable plating/stripping cycling at the current density of 0.2 mA cm^{-2} for 400 hours.[147] However, most works lack the consideration of fire safety evaluation for these modified CSSEs.

In this chapter, we construct a novel CSSE named PMC with a “CIP-PIC” bilayer structure, which is shown in Figure 3.1. This special hierarchical structure is formed due to the gravitational effect of ceramics during preparation, and the distribution of layers can be adjusted flexibly. With this unique structure, PMCs show inhibited crystalline ability and improved mechanical properties. Since its compatible contact interface and crystallization inhibition effect, the bilayer CSSE modified with 10% LLZTO (PMC10) shows an optimal ionic conductivity of 2.33×10^{-4} S cm^{-1} at 50°C, stable plating/stripping galvanostatic cycles for 900 h under 0.2 mA cm^{-2} and a favorable capacity retention efficiency of 80.3% after 200 cycles. Moreover, PMC10 demonstrates a significant enhancement in fire safety, as evidenced by a notable 33.4% reduction in heat release capacity (HRC).

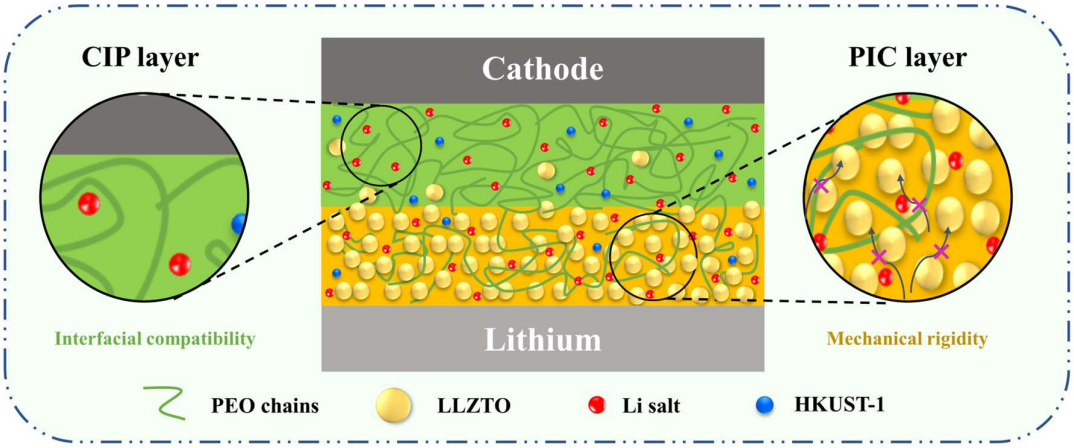

Figure 3.1 Schematic diagram of the hierarchical "CIP-PIC" PMC CSSEs for safer LIBs.

3.2. Experiment

3.2.1. Preparation of PMC solid-state electrolytes

Electrolyte membranes were prepared by the solution casting method. Briefly, 0.7 g PEO and 0.31 g LiTFSI (Li^+: EO = 1:15) were dispersed in acetonitrile and magnetically stirred overnight at room temperature to form a homogeneous solution, which was followed by adding 5 wt% activated HKUST-1 MOFs inside and stirring for another 2 h until evenly dispersed. Subsequently, pre-milled LLZTO powder (10, 30, and 50 wt%) was added to the slurry and stirred overnight. The blend was finally cast onto a horizontal Teflon plate and volatilized for 48 h to remove most of the solvent, then continued to dry in a dynamic vacuum oven at 40°C for another 48 h to make solvents evaporate completely. Hence, these CSSE membranes with a thickness of ~150 μm could be obtained and abbreviated as PMC10, PMC30, and PMC50 separately. PMC membranes were cut into circles with a 16 mm-diameter hole punch and transferred into the Ar-filled glove box after final vacuum drying for 6 h. Three control groups (PEO, PM, and PC10) were fabricated by similar preparation procedures as shown in Table 3.1, where the PEO group means without any additives except for Li salt (distinguishes from the pure PEO, which is commercial polymeric products without any treatment); the PM group was obtained by adding same concentration of MOFs based on PEO group; PC10 group was prepared by adding 10 wt% of LLZTO based on PEO group.

Table 3.1 Composition of various solid electrolytes for LIBs.

Group	Electrolyte matrix	Modification
Pure PEO	PEO	-
PEO	PEO + LiTFSI	-
PM	PEO + LiTFSI	5 wt% MOF

Group	Electrolyte matrix	Modification
PC10	PEO + LiTFSI	10 wt% LLZTO
PMC10	PEO + LiTFSI	5 wt% MOF + 10 wt% LLZTO
PMC30	PEO + LiTFSI	5 wt% MOF + 30 wt% LLZTO
PMC50	PEO + LiTFSI	5 wt% MOF +50 wt% LLZTO

3.2.2. Fundamental electrochemical measurement

Linear sweep voltammetry (LSV) measurements were performed to examine the ESW by using stainless steel (SS) as the working electrode and lithium metal as the counter electrode, with a scan rate of 0.1 mV s^{-1} from 2.0 to 5.5 V vs Li/Li^+. To determine the ionic conductivities (σ) of PMCs at different temperatures from 25 to 80°C, electrochemical impedance spectroscopy (EIS) was measured with a Biologic SP-200 potentiostat. The electrolyte membranes were squeezed between two pieces of SS for measuring the impedance within the frequency range of 0.1 to 10^6 Hz and an alternating current (AC) potential amplitude of 10 mV. The relevant formula used to calculate the ionic conductivity is as follows:

$$\sigma = \frac{d}{AR_b} \quad \text{Eq 3.1}$$

where d, A, and R_b indicate the thickness of PMC membranes, the electrode contact area, and the resistance obtained from the corresponding Nyquist plot, respectively. The activation energy of PMC electrolytes is calculated following the Arrhenius relation:

$$\sigma = \sigma_0 exp\left(-\frac{E_a}{kT}\right) \quad \text{Eq 3.2}$$

where σ_0, E_a, k, and T are the pre-exponential factor, activation energy, Boltzmann constant, and Kelvin temperature, respectively. In the potential range of 2.5 to 4.0 V vs Li^+/Li at 50°C, cyclic voltammetry (CV) was conducted with the Biologic SP-200 potentiostat at a scan rate of 0.1 mV s^{-1}.

3.2.3. Full cell performance evaluation

Lithium stripping and plating experiments were performed to evaluate the interfacial stability of PMC electrolytes against Li metal. Li|PMC|Li symmetrical cells were fabricated and tested for galvanostatic cycles at a current density of 0.2 mA cm^{-2}, including 0.5 h stripping and 0.5 h plating alternating steps at 50°C. To analyze the cycle life and rate capability, the cathode slurry was prepared by mixing LFP, PVDF, and Super P in NMP solvent at a mass ratio of 8:1:1, and the slurry was scraped onto aluminum foil using the doctor blade technique and dried in a vacuum oven at 80°C for 12 h. Afterward, the cathode sheets were cut into 13 mm discs and dried again at 110°C before being transferred to a glove box. Ultimately, a final loading of ~2

mg cm^{-2} for the active material was obtained. CR2032-type coin cells were assembled in the Ar-filled glovebox with LFP cathodes, PMC electrolytes, and Li metal anodes for cycling tests. Galvanostatic charge/discharge tests were carried out using Neware BTS-4000 charge/discharge battery testers under 50°C within a potential window of 2.5 to 3.8 V vs Li/Li^+ under various current densities; the specific current related to the 1C rate of LFP was assumed to be 170 mA g^{-1}.

3.3. Results and discussion

3.3.1. Structural and morphological characteristics of PMCs

The phase structure of PMC10, PMC30, and PMC50 electrolytes was characterized by XRD as shown in Figure 3.2a. The specific characteristic peaks of PEO, HKUST-1, and LLZTO diffractograms can be found in the patterns of PMC without impurity peaks, indicating that the mild preparation process can efficiently maintain the original structures. Compared to sharp and intense peaks at 19.2° and 23.3° in 2θ of highly crystalline PEO samples, both PMC10 and PMC30 electrolytes show widened and weakened intensity, while the peaks are negligible in PMC50. The comparatively reduced intensities of peaks in the XRD pattern indicate that the crystallization ability of PEO has been remarkably restricted with the increasing content of LLZTO.

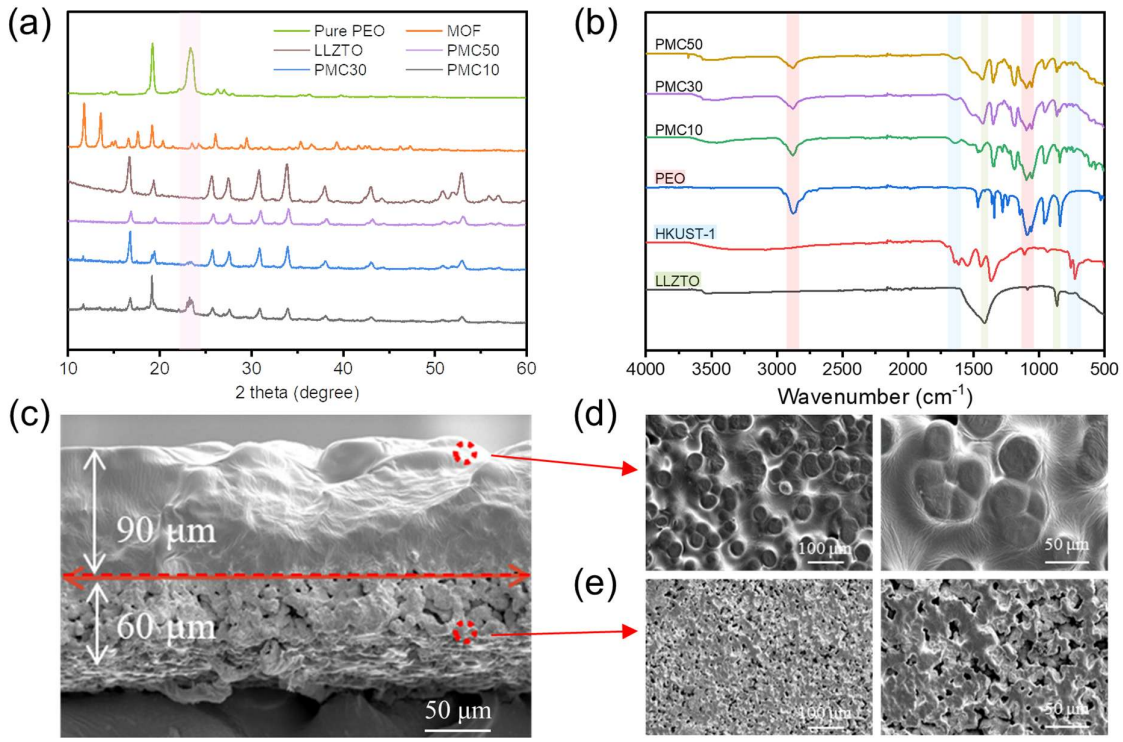

Figure 3.2 (a) XRD diffraction patterns and (b) FTIR spectra of PMCs. (c) Cross-sectional and (d, e) top-view SEM images of PMC50 CSSE.

Figure 3.2b offers the FTIR spectra for analyzing the inner molecular interaction of PMCs. Pure PEO shows a clear signal around 2871 cm^{-1}, attributed to the C-H stretching mode, and shifts to 2881-2884 cm^{-1} after the incorporation of MOF and LLZTO into PEO electrolytes. Furthermore, the semicrystalline phase of PEO is confirmed by the existence of a triplet peak of C-O-C stretching, found at 1144, 1091, and 1058 cm^{-1} vibrations.[148, 149] Compared with pure PEO, PMC electrolytes show a slight shift and broader peaks at 1188, 1096, and 1055 cm^{-1}, confirming the subtle alteration of chemical structure. Meanwhile, two functional groups (1647 cm^{-1} (C=O) and 726 cm^{-1} (C-H)) of HKUST-1 appear, and the characteristic absorption peaks at 862 and 1417 cm^{-1} occur in the spectrum of LLZTO.

Interfacial compatibility and stability are crucial factors affecting the electrochemical performance of solid electrolytes. As shown in SEM images of PMC50, Figure 3.2c, a distinct double-layer structure with a total thickness of ~150 μm is obtained with a smooth upper layer of "CIP" structure, thickened in ~90 μm, and a bottom layer of "PIC" structure, thickened ~60 μm. Furthermore, Figure 3.2d and 3.2e depict the surface topographies of two layers. The CIP layer shows uniformly dispersed island crystalline regions with a feature size of ~40 μm, which are generated due to the volatilization of solvents.[150] This unique structure is created by the gravity effect of LLZTO during the drying procedure and is verified by the EDS elemental mapping as shown in Figure 3.3. While the PIC layer has a relatively rough micrograph and is similar to the morphology of the pristine LLZTO, Figure 3.4a. Meanwhile, the distribution of layers can be adjusted by controlling the feeding ratio of polymers and ceramics. For example, PMC10 in Figure 3.4b displays a CIP-dominated bilayer interface. Contrary to images of PMCs, in Figure 3.4c, PEO SPE (Li^+: EO = 1:15) shows obvious semi-crystalline spherulite morphologies, which can be suppressed to some extent by the plasticizer effect of MOF nanoparticles, as the reduced and smaller spheres in Figure 3.4d.

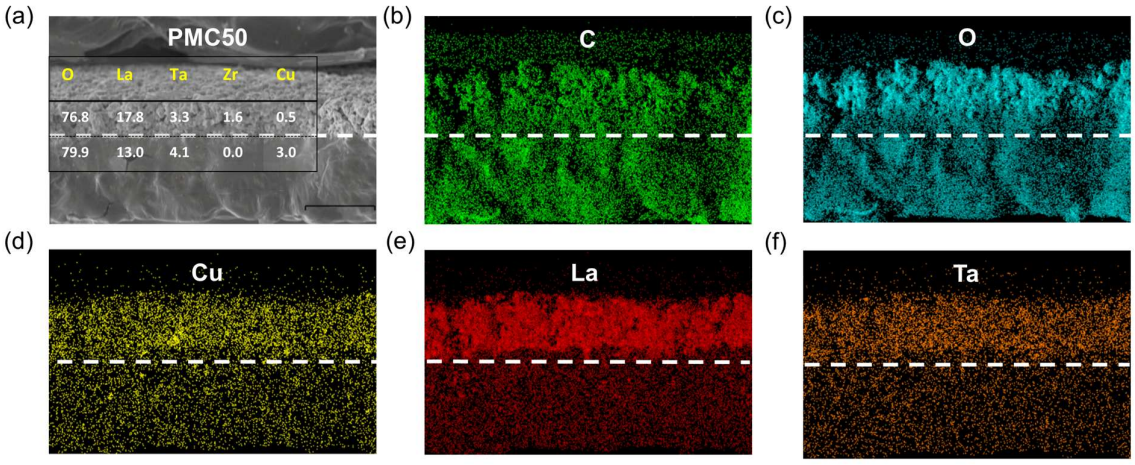

Figure 3.3 (a) Cross-sectional SEM image and corresponding EDS elemental mapping of (b) C, (c) O, (d) Cu, (e) La, and (f) Ta collected from PMC50 CSSE.

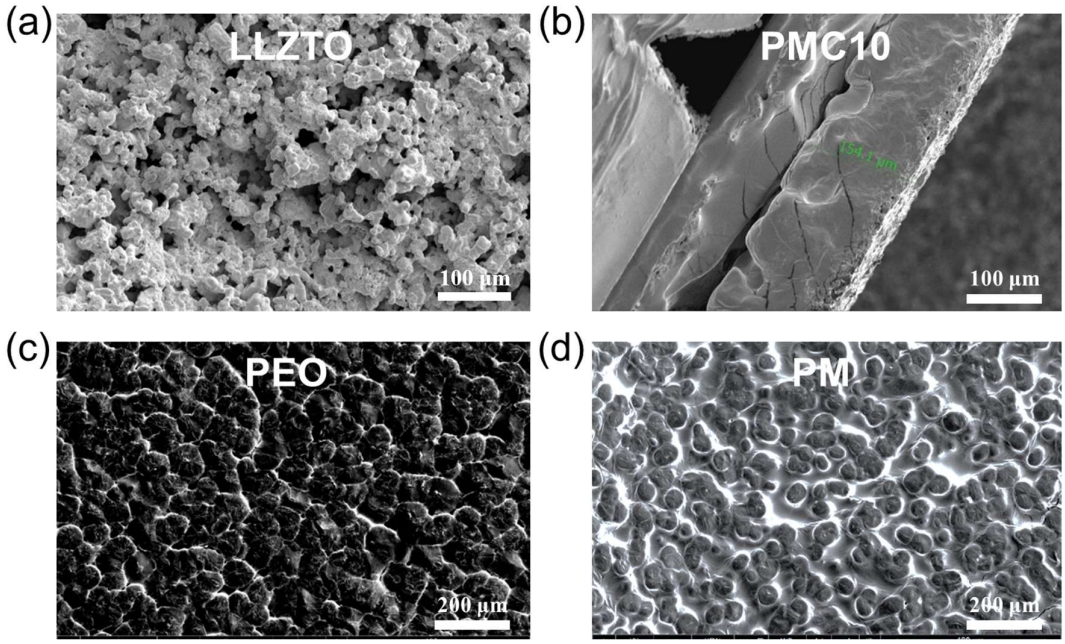

Figure 3.4 (a) SEM image of commercial LLZTO particles, (b) cross-sectional SEM images of PMC10, and top-view SEM images of (c) PEO (Li^+: EO = 1:15) and (d) PM SPEs.

3.3.2. Thermal and mechanical properties of PMCs

DSC test was performed to analyze the thermal-induced phase-change behavior of PMC composite electrolytes, such as glass transition temperature (T_g), melting temperature (T_m), degree of crystallinity (χ_c), and enthalpy value (ΔH_m). As shown in Figure 3.5a and 3.5b, an endothermic peak corresponding to T_m of the crystalline state is found at 64.4°C in the curve of pure PEO, while the T_m of PMC decreases significantly to ~50°C and the endothermic area experiences a notable reduction. The shift of T_m value towards lower temperature symbolizes the increase of amorphous phases, which can be verified by χ_c calculated following Eq 2.1. In comparison to the crystallinity of 66.0% of pure PEO, after being dispersed with different contents of additives, the χ_c of PMCs reduces to 15.2%, 13.7%, and 5.4%, respectively. Meantime, the moderate enhancement in T_g of PMC10, PMC30, and PMC50 is attributed to the coordination effects between additives and polyether chains; data details are given in Table 3.2. Subsequently, the thermal stability of PMCs was assessed by the TGA test. As shown in Figure 3.5c, the slight weight loss (less than 3%) below 100°C is caused by the evaporation of trace moisture, and PMCs undergo a multi-stage decomposition with a major weight loss occurring between 350-450°C, which is contributed by the decomposition of PEO and HKUST-1. The amounts of residue 10.9%, 26.8%, and 54.8% at 800°C are consistent with feeding ratios, whereas the single-modified SPEs (PM and PC10) in Figure 3.5d show finite enhancement. PMCs exhibit improved thermal stability compared to single-modified solid electrolytes, which results from the synergistic influence of the obstruction effect of MOF and the incombustible nature of ceramics.

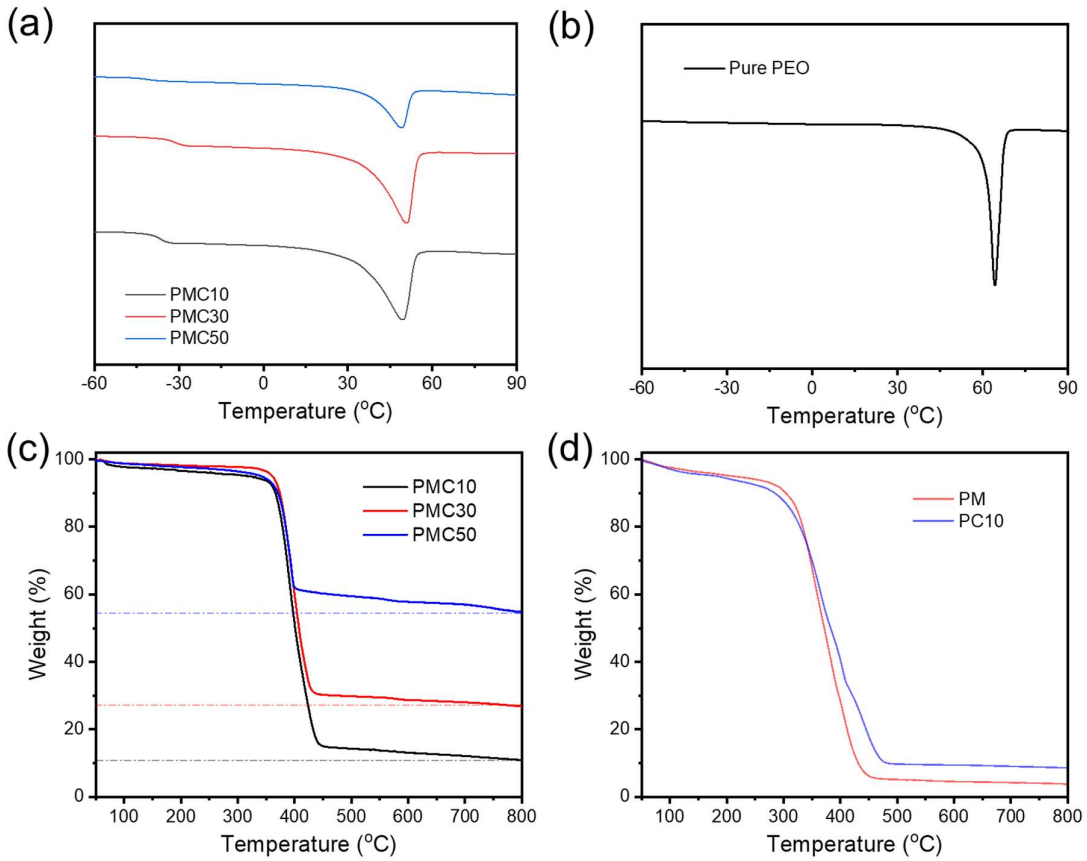

Figure 3.5 DSC of (a) PMC10, 30, 50, and (b) pure PEO, TGA thermograms of (c) PMC10, 30, 50, and (d) PM and PC10 electrolytes.

Table 3.2 DSC data (T_m, T_g, ΔH_m, and χ_c) of Pure PEO, PMC10, 30, and 50 electrolytes.

Samples	T_m (°C)	T_g (°C)	ΔH_m (J g^{-1})	χ_c (%)
Pure PEO	64.4	-51.6	141.0	66.0
PMC10	49.7	-36.5	32.5	15.2
PMC30	50.0	-36.1	27.2	13.7
PMC50	49.3	-39.1	11.5	5.4

Since electrolytes act as the bridge connecting two electrodes, proper mechanical strength is crucial to maintain an intact shape during their lifespan.[151] Ceramics consist of dense pellets with high interfacial resistance and are typically difficult to process owing to their rigid nature[152]. Conversely, PEO, as a conventional thermoplastic polymer, can be easily fabricated into desired shapes, but the soft nature permits notorious dendrite growth, which may induce internal short circuits.[153] PMCs combine the soft interface of PEO and the hard nature of LLZTO. The corresponding uniaxial tensile stress-strain behavior was investigated with DMA. The dependency of tan δ with temperature is obtained from the oscillatory tension deformation

and shown in Figure 3.6a, which is considered as the mechanical damping factor related to molecular movements.[154] As the temperature increases from -80 to 60°C at a rate of 3°C min^{-1}, PMCs undergo three periods progressively. During stage I, PMCs are in the glassy region, the polymer chains are hard and brittle; Stage II is the transition region, where the segmental movement becomes more flexible; Stage III is the rubbery plateau region, where polymer chains exhibit a large elastic deformation.[155] T_g shows a decreasing trend with LLZTO content increased, which conforms to the DSC results listed in Table 3.2. PMC50 exhibits the highest storage modulus (E') in the glass state, benefiting from the contribution of LLZTO (Figure 3.6b and 3.6c). As seen in Figure 3.6d, all samples do not fracture after 400% elongation until limited by the maximum stroke of the machine, confirming the excellent deformability of PMCs. Young's modulus, as an important index commonly used to evaluate the stiffness of materials,[156] is calculated according to Eq 2.2. Owing to the combination of the stiffness from LLZTO and the toughness from polymers with excellent flexibility, Young's modulus of PMC10, PMC30, and PMC50 present 3.1, 4.4, and 5.2 MPa, respectively, which can effectively withstand mechanical stresses, maintain the structural integrity, and meet the mechanical needs of LIBs in the long-term usage, whereas the PEO SPE shows a dissatisfied value of 1.0 MPa and fractures after reaching the maximum strain of 240% (Figure 3.7).

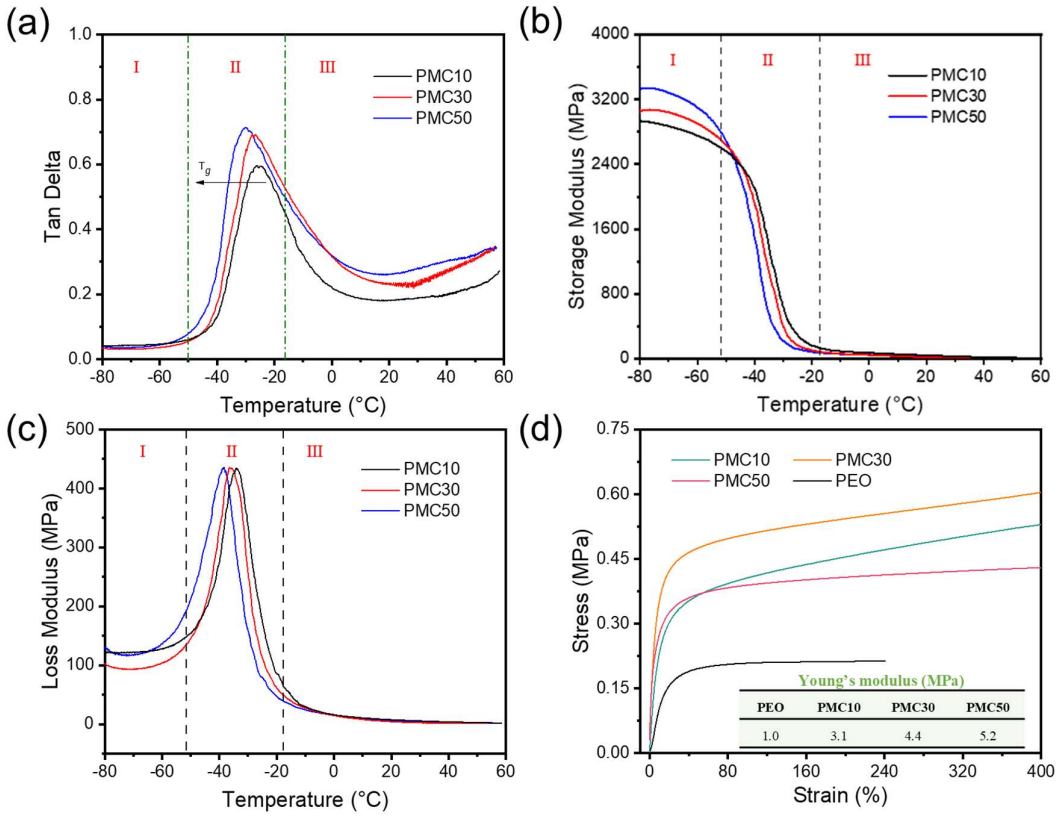

Figure 3.6 Tan δ versus temperature plots, (b) storage modulus, (c) loss modulus plots, and (d) stress-strain curves of PMC10, 30, and 50 electrolytes.

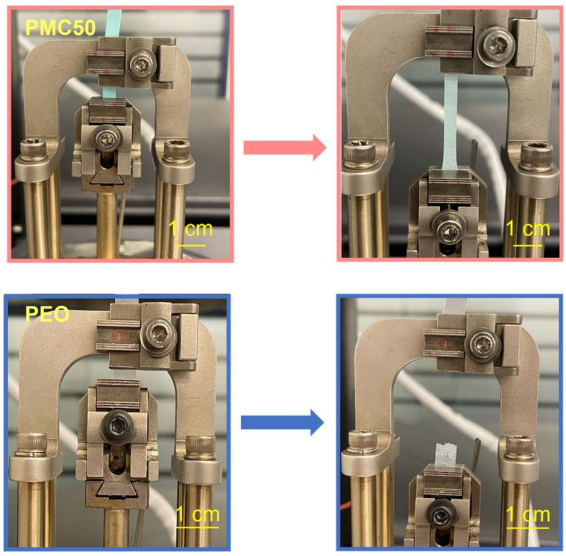

Figure 3.7 Images recorded during tensile testing of PMC50 and PEO SPEs by the dynamic mechanical analyzer.

3.3.3. Fire safety of PMCs

PMCs combine the flame-retardant HKUST-1 and the nonflammable ceramic, the fire safety is hoped to present alleviated combustion behaviors compared to PEO SPE. Hence, the direct burning experiment is performed to track the burning details of PMCs, including burning time, extinguishing time, fire severity, as well as residues. Figure 3.8 records the burning moments for 1 s, 5 s, and 10 s, respectively. Once ignited, the igniter is immediately retracted, and the timing is started.

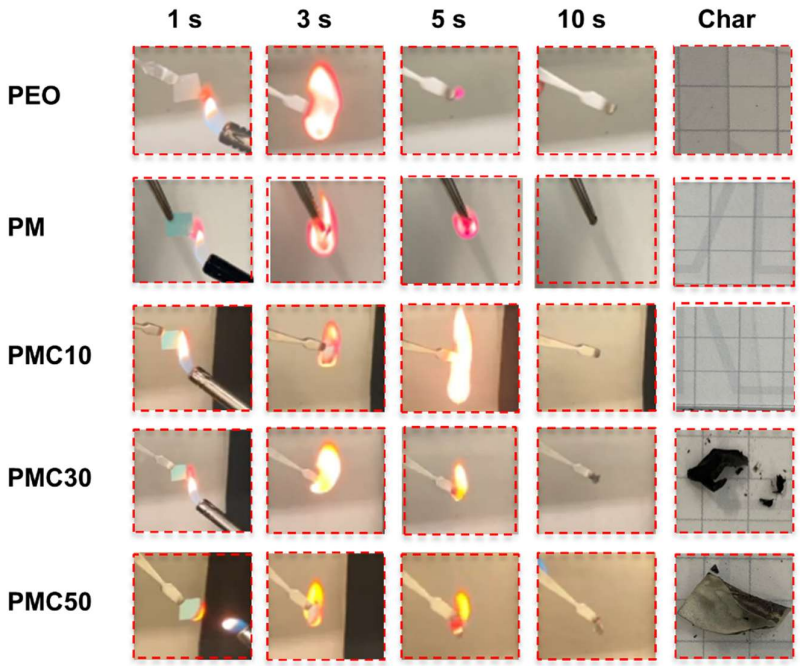

Figure 3.8 Time-resolved photographs of PMC10, PMC30, and PMC50 burning at 1 s, 5 s, and 10 s.

PEO SPE burns most violently with a melt dripping phenomenon and no residue remains, while PM demonstrates a notably subdued burning behavior, though still showing a dripping phenomenon. In contrast, PMCs burn less vigorously and leave residues after extinguishing. Among them, PMC50 exhibits the best flame retardancy and maintains its shape by forming a highly condensed char layer, as revealed by Figure 3.9, which can cover the substrate surface to suppress heat and mass transfer. PMC10 has moderate flame retardancy due to its low ceramic content. Furtherly, MCC is used to measure the released heat from combustible materials as a standard method, which allows a comprehensive assessment of safety concerns, including HRC, peak heat release rate (pHRR), total heat release (THR) values, and temperature of peak heat release rate (T_{max}).[157] As summarized in Table 3.3, the incorporation of HKUST-1 and LLZTO leads to a notable suppression of heat production and a reduced propensity for heat release under elevated temperatures. Compared to PEO SPE, HRC values of PM and PC10 decrease significantly from 374 J g^{-1} K^{-1} to 260 J g^{-1} K^{-1} and 311 J g^{-1} K^{-1}, respectively, where PMC10 shows a decrease of 33.4% in comparison with PEO electrolytes. Meanwhile, pHRR reduces from 355 W g^{-1} to 250 W g^{-1} and 295 W g^{-1} for PM and PC10, respectively. Additionally, the T_{max} and THR of PMCs are remarkably more pronounced decreasing trend due to the synergistic effect of MOFs and LLZTO, for instance, the THR of PMC50 drops to 10.8 kJ g^{-1}, while the THR of PEO membranes is as high as 16 kJ g^{-1}, signifies the improved thermal stability of the PMCs. The utilization of fire-safer PMC electrolytes holds great potential in preventing catastrophic incidents and promoting the widespread adoption of safer energy storage technologies.

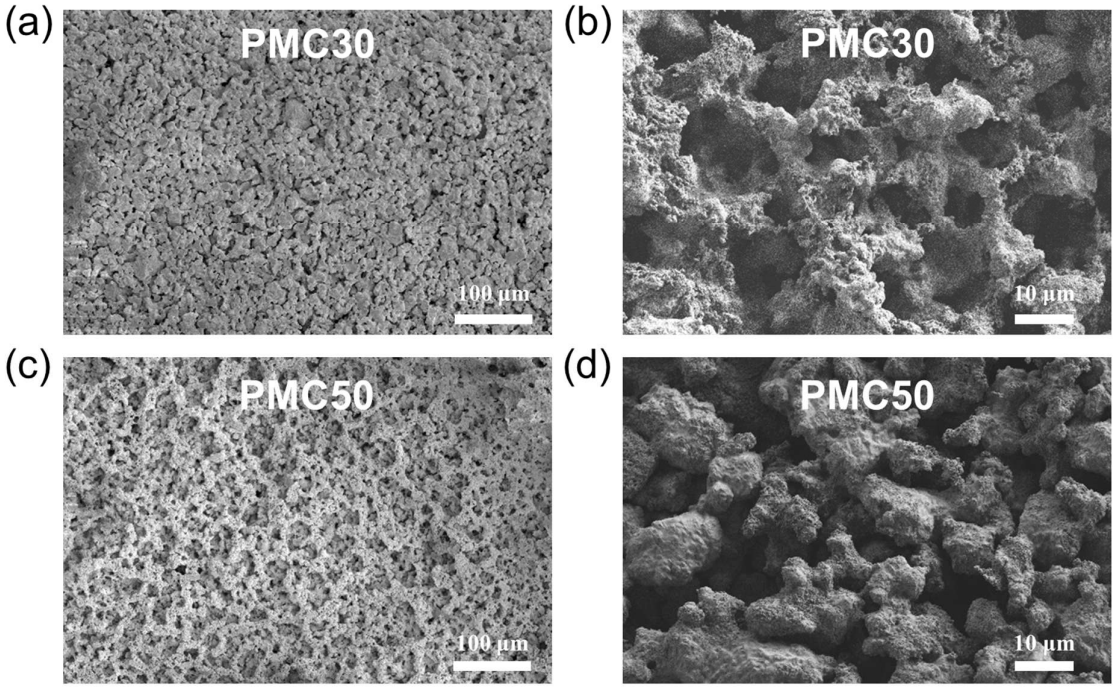

Figure 3.9 The SEM images of (a, b) PMC30 and (c, d) PMC50 char after burning.

Table 3.3 MCC test results of PEO, PC10, PM, PMC10, 30, and 50 membranes.

Samples	HRC ($J\ g^{-1}\ K^{-1}$)	pHRR ($W\ g^{-1}$)	T_{max} (^oC)	THR ($kJ\ g^{-1}$)
PEO	374	355	417	16.0
PC10	260	250	404	15.5
PM	311	295	407	16.3
PMC10	249	237	404	15.9
PMC30	209	197	406	13.9
PMC50	183	174	386	10.8

3.3.4. Electrochemical performance of PMCs

To further investigate the compatibility of PMCs, the ESW was tested by the LSV method from 2.0 to 5.5 V with a sweep rate of 0.1 mV s^{-1} at 50°C. Figure 3.10a compares the potential stability of PMCs with control groups; all electrolytes display a stable platform high to ~3.85 V, which can guarantee the voltage scope required for LFP (~3.8 V vs Li/Li^+). Furthermore, as revealed in the inserted graph, the currents of PMC30 and PMC50 are lower than control groups under high voltage (above 4.0 V), which may result from the hampered oxidation and decomposition of PEO after filler incorporation.[158, 159]

Afterward, EIS measurements were conducted to figure out the influence of additives on Li^+ conduction. Figure 3.10b illustrates the variation of ionic conductivity of PMC10 within a wide temperature range, the resistance decreases sharply as the temperature rises (388 Ω at 30°C), and PMC10 shows an optimal ionic conductivity of 2.33×10^{-4} S cm^{-1} at 50°C. By contrast, in Figure 3.10c, PEO SPE possesses a high interface impedance of 1850 Ω at 30°C and exhibits an ionic conductivity of 6.38×10^{-5} S cm^{-1} at 50°C. This remarkable improvement in conductive ability is a result of the collaborative contribution of both MOF and LLZTO additives. As manifested in Figure 3.10d and 3.10e, PM and PC10 show smaller resistance of 744 Ω and 1009 Ω at 30°C and higher ionic conductivity compared to unmodified PEO electrolytes. In addition, Figure 3.10f gives the relevant Arrhenius plots of PMCs, where PMC10 achieves the highest ionic conductivity among all CSSEs. When the ceramic content is lower than the percolation threshold, the "CIP" structure dominates the transport of Li^+ by the polymer segmental movement, which can well explain the reason for the slope change observed around 50°C in the nonlinear plot. Close to T_m, the increased polymeric mobility promotes easier ionic conduction, the activation energy of PMC10 is 0.32 eV based on Arrhenius relation calculation, which is reduced notably compared to the activation energy of 1.06 eV below 50°C.

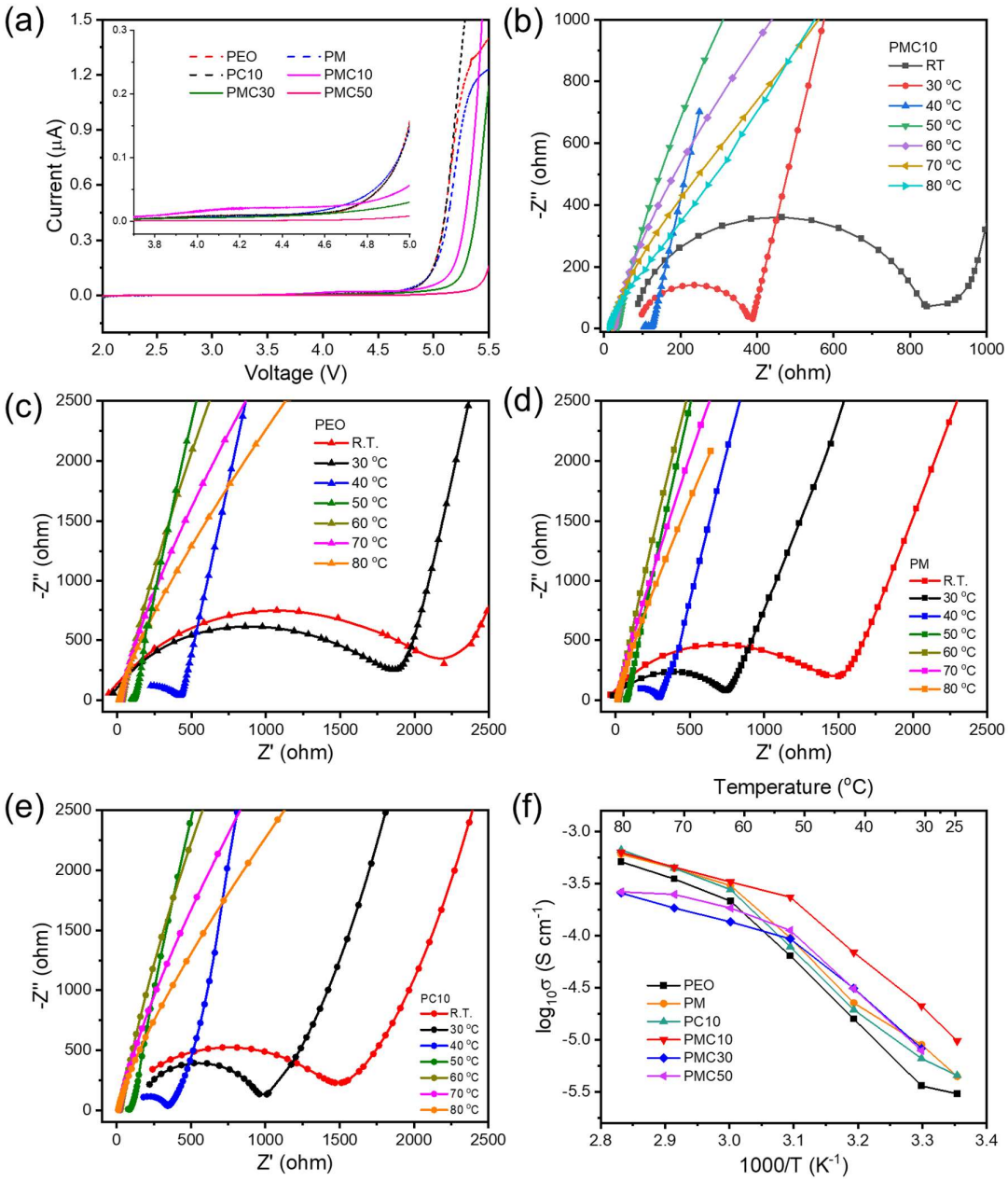

Figure 3.10 (a) Linear sweep voltammetry curves of electrolyte membranes at 50ºC (the inset is an enlarged view from 4.5 to 5.0 V). Nyquist plots of (b) PMC10, (c) PEO, (d) PM, and (e) PC10 SPEs at various temperatures from RT to 80ºC. (f) Temperature dependence of ionic conductivity of PMC electrolytes.

The contact wettability and stability between solid electrolyte and lithium metal, as well as the interfacial stability during lithium intercalation/extraction, are important evaluation parameters for the realization of high specific energy lithium batteries exceeding 350 Wh kg^{-1}. Meanwhile, the thermal runaway of Li batteries typically begins with the failure and decomposition of the SEI.[38] Lithium stripping and plating experiments are performed based on symmetric Li cells to analyze the interfacial compatibility of PMCs against Li metals. As shown in Figure 3.11a, at a constant current density of 0.2 mA cm^{-2}, the potential change of PMC10 is negligible during

the whole cycle of 900 hours, indicating that its interface is moderately stable at such a high current density. On the contrary, PEO SPE and PMC30 experience ISC and manifest continuous potential fluctuations after 50 hours at the same current density; the sudden drop in resistance implies battery failure induced by lithium dendrite growth (Figure 3.11b and 3.11c). Nevertheless, after the current density reduces to 0.1 mA cm^{-2}, PMC30 and PMC50 can deliver a stable plating/stripping behavior to 900 hours, as shown in Figure 3.12.

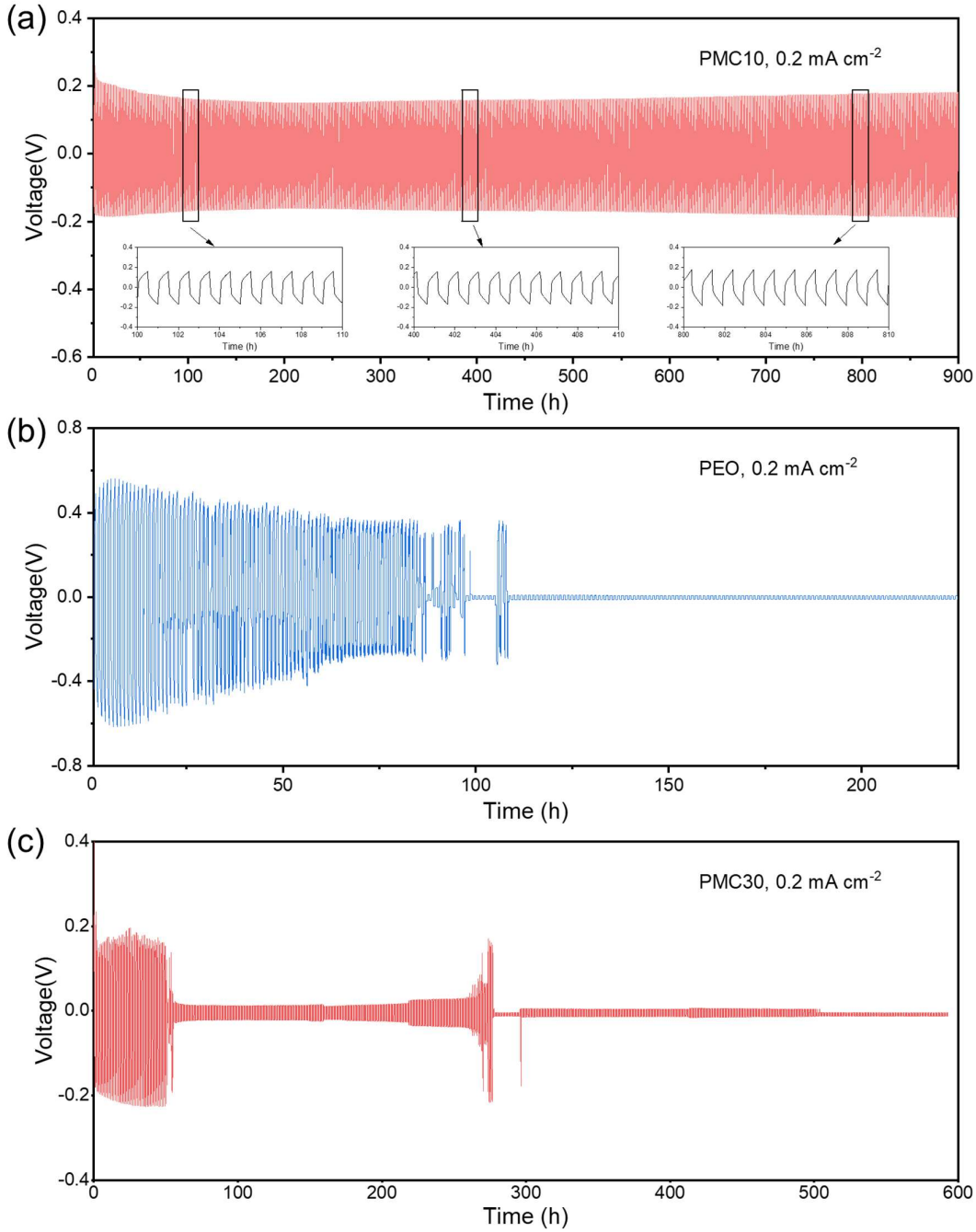

Figure 3.11 Lithium plating/stripping galvanostatic cycles of Li|PMC10|Li cells of (a) PMC10, (b) PEO, and (c) PMC30 SPEs at a current density of 0.2 mA cm^{-2} at 50°C.

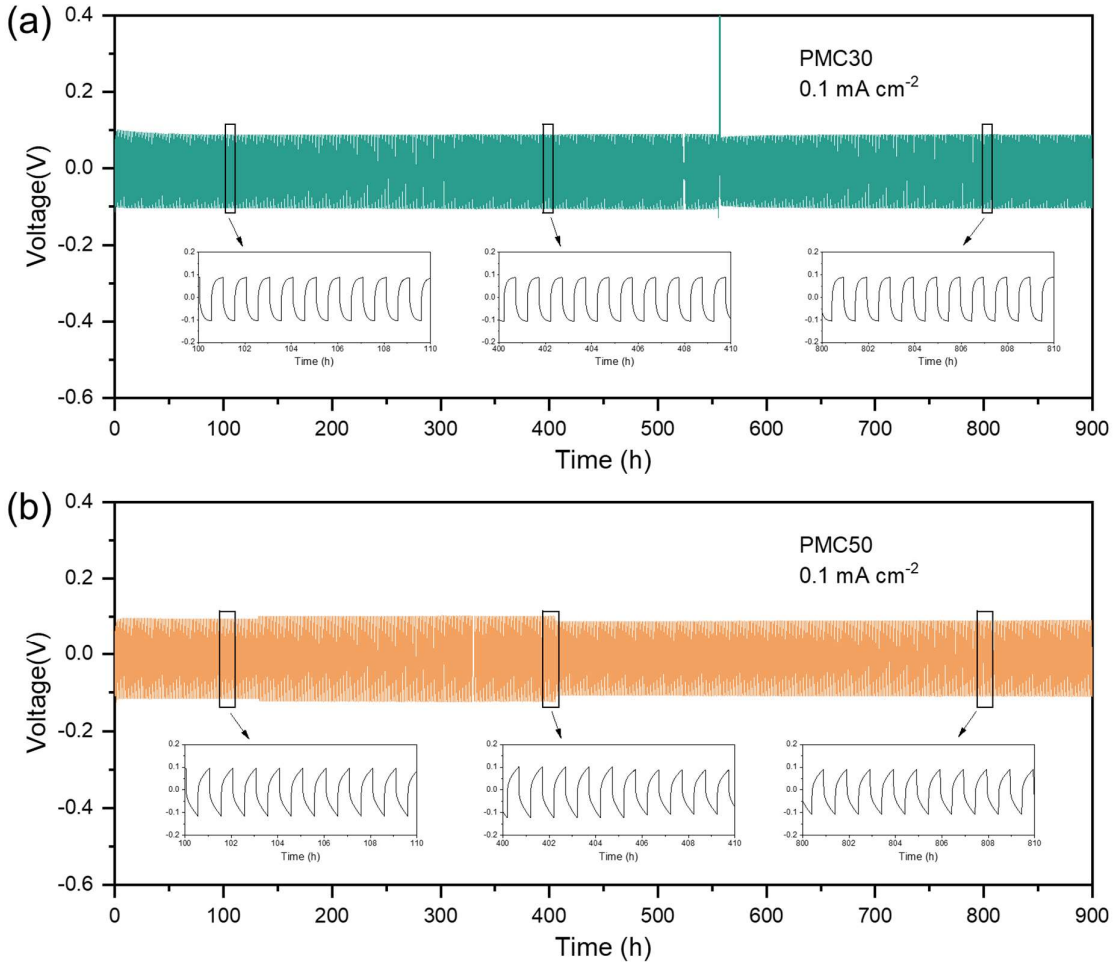

Figure 3.12 Lithium plating/stripping galvanostatic cycles of Li|PMC10|Li cells of (a) PMC30 and (b) PMC50 at a current density of 0.1 mA cm^{-2} at 50°C.

LFP is chosen as the cathode since it has been accepted as the most stable cathodic material during the thermal runaway process, which is ascribed to the strong bond of the octahedral $(PO_4)^{3-}$ structure[37]. As shown in Figure 3.13a, PMC10 first undergoes several activation cycles accompanied by reduced voltage polarization and increased capacity density. At the 8th cycle, a reversible capacity density of 168.5 mAh g^{-1} is achieved with an overpotential of ~0.1 V. In Figure 3.13b, the CV test was conducted between 2.5 to 4.0 V. In the initial cycle, two oxidation and reduction peaks relating to the intercalation/deintercalation of Li^+ from/into the cathode appear at ~3.65 and ~3.23 V, respectively. In the following cycles, the current increases steadily, and the reduction peaks shift to ~3.18 V, implying the decreasing internal polarization and a stabilizing contact interface. The capacity performance of PMCs at various cycling rates at 50°C is presented in Figure 3.13c. In comparison with PEO SPE showing an inevitable capacity decline trend under high currents, PMCs show more stable capacity retentions with steady Coulombic efficiencies, where PMC10 shows the highest capacity density, which mainly benefits from its excellent ionic conductivity and stable interface. The galvanostatic cycling

performance of LFP|PMC|Li batteries at 0.1 C rate is presented in Figure 3.13d; all cells ran 10 activation cycles in advance to achieve their stable capacity. Both PMC10 and PMC30 show excellent cycling behavior with high Coulombic efficiencies after 400 cycles, whereas the capacity density of PMC50 declines inevitably after 80 cycles. The initial specific capacities of PMC10 and PMC30 are 158.5 and 147.9 mAh g^{-1}, respectively, and then drop to 127.3 and 105.8 mAh g^{-1} after 200 cycles, with capacity retention efficiencies of 80.3% and 71.5%, respectively.

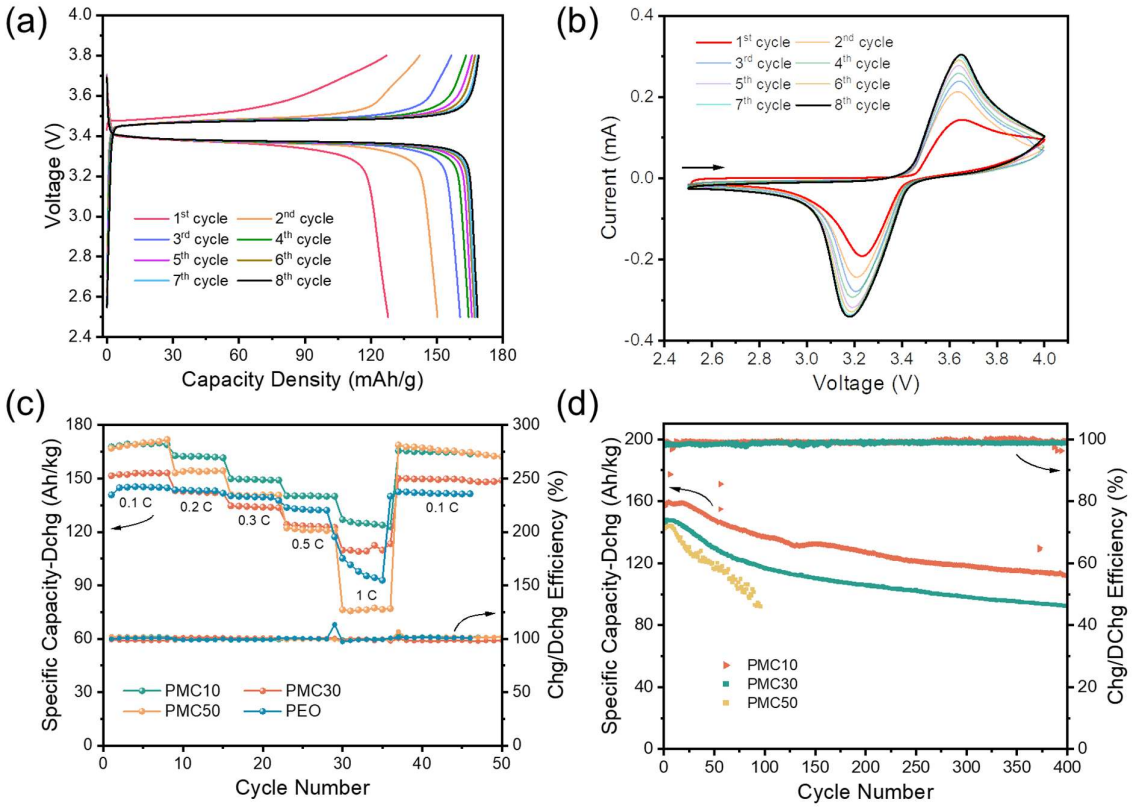

Figure 3.13 (a) Activation process of LFP|PMC10|Li cell, (b) cyclic voltammogram of LFP|PMC10|Li cell at a scan rate of 0.1 mV s^{-1}, (c) rate performances of LFP|PMC|Li cells at serial current rates, and (d) cycling performance of LFP|PMC|Li cells at 0.1 C, all tests were performed at 50°C.

The separate charge/discharge profiles are recorded in Figure 3.14a and 3.14b, where PMC10 keeps a discharging capacity of 105.5 mAh g^{-1} after 500 cycles, whereas the counterpart of PMC30 maintains 87.0 mAh g^{-1}, demonstrating that PMC10 possesses better electrochemical properties. As shown in Figure 3.14c and 3.14d, PMC50 displays inhomogeneous surfaces and contains large areas of roughness after disassembling the batteries; however, the good contact compatibility of PMC10 and PMC30 makes it difficult to strip off.

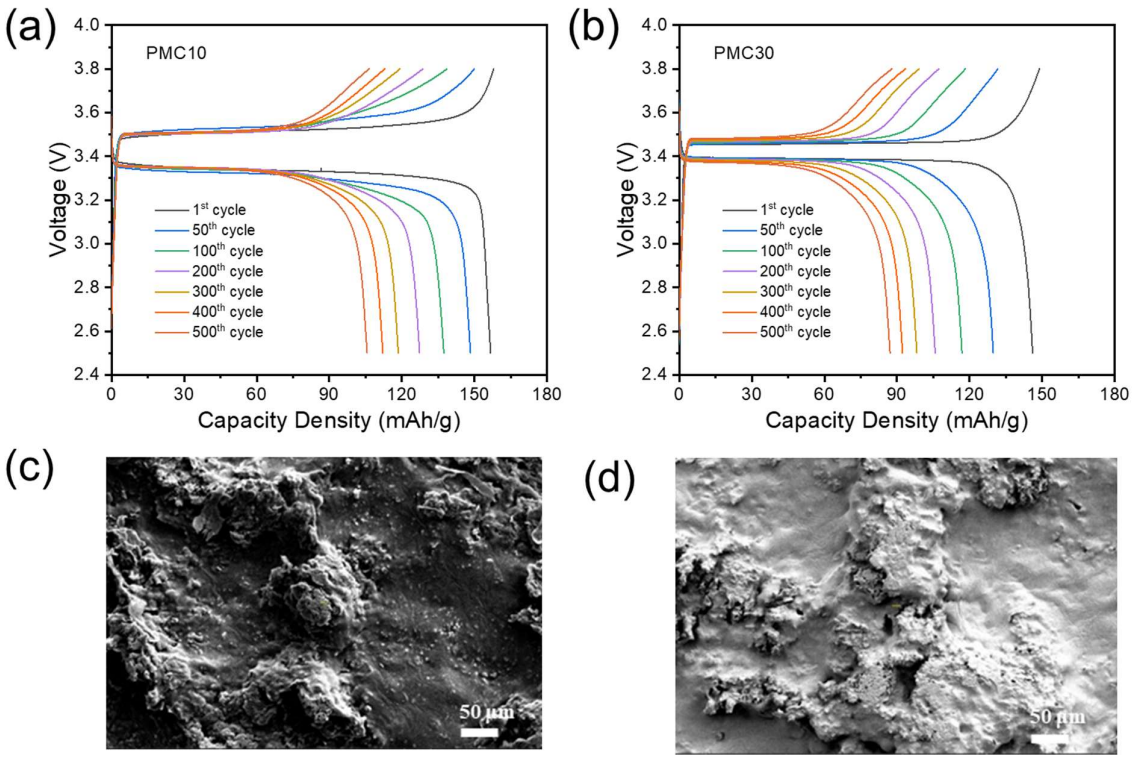

Figure 3.14 The recording of galvanostatic cycling profiles of (a) PMC10 and (b) PMC30 at 0.1 C rate at 50°C, and (c, d) SEM images of PMC50 after 100 cycles at 0.1 C at 50°C.

3.4. Conclusion

To improve the fire safety performance of the CSSEs while ensuring excellent electrochemical performance in LIBs, HKUST-1 and LLZTO with different content ratios were added to the PEO substrate to obtain PMC10, PMC30, and PMC50 CSSEs with a uniform thickness of ~150 μm. Due to the gravitational effect of ceramic particles, a hierarchical CIP-PIC structure is formed. PMCs showed restrained crystallization ability, improved thermal stability, and reinforced mechanical properties, which surpassed conventional PEO SPE from diverse differential requirements. As a result, exceptional electrochemical compatibility (EW to ~4.5 V) and satisfactory ionic conduction (PMC10, 2.33×10^{-4} S cm^{-1} at 50°C) were achieved. Notably, PMC10 exhibited excellent interfacial stability and cycle performance with a stable plating/stripping behavior for 900 hours at a current density of 0.2 mA cm^{-1}, a discharge capacity density of 158.5 mAh g^{-1}, and a capacity retention of 80.3% after 200 cycles. This work contributes to the advancement of safer energy storage technologies and paves the way for the widespread adoption of CSSEs in fire-resistant LIBs.

4. A Benchmarking Approach to Assess Fire Safety of Liquid Electrolytes

4.1. Introduction

Although many works have emphasized their improvement of fire safety with some indicators, the absence of benchmarks leads to the occurrence of multitudinous methods without comparability, and this challenge presents a more formidable situation when considering LEs. Unlike polymeric materials, the combustion process of liquid samples exhibits inherent distinctions, characterized by the simultaneous occurrence of intricate physicochemical processes, including volatilization, vaporization, and pyrolysis.[160] Hence, the distinctive structural and dimensional characteristics of matrices employed for absorbing electrolytes in tests significantly impact combustion behaviors of LEs, which ultimately affect the comparability of final results. The lack of a unified description of SET hinders the effective safety evaluation of LEs and impedes the progress of LIB technology. Therefore, establishing a systematic and normalized electrolyte safety assessment system is crucial. While previous studies have acknowledged this challenge, to the best of our knowledge, the development of benchmarks for the SET method has not been explored yet.[161]

In this chapter, we present a comprehensive introduction and summary of the conventional SET criterion, underscoring the significance of establishing normalized protocols for its measurement and evaluation. To achieve comparability across various studies, we propose a concept of “self-extinguishing efficiency (SEE)” and systematically compare several typical testing methods (both placed and adsorbed methods). In pursuit of repeatability, reliability, low cost, and ease of operation as the reference, two methods are screened: loaded with battery cases and absorbed by separators. Subsequently, 15 commercial FRs are applied to the electrolyte to assess the desirability of the above two methods. Eventually, the unified method of horizontally burning glassfiber separators with a diameter of 16 mm and absorbing 0.1 g of electrolyte is established. Thermocouple detection, FTIR-TGA, SEM, and temperature field simulation are conducted to investigate the difference in flame retardant effectiveness among additives, and the mechanism of FRs in LEs is proposed. Furthermore, machine learning (ML) is used to assist in the analysis of different models to further verify the mechanism.

4.2. Experiment

4.2.1. Fire test

The combustion experiments vary in detail for different materials. Specifically, the wick is hung on an iron stand using a clip and ignited from the bottom end; As for the separator and insulfrax paper, they are positioned horizontally on an iron grid and ignited from the bottom. For the direct combustion method using different containers, the fire source is applied vertically from the top. All the above experiments were conducted using a portable gas igniter and were completed in a windless chamber. Each experiment was repeated five times. The igniter was removed once a stable flame was formed. Note that if the ignition time exceeds 5 seconds without initiating a fire, it is recorded as non-flammable. Meanwhile, it is necessary to store LE samples in sealed, light-proof bottles in the glove box to keep them fresh before the experiment. When conducting combustion tests, the exposure time to air should be shortened as much as possible.

4.2.2. Machine learning approach

The data for building ML models was retrieved from the publications and measured with the lab experiments. Based on the data collected from literature and the conversion formula between SET and SEE, two models, SET(number)-Ref and SEE(number)-Ref, were established. Both models have a range from 0 to over or around 100, depending on the flame retardancy of additives in LEs. Due to the large numerical range of SET, the SEE values of collected data and experimental data are set as target features and divided into 3 categories (F, R, N), marked with numbers 1, 2, and 3. According to their different sources, the data was divided into 3 datasets: SEE(class)-Ref, SEE(class)-BC, and SEE(class)-GFS dataset. The Reference dataset has 181 rows of data, while the latter two datasets possess data sizes of 60 and 60, respectively. Furthermore, we combined the SEE(class)-BC and SEE(class)-GFS datasets with the SEE(class)-Exp dataset, with a size of 120.

As listed in Table 4.1, the selected features in the datasets focus on the properties of additives. For simplification, “SET0” was selected as the representative of blank electrolyte components. The additives were featured with their chemical compositions (the molar content of FR elements and molecular weight) and physical properties (the flashing, boiling, and melting points). Since the measured SET value strongly depends on the specific test method, the “Burn” feature was used to roughly distinguish the differences in characterization. Taking accessibility and generalizability into account, the selected features have covered most of the relevant aspects of flame-retardant LEs. Before modelling and optimization, the collected data was cleaned and processed by using encoders and scalers to construct input datasets with uniform distribution, proper data structure, and selected features. Additionally, the feature map was inspected to

decide which features to discard and retain, as few redundant features as possible. Figure 4.1 depicts the heatmap of Spearman's rank correlation coefficient between two features in the datasets. The highly correlated parameters are concentrated in the properties of FRs such as "BP", "Molar", and "FR(%)". Depending on the models used to predict SEE or SET among different datasets, the selected features can vary in number and type.

Table 4.1 Description of features collected in datasets.

Features	Description
SET0	SET value of blank LE
P_Type	Chemical environment of phosphorus, including phosphate, phosphite, and phosphazene
P(%)	Mass fraction of phosphorus element in FR
N(%)	Mass fraction of nitrogen element in FR
F(%)	Mass fraction of fluorine element in FR
Molar	Molecular weight of FR
FR(n)	Mole fraction of key elements (P, N, F) in FR
FR(%)	Mass fraction of key elements (P, N, F) in FR
Phase	Phase state of FR: liquid or solid
BP	Boiling point of FR
MP	Melting point of FR
FP	Flash point of FR
Mass	Content of FR (wt%)
Burn	The method of combustion test: BC or GFS

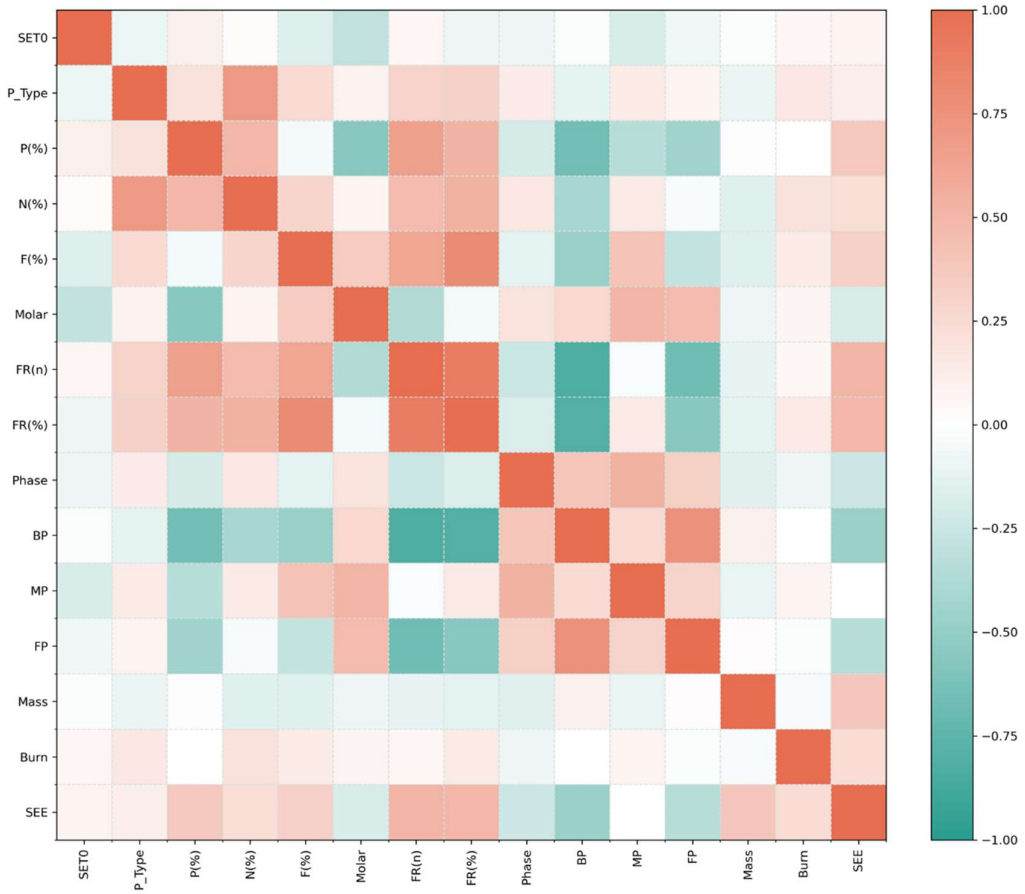

Figure 4.1 Heatmap of Spearman's rank correlation between all features in datasets.

The selected machine learning algorithm is a widely used tree ensemble for supervised learning. This Random Forest (RF) method combines plenty of randomly grown decision trees to lower the variance or bias, reducing the risk of overfitting. While modeling, 85% of the input dataset was considered as a trainset to train the models, and the remaining 15% as a testset to evaluate the predictive accuracy instantly. The split was done randomly and marked as the random state. In the RF algorithm, hyperparameters (HP) are used to control the number, shape, and size of decision trees. Optimization of these HPs is conducted with trainsets, and the trained models are then used to make predictions with testsets to evaluate their predictive accuracy. The optimized HPs of all RF models are explained and listed in Table 4.2 and 4.3, together with the values of model indices in Table 4.4. Except for the R2 scores, mean errors of the predictions compared to the true values were collected to evaluate the predictive performance of ML models. The calculation of feature importance is realized with the built-in function, which represents the percentage impact of an individual feature on the target property. The sum of all features' importance counts as 1. The higher the feature importance is, the more significant the feature is to the change of the target property. Ranking the features by their importance provides a way to filter the necessary features to achieve better predictive performance with simpler models and analyze the underlying mechanisms in the right direction.

Table 4.2 The features used for each dataset ("1" represents valid features and "0" represents unselected parameters).

Features	SET(number)-Ref	SEE(number)-Ref	SEE(class)-Ref	SEE(class)-BC	SEE(class)-GFS	SEE(class)-Exp
SET0	1	1	1	0	0	0
P_Type	1	1	1	1	1	1
P(%)	1	1	1	1	1	1
N(%)	1	1	1	1	1	1
F(%)	1	1	1	1	1	1
Molar	1	1	1	1	1	1
FR(n)	1	1	1	1	1	1
FR(%)	1	1	1	1	1	1
Phase	0	0	0	0	0	0
BP	1	1	1	1	1	1
MP	1	1	1	1	1	1
FP	1	1	1	1	1	1
Mass	1	1	1	1	1	1
Burn	1	1	1	0	0	0

Table 4.3 Hyperparameters of relevant ML models.

Models	criterion	Max_depth	Max_feature	Min_sample_split	N_estimators
SET(number)-Ref	absolute_error	10	sqrt	2	100
SEE(number)-Ref	friedman_mse	20	sqrt	2	100
SEE(class)-Ref	-	10	sqrt	5	1500
SEE(class)-BC	-	10	sqrt	2	100
SEE(class)-GFS	-	10	sqrt	8	500
SEE(class)-Exp	-	10	sqrt	8	1000

Table 4.4 Evaluation indices of relevant ML models.

Models	R2		MAE		MSE	
	train	test	train	test	train	test
SET(number)-Ref	0.96	0.83	4.29	6.36	6.29	9.25
SEE(number)-Ref	0.97	0.84	3.81	8.72	5.18	11.52
SEE(class)-Ref	0.99	0.82	0.01	0.21	0.11	0.53
SEE(class)-BC	1	0.89	0	0.11	0	0.33
SEE(class)-GFS	0.92	0.89	0.10	0.11	0.37	0.33
SEE(class)-Exp	0.88	0.89	0.15	0.11	0.45	0.33

4.2.3. Simulation and computational analysis

A three-dimensional thermal conduction finite element method (FEM) model was established based on the COMSOL Multiphysics 6.1. A membrane with a diameter of 16 mm and a thickness of 0.1 mm was set to have a huge thermal capacity to simulate its state with flame (Table 4.5).

Table 4.5 FEM simulation parameters.

Variable name	Unit	Stainless steel 304	Iron	Membrane
Density	kg m^{-3}	8000	7860	2250
Thermal conductivity	W $(m \cdot K)^{-1}$	16.2	80.0	1.1
Specific capacity	J $(kg \cdot K)^{-1}$	500	450	8×10^5

The initial temperatures of 581.15 K and 695.15 K of the flame for the BC and the grid were set based on the thermocouple test, respectively. The battery case and the grid were constructed from stainless steel and iron, respectively, with an initial temperature set to match the environment at 298.15 K. The durations for the entire thermal conduction process were set at 10 s for the grid and 40 s for the button battery case, following the measurements. The governing equations of energy conservation and thermal conduction are expressed as follows:

$$\rho C_p \left(\frac{\partial T}{\partial t} + \mathbf{u} \cdot \nabla T\right) + \nabla \cdot \mathbf{q} = Q \quad \text{Eq 4.1}$$

$$\mathbf{q} = -k\nabla T \quad \text{Eq 4.2}$$

where ρ is the density (kg m^{-3}), C_p is the specific heat capacity at constant stress (J $(kg \cdot K)^{-1}$), T is the absolute temperature (K), u is the velocity vector of translational motion (m s^{-1}), q is the

heat flux by conduction (W m^{-2}), Q contains additional heat sources (W m^{-3}), and k is the thermal conductivity (W $(m \cdot K)^{-1}$).

4.3. Results and discussion

4.3.1. Limitations of self-extinguishing time and the proposal of self-extinguishing efficiency

In the plastic materials field, Standard 94 of the Underwriters Laboratories (UL94) is accepted worldwide as a predominant standard for the categorization of flame retardancy and an indication of plastic acceptability by considering the burning time, droplet formation, and the duration of afterglow time.[162] Based on this, the modified method, SET, has been created to value the flammability of LEs by immobilizing them in porous carrier materials, such as glassfiber and cotton. Instead of burning time that is dramatically impacted by the sample amount, SET, a normalized value, is thought to reflect the burnability of LEs quantitatively.

Depending on the format of sample handling, SET can generally be divided into two categories: absorbed and placed (Figure 4.2a). However, due to the lack of unified instruction on test details, various types and sizes of adsorbent materials and carrying containers, as well as a wide range of sample mass/volume, have been applied in different studies. To reveal the embarrassment of the current situation, we have listed the testing details of 15 representative works published in the last two decades (2002-2023) in Table 4.6. Plenty of porous carrier materials, such as glassfiber, cotton, separators, and wicks, have been used to soak up LE samples since their superb wettability towards liquids can reduce evaporation during the test. However, the effects of discrepancy in density and size on their wettability and loading capabilities have been neglected. A large amount of work is performed with loadings (usually less than 0.5 g) much below their saturation capacity, which can arouse problems with uneven liquid distribution. Meanwhile, volume (100-500 μL) has been used as the quantitative parameter rather than mass to determine the loading amount, which may cause deviations during calculation. For example, in two works using SET to evaluate the same electrolyte of 1.0 M $LiPF_6$ in EC/DEC=1/1 (w/w), it is astonishing that two works reported SET values of 63.5 and 140 s g^{-1}, respectively,[163, 164] implying the essentiality of establishing a benchmark for the LE safety assessment system. Besides utilizing adsorbent matrices, researchers also take direct burning of LEs as an alternative. Since the combustion of electrolytes occurs in both liquid and gas phases, the exposed area and heat dissipation ability of vessels have a strong influence on the vapor emission rate. The key to this approach is choosing a suitable container with specific shapes and properties, and the common ones now are GW and BC.

Table 4.6 Experimental details in SET tests ([a]: diameter; [b]: thickness; [c]: length; [d]: width)

Ref	Absorb or Place	Materials or Containers	Flammable	Shape (mm)	LE amount	LE composition	SET_0	Comments
[165]	Absorb	Linear-shaped wick	Y	Φ [a]: 3-5	0.05-0.1 g	1.0 M $LiPF_6$ in EC/EMC: 1/1 (w/w)	~60	The first proposed work
[166]	Absorb	Cotton swab wick	Y	Φ: 10	100 μL	1.2 M $LiPF_6$ in EC/EMC: 3/7 (v/v)	23 (in s)	Placed in a fume hood with an airflow (90 ft s^{-1})
[167]	Absorb	Glassfiber wick ball	N	Φ: 3-5	0.1-0.2 g	1.0 M $LiPF_6$ in DMC/EC/EMC: 1/1/1 (v/v/v)	106	Placed on an "O" shaped iron shelf
[168]	Absorb	Glassfiber ball	N	Φ: 10	0.5 g	1.0 M $LiPF_6$ in EC/EMC: 1/3 (v/v)	49	-
[163]	Absorb	Glassfiber separator	N	Φ: 20	500 μL	1.0 M $LiPF_6$ in EC/DEC: 1/1 (w/w)	63.5	A custom-built device with a UV light detector
[169]	Absorb	Glassfiber separator	N	Φ: 12 t [b]: 0.67	400 μL	1.0 M $LiPF_6$ in EC/EMC: 3/7 (v/v)	~70	4 layers of Glassfiber discs suspended on a needle, use stormproof lighters from 3.5 cm height, ignited for 10 s
[170]	Absorb	Glassfiber wick	N	Φ: 8 l [c]: 40	1 g	1.0 M $LiPF_6$ in DMC/EC/EMC: 1/1/1 (w/w/w)	60 (in s)	Placed horizontally on a stand
[171]	Absorb	Glassfiber sheet	N	w [d]: 10 l: 100	4 mL	1.0 M $LiPF_6$ in DMC/EC/PC: 1/1/1 (v/v/v)	47.104/ 47.037/ 46.638	Samples were placed vertically, Bunsen burner ignited below samples 1.0 cm with a different ignition time of 2/3/4 ±0.05 s
[172]	Absorb	Glassfiber sheet	N	w: 20 l: 50	~5 g	1.0 M $LiPF_6$ in EC/EMC: 3/7 (v/v)	~22	Samples hung on an iron shelf
[173]	Place	Watch glass	N	Φ: 70	0.5 g	1.0 M $LiPF_6$ in EC/EMC: 3/7 (w/w)	59±2	Ignited with a barbecue gas burner for 3 s (at most 20 s)
[174]	Place	Battery case	N	Φ: 20	0.5 g	1.0 M $LiPF_6$ in EC/DMC: 3/7 (v/v)	70 (in s)	-
[164]	Absorb	Cotton ball	Y	0.5 g	0.2 g	1.0 M $LiPF_6$ in EC/DEC: 1/1 (w/w)	140	-
[175]	Place	Watch glass	N	-	3 g	1.15 M $LiPF_6$ in EC/EMC: 3/7 (-)	40	-
[176]	Place	Battery case	N	Φ: 20	500 μL	1.0 M $LiPF_6$ in EC/DMC: 1/1 (v/v)	83.6	Use candles as the igniter
[177]	Absorb	Glassfiber strip	N	-	-	1.0 M $LiPF_6$ in EC/DMC: 1/1 (v/v)	17	-

Current commercial LEs consist of $LiPF_6$ salt and carbonates, which are categorized based on the composition of solvents, including EC/DMC (e.g., LP30), EC/DEC (e.g., LP40), EC/EMC (e.g., LP50), and ternary (e.g., LP71). The diversity of components causes different thermal stability properties.[178] In Figure 4.2b, 48 SET_0 values are collected and depicted on a scatter plot; four groups contain 13, 16, 9, and 10 data points, respectively. It is clear that each type of LE has a broad distribution, and the EC/DEC group has the largest range of 231 s g^{-1}. Meanwhile, the thermal stability of different electrolytes shows a dependence on the linear carbonate composition. According to the classification created by Xu et al., values greater than 20 s g^{-1} can be grouped as flammable, which is probably the basis that supports their establishment of classification. Nevertheless, it is imperative to acknowledge that the determination of SET is contingent upon the specific testing methodology employed, highlighting the unreasonable nature of the existing classification criteria. Noteworthy, the above discussion is only for unmodified groups (SET_0); the incomparability also exists or is even amplified in the modified LE system.

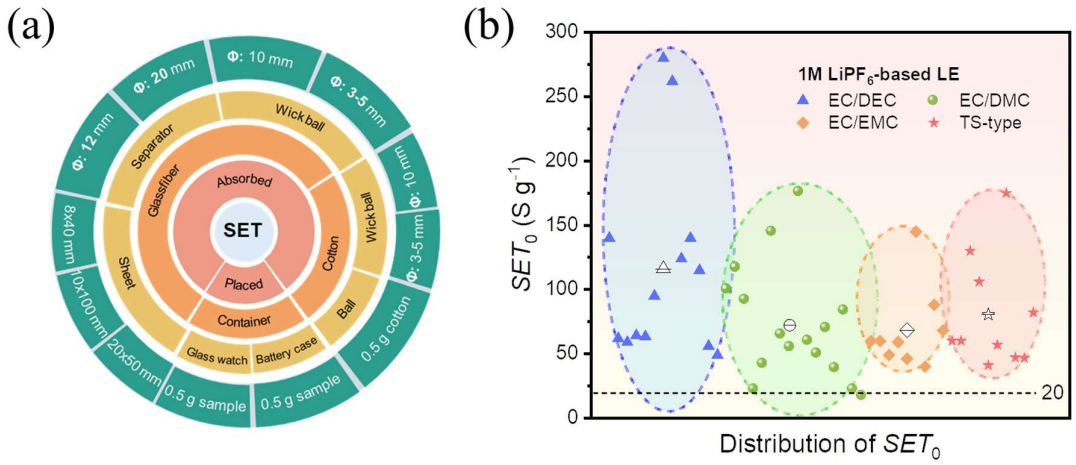

Figure 4.2 (a) Enumeration and classification of SET test experimental details, (b) distribution of SET_0 values for four types of LEs (where EC/DEC group include EC/DEC (1:1, v/v), EC/DEC (1:2, v/v), and EC/DEC (1:1, w/w); EC/DMC group include EC/DMC (1:1, v/v), EC/DMC (2:1, v/v), EC/DMC (3:7, v/v), and EC/DMC (1:1, w/w); EC/EMC group include EC/EMC (1:3, v/v), EC/EMC (1:3, w/w), EC/EMC (1:1, v/v), EC/EMC (1:1, w/w), EC/EMC (3:7, v/v), and EC/EMC (3:7, w/w); TS group include EC/DMC/VC (0.475:0.475:0.5, v/v), EC/DMC/DEC (1:1:1, v/v), EC/DMC/EA (1:1:1, w/w), EC/DMC/PC (1:1:1, v/v), EC/DMC/EMC (1:1:1, v/v), and EC/DEC/EMC (1:1:1, v/v). Hollow icons represent the average value of groups.

To surmount the challenge posed by the incomparability among various studies, the incorporation of relative rates stands out as a viable solution. Based on this, we propose a novel concept of "self-extinguishing efficiency (SEE)".

$$SEE = 1 - \frac{\mathrm{SET}}{SET_0} \qquad \text{Eq 4.3}$$

By using this formula, we convert the SET values collected from literature into SEE and classify them into three groups according to the SET classification; each group consists of 31, 26, and

151 data respectively. These data are summarized from over 50 papers and cover 32 representative FRs, which can be structurally categorized into three types: aliphatic-based phosphate/phosphite, aromatic-based phosphate/phosphite, and cyclophosphazene-based additives, as displayed in Figure 4.3, 4.4, and 4.5.

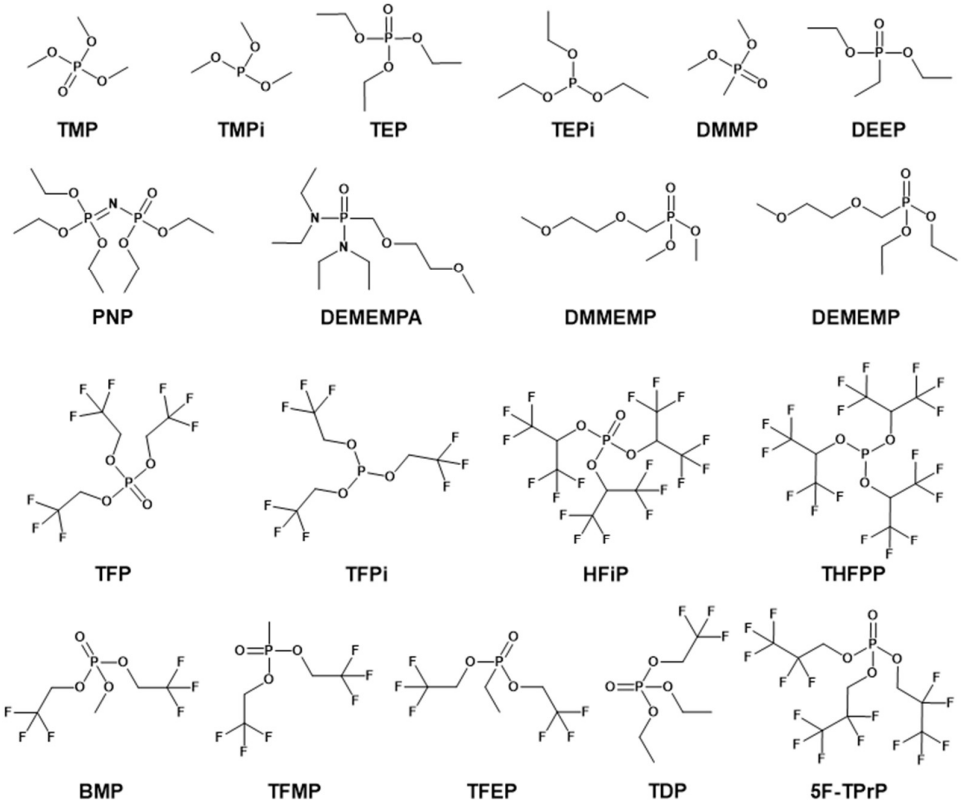

Figure 4.3 Phosphate/phosphite-based aliphatic FRs.

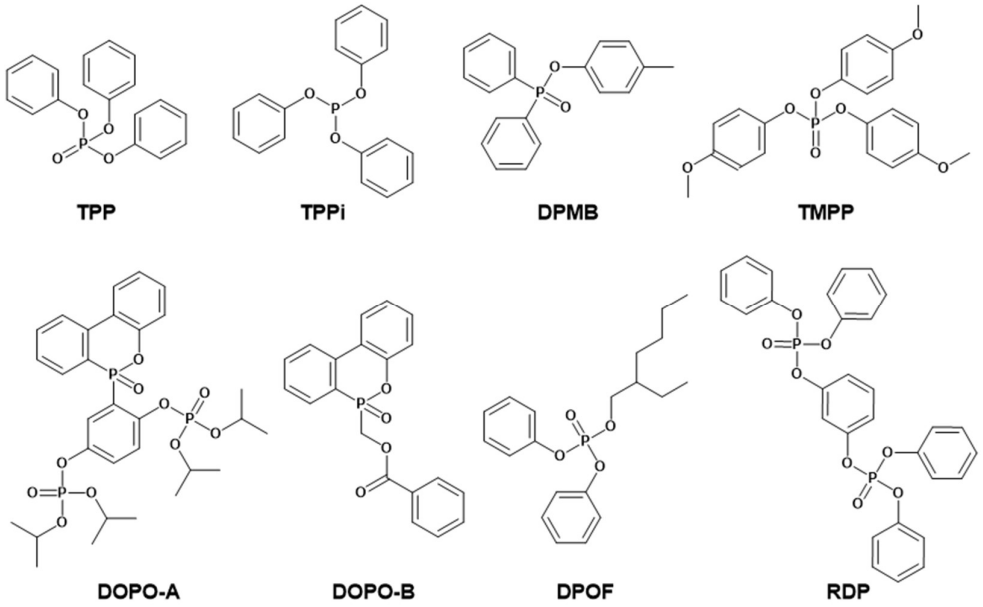

Figure 4.4 Phosphate/phosphite-based aromatic FRs.

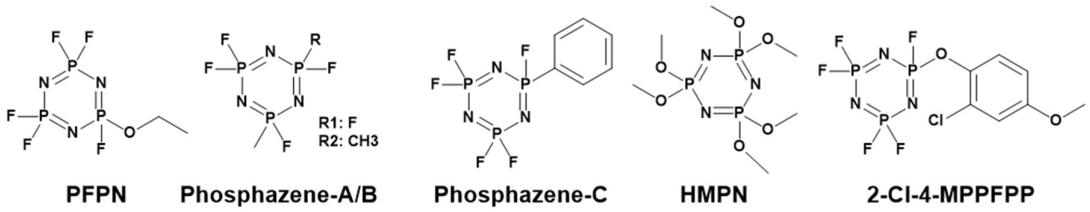

Figure 4.5 Cyclophosphazene-based FRs.

As shown in Figure 4.6a, the "N, Nonflammable" group (SET≤6) manifests a prevailing distribution surpassing 90%, whereas the "R, Flame Retarded" group (6<SET<20) is predominantly situated within the 70-90% range, with the minimum score, lower quartile (Q1), median, upper quartile (Q3), and maximum score of 70%, 75%, 82%, 84%, and 95%, respectively. In contrast, the majority of the "F, Flammable" group (SET≥20) exhibits a distribution below the 70% threshold with a median value of 32%, only 8 points within 151 data discrete outside the range. As shown in Table 4.7, the new SEE evaluation criteria for assessment were put forward based on the above analysis. For data that belong to "Flammable" group according to the SET classification (SET≥20) but are classified into "Flame Retarded" group following the SEE classification (90>SEE>70), it is more reasonable to classify a SET value ~20 s g^{-1} as "Flame Retarded" if it decreases from a highly flammable SET0 value ~200 s g^{-1}, which is likely caused by the testing method.

Table 4.7 SEE-based flammability evaluation criteria for LEs.

SEE (%)	Level	Denotation
SEE≤70	F	Flammable
70<SEE<90	R	Flame Retarded
90≤SEE≤100	N	Nonflammable

The built-in function of the applied RF algorithm to calculate the importance of features, represented by an impurity-based value quantifying the impact of a feature, serves as a powerful tool for selecting features and analyzing the influence factors. The data collected from the literature contribute to the construction of two models: SET(number)-Ref and SEE(number)-Ref models. In testsets, the R2 scores of SET(number)-Ref and SEE(number)-Ref models with the best splitting are 0.83 and 0.84, respectively, implying good prediction accuracy. In both models, the prediction errors in trainsets are from 3 to 5, and around 10 in testsets. These errors are small compared to the distribution range of collected SET and SEE values. Figure 4.6b presents the feature importance of regression models predicting numerical SEE and SET. The total importance of all features is 1, where a higher importance indicates a greater impact of the feature on SEE or SET. In both models, the most significant feature affecting the target properties is "Mass", followed by the features "SET0" and "FR(%)". In detail, the concentration of FR has a more pronounced effect on SEE (0.514) compared to SET (0.383). Moreover,

"SET0" exhibits greater importance in predicting SET, suggesting that SET is more sensitive to the properties of control electrolytes and testing procedures. In contrast, SEE is greatly affected by the inherent characteristics of FRs, offering a means to effectively assess additive efficacy and mitigate the influence of testing methodologies.

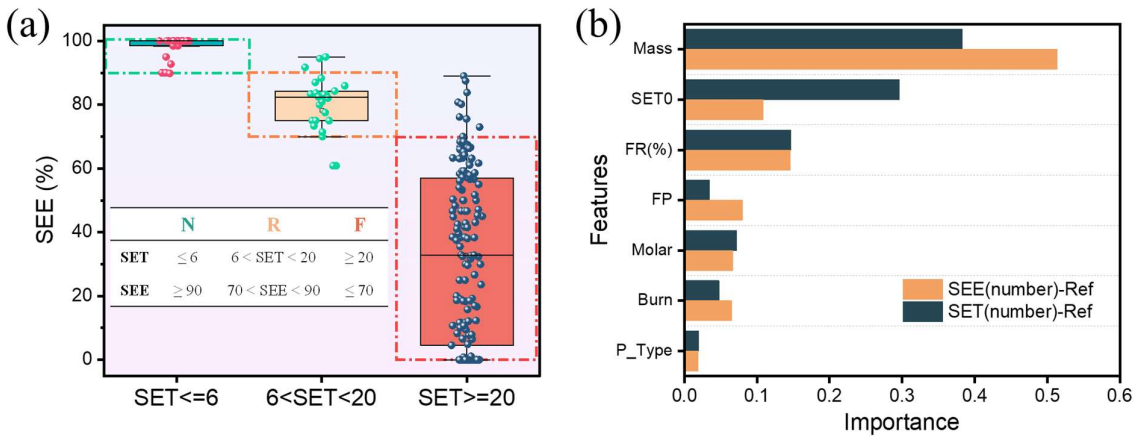

Figure 4.6 (a) Box plot for SEE classification criteria. Data was collected from previous works.[163-174] (b) Feature importance of SEE(number)-Ref and SET(number)-Ref models.

4.3.2. Selection of standardized methods

Though SEE has been created to solve the wide distribution of SET, it cannot avoid the inherent reliance on test methods. Whether SET/SEE can be used as a convincing assessment method is rooted in whether it can reflect the intrinsic flammability of LEs. Furthermore, the existence of a linear correlation between SET and electrolyte mass needs careful investigation. In this regard, we conduct parallel experiments in an attempt to establish a repeatable and reliable normalized method. First of all, we chose two nonflammable materials (IP, GFS) and one flammable matrix (CW) to reveal the influence of the absorbing matrix on SET. IP is used due to its high-temperature stability (up to 1200°C), excellent flexibility, and strong liquid adsorption capacity. Four sizes of IP (10 × 10, 10 × 20, 20 × 20, and 30 × 30 mm^2) are prepared to achieve a wide range of adsorption levels. As shown in Figure 4.7 and Figure 4.8, a higher saturation amount (up to 3.6 g) can be obtained with the increase in size. For the same size, the burning time prolongs with the loading amount increasing, accompanied by a gradual decrease of SET values.

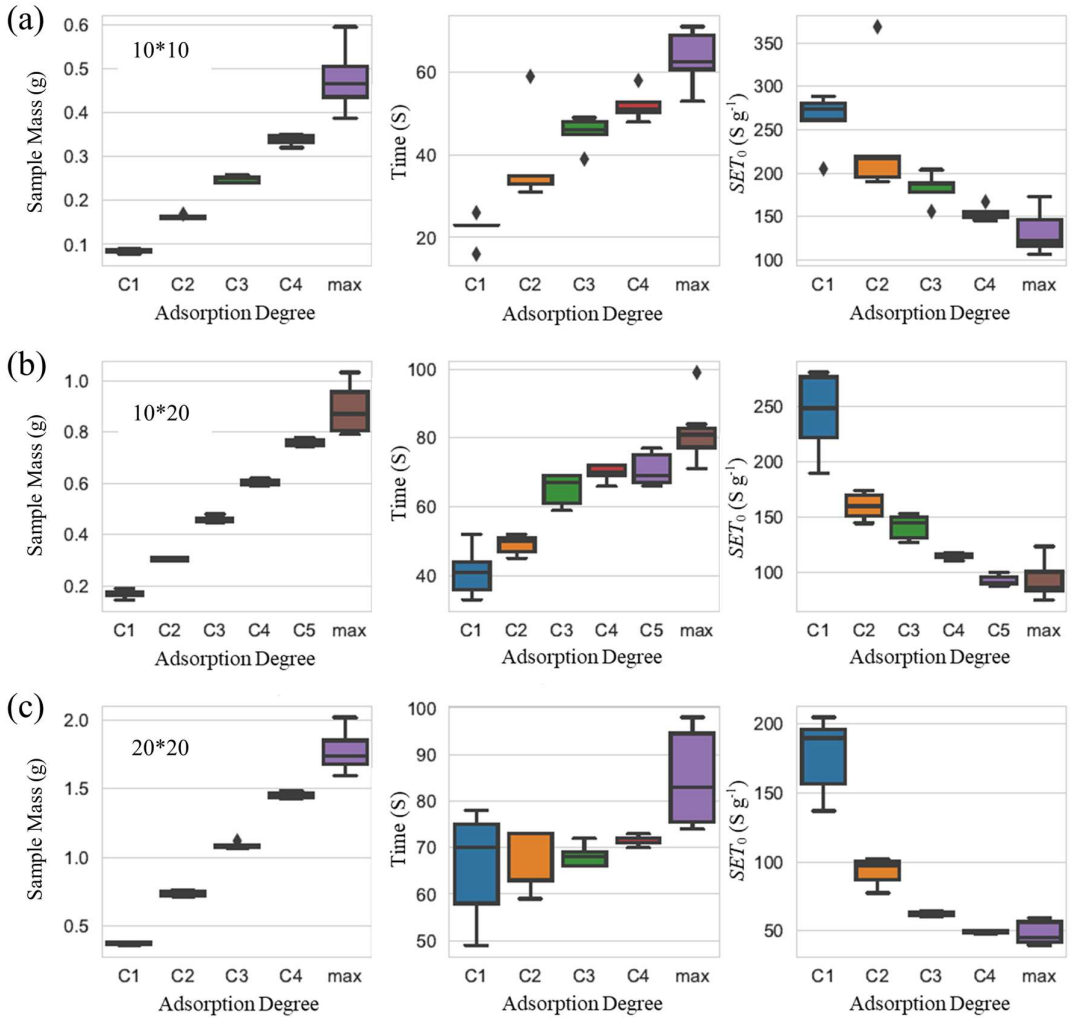

Figure 4.7 A series of adsorption degrees, burning time, and SET versus adsorption amount for different sizes of IP (a) 10×10, (b) 10×20, and (c) 20×20 mm^2.

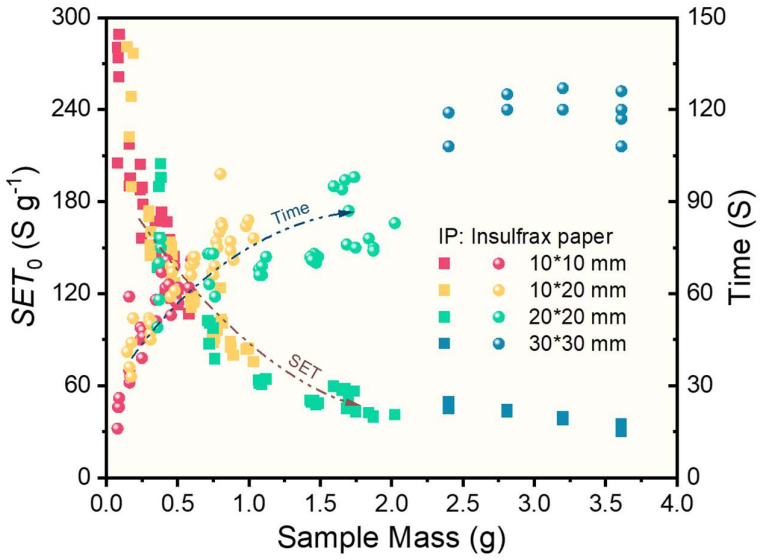

Figure 4.8 The relationship between SET_0 and sample mass tested by IP absorbent matrix.

Currently, CW is widely adopted to absorb LE to conduct the fire safety test. In Figure 4.9a, the saturation amount increases with the length and diameter of the wick, along with the burning time extending and the SET decreasing. Moreover, as the sample mass increases, the spread of data becomes more concentrated. Apart from wick, the separator is another superior adsorbent material owing to its outstanding wetting capability and effective liquid retention. Commercial LIB separators predominantly consist of polyolefin-based materials, such as PE, PP, or their composite materials. Although they have commendable electrochemical stability, they lack heat resistance and struggle to absorb and retain electrolytes, making them unsuitable for combustion experiments.[31] In contrast, glassfiber separators (GFS, Whatman) are used for the burning test in this study due to their excellent solvent resistance and splendid thermal resistance. Five specifications of discs (Φ10, 12.6, 16, 26, and 37 mm) are punched, with saturated masses of 0.04, 0.06, 0.1, 0.3, and 0.5 g, respectively. The horizontal combustion results are recorded in Figure 4.9b, and the counterpart results of vertical burning are given in Figure 4.9c. Similar to the wick case, the value and dispersion of SET significantly decrease as the sample weight increases. When using a fixed diameter diaphragm (Φ16 mm) to adsorb samples of different masses, the more saturated samples tend to have better repeatability both horizontally and vertically. Notably, the outcomes obtained from the vertical test show lower values because the upward propagation of the flame enhances the vaporization and pyrolysis of LEs, leading to more vigorous combustion behaviors. Meanwhile, samples placed vertically are easy to distribute unevenly due to the gravitational effect of droplets. It should be noted that the different heating sources will also exert a considerable influence on the outcomes. In Figure 4.9d, the thermocouple is used to monitor the heating temperature of both the gas lighter and the candle. After applying the igniter for 3 s, the detected temperatures of the gas lighter and candle reach 661 and 418°C respectively. A fast, stable, and clean fire source is more conducive to combustion investigation, while the flame provided by a candle is swaying and mixed with insufficiently oxidized wax, which will interfere with the repeatability and reliability of tests. Furthermore, the ignition method also plays an important role in the initial heating process. Figure 4.9e displays the effect of two igniting methods. Compared with the method of removing the fire source immediately after the flame has grown, the SET value obtained by continuously applying the fire source for three seconds is relatively low. Both ignition methods achieve good repeatability, but it is critical to maintain consistency in the ignition method.

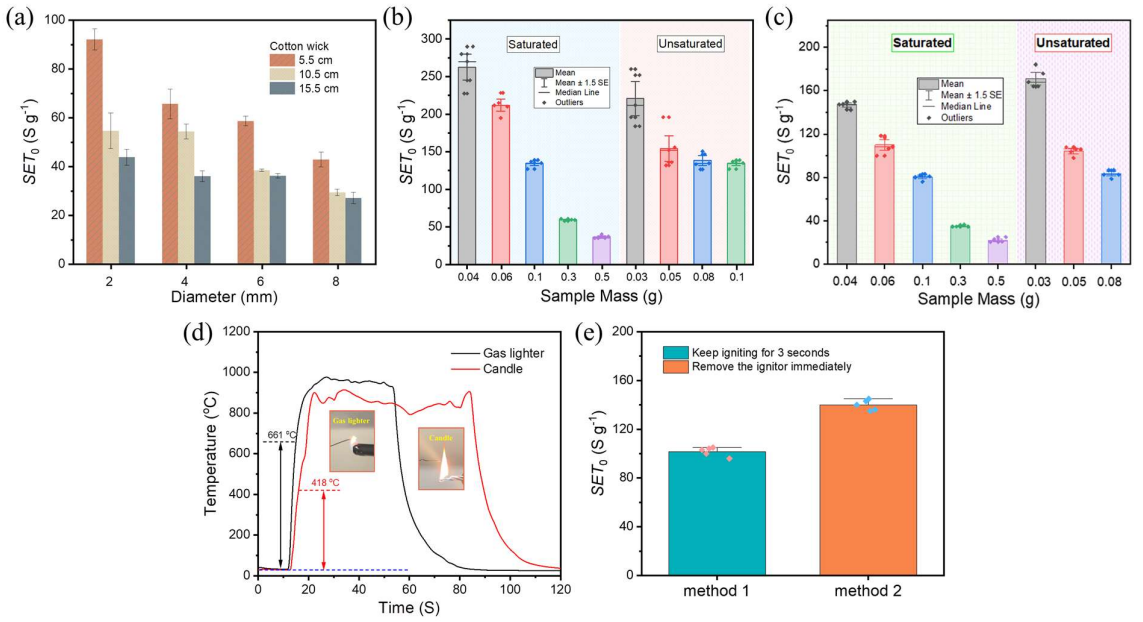

Figure 4.9 (a) SET_0 results obtained using CW of different lengths/diameters. Graph of SET_0 and sample mass tested with GFS (b) horizontally and (c) vertically, both saturated and unsaturated, the saturated group contains GFS of different sizes (Φ10, 12.6, 16, 26, and 37 mm), and the unsaturated group corresponds to the fixed size (Φ16 mm). (d) Temperature monitor of different heating sources: gas lighter and candle, and (e) SET_0 results obtained from GFS by applying different ignition methods.

Figure 4.10a offers a summary of results gained from the absorbed method, in the range of 0-6 g, it is obvious that the linear relationship between SET and sample mass does not exist. On the contrary, SET shows an exponential decrease with the consistent increase of sample weight, regardless of the adsorption material. A higher sample mass tends to offer a lower SET value, and when the sample mass exceeds 1 g, the impact of mass fluctuations on SET becomes relatively insignificant. However, the stringent requirements on sample mass are unfriendly to test costs and the environment. Therefore, we list and compare three mass (0.1, 0.3, 0.5 g) groups from the absorbed method in Figure 4.10b.

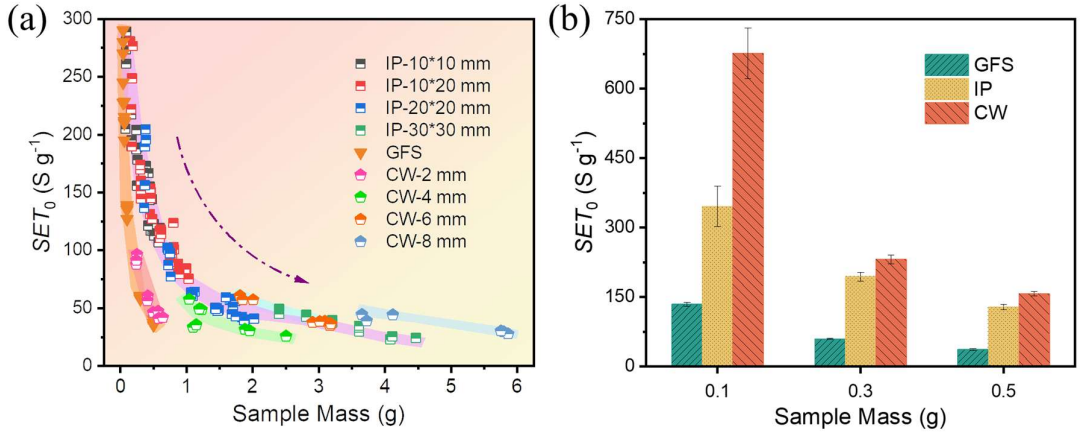

Figure 4.10 (a) Summary of all data obtained by the absorbing method, and (b) comparison between GFS, IP, and CW methods at several specific masses of samples: 0.1, 0.3, 0.5 g, blank LE used is 1.0 M $LiPF_6$ in EC/EMC=1/1 (v/v).

The gap between the SET values tested by the different methods is narrowed as the sample mass increases. It is worth noting that when adsorbing 0.1 g of electrolyte in the fluctuation zone, GFS obtained outcomes with a lower standard deviation (SD) of 4.6, while the SDs of IP and CW are equal to 44.0 and 55.0, respectively. Utilizing a 16 mm GFS to load 0.1 g of LE presents notable advantages over IP and CW methods, which include superb test repeatability, commercial availability of separators, and alignment with the electrolyte quality assembled in laboratories. The direct burning of LE with nonflammable containers has been exploited as the simplest way to perform the assessment, where test details are recorded in Figure 4.11.

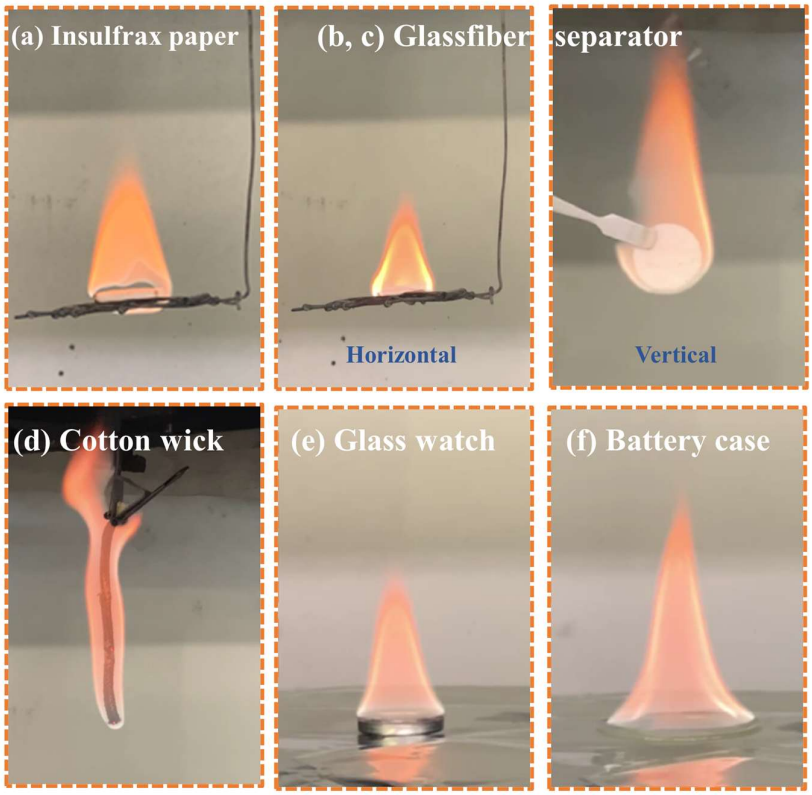

Figure 4.11 Photos recorded during different tests by (a) insulfrax paper, (b,c) glassfiber separator, (d) cotton wick, (e) battery case, and (f) glass watch.

As detailed in Figure 4.12a, three types of vessels: BC, GW, and Al pans (LL, LH, SL, and SH) are chosen and used to analyze the effect of the container on the burning behavior. The diameter of the generally used BC is 20 mm, with a maximum loadable weight of LEs of ~0.5 g, and the minimum mass required to cover the bottom evenly is ~0.4 g. In Figure 4.12b, the results obtained under the two masses are closely aligned (~75 s g^{-1}), showcasing good repeatability in both instances. Whereas the distribution of results obtained using GW is more dispersed, especially in the low mass range in fixed diameter (Figure 4.12c), implying a strong reliance on exposed areas. This dependency becomes more evident when employing Al lids with varying diameters and heights.

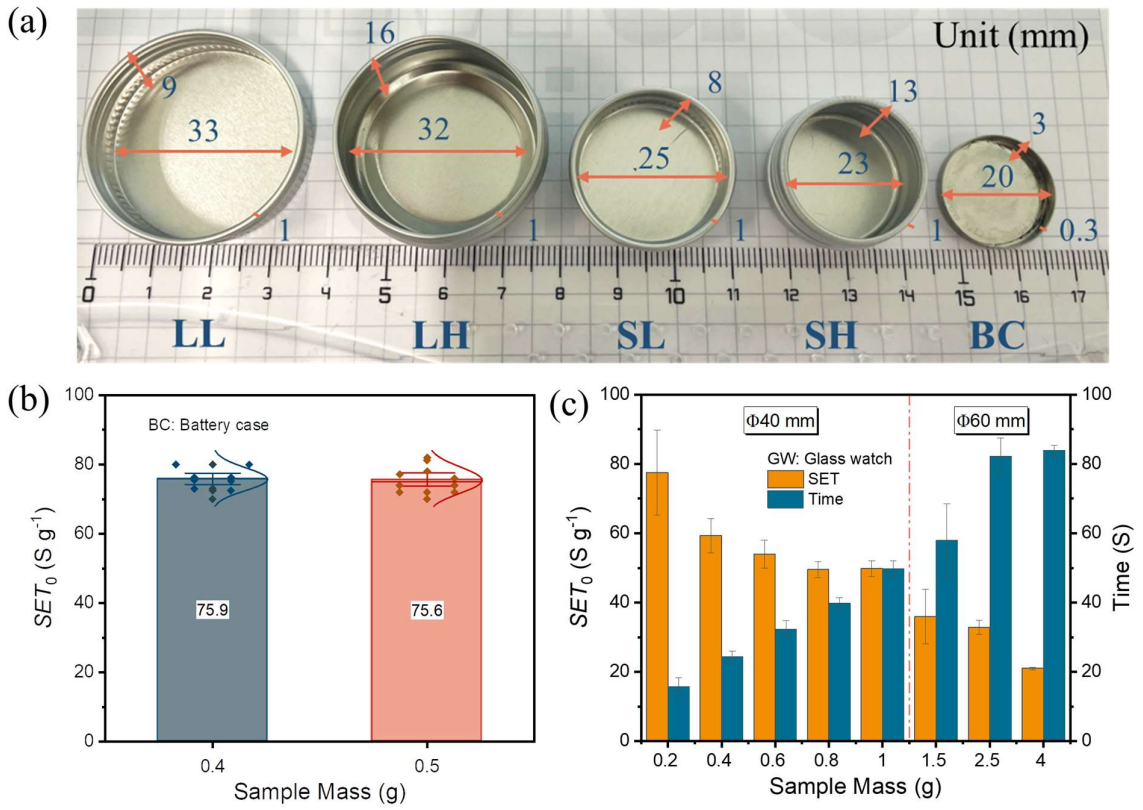

Figure 4.12 (a) Size information of vessels for direct burning test. Chart of SET_0 and sample mass tested by (b) BC containing 0.4 and 0.5 g of LE and (c) GW (Φ40, 60 mm).

By comparing the data in Figure 4.13a, it is apparent that for the same mass of LE loaded, smaller exposed areas and higher heights are prone to produce higher SET values. During combustion, a robust heat transfer process occurs between the system and the surrounding air, leading to the dissipation of a portion of the heat, and the rate of heat exchange is significantly influenced by the exposed surface area and the depth of the container. It is worth mentioning that a windless chamber is also necessary for conducting the experiments. Figure 4.13b offers a summary of data tested by all methods above, while the results of the "Absorbed" method are severely influenced by the electrolyte sample; the results of the "Placed" method are relatively unaffected. Additionally, burning 0.5 g electrolytes with BC demonstrates comparable results to the average values achieved with the SL pan in the 0.4-2 g range, ensuring reliability at lower mass levels. The generality of the method for electrolytes is illustrated in Figure 4.13c. Besides the EC/EMC system, the similarity and repeatability of the test results of BC and SL pan methods are also reflected in EC/DMC LEs. However, there are significant discrepancies in the results obtained from testing the EC/DEC LEs, potentially attributed to the high volatility of DEC. The trend of LE thermal stability is EC/DMC> EC/EMC>EC/DEC, which is consistent with the reciprocal order of boiling points of linear carbonates. Notably, the freshness of the electrolyte needs to be guaranteed during the experiment, and the exposure time to air should be shortened as much as possible before the combustion test. As shown in Figure 4.13d, upon

exposure to air and storage in the atmosphere overnight, the test results of electrolytes undergo considerable divergence. Specifically, the overall dispersion of data has increased. The EC/DMC group exhibits good stability, whereas the dispersion in the EMC and DEC groups is more pronounced, which aligns precisely with the respective volatility of the linear carbonate components. Constituent solvents with different volatilization capabilities will lead to changes in the composition of LEs, which was confirmed by the NMR track in Figure 4.14. The increase of the relative intensity of peaks a, b, and c verifies the increase of the EC/DEC ratio. Additionally, results obtained from testing non-fresh DEC electrolytes in two different containers are close, suggesting that smaller vessels (such as BC) are more indicative of the combustion conditions.

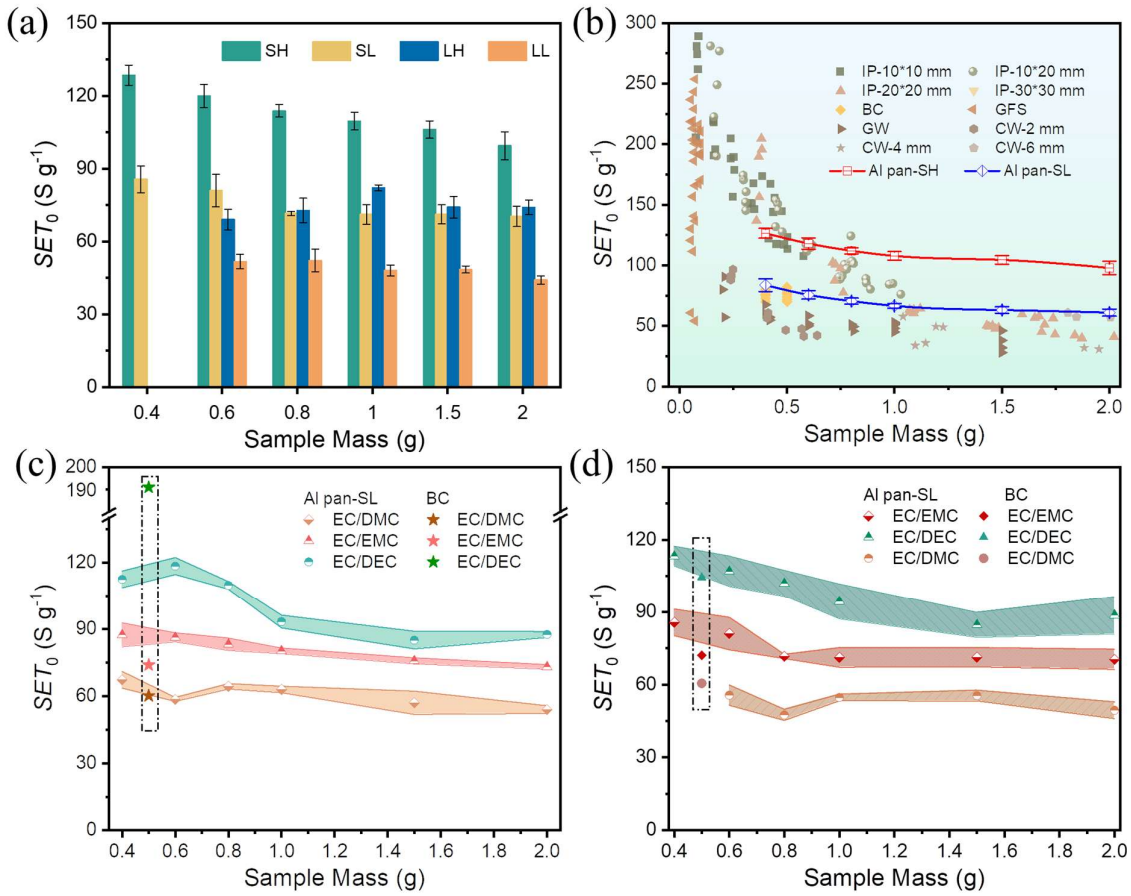

Figure 4.13 (a) SET_0 results tested by Al pan loading with 0.4-2 g LE. (b) Summary and comparison of SET_0 data in the sample range of 0-2 g, the LE used is 1.0 M $LiPF_6$ in EC/EMC=1/1 (v/v). SET_0 of three types of (c) fresh LE and (d) LE exposed in the atmosphere overnight obtained by the direct burning method: 1.0 M $LiPF_6$ in EC/DMC=1/1 (v/v); 1.0 M $LiPF_6$ in EC/EMC=1/1 (v/v); 1.0 M $LiPF_6$ in EC/DEC=1/1 (v/v).

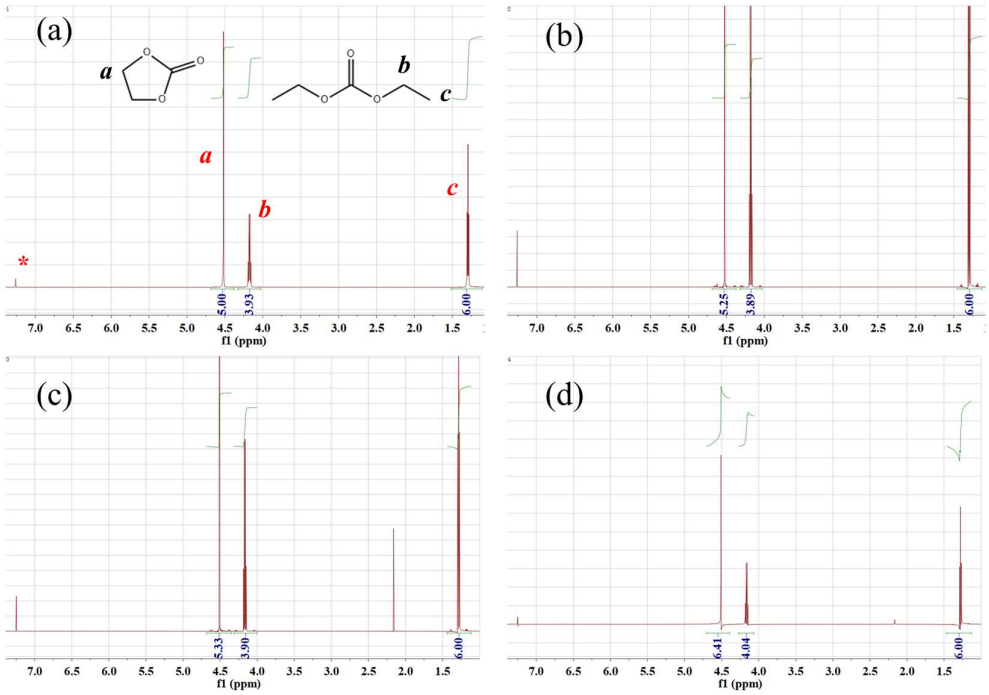

Figure 4.14 NMR track results of electrolytes stored under natural light at (a) day 1, (b) day 2, (c) day 3, and (d) day 5, the composition of LE is 1.0 M $LiPF_6$ in EC/DEC=1/1 (v/v).

4.3.3. Feasibility verification based on flame-retardant electrolytes

An appropriate evaluation of flame retardancy in electrolytes is imperative to provide scientific insights for the design of novel and safer electrolytes. To thoroughly study the impact of diverse fire-safety features on the LE combustion behavior and check the feasibility of uniformized methods, we collected 15 representative commercial FRs as listed in Table 4.8, including phosphates, fluorinated phosphates, phosphites, phosphonates, and cyclophosphazenes, which can be generally divided into phosphate (ppa), phosphite (ppi), and phosphazene (ppz) according to the chemical structure. Meanwhile, a series of important parameters are gathered for analysis, such as melting point, boiling point, percentage of FR elements (N, P, F), molecular mass, etc. To begin with, the fire tests of LEs modified with additives at four concentrations of 5, 10, 20, and 30 wt% are performed by BC and GFS methods, respectively. Figure 4.15a presents the SET and SEE results from the BC method (0.5 g). In comparison to SET_0 (75.6 s g^{-1}), most SET values exhibit a decrease upon the introduction of additives. However, the extent of this reduction is not prominent, and an anomalous phenomenon of prolonged combustion time is observed, which has not been reported in previous studies. According to the different phenomena, all FRs can be generally divided into three categories: (i) significant group includes TEPi, TMPi, TPPi, TTFPi, PFPN, and FPPN, which are composed of phosphite and cyclophosphazene; (ii) moderate type consists of TEP, TMP, DMMP, TFMP, and TFP, which are phosphate-based; and (iii) prolonged class involves TOP, DPOF, CDP, and TPP, which possess benzene rings or long alkyl chains in structure.

Table 4.8 Structure and basic information of FRs. ([a]: phosphate; [b]: phosphite; [c]: phosphazene; [d]: boiling point; [e]: melting point; [f]: flash point; [g]: molecule weight)

NO	Chemical Name	Abbr	Structure	Types	BP[d]	MP[e]	FP[f]	MW[g]	Ref
1	Triethyl phosphate	TEP		ppa[a]	215	-56.4	117	182.2	108, 170, 179, 180
2	Triethyl phosphite	TEPi		ppi[b]	156.6	-112	54	166.2	179
3	Trimethyl phosphate	TMP		ppa	197	-46	107	140.1	170, 108
4	Trimethyl phosphite	TMPi		ppi	110	-78	28	124.1	181, 182
5	Trioctyl phosphate	TOP	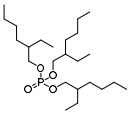	ppa	370	-70	216	434.6	183
6	Dimethyl methylphosphonate	DMMP		ppa	180	-50	68.9	124.1	184-186
7	2-Ethylhexyl diphenyl phosphate	DPOF	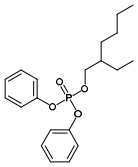	ppa	375	-54	224	362.4	187
8	Cresyl diphenyl phosphate	CDP	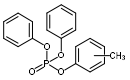	ppa	255	-30	232	340.3	170
9	Triphenyl phosphate	TPP	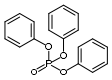	ppa	370	49	220	326.3	166, 188
10	Triphenyl phosphite	TPPi	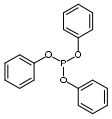	ppi	360	23	218	310.3	189
11	Bis(2,2,2-trifluoroethyl)methylphosphonate	TFMP	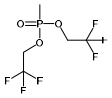	ppa	184	26	80	260.1	185
12	Tris(2.2.2-trifluoroethyl)phosphate	TFP	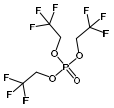	ppa	178	-19.6	60.4	344.1	190
13	Tris(2,2,2-trifluoroethyl)phosphite	TFPi	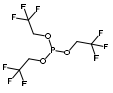	ppi	130	-28.5	113	328.1	191
14	Ethoxy(pentafluoro)cyclotriphosphazene	PFPN	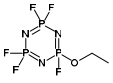	ppz[c]	125	-34	-	275.0	172, 192
15	Pentafluoro(phenoxy)cyclotriphosphazene	FPPN	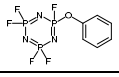	ppz	-	-	-	323.0	193

In parallel, Figure 4.15b provides the results evaluated by the GFS method. The efficacy of additives in fire suppression becomes more prominent after utilizing diaphragms as adsorption bases, particularly noteworthy when the additive amounts up to 20%, the majority of SEE clusters are within the range of 90-100%. Remarkably, within the above-prolonged group, CDP and TPP demonstrate flame retardant effects, whereas TOP and DPOF exhibit a decrease in SEE with rising contents.

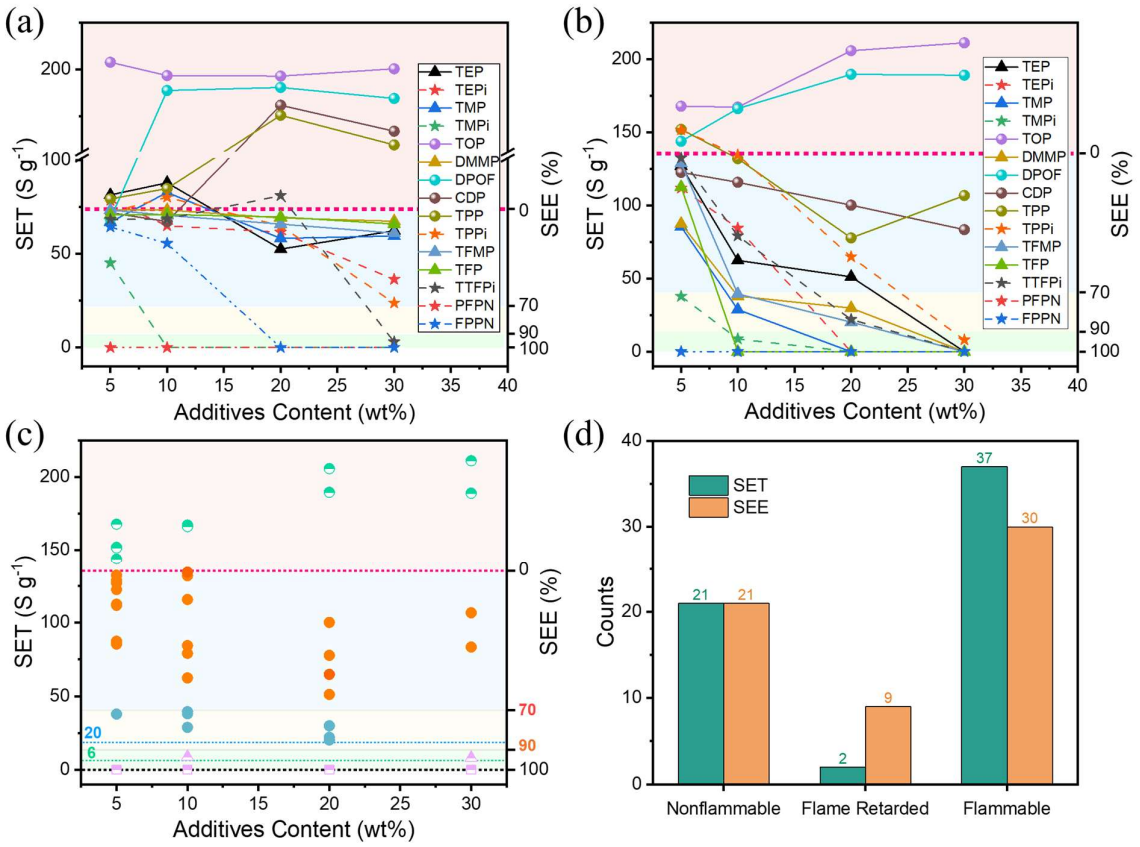

Figure 4.15 Fire safety performance of modified LEs evaluated by (a) BC and (b) GFS methods. (c) Distribution diagrams and (d) classification statistics of SET and SEE of electrolytes added with FRs obtained by the GFS method, where the results of SET classification are represented by different pattern shapes (circles ●, triangles ▲, squares ■), and the results of SEE classification are distinguished by different pattern colors (orange, blue, lavender).

Through the above comparative analysis, it can be inferred that the direct combustion method provides a more rigorous evaluation compared to the adsorption one. Figure 4.15c provides the SET and SEE classification distribution based on the results obtained from the GFS method, where the categorization of SET and SEE is distinguished by pattern shapes and colors, respectively. In Figure 4.15d, there is no objection to the classification of the "Nonflammable" group, the main statistical dissent lies in the classification of "Flame Retarded" group and "Flammable" group. Compared with the blank LE with a SET0 of 134.6 s g^{-1}, the SET values of 40 s g^{-1} (SEE ~70%) and 13 s g^{-1} (SEE ~90%) present diverse extents of flame retardancy,

corresponding to the boundaries between flammable and flame-retardant, flame-retardant and non-flammable, respectively, instead of the fixed boundaries in SET classification. In the form of relative rate boundaries (70% and 90%), SEE can avoid the irrationality caused by the fixed boundary value (20 and 6 s g^{-1}) in the SET classification, which permits the specific boundary value converted by SET0 for different system (represent different test methods), thereby achieving comparability and reference significance between different works.

To clarify the reasons for the varying behaviors of different FRs in LE, the real-time FTIR facility is employed to detect the fragments released by additives in the TGA test. TMP and TFP are selected as representatives of moderately significant FRs, while TPP, DPOF, and CDP are chosen as examples of the prolonged group. As shown in Figure 4.16a and 4.16b, compared with TPP, TMP exhibits a lower temperature of decomposition and higher intensity of released fragments. The released products mainly contained phosphorus-based and carbon-based structures,[194-197], including P=O (1301 cm^{-1}), P-O (846 cm^{-1}), C-O (1056 cm^{-1}), and -CH_3 (2963 and 2862 cm^{-1}). For the TFP compound, Figure 4.16c confirms the existence of fluorine-containing structures (-CF_3, 1182 cm^{-1}). In contrast, Figure 4.16d shows that fewer phosphorus-based fragments are generated from TPP, similar to observations with CDP and DPOF (Figure 4.17). Meanwhile, the morphology of separators after burning is recorded by SEM. After being immersed in LE, the fibrous structure on the surface remains well after combustion, which is attributed to the exceptional thermal stability of GFS (Figure 4.18a and 4.18b). Whereas the burned separator exhibits persistent areas of carbon residue with many hole structures after the addition of 20% TMP/TFP to LE (Figure 4.18c and 4.18d). When the same concentration of TPP/CDP is introduced, a denser carbon residue is observed (Figure 4.18e and 4.18f). This is ascribed to the heightened thermal stability of additives, leading to the production of limited gas-phase components, with a greater retention in the condensed phase to form a protective layer.

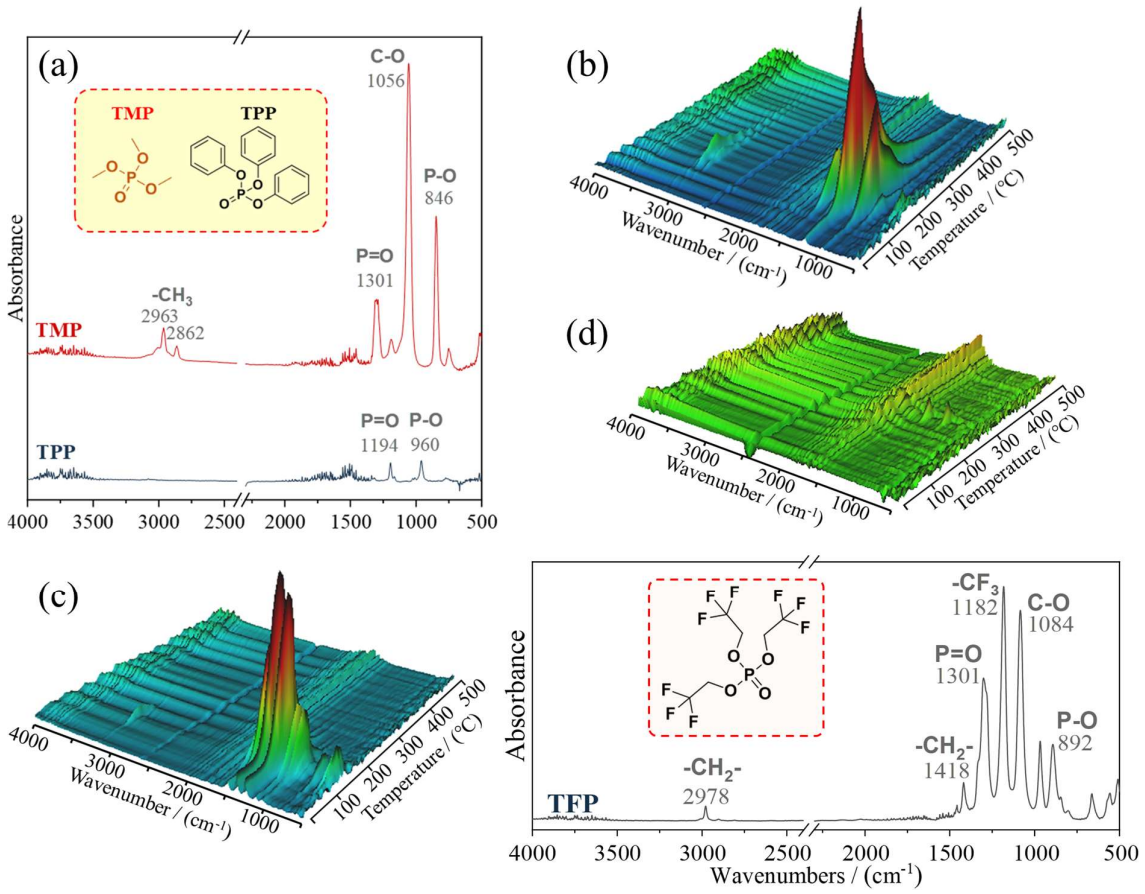

Figure 4.16 (a) The FTIR spectra of volatile products released at the maximum decomposition rate of TMP and TPP. Real-time FTIR spectra of (b) TMP, (c) TFP, and (d) TPP.

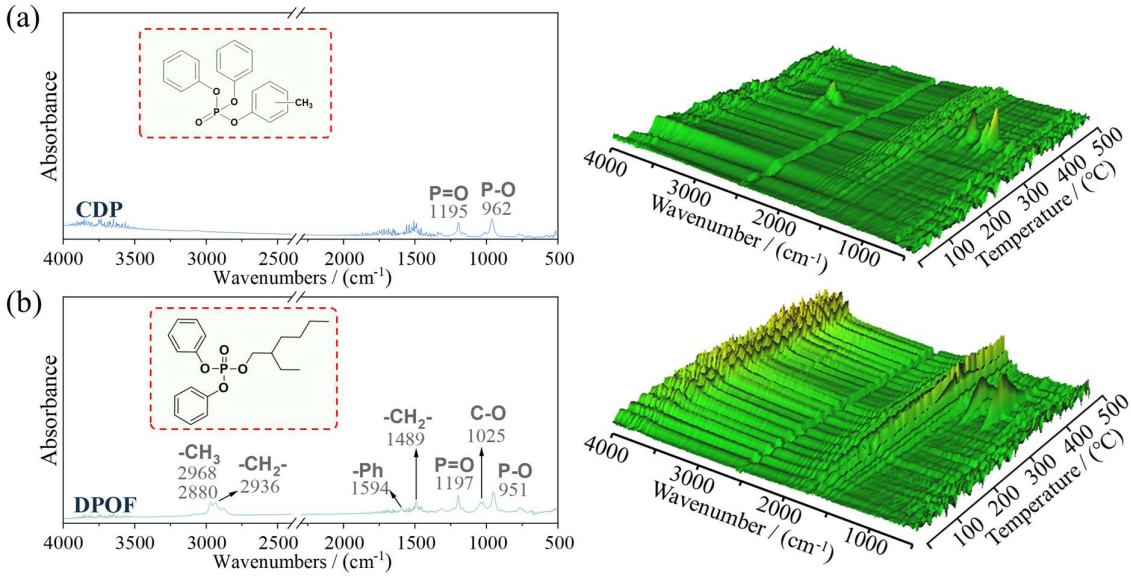

Figure 4.17 The FTIR spectra of volatile products released at the maximum decomposition rate and real-time FTIR spectra of (a) CDP and (b) DPOF.

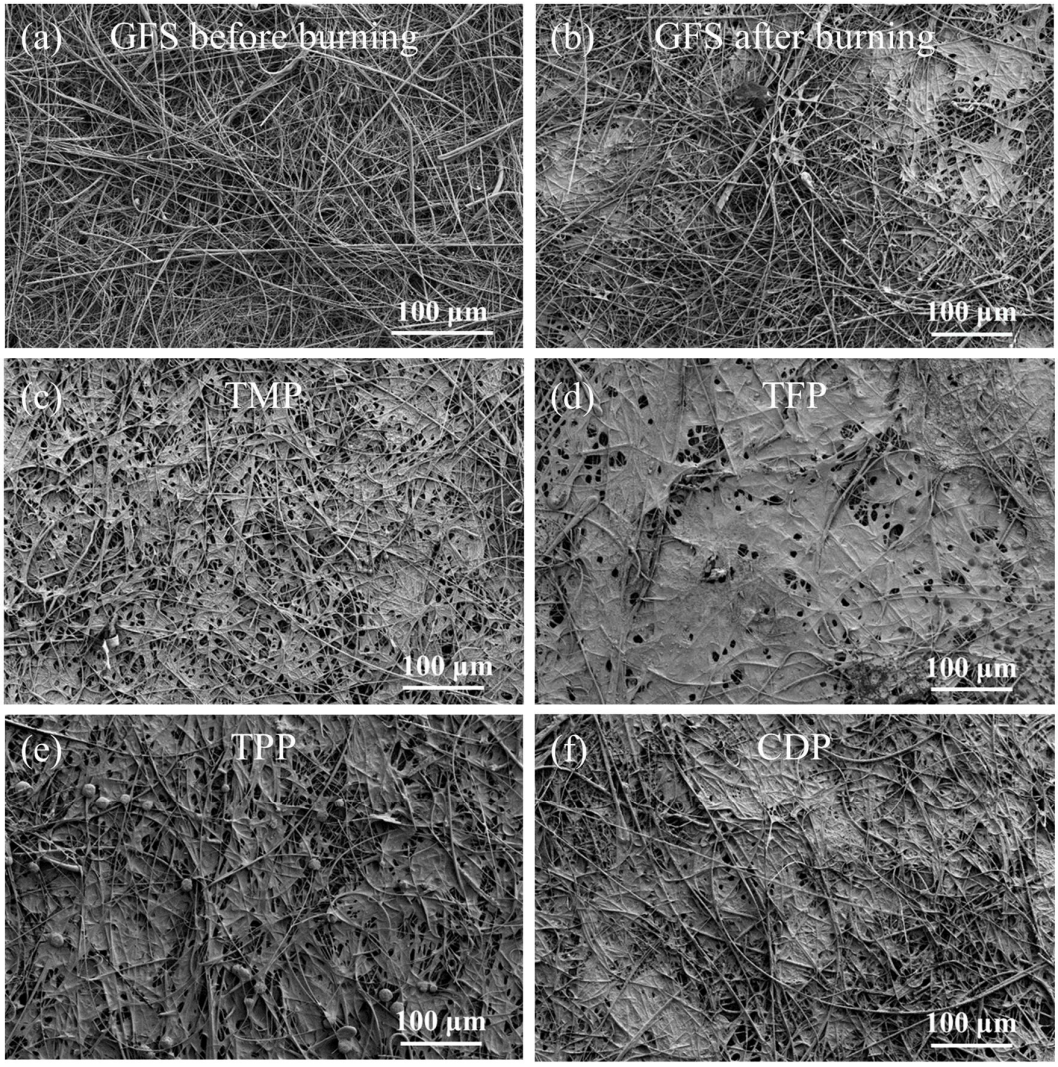

Figure 4.18 SEM images of (a) commercial GFS before burning and separators after burning that were absorbed with (b) blank LE, (c) LE with 20 wt% TMP, (d) LE with 20 wt% TFP, (e) LE with 20 wt% TPP, and (f) LE with 20 wt% CDP.

The distinction in thermal stability among various additive types is more intuitive in the differential thermal analysis (DTA) curves. In Figure 4.19a, the peak decomposition rates of TMP, TFP, and DMMP occur at 89.4, 83.1, and 104.8°C, respectively, while the onset temperature of degradation of TPP, DPOF, and CDP are found around 150°C and their peak decomposition rates appear at 238.6, 243.1, and 264.8°C, respectively. Besides, there is no residue remaining after 400°C for all additives. To comprehend the differences in results obtained by the two methods, we initially employ thermocouples to separately monitor the temperature changes of two sites during combustion. In the BC method, the selected spots are (1) the bottom of BC and (2) the center of the flame. For the GFS method, the selected points are (1) the surface of the diaphragm and (2) the center of the flame. As shown in Figure 4.19b and 4.19c, the LE loaded at the bottom of BC reaches a maximum temperature of 308°C, and

the flame center achieves a maximum temperature of 852°C. On the other hand, the surface of the diaphragm attains a peak temperature of 422°C with a maximum flame core temperature of 785°C. It indicates that the gas-phase combustion associated with the direct combustion method is more vigorous, which allows FRs with a lower boiling/decomposition point to release into the gas phase to exert the flame retardant effect. Whereas the adsorption method, represented by GFS, can concentrate more heat in the condensed phase, which facilitates the gasification and pyrolysis of more stable FRs.

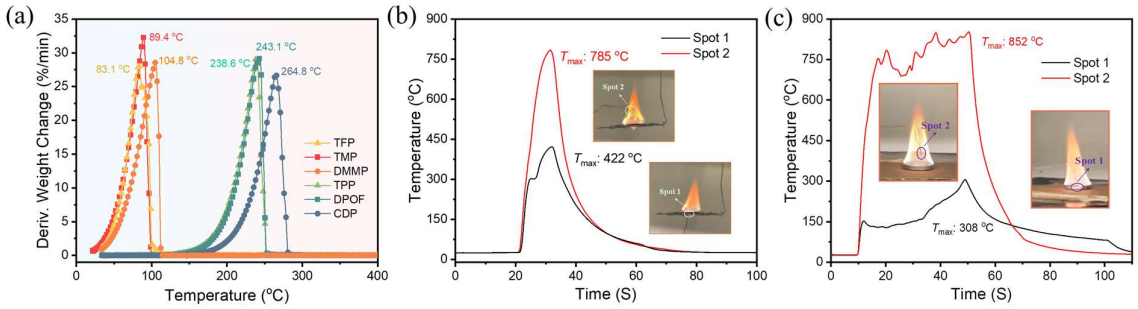

Figure 4.19 (a) DTA curves for some representative FRs: TFP, TMP, DMMP, TPP, DPOF, and CDP. Separate temperature monitoring during the electrolyte combustion by using (b) GFS and (c) BC method.

When the temperatures of these two points are monitored simultaneously, the results are similar (Figure 4.20a). Furthermore, the results of ignition using different fire sources are also compared in Figure 4.20b. The overall temperature of combustion using candle ignition is lower than that using a gas igniter, emphasizing the difference in the impact of different igniters. As indicated by the FEM simulation in Figure 4.21, the iron grid platform dissipates less heat than BC during the LE combustion process, validating the distinct temperature distribution of two methods in Figure 4.19b and indicating a preferable choice of using GFS method.

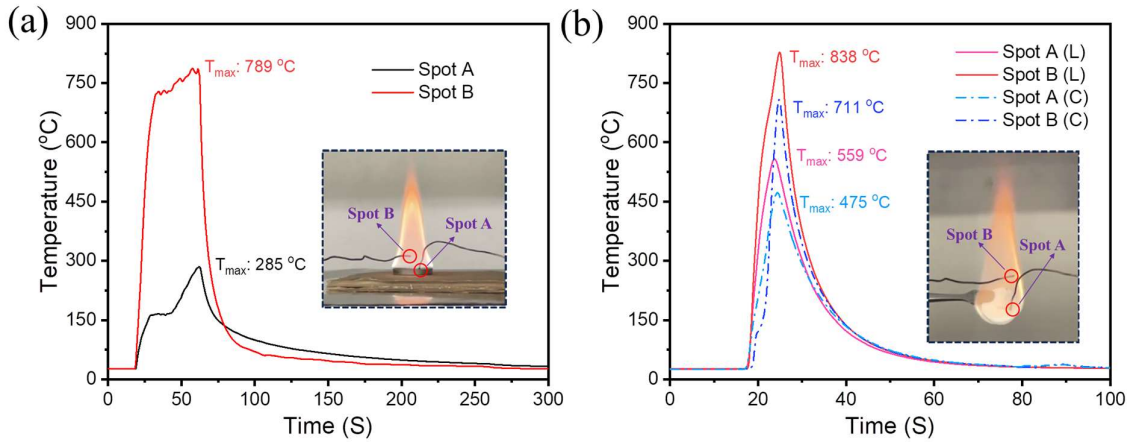

Figure 4.20 The simultaneous temperature monitoring result by using (a) BC and (b) GFS methods.

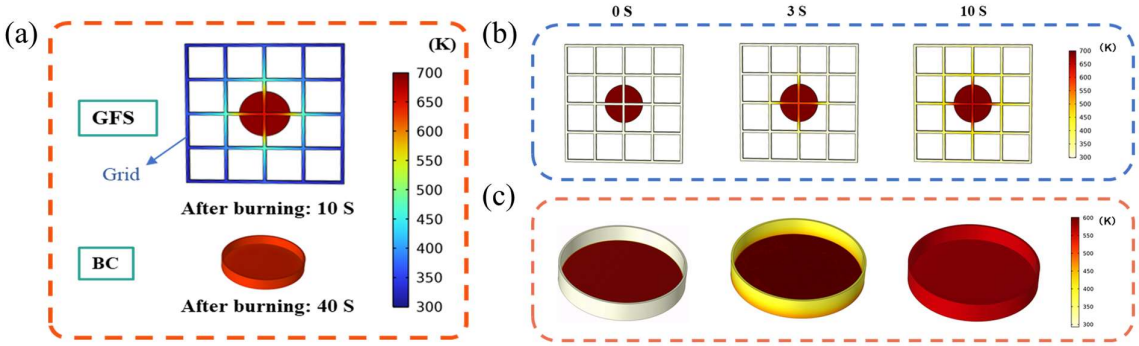

Figure 4.21 (a) Temperature field of the test platform of the grid and BC during burning. Temperature field evolution of the test platform of (b) grid and (c) BC with an initial temperature of 695.15 K and 581.15 K, respectively, corresponding to the temperature test by thermocouple. The button of BC and the grid were set with an initial temperature of 298.15 K to match the environment.

4.3.4. Flame retardant mechanism in liquid electrolytes

Combined with the above results, the working principle of FRs is proposed and illustrated in Figure 4.22. Additives with high volatility and low boiling points, such as phosphite, are susceptible to vaporization upon ignition of the LEs. The pronounced release during vaporization and pyrolysis, whether as entire molecules or smaller fragments, likely plays a crucial role in the dilution effect observed with these additives. For phosphates such as TMP, it is speculated that they first vaporize and then crack to perform their fire resistance effects. Specifically, the non-combustible gases generated during gasification can effectively dilute the concentration of vaporized LEs. With the temperature increases, FRs undergo further decomposition, and the resulting phosphorus-containing fragments can exert a quenching effect.[188]

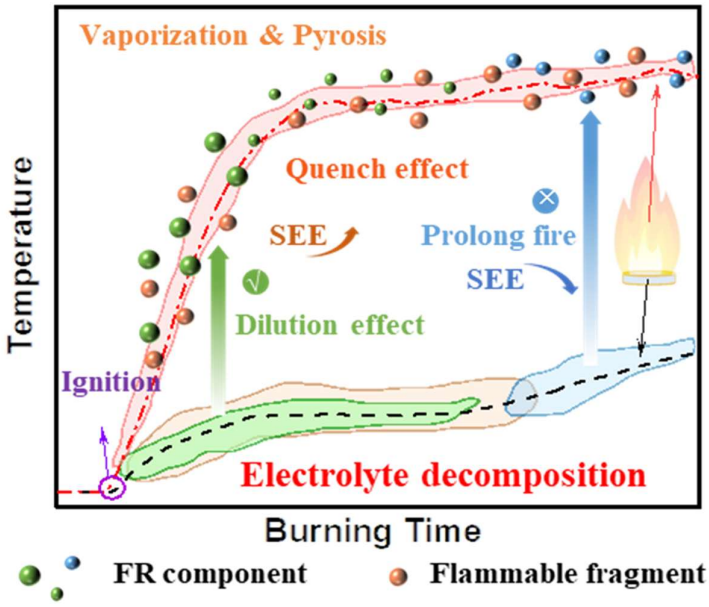

Figure 4.22 The proposed mechanism of FRs in LEs.

Regards to phenyl-phosphate, such as TPP, their limited release of gas-phase products leads to a suboptimal dilution effect during the electrolyte decomposition process.[198, 199] Although some phosphorus-based fragments (such as P=O, P-O) that can quench the combustion reaction are generated during the flame propagation, the combustion is difficult to suppress due to the full development of the fire, which instead results in prolonged burning time and the negative SEE values.

To compare the impact of various features on SEE between the Reference- and Experiment-datasets, three classification models are built with the Reference-, BC-, and GFS-datasets, respectively. Starting from the FR mechanism in LEs, we specify the features with comprehensiveness and generality as described in the Experimental section. All three models show satisfactory performance with high R2 over 0.82 in testsets and negligible prediction errors in trainsets and below 1 in testsets. As shown in Figure 4.23a, "Mass" is the dominant feature with an importance of 0.521 in the Reference-model, while the most significant influencing factor in the BC- and GFS-models is the effective element content ("FR(%)" in Figure 4.23b and 4.23c), accounting for 0.270 and 0.439, respectively. This clear difference suggests that the intrinsic properties of FRs have a greater impact on the experimental group models compared to the Reference-model. Except for chemical composition, the boiling point ("BP") of additives contributes significantly to influencing the SEE, and it occupies an importance of 0.228 in the SEE(class)-BC model, which is consistent with the above description that the vapor phase combustion of electrolytes in BC method is more vigorous (Figure 4.20). The ranking outcome tangentially validates our aforementioned hypothesis (Figure 4.22): the pivotal aspect of flame retardancy involves disrupting the reaction chain during LE combustion, so the abundance of effective FR components in the gas phase significantly influences the self-extinguishing behavior of LEs. Besides, flash point ("FP") has an insignificant influence on all models, which fits well with previous studies that the higher FP of FRs is prone to help inhibit the flammability of electrolytes.[173] However, "P_Type" as the type of phosphorus in the additive molecules, is almost the least important feature in all models. Overall, the selection of FRs influences SEE results strongly, which can also be observed by the feature importance bar chart from one model using both BC- and GFS-datasets (SEE(class)-Exp model, Figure 4.24). The difference between reference and experimental models might be caused by the dissimilar testing methods of SET. In the SET characterization, the loading method, mass of electrolyte, combustion surface area, and ignition behavior will influence the measuring results considerably. These features are difficult to extract completely from the limited description in publications, remaining obstacles in the precise modeling, which again emphasizes the necessity of this work to establish guidelines to evaluate the self-extinguishing behavior of LE.

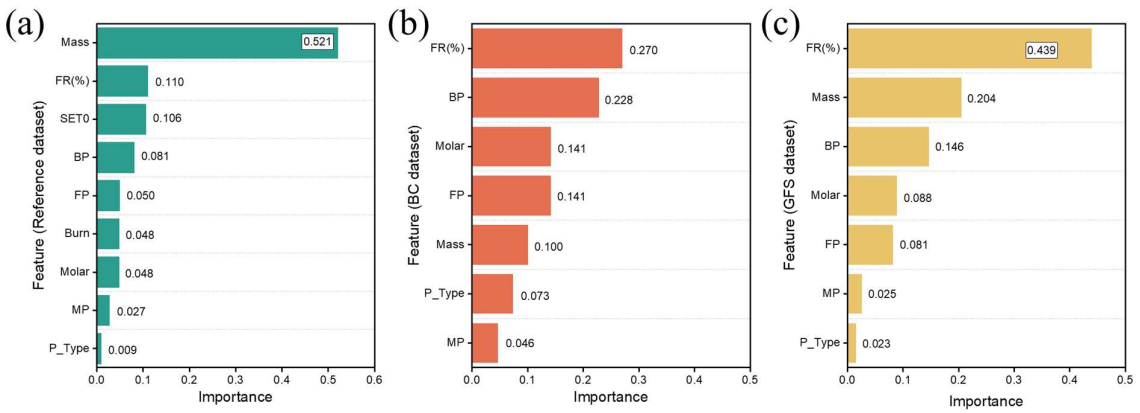

Figure 4.23 The feature importance of (a) SEE(class)-Ref, (b) SEE(class)-BC, and (c) SEE(class)-GFS models.

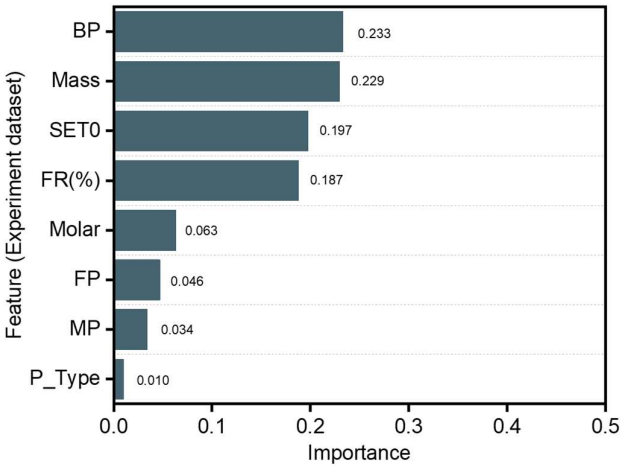

Figure 4.24 Feature importance of the SEE(class)-Exp model.

4.4. Conclusion

In this chapter, we proposed a novel concept of "self-extinguishing efficiency, SEE", and screened a reliable test protocol to establish a comparable safety assessment for LEs, that is, burning a 16 mm diameter GFS with the absorption of 0.1 g LE horizontally. The impact of test conditions on the assessment results was demonstrated, including ignitor source, placement, ignition method, etc., and the critical effects of using a clean fire source, ensuring a wind-free chamber, and employing a fixed ignition method on experimental repeatability were highlighted. The combination of a standardized test method and the dimensionless SEE metric enabled consistent and quantitative comparison across various studies. Based on data collection and analysis, the SEE-based flammability evaluation criteria were defined as follows: SEE≤70, Flammable; 70<SEE<90, Flame Retarded; and 90≤SEE≤100, Nonflammable. Meanwhile, 15 representative commercial FRs were evaluated using the proposed SEE index. Based on their influence on electrolyte burning behavior, they were classified into three categories-significant, moderate, and prolonged-corresponding to phosphite and cyclophosphazene, phosphate, and

additives containing benzene rings or long alkyl chains, respectively. The flame-retardant mechanism was formulated to elucidate the role of FRs in LEs, which pointed out that the vaporization and/or pyrolysis of additives preceding or synchronizing with the decomposition range of LE is conducive to flame retardancy. Meanwhile, ML was utilized to analyze the impact of different FR features on the combustion behavior of LEs, further verifying the mechanism. This study enables a comparative analysis of the fire safety performance of LEs in LIBs, which offers reliable support for choosing suitable electrolyte candidates in industrial applications and provides a reference for establishing standardized evaluation methods for batteries on different scales.

5. Relationship Between Electrolyte Flammability and Battery Fire Safety

5.1. Introduction

While the development of high-performance battery materials is crucial for advancing energy storage technologies, it is equally important to conduct comprehensive evaluations of batteries at various levels; however, the distinct research objectives at the laboratory and industrial levels dramatically constrain relevance and comparability. It is thought-provoking that the battery safety community appears to have reached a tacit consensus that a safer single component (in most cases, is electrolyte) can help build a safer battery. Supported by this, even if the existing safety analysis is limited to single materials, once a considerable safety improvement effect is achieved (which is significantly affected by the characterization method), it is taken for granted that it contributes to battery safety. However, the diversity of battery components complicates the validity of this proposition.[200] Although numerous novel solid electrolytes have been developed and demonstrate outstanding advantages, LEs still dominate the market due to their mature manufacturing processes. In Chapter 4, we found that the presence, type, and dimension of the adsorption substrates have a great influence on the combustion behavior of the same LE. Given that all components except LE can be regarded as part of the adsorption matrix, this substantial impact becomes readily apparent. Besides, the current flammability assessment of electrolytes is conducted under open-atmosphere conditions (ambient pressure and temperature). Nevertheless, electrolyte combustion in practical batteries occurs in confined environments, where pressure and temperature dictate combustion dynamics. Hence, it is one-sided and unconvincing to infer the safety of the entire battery based on the safety of a single component. As illustrated in Figure 5.1, akin to a bridge connecting two cliffs, it is essential to develop a safety assessment framework at the single-cell level. Researchers have developed tailored FR approaches to enhance the safety of specific components; however, there is skepticism as to whether these strategies inadvertently alter the combustion behavior of the whole battery.

Figure 5.1 Schematic diagram of the assessment of single cells as a bridge between single components and large-scale battery safety evaluation.

Although some work has dictated completing the fire safety assessments at a single battery level, as far as we know, there is hardly any research confirming the validity of the notion that a safer single component contributes to a safer battery.[201-203] Perrine et al. conducted combustion tests on commercial pouch cells using a fire propagation apparatus (Tewarson calorimeter) to reveal their fire risk and evaluated the dangerousness of toxic gases (such as HF, CO, NO, SO_2, and HCl) produced by fire combustion.[204] However, since these cells were obtained commercially and the specific components were unknown, they disassembled these batteries and used XRD, electrospray ionization high-resolution mass spectrometry (ESI-HRMS), and gas chromatography-mass spectrometry (GC-MS) techniques to decipher the unclear composition information, such as the component materials and corresponding content ratios. Zhong et al. employed a cone calorimeter to investigate the fire behavior of a single 18650 battery by utilizing a customized hollow copper cylinder heater to achieve uniform battery heating. While this study has guiding significance for the thermal failure behavior of single cylindrical batteries, its applicability remains limited due to a lack of universality.[205] Not only is it limited by the above-mentioned unknown components and uneven heating, but a greater challenge is to confirm whether the safety improvement effect currently established based on individual electrolytes can be reflected at the battery level. In this chapter, we selected pouch cells as research object for the following reasons: (i) their dimensions can be customized adaptably to ensure uniform heating; (ii) their flexible nature allows for easy deformation and rapid release of internal pressure, effectively preventing pressure accumulation and significantly reducing operational risks, and (iii) all electrodes, separators, electrolytes, and FRs are commercially available, ensuring the traceability and repeatability of the materials.

5.2. Experiment

5.2.1. Assembly technique and battery test of pouch cells

The assembly of single-layer pouch cells was operated in an Argon-filled glove box with H_2O levels below 0.01 ppm. The electrode and separator were folded up in sequence, and 1 mL of liquid electrolyte was injected before the final edge sealing process. To achieve adequate soaking, the assembled pouch cell was clamped by a holder and left overnight at room temperature, followed by the formation process of two cycles at 0.2 mA cm^{-2} under 25°C. Afterward, all batteries were electrically preconfigured by five galvanostatic charge/discharge cycles at 0.4 mA cm^{-2} and then charged to the wanted state-of-charge (SOC 0%, 50%, 100%). To reduce self-discharge and storage effect intervention, all cycling was completed less than 24 hours before calorimetric testing. EIS was measured with a Biologic SP-200 potentiostat within the frequency range of 0.1-10^6 Hz and an AC potential amplitude of 10 mV. Galvanostatic charge/discharge tests were carried out using the NEWARE battery testing system within a potential window of 2.5-3.8 V vs Li/Li^+.

5.2.2. Cone calorimeter test

The cone calorimeter test (CCT) was implemented with a dual cone calorimeter from Fire Testing Technology Inc., and the calibration was performed according to ISO 5660-1 standards before the experiment. All tests were conducted at a heat flux of 35 kW m^{-2} and a distance of 60 mm to avoid contact between the heating coil and swollen cells. The central back temperature of pouch cells was monitored with K-type thermocouples fixed by a sample holder. Ultra-high temperature measurement thermal Camera (AT31UZ) purchased from IRay Technology Co Ltd.

5.2.3. Simulation and computational analysis

The mass transfer of the gas is controlled by the convection-diffusion equation:

$$\frac{\partial c}{\partial t} + \vec{u} \cdot \nabla c = D\nabla^2 c + R \quad \text{Eq 5.1}$$

where c is the concentration of the gas, t is time, $\vec{u}$ is the velocity, D is the diffusion coefficient, and R is the source term, representing the rate of production or consumption of the gas per unit volume.

The incompressible flow is described by the Navier-Stokes equation:

$$\rho\left(\frac{\partial \vec{u}}{\partial t} + \vec{u} \cdot \nabla \vec{u}\right) = -\nabla p + \mu\nabla^2 \vec{u} + \rho\vec{g} + \overrightarrow{F_{st}} \quad \text{Eq 5.2}$$

where p is the pressure, μ is the dynamic viscosity of the electrolyte, $\rho\vec{g}$ is the gravity, $\overrightarrow{F_{st}}$ is the surface tension.

The continuity equation describing mass conservation is:

$$\nabla \cdot \vec{u} = 0 \quad \text{Eq 5.3}$$

The convection-diffusion equation for temperature (T) of the incompressible fluid is:

$$\frac{\partial T}{\partial t} + \vec{u} \cdot \nabla T = \alpha\nabla^2 T + S \quad \text{Eq 5.4}$$

where α is the thermal diffusivity of the substance, which is defined as $\alpha = \frac{k}{\rho c_p}$, k is the thermal conductivity, c_p is the specific heat capacity at constant pressure. S is the rate of internal heat generation (or consumption) per unit volume, divided by ρc_p. The initial temperature of the air was set as the room temperature, and the investigated sample was set as 553.15 K (280°C, according to experimental measurement). Then, a two-dimensional numerical calculation was performed by COMSOL Multiphysics 6.3.

5.3. Results and discussion

5.3.1. Assembly and electrochemical performance of cells

CCT is one of the most recognized apparatuses in fire assessment for polymeric materials, which has been adopted by the International Organization for Standardization (ISO 5660-1) and can offer various key parameters like HRR, mass loss rate, effective combustion heat, total smoke production (TSP), smoke release rate, etc.[206, 207] During the combustion process, HRR is proportional to the oxygen consumed.[208] As explained in Eq 5.5, CCT can estimate the heat generation with an average value of the heat of combustion for oxygen consumption of 13.1 kJ g^{-1}.

$$\dot{q} = (13.1 \cdot 10^3) \cdot 1.10C \frac{(0.2095 - X_{O_2})}{(1.105 - 1.5X_{O_2})} \quad \text{Eq 5.5}$$

where $\dot{q}$ is the rate of heat release (kW), C is the orifice plate coefficient ($kg^{½}m^{½}K^{½}$), and X_{O_2} corresponds to the oxygen mole fraction in the exhaust air.

As depicted in Figure 5.2a, a specialized size of 10 cm × 10 cm pouch cell is designed to achieve uniform heating by using a radiative heater, which can simulate thermal abuse conditions of LIBs. The specimen is covered by high-temperature endurable insflux paper for thermal insulation before the test. All experiments are conducted at a heat flux of 35 kW m^{-2} and a distance of 60 mm, which can ensure the occurrence of thermal runaway while the surface of bulged cells will not contact the coils.

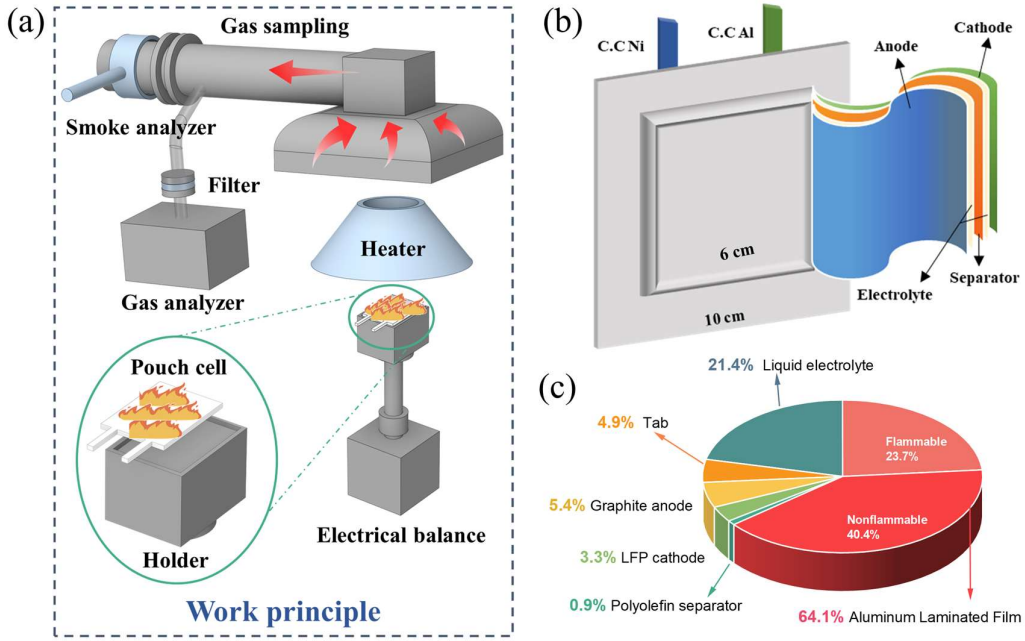

Figure 5.2 (a) Illustration of the safety assessment for the designed SLP utilizing the cone calorimeter test. (c) Structural information of the designed cell. (d) Mass distribution of all components in SLP.

Figure 5.2b describes the composition of the designed single-layer pouch cell (SLP), and the corresponding mass distribution is displayed in Figure 5.2c. The outer package is made of aluminum laminated film with a thickness of 113 μm, which is composed of an outer protective layer (ON), barrier layer (AL), and heat-sealing layer (CPP), where the nonflammable parts account for 40.4% of the whole composition. The electrode materials constitute 8.7% of the total weight, comprising 5.4% graphite anode and 3.3% LFP cathode; the capacity ratio between the anode and cathode (the N/P ratio) is maintained at ~1.26. Among the whole components, the LE ranks as the second most flammable part and occupies 39.1% of all flammable elements (Figure 5.3a), making it reasonable to evaluate the effectiveness of flame-retarding strategies of FR-modified cells.

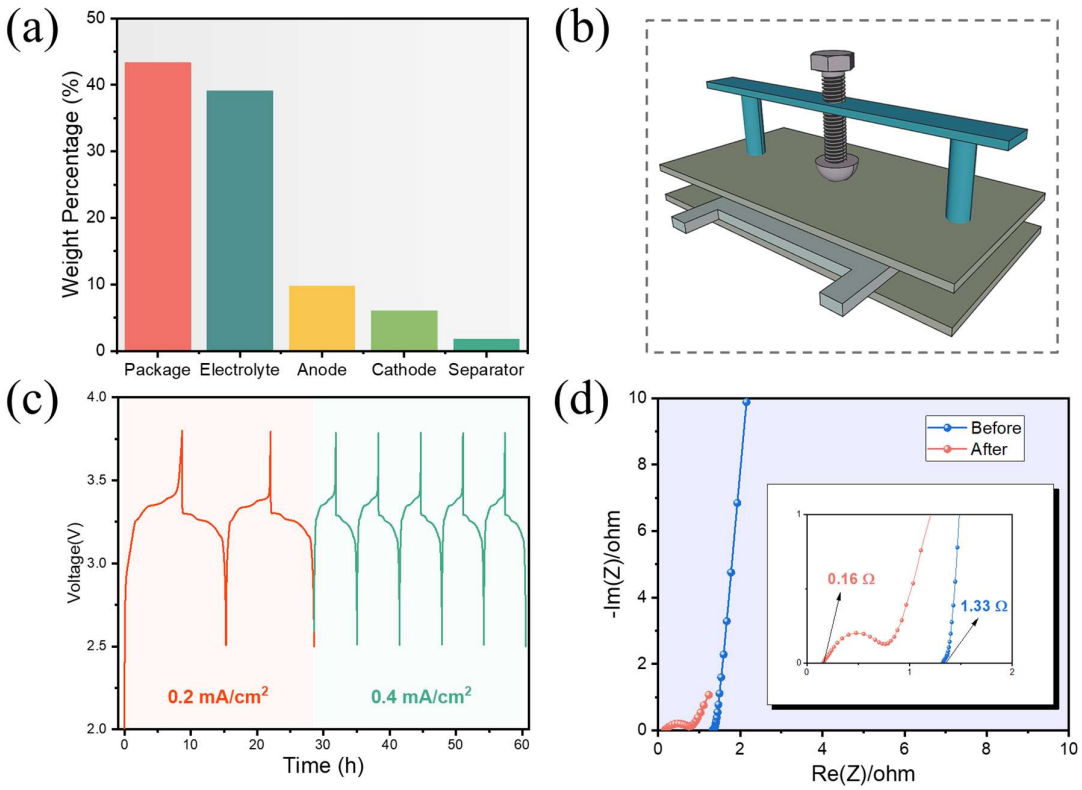

Figure 5.3 (a) The weight percentage of all flammable components in SLP. (b) Scheme of the holder used for imposing pressure on SLPs. (c) Galvanostatic charge-discharge curves of SLP at different current densities. (d) Electrochemical impedance spectroscopy curves of SLP before and after cycles.

Before the CCT assessment, the freshly assembled cell was subjected to electrochemical performance testing to ensure optimal performance and to validate both the feasibility and reproducibility of the battery assembly technique. SLP was imposed pressure by a holder (Figure 5.3b) to facilitate tight electrode contact and complete electrolyte wetting. Subsequently, SLP was formatted at a current density of 0.2 mA cm^{-2}, corresponding to a C rate of ~ 0.12. As shown in Figure 5.3c, SLP composed of blank liquid electrolyte (BLE) achieves a specific capacity density of 119.56 mAh g^{-1} and a Coulombic efficiency of 76.13% at the first cycle. In the following 5 cycles at a current density of 0.4 mA cm^{-2}, an average specific capacity density

of 112.73 mAh g^{-1} is obtained. As depicted in Figure 5.3d, EIS analysis demonstrates the successful establishment of a stable SEI layer, exhibiting a characteristic interface impedance of 0.60 Ω. The optimized electrolyte-electrode interfacial wetting characteristics led to a remarkable reduction of bulk impedance from 1.33 Ω to 0.16 Ω, indicating improved ion transport kinetics across the electrode-electrolyte interface. Figure 5.4a presents the galvanostatic charge-discharge curve of SLPs at the current density of 0.4 mA cm^{-2}. The capacity maintained 25.78 mAh after 20 cycles, accompanied by an average Coulombic efficiency of 99.46% and a low fading rate of 0.088 mAh per cycle, suggesting highly reversible lithium-ion intercalation/deintercalation processes and robust electrochemical performance. Figure 5.4b and 5.4c record the cycle stability of two individual SLPs, confirming that the battery assembly procedure can guarantee the repeatability of battery performance. To investigate the influence of SOC on the combustion characteristics of SLPs, three distinct SOC (0%, 50%, 100%) are marked in Figure 5.4d through varying depths of discharge.

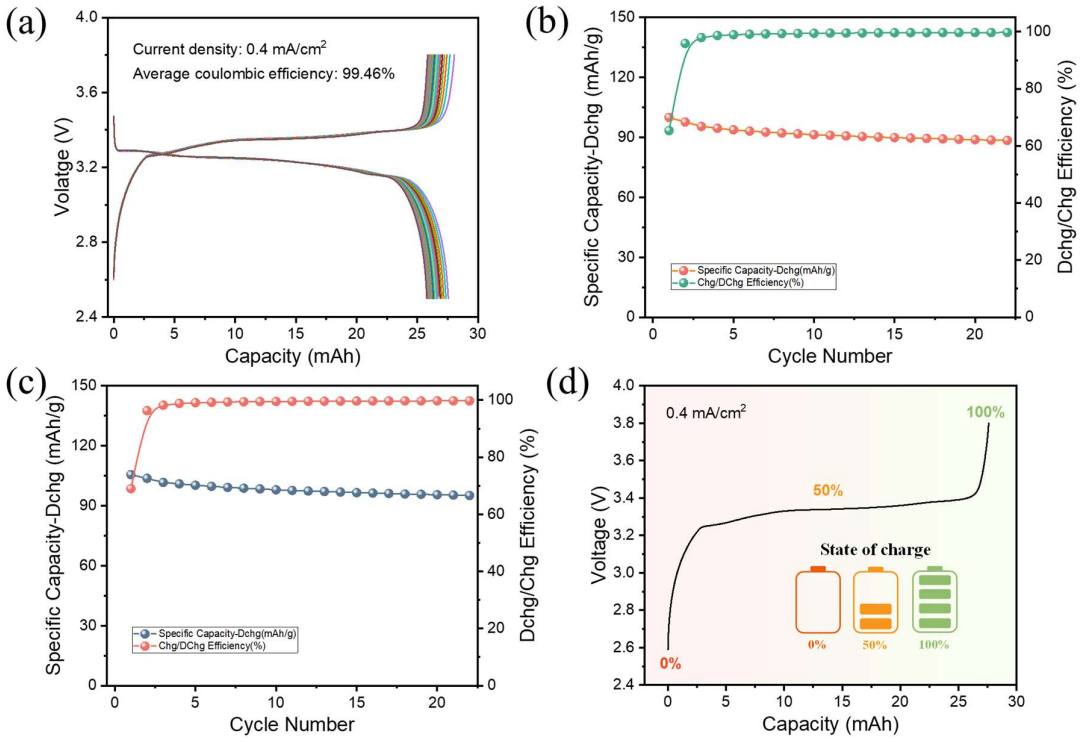

Figure 5.4 (a) Galvanostatic charge-discharge curves of SLP at the current density of 0.4 mA cm^{-2}. (b, c) Cycling performance of SLPs, the first two cycles were completed at 0.2 mA cm^{-2}, and the remaining cycles were performed at 0.4 mA cm^{-2}. (d) SOC (0%, 50%, 100%) is set based on the discharge capacity of SLP at the current density of 0.4 mA cm^{-2}.

To avoid contact between the expanded battery surface and the heating coil while ensuring repeatable ignition of the BLE-SLP, CCT was conducted under the heat flux of 35 kW m^{-2} and a distance of 60 mm. During controlled thermal abuse testing, the failure progression of LIB thermal runaway proceeds in a sequential manner. Figure 5.5a delineates the four distinct phases in thermal response: (i) initial stable state, (ii) venting with smoke emission, (iii) open flame

combustion, and (iv) afterglow smoldering. In detail, the internal pressure of cells will increase sharply when the heat and temperature of initially stable cells accumulate and reach the component's evaporation or decomposition thresholds. This culminates in pouch cell venting when inner pressure exceeds the aluminum laminate's mechanical integrity limit, accompanied by vigorous electrolyte aerosol and smoke emission. As smoke continues to be released, when the concentration of the resultant combustible fragment reaches the lower flammable limit (LFL), violent combustion ignited by the arc will occur and persist until fuel depletion below the LFL. Following flame extinction, the cell enters a smoldering phase characterized by persistent exothermic reactions, continuous aerosol emission, and sustained temperature rise until the remaining combustible material is consumed.

5.3.2. Fire behavior of blank electrolyte-based cells

To establish a comparative framework for evaluating FR-SLPs, the baseline characterization was performed on BLE-SLPs across three representative SOC states (0%, 50%, and 100%). As shown in Table 5.1, the time-to-ignition (TTI) exhibits an inverse correlation with increasing SOC, with measured values of 25, 21, and 16 seconds, respectively. As illustrated in Eq 5.6, the total heat generation (Q_t) during battery thermal runaway primarily originates from three sources: (i) ISC-induced Joule heat (Q_j), (ii) cross-component exothermic reactions (Q_r), and (iii) combustion heat (Q_c).[209, 210] The heat measured by CCT belongs to combustion heat, which is calculated based on oxygen consumption. Notably, since electrode materials release oxygen during thermal decomposition, which may subsequently participate in combustion reactions, this additional oxygen consumption (Q_{O2}) should be considered.[48, 211] The refined combustion heat formulation is presented in Eq 5.7.

$$Q_t = Q_j + Q_r + Q_c \quad \text{Eq 5.6}$$

$$Q_c = Q_{CCT} + Q_{O2} \quad \text{Eq 5.7}$$

The electrochemical (de)intercalation of Li in LFP follows the reversible redox reaction depicted in Eq 5.8. At the anode, graphite transitions from lithium-deficient phases (C_6 at 0% SOC) through staged intercalation compounds (e.g., LiC_{12} at 50% SOC) to fully lithiated LiC_6 (100% SOC). Meanwhile, LFP cathodes maintain coherent two-phase interfaces ($LiFePO_4/FePO_4$) with SOC-dependent phase fractions following the Gibbs phase rule. SOC critically determines the lithium stoichiometry in the cathode ($Li_{1-x}FePO_4$), which in turn governs its thermal degradation behavior and the oxygen evolution capacity.[212, 213] Notably, the thermal stability of LFP remains debated: while some studies indicated it maintains oxygen stability at high temperatures, others suspected that delithiated $FePO_4$ undergoes thermal decomposition with concomitant oxygen release as quantitatively described by Eq 5.9. [124, 214]

$$LiFePO_4 + 6C \leftrightarrow Li_{1-x}FePO_4 + Li_xC_6 \quad \text{Eq 5.8}$$

$$4FePO_4 \rightarrow 2Fe_2P_2O_7 + O_2 \quad \text{Eq 5.9}$$

At 100% SOC, $LiFePO_4$ undergoes complete conversion to $FePO_4$, and the released oxygen generates additional heat totaling 0.18 kJ (0.02 MJ m^{-2}), whereas the compensation heat at 0% and 50% SOC is calculated to be 0 kJ and 0.09 kJ (0 and 0.01 MJ m^{-2}), respectively. The compensation heat is negligible compared to Q_{CCT}. As illustrated in Figure 5.5b, the THR of SLPs at different SOCs is invariant, suggesting similar oxygen consumption capacity. Nevertheless, the pHRR exhibits a marked SOC dependence. Compared with the fully charged cell, the pHRR value of the fully discharged counterpart is reduced by 19.6%. The smoke production profile during thermal runaway events serves as a critical indicator of the underlying failure mechanism and combustion behavior. As evidenced in Figure 5.5c, SLPs exhibit continuous smoke generation throughout the entire thermal runaway progression, indicating sustained material pyrolysis.

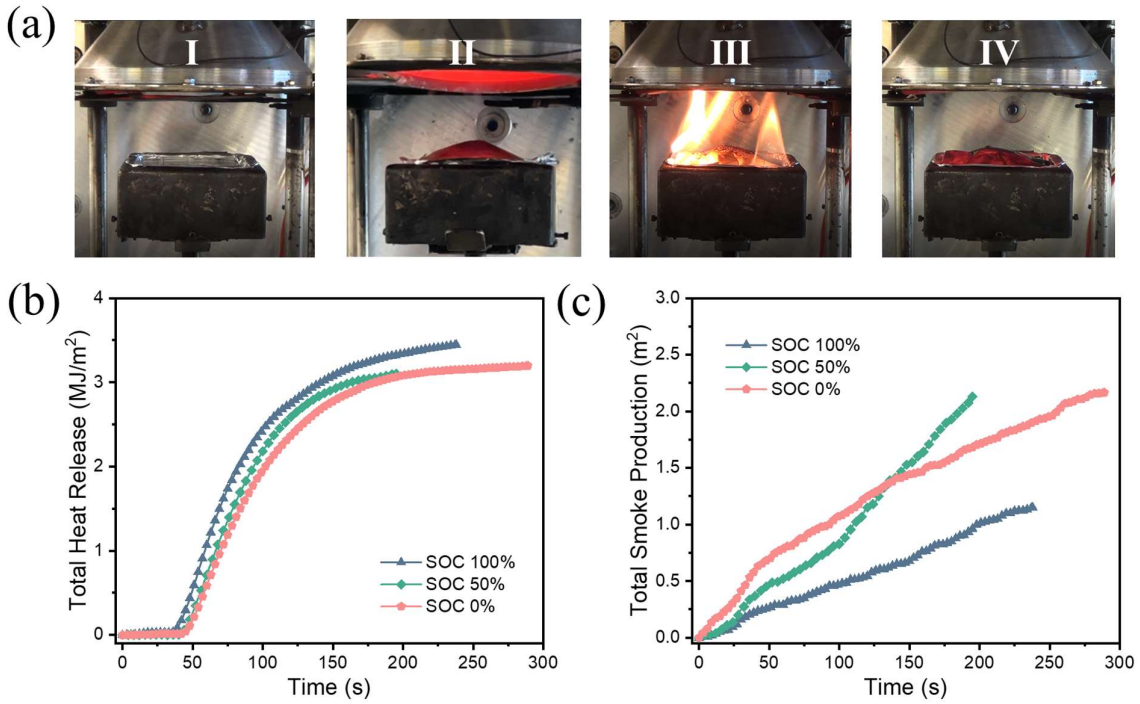

Figure 5.5 (a) Four stages of SLP thermal runaway during CCT. (b) Total heat release and (c) total smoke production curves of BLE-SLP at different SOCs of 0%, 50%, and 100%.

Figure 5.6a reveals distinct smoke generation rates across the three combustion stages: ignition, fully developed fire, and smoldering. Quantitative analysis demonstrates that the discharged state (0% SOC) exhibits higher smoke production during the initial phase, which correlates strongly with the elevated carbon monoxide emissions (Figure 5.6b) and a higher CO/CO_2 ratio (Figure 5.6c), indicating that the combustion at 0% SOC is relatively incomplete. Battery components undergo dynamic and often irreversible compositional changes during cycling,

where the SOC plays a critical role in governing their chemical evolution. However, it is worth noting that, as shown in Figure 5.3a, the combustible packaging part constitutes the predominant mass fraction among all flammable components in SLPs. Consequently, when scaling the analysis to individual cells, SOC also influences the combustion completeness of the package. As illustrated in Figure 5.6d, under identical thermal abuse conditions, the battery at 100% SOC exhibits significantly higher back surface temperatures compared to the half-charged (50% SOC) SLP. After 200 seconds of exposure to a radiative heat flux of 35 kW m^{-2}, the backside temperatures of the 100% SOC and 50% SOC SPLs reach 307.3°C and 266.1°C, respectively. Furthermore, Figure 5.6e reveals that the 100% SOC SLP attains a heating rate of 2°C s^{-1} at a notably lower temperature (66.8°C) than the 50% SOC SLP (95.9°C). Both cells attained their maximum heating rates near 150°C, with the fully charged battery exhibiting more violent thermal runaway characteristics, as evidenced by its 67% higher peak heating rate (6.5°C s^{-1}) compared to the half-charged battery (3.9°C s^{-1}).

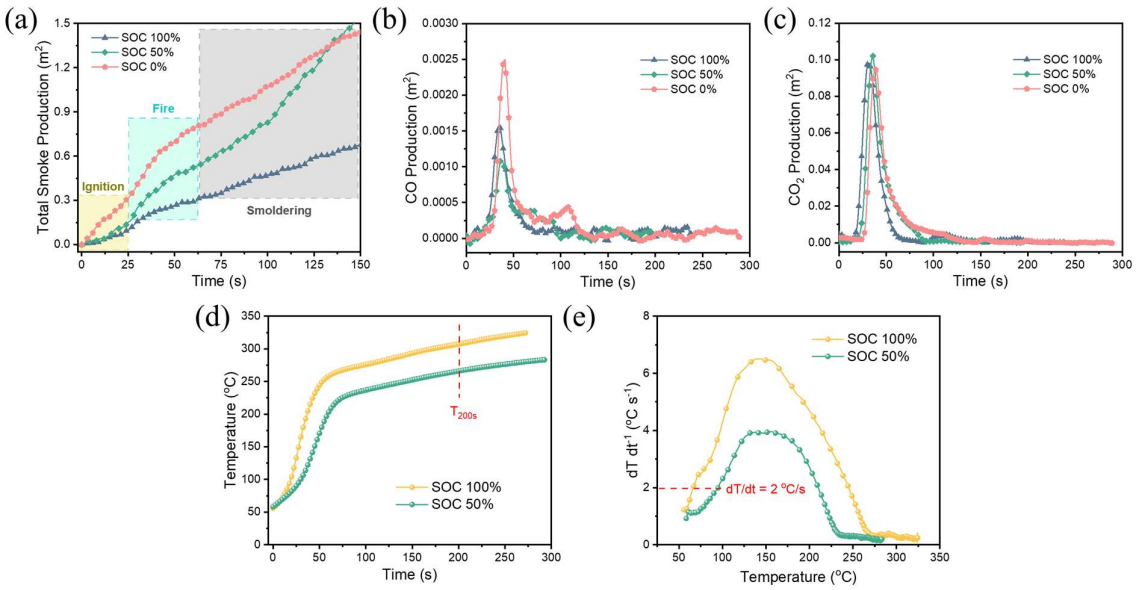

Figure 5.6 (a) The total smoke production, (b) CO production, and (c) CO_2 production curves of BLE-SLP at varying SOCs of 0%, 50%, and 100%. (d) Temperature monitoring profiles and (e) temperature change rate curves of SLPs at 50% and 100% SOC.

Table 5.1 Key descriptors of CCT for BLE-SLPs at 0%, 50%, and 100% SOC. (TTI: time to ignition; pHRR: peak heat release rate; THR: total heat released; TSP: total smoke production; CO_{max}: the maximum CO production; $(CO_2)_{max}$: the maximum CO_2 production)

Sample	TTI (s)	pHRR (kW m^{-2})	THR (MJ m^{-2})	TSP (m^2 m^{-2})	$(CO)_{max}$ (g s^{-1})	$(CO_2)_{max}$ (g s^{-1})
BLE-SLP, 0%	25	43.3	3.2	209	0.003	0.094
BLE-SLP, 50%	21	46.5	3.1	228	0.001	0.102
BLE-SLP, 100%	16	53.9	3.4	124	0.002	0.098

5.3.3. Fire behavior of flame retardant-modified cells

The strategic incorporation of FRs presents a viable pathway to mitigate electrolyte flammability in LIBs.[30] Through systematic evaluation of 15 representative FRs, we established a tripartite classification scheme based on their suppression efficacy: (I) highly effective agents (e.g., volatile phosphites and cyclophosphazenes), (II) moderately effective compounds (e.g., phosphates with thermal decomposition thresholds near 100°C), and (III) prolonged variants (e.g., phenyl/alkyl-substituted phosphates with degradation temperatures approaching 250°C).[215] Crucially, our analysis reveals that optimal flame-retardant performance requires precise synchronization between the additive's activation temperature and the electrolyte's decomposition range, while noting that assessment methodologies can significantly influence observed effectiveness. Figure 5.7a reveals significant methodological dependencies in evaluating flammability, as demonstrated by the divergent SET and SEE measured using BC containers versus GFS substrates. Notably, trimethyl phosphite (TMPi) exhibits exceptional methodological robustness, achieving superior flame suppression at merely 5% concentration regardless of the testing protocol, and achieving nonflammability at 10% addition. Dimethyl methylphosphonate (DMMP) shows moderate sensitivity, with BC methods better exhibiting its flame-retardant capability. Strikingly, cresyl diphenyl phosphate (CDP) displays strong methodology dependence, where GFS testing paradoxically extends electrolyte combustion.

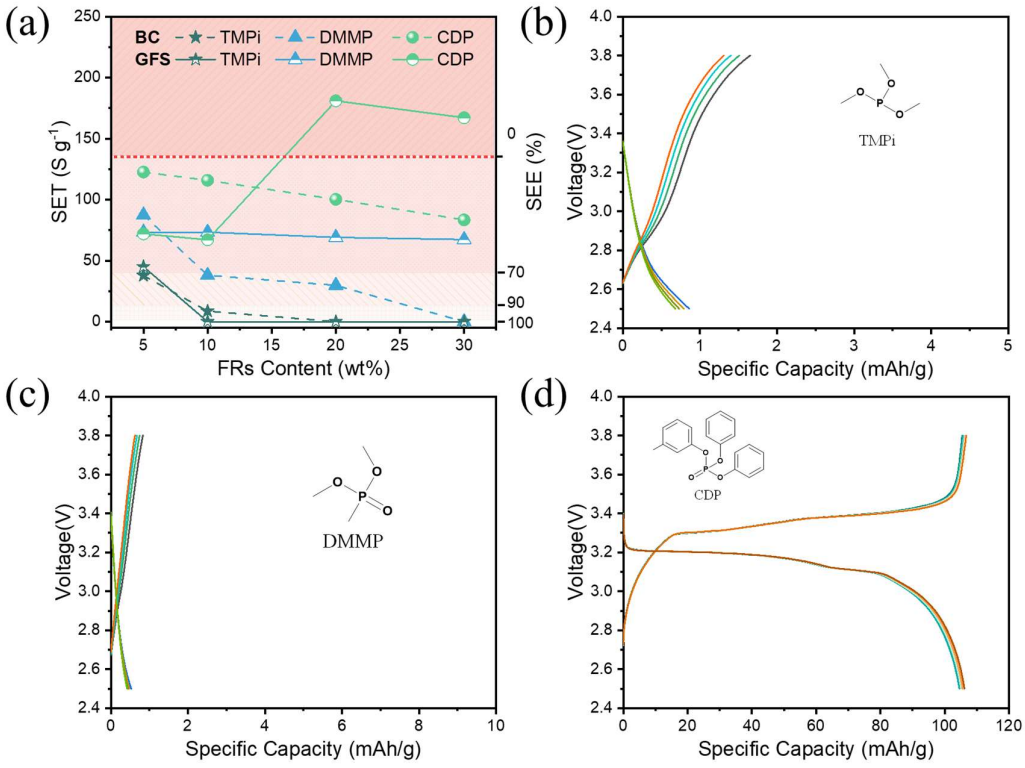

Figure 5.7 (a) SET and SEE values of the CDP, DMMP, and TMPi modified LEs tested by BC and GFS methods at various concentrations. Galvanostatic charge-discharge curves of (a) TMPi-SLP, (b) DMMP-SLP, and (c) CDP-SLP at the current density of 0.2 mA cm^{-2}.

The key property parameters of electrolyte solvents and FRs are provided in Table 5.2. Transitioning from single electrolyte systems to full cells introduces significant complexity in flame-retardant behavior due to multi-component interactions and confined space. To elucidate flame-retardant mechanisms at the battery level and evaluate whether flame-resistant electrolytes help build safer batteries, we incorporated TMPi, DMMP, and CDP (20 wt%) into BLE and assembled FR-SLPs. Figure 5.7b-d corresponds to their galvanostatic charge-discharge curves at the current density of 0.2 mA cm^{-2}. The introduction of the above FRs has a different influence on the performance of batteries, which is consistent with previous reports that phosphorus additives have a negative impact on electrochemical performance due to poor redox stability.[216, 217] Among them, CDP is electrochemically friendly and achieves a specific capacity of 106.14 mAh g^{-1} and a Coulombic efficiency of 99.46% in the fifth cycle.

Table 5.2 Key physical properties of solvents (EC, EMC) and flame retardants (TMPi, DMMP, CDP), T_{max} is the temperature corresponding to the maximum rate of mass loss in the TGA test, other values are sourced from previous publications.[215, 218-220]

Sample	Boiling point (°C)	Melting point (°C)	Flash point (°C)	Vapor pressure (25°C, mmHg)	T_{max} (°C)
EC	248	39	160	9.8×10^{-3}	156.4
EMC	109	-55	23	32	35.5
TMPi	110	-78	28	24	55.4
DMMP	180	-50	69	1	104.8
CDP	255	-30	232	1.04×10^{-6}	264.8

To eliminate SOC-dependent variables, CCT is carried out at 50% SOC. While FRs induce varying degrees of capacity fade, the resulting differences in oxygen consumption capacity, attributable to lithium intercalation/deintercalation in graphite or LFP electrodes at this intermediate SOC, are considered negligible. This assumption is justified by the relatively low proportion of electrodes in SLPs and the negligible oxygen release from the electrodes. As given in Table 5.3, although the addition of TMPi and CDP did not delay the ignition time, they reduced pHRR values compared to the baseline electrolyte (BLE-SLP). In particular, the introduction of 20% DMMP can effectively prevent the combustion of cells, with no observable flame throughout testing. As shown in Figure 5.8a, the incorporation of 20% TMPi, DMMP, and CDP into BLE reduces THR from 3.1 MJ to 2.4, 0.2, and 2.0 MJ respectively, demonstrating effective flame retardation effectiveness and lower oxygen depletion capacity. Interestingly, the flame-retardant performance varies significantly between isolated electrolyte systems and single-cell configurations. As shown by the GFS assessment in Figure 5.7a, three FRs exhibit an efficacy ranking of TMPi>DMMP>CDP in LEs. Strikingly, this trend is reversed in full-cell evaluations, where the ranking shifts to DMMP>CDP>TMPi. While TMPi achieves

superior flame inhibition in electrolyte-level evaluations, it demonstrates the poorest effectiveness in actual cell combustion scenarios. In contrast, DMMP, which displays moderate improvement in LEs, emerges as the most effective FR at the battery level.

Table 5.3 Key descriptor information of CCT for BLE- and FR-SLPs at 50% SOC. (TTI: time to ignition; pHRR: peak heat release rate; THR: total heat released; TSP: total smoke production; CO_{max}: the maximum CO production; $(CO_2)_{max}$: the maximum CO_2 production; Residue: mass remaining)

Sample	TTI (s)	pHRR (kW m^{-2})	THR (MJ m^{-2})	TSP (m^2 m^{-2})	$(CO)_{max}$ (g s^{-1})	$(CO_2)_{max}$ (g s^{-1})	Residue (%)
BLE-SLP	21	46.5	3.1	228.0	0.001	0.102	71.2
TMPi-SLP	18	41.2	2.4	24.1	0.002	0.075	68.5
DMMP-SLP	-	4.3	0.2	109.9	0.001	0.004	78.6
CDP-SLP	18	36.5	2.0	99.9	0.003	0.002	81.7

Similar to the BLE-SLP, FR-SLPs exhibit smoke emission during the entire test (Figure 5.8b). However, Figure 5.8c reveals that FRs dramatically altered the smoke generation dynamics; all FR-SLPs show significantly reduced smoke production rates across distinct combustion phases. Particularly noteworthy is the TMPi-SLP, which achieved remarkable smoke suppression with a TSR of merely 10.6% compared to the BLE-SLP. This remarkable smoke suppression performance primarily originates from the unique chemical activity of trivalent phosphorus (P^{3+}) in TMPi. Compared to pentavalent phosphorus (P^{5+}) in DMMP and CDP, the reduced P^{3+} species exhibits enhanced redox activity, enabling smoke suppression through catalytic oxidation of incipient smoke particles.[221, 222] As shown in Figure 5.8d, the residual weight of CDP- and DMMP-SLPs increased compared to BLE-SLP, confirming that the electrolyte modified by moderately effective and prolonged FRs can improve the residue formation of full cells, the initial mass increase may stem from balance fluctuations caused by internal pressure. The weight loss curve of SLP added with low-boiling-point TMPi is consistent with BLE-SLP, suggesting a slightly weaker char formation ability. Additionally, gas analysis in Figure 5.9a and 5.9b demonstrates that formulations CDP and TMPi produce substantially higher CO peaks but lower CO_2 emissions, reflecting incomplete combustion due to flame inhibition. Remarkably, the introduction of DMMP simultaneously leads to a significant decrease in oxygen consumption and an inhibited generation of CO and CO_2. As demonstrated in Figure 5.9c and summarized in Table 5.4, real-time thermal monitoring of FR-SLPs during CCT revealed significant temperature differentials.

Table 5.4 The backside temperature recording of different SLPs. (T_{200s}: the temperature reached at 200 s; $T_2{}^{o}{}_{C/s}$: the temperature when the heating rate reached 2°C s^{-1}; $(dT/dt)_{max}$: the maximum heating rate)

Sample	Unit	BLE-SLP 100%	BLE-SLP 50%	TMPi-SLP	DMMP-SLP	CDP-SLP
T_{200s}	°C	307.3	266.1	255.9	313.6	217.9
$T_2{}^{o}{}_{C/s}$	°C	66.8	95.9	86.1	53.5	93.4
$(dT/dt)_{max}$	°C s^{-1}	6.5	3.9	2.9	3.0	2.8

At 200 seconds, compared to 266.1°C of BLE-SLP, CDP- and TMPi-SLPs exhibit relatively lower temperatures of 217.9°C and 255.9°C, respectively, while DMMP-SLP reaches the highest temperature of 313.6°C. Intriguingly, DMMP-SLP demonstrates the most aggressive early-stage acceleration, crossing the 2°C s^{-1} threshold at 53.5°C versus 95.9°C for BLE-SLP (Figure 5.9d). Moreover, the maximum heating rates for FR-SLPs are substantially lower than those of BLE-SLP, confirming the efficacy of FRs in exothermic reaction mitigation. A unique bimodal heating rate profile is observed for DMMP-SLP, with a secondary peak emerging at 220.9°C. Although no flaming combustion occurs, the sustained smoldering behavior at elevated temperatures dissipates the energy of the battery as heat.

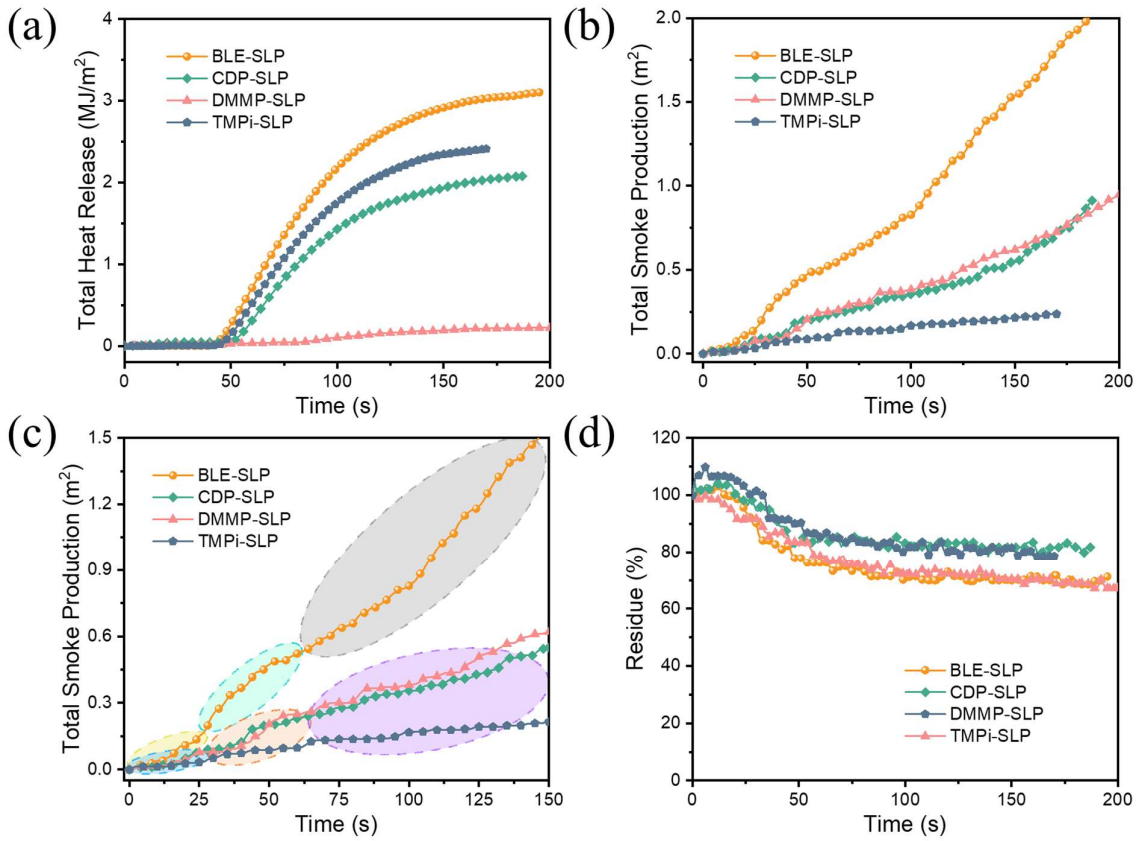

Figure 5.8 (a) Total heat release, (b, c) total smoke production, (d) residue curves of CDP-, DMMP-, and TMPi-SLPs at 50% SOC.

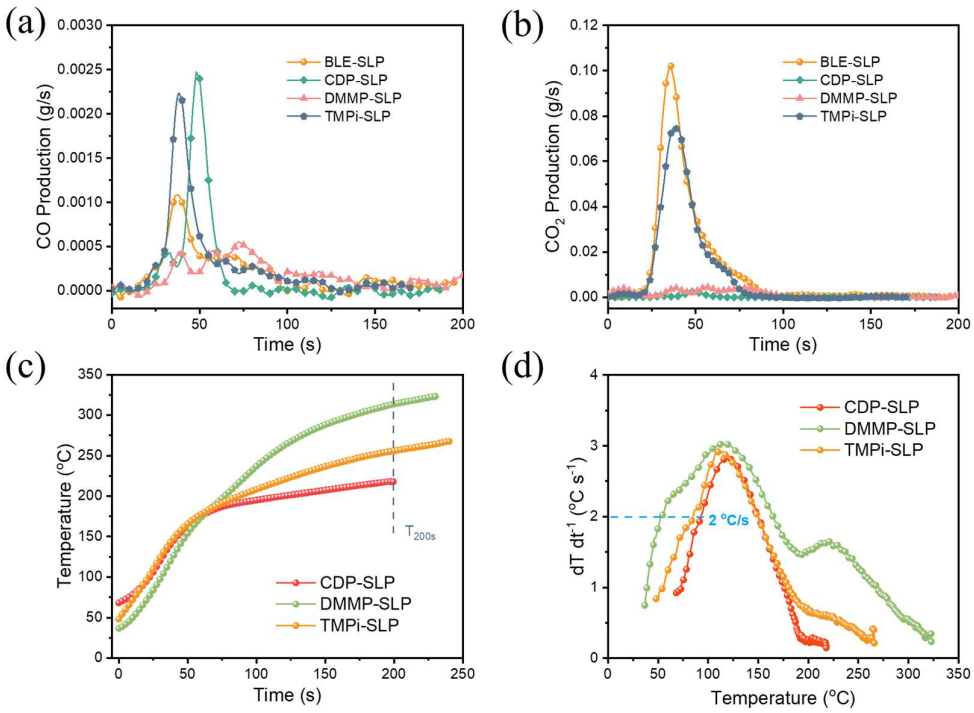

Figure 5.9 (a) CO and (b) CO_2 production of SLPs at 50% SOC. (c) Temperature monitoring profiles and (d) temperature change rate curves of FR-SLPs during CCT.

5.3.4. Post-analysis of burned cells

To gain deeper insights into the failure mechanisms and flame-retardant properties of SLPs, a systematic post-mortem analysis after CCT was conducted. As illustrated in Figure 5.10, the electrodes of the BLE-SLP remained relatively intact, with active materials still firmly adhered to the current collectors. However, copious white particulate deposits (indicated by orange markers), likely salt precipitates from electrolyte decomposition, were observed on the graphite anode. Moreover, the aluminum laminate packaging exhibited obvious softening and deformation (highlighted in red). In contrast, strip-like residues (marked in yellow), presumably remnants of thermally shrunken separators, were identified in all FR-SLPs. CDP-SLP demonstrated superior electrode structural integrity, whereas the DMMP- and TMPi-SLPs suffered from varying degrees of electrode material detachment. To further evaluate the structural competence of the graphite anode, samples were subjected to XRD analysis, and the corresponding diffraction patterns are presented in Figure 5.11a. A sharp diffraction peak corresponding to the (002) plane was observed at 26.71°, along with a characteristic 004 peak, demonstrating the highly crystalline nature and long-range ordered layered structure of graphite. Concurrently, distinct characteristic peaks from the copper current collector were identified at 43.5° (111), 50.6° (200), and 74.3° (220).[223] As shown in Figure 5.11b, the (002) characteristic peak was preserved in both the combusted anode (Anode-B) and the disassembled anodes from BLE- and CDP-SLPs. However, these peaks exhibited noticeable positional shifts and increased full width at half maximum (FWHM), indicating that while the graphite structure remained

largely intact after either standalone combustion or thermal abuse testing in SLPs, certain structural defects were introduced. However, no characteristic graphite peaks were detected in the DMMP- and TMPi-SLPs, which should be attributed to the substantial detachment of active materials from these anodes.

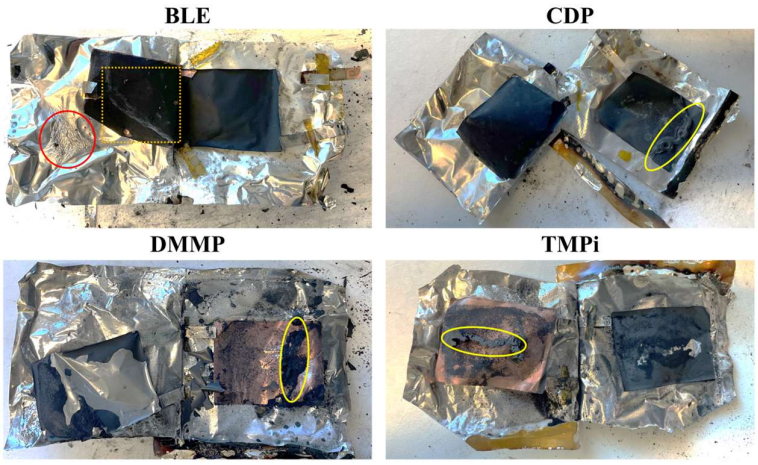

Figure 5.10 Images recorded for BLE- and FR-SLPs disassembly and analysis after CCT.

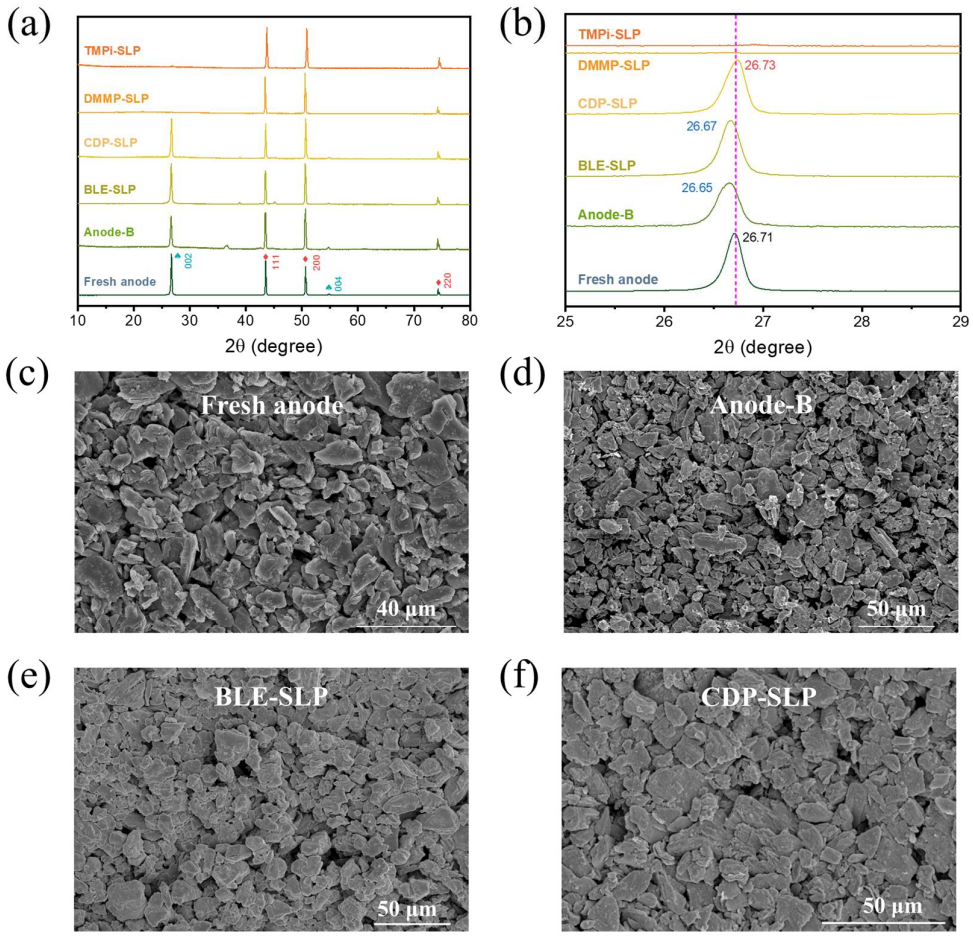

Figure 5.11 (a, b) XRD patterns of fresh anode, anode-B, BLE-, and FR-SLP anodes. SEM images of (c) fresh anode, (d) burned anode, and anodes of (e) BLE-, (f) CDP-SLPs.

Figure 5.11c and 5.11d present the morphological characterization of pristine graphite before and after combustion, respectively, revealing no significant structural differences. After the full cell incorporating BLE and CDP-enhanced electrolyte (Figure 5.11e and 5.11f), the bulk graphite structure remained structurally stable, while minor yet discernible alterations in surface roughness were observed. SEM analysis (Figure 5.12a) revealed homogeneous surface deposition of electrolyte decomposition byproducts, manifesting as densely distributed nanoscale particulates - a consequence of complete electrolyte wetting and subsequent electrochemical cycling. Notably, the graphite of CDP-SLP (Figure 5.12b) displayed a distinctive "rice crust"-like surface morphology analogous to BLE-SLP. This unique topological feature may facilitate the construction of superior electrode/electrolyte interfaces, thereby contributing to the good electrochemical performance observed in both BLE- and CDP-SLPs (Figure 5.7). On the contrary, as shown in Figure 5.12c and 5.12d, DMMP- and TMPi-SLPs showed substantial residual aggregates on copper foils, displaying different structural features compared to the fresh anode.

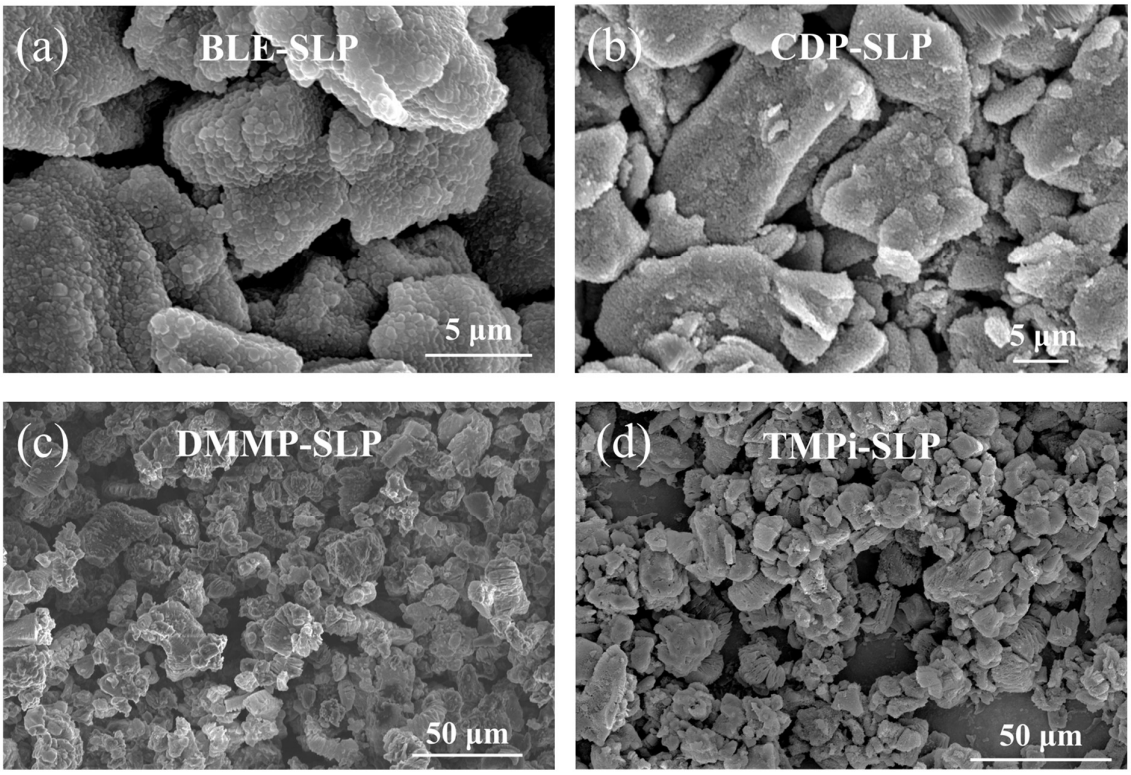

Figure 5.12 SEM images of (a) BLE-SLP, (b) CDP-SLP, (c) DMMP-SLP, and (d) TMPi-SLP anodes.

As evidenced by EDS analysis in Figure 5.13a and 5.13b, the pristine anode maintains exclusive carbon composition (100 at%) after combustion, while the anodes from BLE- and FR-SLPs show additional elements including fluorine (F), phosphorus (P), and oxygen (O), which likely originate from decomposition products of organic solvents, $LiPF_6$ salt, and FRs. In Figure 5.13c and 5.13d, quantitative analysis demonstrates that the BLE-SLP anode exhibits higher F content

(~35.0 at%) with relatively lower carbon retention (52.5 at%). Whereas the CDP-SLP anode displays higher carbon matrix preservation (78.7 at%) along with substantially reduced impurity levels (O: 9.2 at%, F: 11.2 at%, P: 0.9 at%).

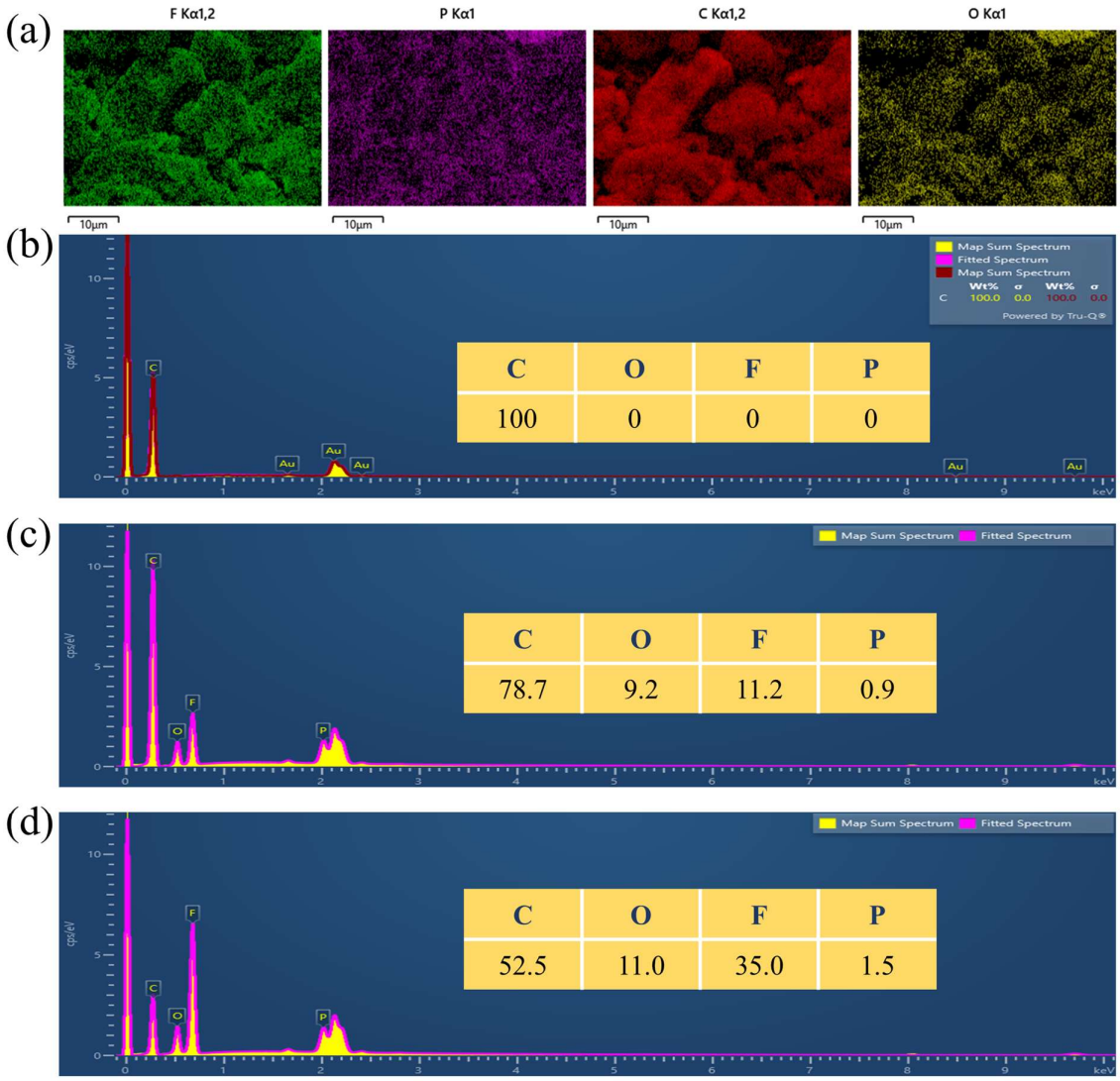

Figure 5.13 (a) F, P, C, O elemental mapping of CDP-SLP anode. EDS spectrum of (b) the burned anode and the anode of (c) CDP-SLP and (d) BLE-SLP.

Table 5.5 provides the elemental distribution analysis of all anode materials. Despite observable morphological differences, the DMMP-SLP residue exhibits the highest carbon content (80.1 at%), while the final composition of TMPi-SLP anode shows high similarity with BLE-SLP, indicating that TMPi incorporation exerts minimal influence on the anode combustion. The cathode exhibits superior compositional stability to the anode under varying electrolyte formulations; the complementary morphological and elemental analyses of pristine, post-combustion, and BLE-, FR-SLP cathodes are presented in Figure 5.14 and Table 5.6. All specimens retained submicron spherical particles with consistent elemental distributions,

confirming the intrinsic thermal robustness of the active material. Strikingly, the BLE-SLP cathode exhibited uniform deposition of faceted polyhedral crystals, attributable to lithium salt supersaturation and precipitation resulting from quick electrolyte decomposition in the absence of FRs (Table 5.4). The complete absence of such deposits in FR-SLPs confirmed that FRs effectively preserve electrode/electrolyte interface stability through modulated decomposition kinetics.

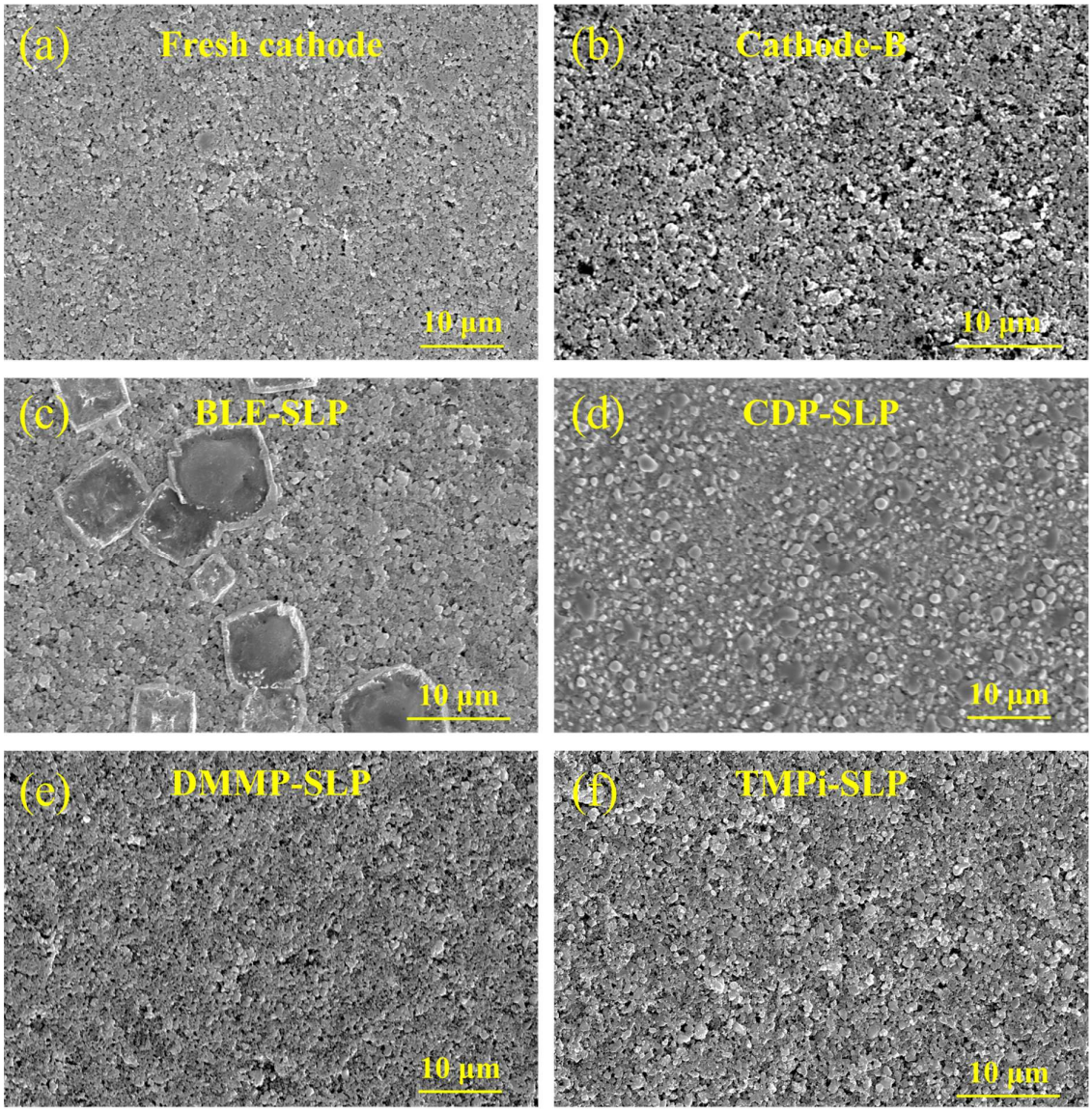

Figure 5.14 SEM images of (a) fresh cathode, (b) burned cathode, and cathodes of (c) BLE-, (d) CDP-, (e) DMMP-, and (f) TMPi-SLPs.

Table 5.5 Distribution (at%) of C, O, F, and P elements of different anode samples.

Sample	C	O	F	P
Gr-B	100	0	0	0
BLE-SLP	52.5	11.0	35.0	1.5
TMPi-SLP	54.8	8.4	34.7	2.1
DMMP-SLP	80.1	14.1	2.7	3.1
CDP-SLP	78.7	9.2	11.2	0.9

Table 5.6 Distribution (at%) of C, O, Fe, and P elements of different cathode samples.

Sample	C	O	Fe	P
LFP-B	40.2	45.1	7.5	7.2
BLE-SLP	44.2	42.7	6.6	6.5
TMPi-SLP	40.3	44.0	8.1	7.6
DMMP-SLP	49.0	35.3	9.3	6.4
CDP-SLP	43.1	44.8	5.1	7.0

5.3.5. Comparison of fire behaviors between single electrolyte and cell

Based on the above analysis, it is clear that identical additives exhibit markedly divergent efficacy in full-cell configurations versus isolated electrolytes. This scale-dependent behavior underscores the necessity for distinct design paradigms in screening and optimizing FRs for battery safety applications. As illustrated in Figure 5.15a, conventional carbonate solvents, characterized by high volatility, low boiling points, and low flash points, undergo rapid ignition upon exposure to ignition sources, which involves a complex cascade of physicochemical processes including volatilization (V_e), vaporization (V_e), and thermal decomposition (F_e). To realize a superior flame-retardant performance or to achieve intrinsic nonflammable electrolytes, the operative temperature window of FRs should either precede or coincide with the pyrolysis regime of the electrolyte components. Thermogravimetric analysis (Figure 5.15b and Table 5.2) reveals the thermal degradation profiles of the three FRs. TMPi shows the poorest thermal stability, whereas DMMP and CDP exhibit maximum mass loss rates at 104.8°C and 264.8°C, respectively. Among them, TMPi exhibits comparable volatility characteristics to EMC, with similar flash/boiling points and marginally lower vapor pressure. This physicochemical similarity enables co-vaporization and synchronous thermal decomposition with the carbonate solvent. The additive functions through a dual flame-retardant mechanism: (i) initial vapor-phase dilution of flammable species during early-stage heating, followed by (ii)

generation of phosphorus-containing radicals that effectively scavenge combustion-sustaining oxygen and hydroxyl radicals. This synergistic effect results in exceptional fire suppression efficiency, significantly reducing electrolyte combustion duration at just 5 wt% loading while achieving complete nonflammability at 10 wt% incorporation. In contrast, type II FRs represented by DMMP and Type III FRs represented by CDP can only play a restricted flame retardant role in the intermediate or late combustion stages due to their reduced volatility and increased thermal stability; CDP even presents a prolongation of burning time.

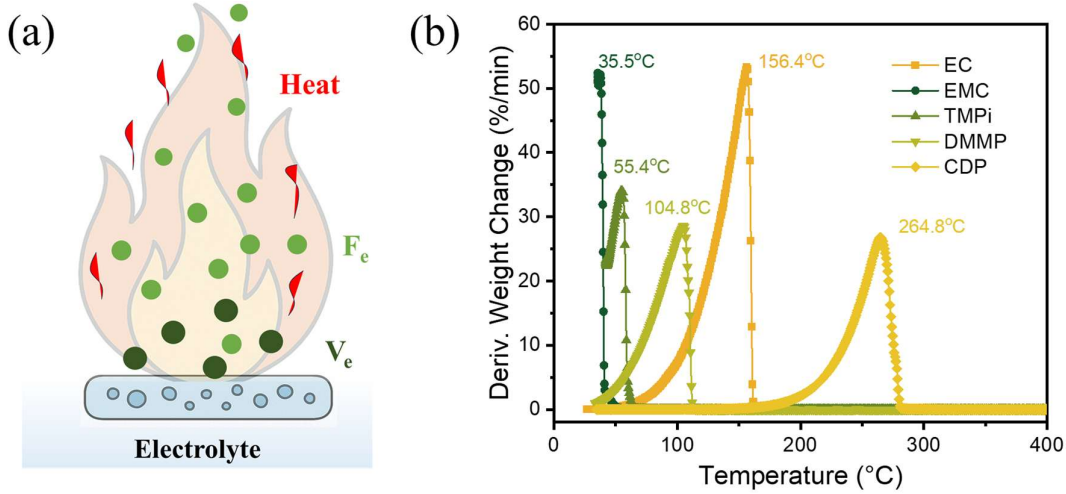

Figure 5.15 (a) Schematic illustration of the conventional electrolyte flammability test, where the investigated electrolyte is soaked by a membrane. (b) DTA curves of electrolyte solvents (EC, EMC) and FRs (TMPi, DMMP, and CDP).

Another fundamental distinction exists between the combustion environment in fire safety assessments of individual electrolytes versus full batteries. Whether it is container loading or substrate adsorption, the ignition test of electrolytes is performed in an open environment, whereas early battery thermal runaway occurs under spatially confined conditions. FEM simulation provides critical insights into the role of spatial confinement on the behavior of generated gases, with paramount importance for battery safety assessment. Figure 5.16 demonstrates that the gaseous products (such as electrolyte vapor, H_2, C_2H_4, etc.) generated by the electrolyte and adsorption substrate can readily diffuse away from the source into the ambient environment under unconfined test conditions. While this scenario approximates certain ex-situ material-level evaluations, it fails to reflect the critical spatial constraints present in operational battery systems. The combustion behavior of SLP during thermal runaway proceeds through five sequential stages: initiation, swelling, venting, ignition, and extinction (Figure 5.17a). The total duration of combustion varies significantly depending on the electrolyte formulation: BLE-, CDP-, DMMP-, and TMPi-SLPs sustain combustion for 75 s, 49 s, 0 s, and 62 s, respectively. Notably, expansion, pressure release, and smoke emission occur in rapid succession, typically within an interval of 10 seconds. As shown in Figure 5.17b, before pressure release, electrolyte vapors and combustible gases produced in the early stage of

combustion remain confined by the cell's restricted geometry. This physical confinement limits mass transport and impedes gas diffusion, leading to the accumulation of gases near the source and within the constrained headspace. While a moderate level of confinement may allow limited gas escape and the establishment of a quasi-steady state, severe confinement inevitably leads to continuous gas accumulation. Once the internal pressure exceeds the mechanical threshold of the cell package, venting is triggered, and a large volume of gases and volatile products is rapidly expelled into the surrounding environment.

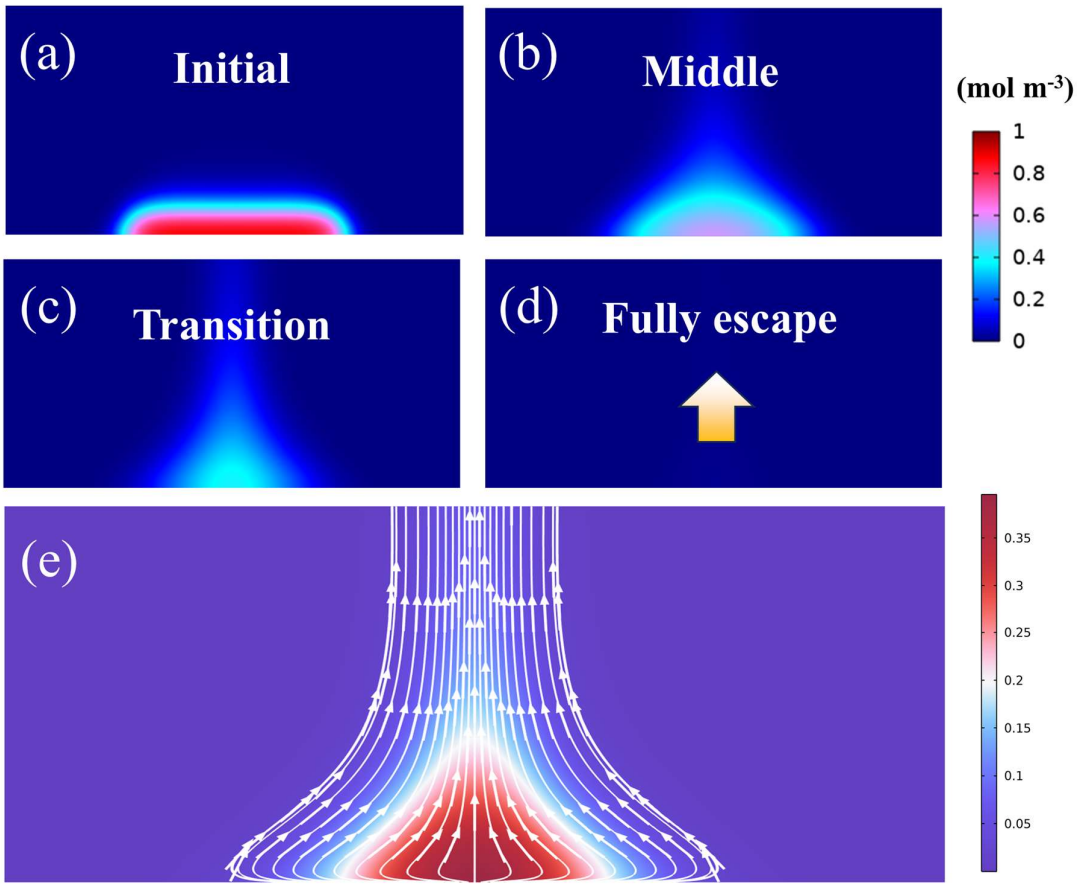

Figure 5.16 (a-d) Temporal evolution of simulated gas concentration profiles of the electrolyte-soaked membrane in free space. (e) Gas concentration field and diffusion streamlines under the absorbing force from the oven. This figure presents the FEM simulated diffusion behavior of gas generated from the bottom central region. The color map represents the gas concentration distribution, with the red region indicating the highest concentration (approximately 0.35 mol m^{-3}) at the center of the source. White arrowed lines represent streamlines, clearly indicating the primary paths and directions of upward and outward gas diffusion and transport. The simulation visually depicts the typical plume-like diffusion pattern formed as gas is released from a localized source into the surrounding fluid or free space.

Owing to their differing thermal stabilities, various FRs decompose to varying extents before venting. Within 10 seconds of test initiation, the backside temperature of the cell reaches ~70°C (Figure 5.9c), at which point both the EMC and TMPi have approached their peak mass loss temperatures. The onset of venting rapidly expels vapor-phase species, compromising the flame retardant integrity and rendering it ineffective in suppressing combustion. Subsequently, other

relatively stable combustible components, such as EC, DMMP, CDP, and particularly the polymeric pouch materials, undergo vaporization and thermal degradation. DMMP exhibits both moderate volatility and decomposition temperature, enabling it to interfere with SLP combustion through a combination of gas-phase radical quenching and dilution effects. In contrast, CDP, with a lower phosphorus content and higher volatilization threshold, primarily contributes to flame suppression through a condensed-phase mechanism, acting in a delayed and sustained manner during SLP combustion. Figure 5.17c and 5.17d highlight the contrasting gas diffusion behaviors between the electrolyte and full-cell configurations. In the electrolyte combustion test, gas molecules diffuse freely along unobstructed pathways, and concentration gradients dissipate rapidly, minimizing the accumulation of localized gas pockets. By comparison, confined geometries in full-cell assemblies impose significant resistance to gas diffusion. Physical boundaries hinder the dilution of internal gases by ambient air, causing gas streamlines to deflect and potentially form recirculation zones within the cell.

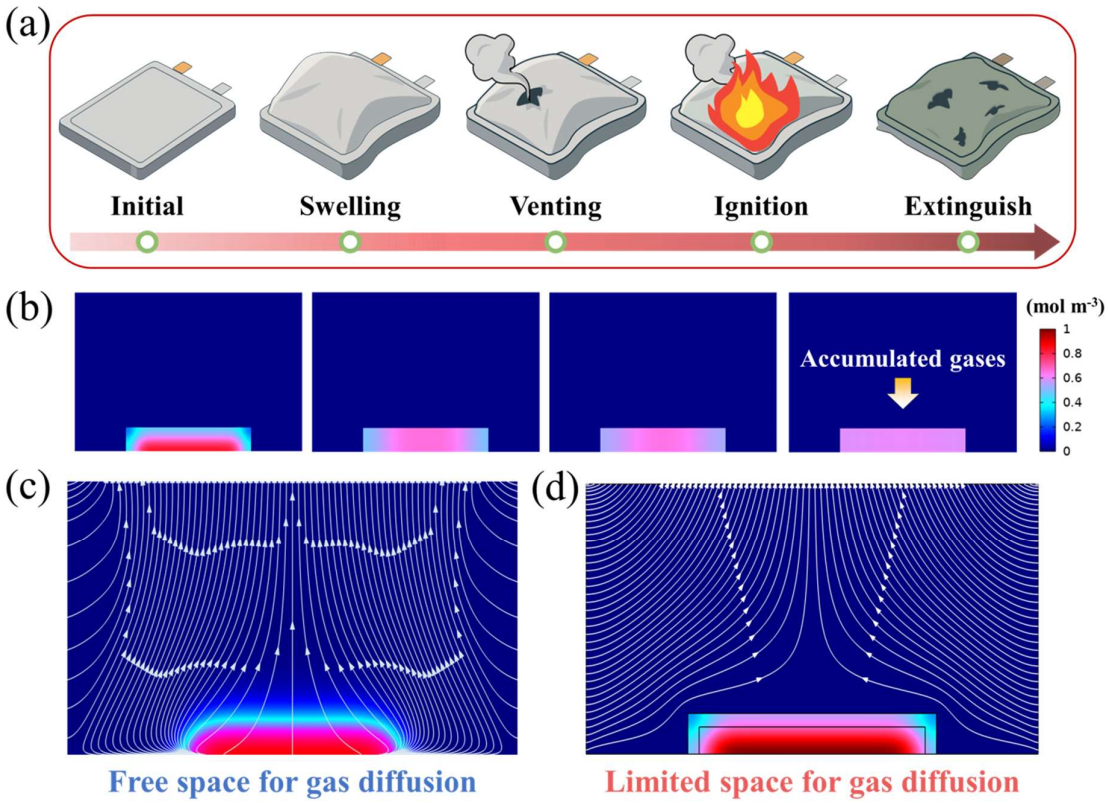

Figure 5.17 (a) Schematic illustration of the thermal runaway process of pouch cells. (b) Temporal evolution of simulated gas concentration profiles in a confined environment representative of pouch cells. Comparative analysis of simulated gas diffusion pathways (white streamlines) (c) under conditions featuring ample free space above the gas-generating source and (d) within a spatially limited volume.

Complementary evidence for the thermal implications of spatial confinement is presented in Figure 5.18, which tracks the temporal evolution of temperature profiles from a localized heat source within a pouch cell environment. As illustrated in Figure 5.18a, the initial temperature

for the thermal field simulation was determined using a thermal camera. Before testing, the sample surface temperature stabilized at ~600°C under the testing radiative condition. While thermal energy readily dissipates into the surroundings under unconfined conditions (top row in Figure 5.18b), spatial confinement markedly impedes thermal transport. This restriction leads to a pronounced accumulation of heat and sustained high temperatures concentrated near the heat source (bottom row in Figure 5.18b). Such thermal confinement, acting in concert with gas accumulation, markedly amplifies the severity of thermal runaway in confined systems compared to conventional unconfined environments, underscoring the fundamental disparity between single-electrolyte and full-cell evaluations. This finding highlights the critical role of cell-level confinement in shaping thermal and combustion behaviors. Notably, it also calls into question the validity of using standalone electrolyte tests as proxies for real-world battery safety. The inherently different physicochemical environments between single-component and integrated cell systems render direct comparisons unreliable. A fire-safe electrolyte cannot ensure a safer battery. To advance meaningful safety assessments, future research should prioritize evaluating FRs and electrolyte formulations under full-cell conditions.

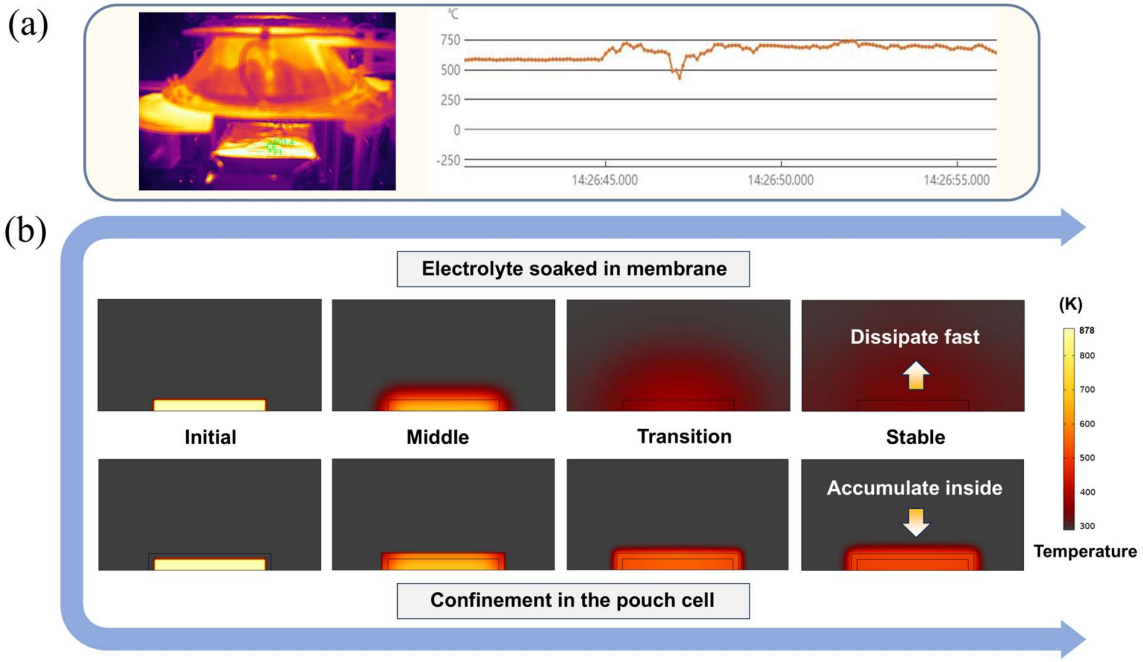

Figure 5.18 (a) Infrared imager measurements are used to determine the initial temperature for thermal field simulations. (b) Comparison of the impact of spatial confinement on heat dissipation in free space (top row) and confined space (bottom row).

5.4. Conclusion

In summary, this chapter reveals a pronounced divergence in flame-retardant performance between isolated electrolytes and full battery configurations, demonstrating that effective retardancy is highly dependent on environmental context and the temporal synchronization of

functional responses. All FRs (CDP, DMMP, and TMPi) showed a certain degree of flame retardancy at the full-cell level in CCT. However, the extent of fire inhibition significantly depended on the electrolyte formulation, showing a completely different trend compared to their performance in single-electrolyte systems. Although TMPi exhibited strong flame inhibition at the electrolyte level and achieved nonflammability at a concentration as low as 10%, its enhancement of full-cell fire safety performance remains limited, which was evidenced by the THR of TMPi-SLP being reduced only modestly from 3.1 MJ m^{-2} in BLE-SLP to 2.4 MJ m^{-2}. Instead, DMMP demonstrated moderate intrinsic flame-retardant properties in electrolytes, it effectively suppressed combustion at the full-cell level, with the THR reduced to 0.2 MJ m^{-2} for DMMP-SLP and the pHRR significantly decreased from 46.5 kW m^{-2} (BLE-SLP) to 4.3 kW m^{-2}. FEM simulations further elucidated the mechanistic disparities in combustion behavior between component-level and cell-level evaluations, confirming that component-based metrics are insufficient proxies for real battery safety. Electrolyte combustion involves processes such as volatilization, vaporization, and thermal decomposition, during which the resulting flammable gases can easily diffuse into the surrounding environment. In contrast, combustion in full cells follows a more complex sequence, typically consisting of five stages: initiation, swelling, venting, ignition, and extinction. The buildup of internal pressure caused by decomposition products triggers venting, which facilitates pressure release and enables heat exchange and gas diffusion between the battery interior and the external environment. These findings underscore the limitations of reductionist, material-level assessments, demonstrating that fire-retardant electrolytes alone cannot guarantee comprehensive battery safety, and highlight the urgent need for a cell-level safety framework to guide the practical design of intrinsically safe electrolytes. This work advocates for a paradigm shift away from isolated component analysis toward holistic, cell-level safety strategies, offering a critical foundation for the next generation of inherently safe battery technologies.

6. Conclusion and Future Work

6.1. Conclusion

This thesis aims to enhance the fire safety of LIBs and contribute to the establishment of a more rational safety evaluation framework by addressing the problem from multiple perspectives, including material development, evaluation methodology, and mechanistic understanding. (i) Chapter 3 presents the development of a novel PMC-CSSE, which simultaneously achieves excellent flame retardancy and electrochemical performance. At 50°C, the ionic conductivity of conventional PEO SPE is 6.38×10^{-5} S cm^{-1}, whereas PMC10 exhibits a significantly higher conductivity of 2.33×10^{-4} S cm^{-1}. Moreover, combustion tests show that the HRC value of PMC10 decreases by 33.4% compared to PEO electrolyte, indicating improved flame suppression. (ii) In Chapter 4, a standardized SET test is proposed to address the current inconsistency in evaluating LE flammability. Based on this methodology, the concept of the SEE is introduced, which enables the investigation of the flame-retardant mechanisms of representative additives by analyzing their effects on the combustion behavior of electrolytes. (iii) Chapter 5 explores the relationship between the flammability of isolated electrolytes and the overall fire behavior of full cells. It is revealed that improvements in electrolyte-level flame retardancy do not directly translate to enhanced safety at the cell level, which arises primarily from the structural complexity and spatial confinement within battery cells. The key findings are summarized as follows:

6.1.1. Development of PMC composite electrolytes

By simultaneously introducing HKUST-1 MOF as FR and LLZTO ceramic as active filler, a novel CSSE named PMC with a unique “CIP-PIC” hierarchical architecture is developed, where the structure is formed through the gravity-induced distribution of LLZTO during the drying process. In this configuration, the CIP layer ensures strong interfacial adhesion with the lithium metal surface, while the PIC layer provides enhanced mechanical strength to support the structural integrity of the overall electrolyte membrane. This special architecture enables PMCs to exhibit significantly enhanced mechanical strength, thermal stability, and fire resistance compared to conventional PEO SPEs. The optimized formulation, PMC10, achieves a low crystallinity of 15.2%, a Young’s modulus of 3.1 MPa, and a high ionic conductivity of 2.33×10^{-4} S cm^{-1} at 50°C. The excellent interfacial compatibility with lithium metal allows symmetric Li|PMC10|Li cells to cycle stably for over 900 hours at 0.2 mA cm^{-2} without short-circuiting. In contrast, PEO SPEs exhibit ISC and show persistent voltage fluctuations after only 50 hours under the same current density. The improved electrochemical performance is also evident in full-cell testing: the LFP|PMC10|Li battery delivers an initial capacity of 158.5

mAh g^{-1} and retains 80.3% of its capacity after 200 cycles. Furthermore, the HRC of PMC10 is reduced by 33.4% compared to pure PEO SPE, with simultaneous decreases in pHRR and T_{max}, confirming its superior flame-retardant capability and improved fire safety.

6.1.2. Methodology for assessing the flammability of liquid electrolytes

To standardize the flammability assessment of LEs, a reliable protocol centered around the widely used SET indicator has been established. Through systematic analysis of key test parameters, it is found that critical factors - such as ignition source, matrix or container types and sizes, ignition source, and chamber environment - have a significant impact on SET results. Ensuring a clean ignition source, a wind-free chamber, and a fixed ignition method is essential for obtaining consistent and reliable outcomes. Based on considerations of repeatability and reliability, burning a GFS (Φ16 mm) saturated with 0.1 g of LE is proposed as the unified method. To facilitate quantitative evaluation, the concept of SEE is further introduced, along with a classification criterion: (i) SEE≤70, Flammable; (ii) 70<SEE<90, Flame-Retarded; (iii) 90≤SEE≤100, Nonflammable. The feasibility of this protocol and the proposed SEE concept is verified by assessing the combustion behavior of LEs containing 15 representative commercial FRs. Meanwhile, the underlying flame-retardant mechanism is elucidated, showing that FRs that vaporize and/or pyrolyze before or concurrently with LE decomposition effectively contribute to flame suppression. Additionally, ML is employed to analyze the influence of various FR features on SEE. All constructed models demonstrate strong predictive capability, with R2 values exceeding 0.8 in testsets and negligible prediction errors in trainsets and below 1 in testsets. The most influential factors identified are the additive dosage and the content of effective flame-retardant elements. The boiling point of FRs is also shown to play a crucial role in determining flame-retardant performance, further supporting the proposed mechanism.

6.1.3. Relationship between electrolyte flammability and battery fire safety

The safety of electrolytes plays a pivotal role in determining the overall performance of lithium-ion batteries, yet current safety evaluations focus mainly on the material level, overlooking behavior under practical battery operating conditions. A widely held assumption that flame-retardant electrolytes inherently enhance battery-level fire safety remains unverified. To address this gap, the fire safety of cells containing three representative flame-retardant electrolytes (TMPi, DMMP, and CDP) was systematically evaluated using CCT. Compared to BLE-SLP, the incorporation of 20% TMPi, DMMP, and CDP into BLE reduces THR from 3.1 MJ to 2.4, 0.2, and 2.0 MJ respectively, demonstrating effective flame retardation effectiveness and lower oxygen depletion capacity. However, no direct correlation between the intrinsic flame retardancy of electrolytes and the overall fire resistance of the batteries. Interestingly, TMPi, despite its excellent flame-retardant properties in the electrolyte, did not significantly enhance cell-level fire safety. In contrast, DMMP, with moderate flame retardancy, effectively

rendered the entire cell non-flammable. FEM simulations further elucidated fundamental differences in flammable gas distribution and temperature fields between isolated electrolytes and full cell combustion behaviors. These results highlight the complexity of battery fire behavior and demonstrate that material-level flame retardancy does not necessarily translate to improved cell-level safety. Future electrolyte design should therefore consider cell-level performance, underscoring the importance of a battery-oriented safety evaluation framework.

6.2. Future work

While this thesis provides valuable insights into the thermal runaway investigation of LIBs from the perspectives of materials, assessment, and mechanisms, several important research opportunities remain to be explored. These include but are not limited to: (1) the development of intrinsically non-flammable LEs that maintain excellent electrochemical performance; and (2) the design of high-performance gel polymer electrolytes capable of ensuring full-cell fire safety with extremely limited LE content.

6.2.1. Construction of non-flammable localized concentrated electrolytes

As mentioned in Section 1.3.3, conventional electrolytes based on carbonate solvents typically form SSIP structures, enabling free anions to construct an organic-rich SEI. When the salt concentration is increased, CIP and AGG structures emerge, facilitating the formation of an inorganic-rich SEI, which is more favorable for interfacial stability and safety. However, most solvents used in concentrated systems are flammable, posing a risk of thermal runaway. Moreover, the high viscosity of these electrolytes significantly impedes Li^+ transport, compromising overall electrochemical performance.

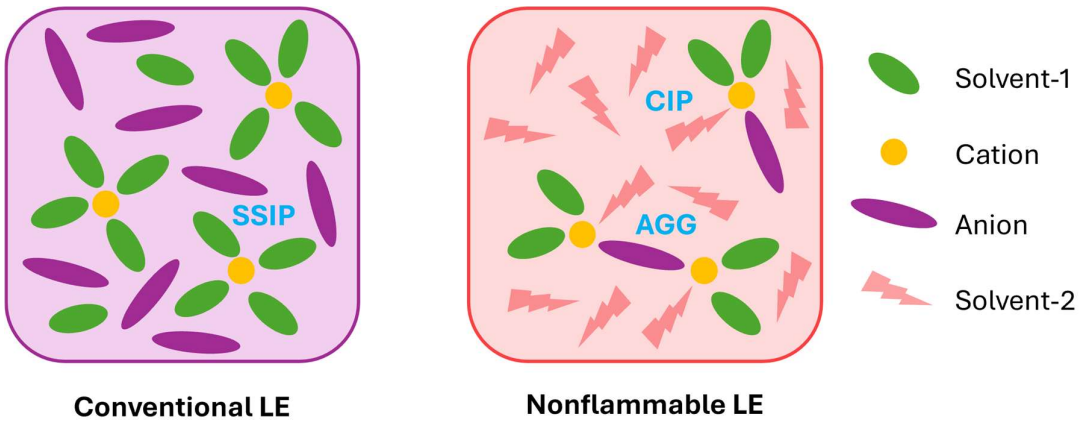

Figure 6.1 Schematic diagram of using non-flammable FR as a diluent for concentrated electrolyte.

These issues can be mitigated by employing a high dielectric constant solvent (solvent-1 in Figure 6.1) that actively participates in Li^+ solvation and a low-viscosity FR as diluent (solvent-2 in Figure 6.1). While the dielectric constant of solvent-2 has limited influence on ion transport, it plays a critical role in creating a non-flammable environment, significantly reducing fire risk

at the cell level. Meanwhile, this solvation structure supports the formation of CIP and AGG structures, ensuring efficient Li^+ transport and stable electrochemical performance. Through this dual-solvent design, it becomes possible to construct intrinsically non-flammable electrolytes without sacrificing ionic conductivity or interfacial stability.

6.2.2. Preparation of self-extinguishing gel polymer electrolyte

In addition to CSSEs such as PMCs discussed in Chapter 3, gel polymer electrolytes (GPEs) have emerged as a promising strategy for mitigating thermal runaway. GPEs are typically composed of a porous polymer matrix infused with a limited amount of liquid organic electrolytes, effectively combining the mechanical stability of solids with the high ionic conductivity of liquids.[224] Compared to SPEs, GPEs offer superior room-temperature ionic conductivity and the dual functionality of both electrolyte and separator, making them increasingly attractive for practical applications.

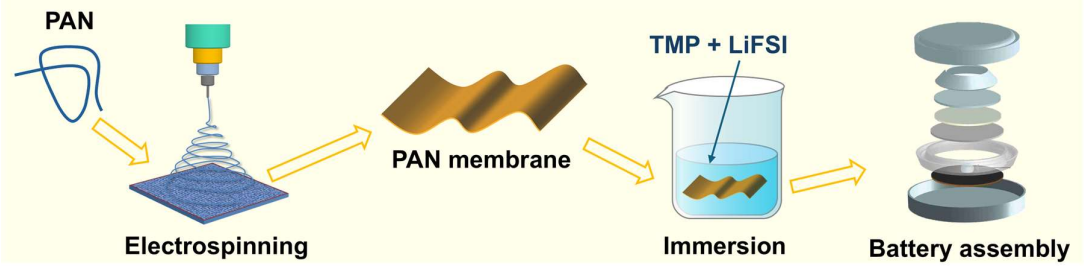

Figure 6.2 Illustration of the preparation process of the GPE.

The performance of GPEs largely depends on the rational design of their components, specifically, the choice of polymer matrix, lithium salt, and liquid-phase filler. To achieve intrinsic flame retardancy, PAN is a strong candidate for the polymer framework due to its excellent thermal stability and robust mechanical properties. However, the key challenge lies in selecting an appropriate flame-retardant electrolyte system (Figure 6.2). Among various candidates, TMP stands out as a promising FR component. As a traditional phosphate-based solvent, TMP offers a unique combination of properties, including a high dielectric constant (21.6), low viscosity (1.3 mPa s), broad liquid-phase temperature range (-46°C to 197°C), high flash point (148°C), wide electrochemical stability window, and outstanding flame-retardant capability. These attributes make it particularly suitable for constructing self-extinguishing GPEs that ensure both electrochemical performance and fire safety at the full-cell level.[225, 226]

7. List of Publications and Conferences

7.1. Publications

1) M Zhang, J Xiao, W Tang, Y He, P Tan, M Haranczyk, D-Y Wang*. (2024) A Novel Benchmarking Approach to Assess Fire Safety of Liquid Electrolytes in Lithium-Ion Batteries. Advanced Energy Materials (Back Cover), 2401241. https://doi.org/10.1002/aenm.202401241.

2) M Zhang, A Yusuf, D-Y Wang*. (2024) A novel hierarchical “ceramic in polymer-polymer in ceramic” structure composite solid-state electrolyte for safer lithium-ion batteries. Journal of Power Sources, 591, 233812. https://doi.org/10.1016/j.jpowsour.2023.233812.

3) M Zhang, M Gomes, A Yusuf, G-Z Yin, C-C Sun, D-Y Wang*. (2024) Flame-retardant reinforced halloysite nanotubes as multi-functional fillers for PEO-based polymer electrolytes. European Polymer Journal, 215, 113246. https://doi.org/10.1016/j.eurpolymj.2024.113246.

4) M Zhang, Y He, X Ao, A Ghosh, X He, J Hobson, P Tan, D-Y Wang*. (2025) Do fire-safe electrolytes guarantee enhancd fire safety for lithium-ion batteries? (Under Review)

5) M Zhang, Y He, D-Y Wang*. Thermal runaway evaluation and modeling of lithium-ion batteries: Recent progress and perspectives (In Preparation)

6) A Ghosh, S Tian, M Zhang, I Gómez, Q Chen, S Prolongo, D-Y Wang*. (2025) Deciphering a new electrolyte formulation for thermal shutdown to improve the safety of lithium-ion batteries. Advanced Functional Materials, 2502761. https://doi.org/10.1002/adfm.202502761.

7) J Hobson, G-Z Yin, X Ao, M Zhang, J Fernández, D-Y Wang*. (2025) A phosphorus and nitrogen containing halloysite derivative as multifunctional flame retardant for biobased polyamide 56. Advanced Engineering Materials, 2500291. https://doi.org/10.1002/adem.202500291.

8) A Yusuf, V Avvaru, J De La Vega, J Molleja, M Zhang, D-Y Wang*. (2023) Revealing the Fire Suppression Behavior of Fluorinated-phosphazene Based Electrolytes and their in-situ Interphase Generation in $LiFePO_4$ Cathodes. Chemical Engineering Journal, 455, 140678. https://doi.org/10.1016/j.cej.2022.140678.

9) Q Chen, A Ghosh, W Tang, G-Z Yin, J Fernández, M Zhang, D-Y Wang*. (2025) Alpha-cyclodextrin-based polyrotaxane combining phytate lithium salt as a novel biobased flame-

retardant solid polymer electrolyte for all-solid-state lithium metal batteries. Chemical Eng ineering Journal, 512, 162376. https://doi.org/10.1016/j.cej.2025.162376.

7.2. Conferences

1) M Zhang, A Yusuf, D-Y Wang*. The flame retardant materials for lithium-ion batteries. Student Oral Presentation in 19th European Meeting on Fire Retardant Polymeric Materials, June 2023, Zurich, Switzerland.
2) M Zhang, D-Y Wang*. A Novel Benchmarking Approach to Assess Fire Safety of Liquid Electrolytes in Lithium-Ion Batteries. Student Oral Presentation in 37th Topical Meeting of the International Society of Electrochemistry, June 2024, Stresa, Italy.
3) M Zhang, D-Y Wang*. Do fire-safe electrolytes guarantee enhancd fire safety for lithium-ion batteries? Student Oral Presentation in 20th European Meeting on Fire Retardant Polymeric Materials (**Best Student Oral Award**), June 2025, Madrid, Spain.

References

1. Papadis, E.; Tsatsaronis, G., Challenges in the decarbonization of the energy sector. *Energy* **2020,** *205*, 118025. https://doi.org/10.1016/j.energy.2020.118025.
2. Yang, Z.; Zhang, J.; Kintner-Meyer, M. C.; Lu, X.; Choi, D.; Lemmon, J. P.; Liu, J., Electrochemical energy storage for green grid. *Chemical Reviews* **2011,** *111* (5), 3577-3613. https://doi.org/10.1021/cr100290v.
3. He, Y.; Zhao, Z.; Cui, Y.; Shang, W.; Chen, Y.; Tan, P., Boosting gaseous oxygen transport in a Zn-air battery for high-rate charging by a bubble diode-inspired air electrode. *Energy Storage Materials* **2023,** *57*, 360-370. https://doi.org/10.1016/j.ensm.2023.02.030.
4. He, Y.; Cui, Y.; Shang, W.; Zhao, Z.; Tan, P., Insight into potential oscillation behaviors during Zn electrodeposition: Mechanism and inspiration for rechargeable Zn batteries. *Chemical Engineering Journal* **2022,** *438*, 135541. https://doi.org/10.1016/j.cej.2022.135541.
5. Gogotsi, Y.; Simon, P., True performance metrics in electrochemical energy storage. *Science* **2011,** *334* (6058), 917-918. https://doi.org/10.1126/science.1213003.
6. Raccichini, R.; Varzi, A.; Passerini, S.; Scrosati, B., The role of graphene for electrochemical energy storage. *Nature Materials* **2015,** *14* (3), 271-279. https://doi.org/10.1038/nmat4170.
7. Kundu, D.; Talaie, E.; Duffort, V.; Nazar, L. F., The emerging chemistry of sodium ion batteries for electrochemical energy storage. *Angewandte Chemie International Edition* **2015,** *54* (11), 3431-3448. https://doi.org/10.1002/anie.201410376.
8. Yoo, H. D.; Markevich, E.; Salitra, G.; Sharon, D.; Aurbach, D., On the challenge of developing advanced technologies for electrochemical energy storage and conversion. *Materials Today* **2014,** *17* (3), 110-121. https://doi.org/10.1016/j.mattod.2014.02.014.
9. Scrosati, B., Recent advances in lithium ion battery materials. *Electrochimica Acta* **2000,** *45* (15-16), 2461-2466. https://doi.org/10.1016/S0013-4686(00)00333-9.
10. Armand, M., "Intercalation electrodes" in Materials for Advanced Batteries, Plenum, New York, **1980**, 145-161.
11. Roy, P.; Srivastava, S. K., Nanostructured anode materials for lithium ion batteries. *Journal of Materials Chemistry A* **2015,** *3* (6), 2454-2484. https://doi.org/10.1039/C4TA04980B.
12. Fergus, J. W., Recent developments in cathode materials for lithium ion batteries. *Journal of Power Sources* **2010,** *195* (4), 939-954. https://doi.org/10.1016/j.jpowsour.2009.08.089.

13. Murdock, B. E.; Toghill, K. E.; Tapia-Ruiz, N., A perspective on the sustainability of cathode materials used in lithium-ion batteries. *Advanced Energy Materials* **2021,** *11* (39), 2102028. https://doi.org/10.1002/aenm.202102028.

14. Zhang, S. S., A review on electrolyte additives for lithium-ion batteries. *Journal of Power Sources* **2006,** *162* (2), 1379-1394. https://doi.org/10.1016/j.jpowsour.2006.07.074.

15. Cabana, J.; Monconduit, L.; Larcher, D.; Palacin, M. R., Beyond intercalation-based Li-ion batteries: the state of the art and challenges of electrode materials reacting through conversion reactions. *Advanced Materials* **2010,** *22* (35), E170-E192. https://doi.org/10.1002/adma.201000717.

16. Cheng, H.; Shapter, J. G.; Li, Y.; Gao, G., Recent progress of advanced anode materials of lithium-ion batteries. *Journal of Energy Chemistry* **2021,** *57*, 451-468. https://doi.org/10.1016/j.jechem.2020.08.056.

17. Feng, K.; Li, M.; Liu, W.; Kashkooli, A. G.; Xiao, X.; Cai, M.; Chen, Z., Silicon-based anodes for lithium-ion batteries: from fundamentals to practical applications. *Small* **2018,** *14* (8), 1702737. https://doi.org/10.1002/smll.201702737.

18. Casimir, A.; Zhang, H.; Ogoke, O.; Amine, J. C.; Lu, J.; Wu, G., Silicon-based anodes for lithium-ion batteries: Effectiveness of materials synthesis and electrode preparation. *Nano Energy* **2016,** *27*, 359-376. https://doi.org/10.1016/j.nanoen.2016.07.023.

19. Cha, H.; Kim, J.; Lee, Y.; Cho, J.; Park, M., Issues and challenges facing flexible lithium-ion batteries for practical application. *Small* **2018,** *14* (43), 1702989. https://doi.org/10.1002/smll.201702989.

20. Liu, C.; Neale, Z. G.; Cao, G., Understanding electrochemical potentials of cathode materials in rechargeable batteries. *Materials Today* **2016,** *19* (2), 109-123. https://doi.org/10.1016/j.mattod.2015.10.009.

21. Ling, J.; Karuppiah, C.; Krishnan, S. G.; Reddy, M.; Misnon, I. I.; Ab Rahim, M. H.; Yang, C.-C.; Jose, R., Phosphate polyanion materials as high-voltage lithium-ion battery cathode: a review. *Energy & Fuels* **2021,** *35* (13), 10428-10450. https://doi.org/10.1021/acs.energyfuels.1c01102.

22. Hossain, M. H.; Chowdhury, M. A.; Hossain, N.; Islam, M. A.; Mobarak, M. H., Advances of lithium-ion batteries anode materials - A review. *Chemical Engineering Journal Advances* **2023,** *16*, 100569. https://doi.org/10.1016/j.ceja.2023.100569.

23. Lee, J. K.; Oh, C.; Kim, N.; Hwang, J.-Y.; Sun, Y.-K., Rational design of silicon-based composites for high-energy storage devices. *Journal of Materials Chemistry A* **2016,** *4* (15), 5366-5384. https://doi.org/10.1039/C6TA00265J.

24. Pigłowska, M.; Kurc, B.; Galiński, M.; Fuć, P.; Kamińska, M.; Szymlet, N.; Daszkiewicz, P., Challenges for Safe Electrolytes Applied in Lithium-Ion Cells—A Review. *Materials* **2021,** *14* (22), 6783. https://doi.org/10.3390/ma14226783.

25. Liu, Y. K.; Zhao, C. Z.; Du, J.; Zhang, X. Q.; Chen, A. B.; Zhang, Q., Research Progresses of Liquid Electrolytes in Lithium-Ion Batteries. *Small* **2023,** *19* (8), 2205315. https://doi.org/10.1002/smll.202205315.

26. Wang, Q.; Jiang, L.; Yu, Y.; Sun, J., Progress of enhancing the safety of lithium ion battery from the electrolyte aspect. *Nano Energy* **2019,** *55*, 93-114. https://doi.org/10.1016/j.nanoen.2018.10.035.

27. McKerracher, R. D.; Guzman-Guemez, J.; Wills, R. G.; Sharkh, S. M.; Kramer, D., Advances in prevention of thermal runaway in Lithium-Ion batteries. *Advanced Energy and Sustainability Research* **2021,** *2* (5), 2000059. https://doi.org/10.1002/aesr.202000059.

28. Wang, Q.; Ping, P.; Zhao, X.; Chu, G.; Sun, J.; Chen, C., Thermal runaway caused fire and explosion of lithium ion battery. *Journal of Power Sources* **2012,** *208*, 210-224. https://doi.org/10.1016/j.jpowsour.2012.02.038.

29. He, Y.; Cui, Y.; Zhao, Z.; Chen, Y.; Shang, W.; Tan, P., Strategies for bubble removal in electrochemical systems. *Energy Reviews* **2023**, 100015. https://doi.org/10.1016/j.enrev.2023.100015.

30. Deng, K.; Zeng, Q.; Wang, D.; Liu, Z.; Wang, G.; Qiu, Z.; Zhang, Y.; Xiao, M.; Meng, Y., Nonflammable organic electrolytes for high-safety lithium-ion batteries. *Energy Storage Materials* **2020,** *32*, 425-447. https://doi.org/10.1016/j.ensm.2020.07.018.

31. Ouyang, D.; Chen, M.; Huang, Q.; Weng, J.; Wang, Z.; Wang, J., A review on the thermal hazards of the lithium-ion battery and the corresponding countermeasures. *Applied Sciences* **2019,** *9* (12), 2483. https://doi.org/10.3390/app9122483.

32. Chawla, N.; Bharti, N.; Singh, S., Recent advances in non-flammable electrolytes for safer lithium-ion batteries. *Batteries* **2019,** *5* (1), 19. https://doi.org/10.3390/batteries5010019.

33. Dubaniewicz Jr, T. H.; DuCarme, J. P., Further study of the intrinsic safety of internally shorted lithium and lithium-ion cells within methane-air. *Journal of Loss Prevention in The Process Industries* **2014,** *32*, 165-173. https://doi.org/10.1016/j.jlp.2014.09.002.

34. Lai, X.; Zheng, Y.; Zhou, L.; Gao, W., Electrical behavior of overdischarge-induced internal short circuit in lithium-ion cells. *Electrochimica Acta* **2018,** *278*, 245-254. https://doi.org/10.1016/j.electacta.2018.05.048.

35. Larsson, F.; Andersson, P.; Blomqvist, P.; Lorén, A.; Mellander, B.-E., Characteristics of lithium-ion batteries during fire tests. *Journal of Power Sources* **2014,** *271*, 414-420. https://doi.org/10.1016/j.jpowsour.2014.08.027.

36. Zhang, H.; Wang, L.; He, X., Trends in a study on thermal runaway mechanism of lithium-ion battery with $LiNi_xMn_yCo_{1-x-y}O_2$ cathode materials. *Battery Energy* **2022,** *1* (1), 20210011. https://doi.org/10.1002/bte2.20210011.

37. Feng, X.; Ouyang, M.; Liu, X.; Lu, L.; Xia, Y.; He, X., Thermal runaway mechanism of lithium ion battery for electric vehicles: A review. *Energy storage materials* **2018,** *10*, 246-267. https://doi.org/10.1016/j.ensm.2017.05.013.

38. Wu, Y.; Zeng, Z.; Lei, S.; Liu, M.; Zhong, W.; Qin, M.; Cheng, S.; Xie, J., Passivating lithiated graphite via targeted repair of SEI to inhibit exothermic reactions in early-stage of thermal runaway for safer lithium-ion batteries. *Angewandte Chemie International Edition* **2023,** *62* (10), e202217774. https://doi.org/10.1002/anie.202217774.

39. Zu, C.; Yu, H.; Li, H., Enabling the thermal stability of solid electrolyte interphase in Li-ion battery. *InfoMat* **2021,** *3* (6), 648-661. https://doi.org/10.1002/inf2.12190.

40. Li, Y.; Pu, H.; Wei, Y., Polypropylene/polyethylene multilayer separators with enhanced thermal stability for lithium-ion battery via multilayer coextrusion. *Electrochimica Acta* **2018,** *264*, 140-149. https://doi.org/10.1016/j.electacta.2018.01.114.

41. Zhang, S. S., A review on the separators of liquid electrolyte Li-ion batteries. *Journal of Power Sources* **2007,** *164* (1), 351-364. https://doi.org/10.1016/j.jpowsour.2006.10.065.

42. Nagai, A., Applications of polyvinylidene fluoride-related materials for lithium-ion batteries. *Lithium-Ion Batteries: Science and Technologies* **2009**, 155-161. https://doi.org/10.1007/978-0-387-34445-4_6.

43. Le, A. V.; Wang, M.; Noelle, D. J.; Shi, Y.; Qiao, Y., Mitigating thermal runaway of lithium-ion battery by using thermally sensitive polymer blend as cathode binder. *Journal of Applied Polymer Science* **2018,** *135* (4), 45737. https://doi.org/10.1002/app.45737.

44. Hu, E.; Bak, S.-M.; Liu, J.; Yu, X.; Zhou, Y.; Ehrlich, S. N.; Yang, X.-Q.; Nam, K.-W., Oxygen-release-related thermal stability and decomposition pathways of $Li_xNi_{0.5}Mn_{1.5}O_4$ cathode materials. *Chemistry of Materials* **2014,** *26* (2), 1108-1118. https://doi.org/10.1021/cm403400y.

45. Luo, K.; Roberts, M. R.; Hao, R.; Guerrini, N.; Pickup, D. M.; Liu, Y.-S.; Edström, K.; Guo, J.; Chadwick, A. V.; Duda, L. C., Charge-compensation in 3 d-transition-metal-oxide intercalation cathodes through the generation of localized electron holes on oxygen. *Nature chemistry* **2016,** *8* (7), 684-691. https://doi.org/10.1038/NCHEM.2471.

46. Yuan, Y.; Amine, K.; Lu, J.; Shahbazian-Yassar, R., Understanding materials challenges for rechargeable ion batteries with in situ transmission electron microscopy. *Nature communications* **2017,** *8* (1), 15806. https://doi.org/10.1038/ncomms15806.

47. Zheng, J.; Liu, T.; Hu, Z.; Wei, Y.; Song, X.; Ren, Y.; Wang, W.; Rao, M.; Lin, Y.; Chen, Z., Tuning of thermal stability in layered Li $(Ni_xMn_yCo_z)O_2$. *Journal of the American Chemical Society* **2016,** *138* (40), 13326-13334. https://doi.org/10.1021/jacs.6b07771.

48. Sharifi-Asl, S.; Lu, J.; Amine, K.; Shahbazian-Yassar, R., Oxygen release degradation in Li-ion battery cathode materials: mechanisms and mitigating approaches. *Advanced Energy Materials* **2019,** *9* (22), 1900551. https://doi.org/10.1002/aenm.201900551.

49. Hu, D.; Huang, S.; Wen, Z.; Gu, X.; Lu, J., A review on thermal runaway warning technology for lithium-ion batteries. *Renewable and Sustainable Energy Reviews* **2024,** *206*, 114882. https://doi.org/10.1016/j.rser.2024.114882.

50. Rao, K. D.; Rao, K. D.; Pavani, P.; Prasad, K. V. S. R.; Indira, D.; Phaniteja, B., A critical review on lithium ion battery modeling, battery management system and thermal runaway issues. *Electrical Engineering* **2025**, 1-37. https://doi.org/10.1007/s00202-025-03102-x.

51. Hyung, Y. E.; Vissers, D. R.; Amine, K., Flame-retardant additives for lithium-ion batteries. *Journal of Power Sources* **2003,** *119*, 383-387. https://doi.org/10.1016/S0378-7753(03)00225-8.

52. Gao, Z.; Rao, S.; Zhang, T.; Li, W.; Yang, X.; Chen, Y.; Zheng, Y.; Ding, Y.; Dong, T.; Li, S., Design strategies of flame-retardant additives for lithium ion electrolyte. *Journal of Electrochemical Energy Conversion and Storage* **2022,** *19* (3), 030910. https://doi.org/10.1115/1.4053968.

53. Dagger, T.; Rad, B. R.; Schappacher, F. M.; Winter, M., Comparative performance evaluation of flame retardant additives for lithium ion batteries–I. Safety, chemical and electrochemical stabilities. *Energy Technology* **2018,** *6* (10), 2011-2022. https://doi.org/10.1002/ente.201800132.

54. Kim, J. H.; Hyun, J. H.; Kim, S.; Park, W. H.; Yu, S. H., Phosphorus-Based Flame-Retardant Electrolytes for Lithium Batteries. *Advanced Energy Materials* **2025**, 2500587. https://doi.org/10.1002/aenm.202500587.

55. Wang, X.; Yasukawa, E.; Kasuya, S., Nonflammable trimethyl phosphate solvent-containing electrolytes for lithium-ion batteries: I. Fundamental properties. *Journal of The Electrochemical Society* **2001,** *148* (10), A1058. https://doi.org/10.1149/1.1397773.

56. Xu, F.; Cai, X.; Zhang, J.; Zhang, L.; Wang, J.; Zhang, N.; Li, S., Improving compatibility between trimethyl phosphate and graphite anodes by preconstructing a stable solid electrolyte interphase film. *ACS Applied Energy Materials* **2022,** *5* (9), 11370-11378. https://doi.org/10.1021/acsaem.2c01862.

57. Zhu, Y.; Luo, X.; Zhi, H.; Liao, Y.; Xing, L.; Xu, M.; Liu, X.; Xu, K.; Li, W., Diethyl (thiophen-2-ylmethyl) phosphonate: a novel multifunctional electrolyte additive for high voltage batteries. *Journal of Materials Chemistry A* **2018,** *6* (23), 10990-11004. https://doi.org/10.1039/C8TA01236A.

58. Hu, J.; Jin, Z.; Zhong, H.; Zhan, H.; Zhou, Y.; Li, Z., A new phosphonamidate as flame retardant additive in electrolytes for lithium ion batteries. *Journal of Power Sources* **2012,** *197*, 297-300. https://doi.org/10.1016/j.jpowsour.2011.09.012.

59. Nilsson, V.; Liu, S.; Battaglia, C.; Kühnel, R.-S., Electrolytes with flame retardant pentafluoro (phenoxy) cyclotriphosphazene for nickel-rich layered oxide/graphite cells. *Electrochimica Acta* **2022,** *427*, 140867.

60. Wu, H.-L.; Chong, Y.-H.; Ong, H.-C.; Shu, C.-M., Thermal stability of modified lithium-ion battery electrolyte by flame retardant, tris (2, 2, 2-trifluoroethyl) phosphite. *Journal*

of Thermal Analysis and Calorimetry **2022,** *147* (6), 4245-4252. https://doi.org/10.1007/s10973-021-10824-0.

61. Wang, Y.; Mao, Y.; Bai, Q.-Y.; Li, C.-L.; Guo, R.; Xie, J.-Y., Safety optimization enabled by tris (2, 2, 2-trifluoroethyl) phosphite additive for advanced pouch lithium ion batteries. *Solid State Ionics* **2019,** *337*, 7-11. https://doi.org/10.1016/j.ssi.2019.03.028.

62. Wang, W.; Liao, C.; Liu, L.; Cai, W.; Yuan, Y.; Hou, Y.; Guo, W.; Zhou, X.; Qiu, S.; Song, L., Comparable investigation of tervalent and pentavalent phosphorus based flame retardants on improving the safety and capacity of lithium-ion batteries. *Journal of Power Sources* **2019,** *420*, 143-151. https://doi.org/10.1016/j.jpowsour.2019.02.037.

63. Li, X.; Li, Z.; Zhang, W.; Jiang, X.; Han, L.; Wang, X.; Kan, Y.; Song, L.; Hu, Y., Flame-retardant in-situ formed gel polymer electrolyte with different valance states of phosphorus structures for high-performance and fire-safety lithium-ion batteries. *Chemical Engineering Journal* **2024,** *490*, 151568. https://doi.org/10.1016/j.cej.2024.151568.

64. Pushparaj, R. I.; Kumar, A. R.; Xu, G., Enhancing safety in lithium-ion batteries with additive-based liquid electrolytes: A critical review. *Journal of Energy Storage* **2023,** *72*, 108493. https://doi.org/10.1016/j.est.2023.108493.

65. Hou, J.; Wang, L.; Feng, X.; Terada, J.; Lu, L.; Yamazaki, S.; Su, A.; Kuwajima, Y.; Chen, Y.; Hidaka, T., Thermal runaway of lithium-ion batteries employing flame-retardant fluorinated electrolytes. *Energy & Environmental Materials* **2023,** *6* (1), e12297. https://doi.org/10.1002/eem2.12297.

66. Jaumaux, P.; Wu, J.; Shanmukaraj, D.; Wang, Y.; Zhou, D.; Sun, B.; Kang, F.; Li, B.; Armand, M.; Wang, G., Non-flammable liquid and quasi-solid electrolytes toward highly-safe alkali metal-based batteries. *Advanced Functional Materials* **2021,** *31* (10), 2008644. https://doi.org/10.1002/adfm.202008644.

67. Murmann, P.; von Aspern, N.; Janssen, P.; Kalinovich, N.; Shevchuk, M.; Röschenthaler, G.-V.; Winter, M.; Cekic-Laskovic, I., Influence of the fluorination degree of organophosphates on flammability and electrochemical performance in lithium ion batteries. *Journal of The Electrochemical Society* **2018,** *165* (9), A1935. https://doi.org/10.1149/2.0011810jes.

68. Murmann, P.; Mönnighoff, X.; von Aspern, N.; Janssen, P.; Kalinovich, N.; Shevchuk, M.; Kazakova, O.; Röschenthaler, G.-V.; Cekic-Laskovic, I.; Winter, M., Influence of the fluorination degree of organophosphates on flammability and electrochemical performance in lithium ion batteries: Studies on fluorinated compounds deriving from triethyl phosphate. *Journal of The Electrochemical Society* **2016,** *163* (5), A751. https://doi.org/10.1149/2.1031605jes.

69. Kim, S.; Han, T.; Jeong, J.; Lee, H.; Ryou, M.-H.; Lee, Y. M., A flame-retardant composite polymer electrolyte for lithium-ion polymer batteries. *Electrochimica Acta* **2017,** *241*, 553-559. https://doi.org/10.1016/j.electacta.2017.04.129.

70. Chen, M.; Mei, J.; Wang, S.; Chen, Q.; Zhao, L.; Kong, Q.; Wu, X., Comparative studies on the combustion characters of the lithium-ion battery electrolytes with composite flame-retardant additives. *Journal of Energy Storage* **2022,** *47*, 103642. https://doi.org/10.1016/j.est.2021.103642.

71. Long, M.-C.; Duan, P.-H.; Gao, Y.; Wang, X.-L.; Wu, G.; Wang, Y.-Z., Boosting safety and performance of lithium-ion battery enabled by cooperation of thermotolerant fire-retardant composite membrane and nonflammable electrolyte. *Chemical Engineering Journal* **2022,** *432*, 134394. https://doi.org/10.1016/j.cej.2021.134394.

72. Yusuf, A.; Avvaru, V. S.; De la Vega, J.; Zhang, M.; Molleja, J. G.; Wang, D.-Y., Unveiling the structure, chemistry, and formation mechanism of an in-situ phosphazene flame retardant-derived interphase layer in LiFePO4 cathode. *Chemical Engineering Journal* **2023,** *455*, 140678. https://doi.org/10.1016/j.cej.2022.140678.

73. Zhao, W.; Yi, J.; He, P.; Zhou, H., Solid-state electrolytes for lithium-ion batteries: fundamentals, challenges and perspectives. *Electrochemical Energy Reviews* **2019,** *2*, 574-605. https://doi.org/10.1007/s41918-019-00048-0.

74. Manthiram, A.; Yu, X.; Wang, S., Lithium battery chemistries enabled by solid-state electrolytes. *Nature Reviews Materials* **2017,** *2* (4), 1-16. https://doi.org/10.1038/natrevmats.2016.103.

75. Zheng, F.; Kotobuki, M.; Song, S.; Lai, M. O.; Lu, L., Review on solid electrolytes for all-solid-state lithium-ion batteries. *Journal of Power Sources* **2018,** *389*, 198-213. https://doi.org/10.1016/j.jpowsour.2018.04.022.

76. Gao, J.; Zhao, Y.-S.; Shi, S.-Q.; Li, H., Lithium-ion transport in inorganic solid state electrolyte. *Chinese Physics B* **2015,** *25* (1), 018211. https://doi.org/10.1088/1674-1056/25/1/018211.

77. Bachman, J. C.; Muy, S.; Grimaud, A.; Chang, H.-H.; Pour, N.; Lux, S. F.; Paschos, O.; Maglia, F.; Lupart, S.; Lamp, P., Inorganic solid-state electrolytes for lithium batteries: mechanisms and properties governing ion conduction. *Chemical Reviews* **2016,** *116* (1), 140-162. https://doi.org/10.1021/acs.chemrev.5b00563.

78. Yu, X.; Manthiram, A., Electrode–electrolyte interfaces in lithium–sulfur batteries with liquid or inorganic solid electrolytes. *Accounts of Chemical Research* **2017,** *50* (11), 2653-2660. https://doi.org/10.1021/acs.accounts.7b00460.

79. Li, X.-S.; Liang, J.; Cao, X.; Zhu, S.-Y.; Bai, Y.-F.; Sun, J.-W.; Luo, H.-B.; Kong, J., Research progress of inorganic solid electrolyte materials for all-solid-state sodium-ion batteries. *Rare Metals* **2025**, 1-29. https://doi.org/10.1007/s12598-024-03150-5.

80. An, Y.; Han, X.; Liu, Y.; Azhar, A.; Na, J.; Nanjundan, A. K.; Wang, S.; Yu, J.; Yamauchi, Y., Progress in solid polymer electrolytes for lithium-ion batteries and beyond. *Small* **2022,** *18* (3), 2103617. https://doi.org/10.1002/smll.202103617.

81. Xue, Z.; He, D.; Xie, X., Poly (ethylene oxide)-based electrolytes for lithium-ion batteries. *Journal of Materials Chemistry A* **2015,** *3* (38), 19218-19253. https://doi.org/10.1039/C5TA03471J.

82. Li, Z.; Fu, J.; Zhou, X.; Gui, S.; Wei, L.; Yang, H.; Li, H.; Guo, X., Ionic conduction in polymer-based solid electrolytes. *Advanced Science* **2023,** *10* (10), 2201718. https://doi.org/10.1002/advs.202201718.

83. Jiang, Y.; Yan, X.; Ma, Z.; Mei, P.; Xiao, W.; You, Q.; Zhang, Y., Development of the PEO based solid polymer electrolytes for all-solid state lithium ion batteries. *Polymers* **2018,** *10* (11), 1237. https://doi.org/10.3390/polym10111237.

84. Murata, K.; Izuchi, S.; Yoshihisa, Y., An overview of the research and development of solid polymer electrolyte batteries. *Electrochimica Acta* **2000,** *45* (8-9), 1501-1508. https://doi.org/10.1016/S0013-4686(99)00365-5.

85. Liu, X.; Jia, H.; Li, H., Flame-retarding quasi-solid polymer electrolytes for high-safety lithium metal batteries. *Energy Storage Materials* **2024,** *67*, 103263. https://doi.org/10.1016/j.ensm.2024.103263.

86. Yao, P.; Yu, H.; Ding, Z.; Liu, Y.; Lu, J.; Lavorgna, M.; Wu, J.; Liu, X., Review on polymer-based composite electrolytes for lithium batteries. *Frontiers in Chemistry* **2019,** *7*, 522. https://doi.org/10.3389/fchem.2019.00522.

87. Lu, X.; Wang, Y.; Xu, X.; Yan, B.; Wu, T.; Lu, L., Polymer-based solid-state electrolytes for high-energy-density lithium-ion batteries–review. *Advanced Energy Materials* **2023,** *13* (38), 2301746. https://doi.org/10.1002/aenm.202301746.

88. Kanimozhi, G.; Naresh, N.; Kumar, H.; Satyanarayana, N., Review on the recent progress in the nanocomposite polymer electrolytes on the performance of lithium-ion batteries. *International Journal of Energy Research* **2022,** *46* (6), 7137-7174. https://doi.org/10.1002/er.7740.

89. Lv, F.; Wang, Z.; Shi, L.; Zhu, J.; Edström, K.; Mindemark, J.; Yuan, S., Challenges and development of composite solid-state electrolytes for high-performance lithium ion batteries. *Journal of Power Sources* **2019,** *441*, 227175. https://doi.org/10.1016/j.jpowsour.2019.227175.

90. Zheng, J.; Ju, Z.; Zhang, B.; Nai, J.; Liu, T.; Liu, Y.; Xie, Q.; Zhang, W.; Wang, Y.; Tao, X., Lithium ion diffusion mechanism on the inorganic components of the solid–electrolyte interphase. *Journal of Materials Chemistry A* **2021,** *9* (16), 10251-10259. https://doi.org/10.1039/D0TA11444H.

91. Zhang, D.; Xu, X.; Qin, Y.; Ji, S.; Huo, Y.; Wang, Z.; Liu, Z.; Shen, J.; Liu, J., Recent progress in organic–inorganic composite solid electrolytes for all-solid-state lithium batteries. *Chemistry–A European Journal* **2020,** *26* (8), 1720-1736. https://doi.org/10.1002/chem.201904461.

92. Zheng, Y.; Yao, Y.; Ou, J.; Li, M.; Luo, D.; Dou, H.; Li, Z.; Amine, K.; Yu, A.; Chen, Z., A review of composite solid-state electrolytes for lithium batteries: fundamentals, key materials and advanced structures. *Chemical Society Reviews* **2020,** *49* (23), 8790-8839. https://doi.org/10.1039/D0CS00305K.

93. Tang, S.; Guo, W.; Fu, Y., Advances in composite polymer electrolytes for lithium batteries and beyond. *Advanced Energy Materials* **2021,** *11* (2), 2000802. https://doi.org/10.1002/aenm.202000802.

94. Jiang, G.; Li, F.; Wang, H.; Wu, M.; Qi, S.; Liu, X.; Yang, S.; Ma, J., Perspective on high-concentration electrolytes for lithium metal batteries. *Small Structures* **2021,** *2* (5), 2000122. https://doi.org/10.1002/sstr.202000122.

95. Giffin, G. A., The role of concentration in electrolyte solutions for non-aqueous lithium-based batteries. *Nature Communications* **2022,** *13* (1), 5250. https://doi.org/10.1038/s41467-022-32794-z.

96. Cao, X.; Jia, H.; Xu, W.; Zhang, J.-G., Localized high-concentration electrolytes for lithium batteries. *Journal of The Electrochemical Society* **2021,** *168* (1), 010522. https://doi.org/10.1149/1945-7111/abd60e.

97. Yamada, Y.; Wang, J.; Ko, S.; Watanabe, E.; Yamada, A., Advances and issues in developing salt-concentrated battery electrolytes. *Nature Energy* **2019,** *4* (4), 269-280. https://doi.org/10.1038/s41560-019-0336-z.

98. Yuan, S.; Ding, K.; Zeng, X.; Bin, D.; Zhang, Y.; Dong, P.; Wang, Y., Advanced nonflammable organic electrolyte promises safer Li-metal batteries: from solvation structure perspectives. *Advanced Materials* **2023,** *35* (13), 2206228. https://doi.org/10.1002/adma.202206228.

99. Wang, J.; Zheng, Q.; Fang, M.; Ko, S.; Yamada, Y.; Yamada, A., Concentrated electrolytes widen the operating temperature range of lithium-ion batteries. *Advanced Science* **2021,** *8* (18), 2101646. https://doi.org/10.1002/advs.202101646.

100. Yamada, Y.; Furukawa, K.; Sodeyama, K.; Kikuchi, K.; Yaegashi, M.; Tateyama, Y.; Yamada, A., Unusual stability of acetonitrile-based superconcentrated electrolytes for fast-charging lithium-ion batteries. *Journal of the American Chemical Society* **2014,** *136* (13), 5039-5046. https://doi.org/10.1021/ja412807w.

101. Zhou, P.; Xiang, Y.; Liu, K., Understanding and Applying Donor Number of Electrolytes in Lithium Metal Batteries. *Energy & Environmental Science* **2024**. https://doi.org/10.1039/D4EE02989E.

102. Liu, J.; He, S.; Liu, S.; Wang, S.; Zhang, J., Advanced electrolyte systems with additives for high-cell-voltage and high-energy-density lithium batteries. *Journal of Materials Chemistry A* **2022,** *10* (43), 22929-22954. https://doi.org/10.1039/D2TA07696A.

103. Zheng, J.; Lochala, J. A.; Kwok, A.; Deng, Z. D.; Xiao, J., Research progress towards understanding the unique interfaces between concentrated electrolytes and electrodes for

energy storage applications. *Advanced Science* **2017,** *4* (8), 1700032. https://doi.org/10.1002/advs.201700032.

104. Arbizzani, C.; Gabrielli, G.; Mastragostino, M., Thermal stability and flammability of electrolytes for lithium-ion batteries. *Journal of Power Sources* **2011,** *196* (10), 4801-4805. https://doi.org/10.1016/j.jpowsour.2011.01.068.

105. Liu, M.; Zeng, Z.; Wu, Y.; Zhong, W.; Lei, S.; Cheng, S.; Wen, J.; Xie, J., Reviewing recent progress of liquid electrolyte chemistry for mitigating thermal runaway in lithium–ion batteries. *Energy Storage Materials* **2024,** *65*, 103133. https://doi.org/10.1016/j.ensm.2023.103133.

106. Zhang, M.; Gomes, M. B.; Yusuf, A.; Yin, G.-Z.; Sun, C.-C.; Wang, D.-Y., Flame-retardant reinforced halloysite nanotubes as multi-functional fillers for PEO-based polymer electrolytes. *European Polymer Journal* **2024,** *215*, 113246. https://doi.org/10.1016/j.eurpolymj.2024.113246.

107. Ouyang, D.; Chen, M.; Weng, J.; Wang, K.; Wang, J.; Wang, Z., Exploring the thermal stability of lithium-ion cells via accelerating rate calorimetry: A review. *Journal of Energy Chemistry* **2023,** *81*, 543-573. https://doi.org/10.1016/j.jechem.2023.02.030.

108. Xu, K.; Ding, M. S.; Zhang, S.; Allen, J. L.; Jow, T. R., Evaluation of Fluorinated Alkyl Phosphates as Flame Retardants in Electrolytes for Li-Ion Batteries: I. Physical and Electrochemical Properties. *Journal of The Electrochemical Society* **2003,** *150* (2). https://doi.org/10.1149/1.1533040.

109. Chang, Z.; Ma, C.; Wang, R.; Wang, B.; Yang, M.; Li, B.; Zhang, T.; Li, Z.; Zhao, P.; Qi, X., Design and Mechanism Study of High-Safety and Long-Life Electrolyte for High-Energy-Density Lithium-Ion Batteries. *ACS Applied Materials & Interfaces* **2024,** *16* (15), 18980-18990. https://doi.org/10.1021/acsami.4c02237.

110. Izquierdo-Gonzales, S.; Li, W.; Lucht, B. L., Hexamethylphosphoramide as a flame retarding additive for lithium-ion battery electrolytes. *Journal of Power Sources* **2004,** *135* (1-2), 291-296. https://doi.org/10.1016/j.jpowsour.2004.04.011.

111. Li, Q.; Zhang, Z.; Li, Y.; Li, H.; Liu, Z.; Liu, X.; Xu, Q., Rapid self-healing gel electrolyte based on deep eutectic solvents for solid-state lithium batteries. *ACS Applied Materials & Interfaces* **2022,** *14* (44), 49700-49708. https://doi.org/10.1021/acsami.2c12445.

112. Logan, M. W.; Langevin, S.; Tan, B.; Freeman, A. W.; Hoffman, C.; Trigg, D. B.; Gerasopoulos, K., UV-cured eutectic gel polymer electrolytes for safe and robust Li-ion batteries. *Journal of Materials Chemistry A* **2020,** *8* (17), 8485-8495. https://doi.org/10.1039/D0TA01901A.

113. Pirsaheb, M.; Seifi, H.; Gholami, T.; Ganduh, S. H.; Jasim, L. S.; Mahdi, M. A.; Salavati-Niasari, M., Thermal analysis techniques for evaluating the thermal stability of battery materials: A comprehensive review. *Journal of Analytical and Applied Pyrolysis* **2023,** *174*, 106136. https://doi.org/10.1016/j.jaap.2023.106136.

114. Swiderska-Mocek, A.; Jakobczyk, P.; Rudnicka, E.; Lewandowski, A., Flammability parameters of lithium-ion battery electrolytes. *Journal of Molecular Liquids* **2020,** *318*, 113986. https://doi.org/10.1016/j.molliq.2020.113986.

115. Zhang, Z.; Fouchard, D.; Rea, J., Differential scanning calorimetry material studies: implications for the safety of lithium-ion cells. *Journal of Power Sources* **1998,** *70* (1), 16-20. https://doi.org/10.1016/S0378-7753(97)02611-6.

116. Duh, Y.-S.; Lee, C.-Y.; Chen, Y.-L.; Kao, C.-S., Characterization on the exothermic behaviors of cathode materials reacted with ethylene carbonate in lithium-ion battery studied by differential scanning calorimeter (DSC). *Thermochimica Acta* **2016,** *642*, 88-94. https://doi.org/10.1016/j.tca.2016.09.007.

117. Lamb, J.; Torres-Castro, L.; Hewson, J. C.; Shurtz, R. C.; Preger, Y., Investigating the role of energy density in thermal runaway of lithium-ion batteries with accelerating rate calorimetry. *Journal of The Electrochemical Society* **2021,** *168* (6), 060516. https://doi.org/10.1149/1945-7111/ac0699.

118. Zhao, C.; Wang, T.; Huang, Z.; Wu, J.; Zhou, H.; Ma, M.; Xu, J.; Wang, Z.; Li, H.; Sun, J., Experimental study on thermal runaway of fully charged and overcharged lithium-ion batteries under adiabatic and side-heating test. *Journal of Energy Storage* **2021,** *38*, 102519. https://doi.org/10.1016/j.est.2021.102519.

119. Feng, X.; Fang, M.; He, X.; Ouyang, M.; Lu, L.; Wang, H.; Zhang, M., Thermal runaway features of large format prismatic lithium ion battery using extended volume accelerating rate calorimetry. *Journal of Power Sources* **2014,** *255*, 294-301. https://doi.org/10.1016/j.jpowsour.2014.01.005.

120. Son, K.; Hwang, S. M.; Woo, S.-G.; Koo, J. K.; Paik, M.; Song, E. H.; Kim, Y.-J., Comparative study of thermal runaway and cell failure of lab-scale Li-ion batteries using accelerating rate calorimetry. *Journal of Industrial and Engineering Chemistry* **2020,** *83*, 247-251. https://doi.org/10.1016/j.jiec.2019.11.034.

121. Lai, X.; Yao, J.; Jin, C.; Feng, X.; Wang, H.; Xu, C.; Zheng, Y., A review of lithium-ion battery failure hazards: Test standards, accident analysis, and safety suggestions. *Batteries* **2022,** *8* (11), 248. https://doi.org/10.3390/batteries8110248

122. Gabbar, H. A.; Othman, A. M.; Abdussami, M. R., Review of battery management systems (BMS) development and industrial standards. *Technologies* **2021,** *9* (2), 28. https://doi.org/10.3390/technologies9020028.

123. Lin, C.; Burggräf, P.; Liu, L.; Adlon, T.; Mueller, K.; Beyer, M.; Xu, T.; Kammerer, V.; Hu, J.; Liu, S., Deep-Dive analysis of the latest Lithium-Ion battery safety testing standards and regulations in Germany and China. *Renewable and Sustainable Energy Reviews* **2023,** *173*, 113077. https://doi.org/10.1016/j.rser.2022.113077.

124. Ping, P.; Wang, Q.; Huang, P.; Li, K.; Sun, J.; Kong, D.; Chen, C., Study of the fire behavior of high-energy lithium-ion batteries with full-scale burning test. *Journal of Power Sources* **2015,** *285*, 80-89. https://doi.org/10.1016/j.jpowsour.2015.03.035.

125. Jin, Y.; Zhao, Z.; Miao, S.; Wang, Q.; Sun, L.; Lu, H., Explosion hazards study of grid-scale lithium-ion battery energy storage station. *Journal of Energy Storage* **2021,** *42*, 102987. https://doi.org/10.1016/j.est.2021.102987.

126. Mishra, D.; Tummala, R.; Jain, A., Investigation of propagation of thermal runaway during large-scale storage and transportation of Li-ion batteries. *Journal of Energy Storage* **2023,** *72*, 108315. https://doi.org/10.1016/j.est.2023.108315.

127. Qi, X.-L.; Zhou, D.-D.; Zhang, J.; Hu, S.; Haranczyk, M.; Wang, D.-Y., Simultaneous improvement of mechanical and fire-safety properties of polymer composites with phosphonate-loaded MOF additives. *ACS Applied Materials & Interfaces* **2019,** *11* (22), 20325-20332. https://doi.org/10.1021/acsami.9b02357.

128. Shin, J.; Kim, K.; Ahn, H.; Ahn, J., Electrochemical properties and interfacial stability of $(PEO)_{10}LiCF_3SO_3–Ti_nO_{2n–1}$ composite polymer electrolytes for lithium/sulfur battery. *Materials Science and Engineering: B* **2002,** *95* (2), 148-156. https://doi.org/10.1016/S0921-5107(02)00226-X.

129. Dewaghe, C.; Lew, C.; Claes, M.; Belgium, S.; Dubois, P., Fire-retardant applications of polymer–carbon nanotubes composites: Improved barrier effect and synergism. *Polymer–Carbon Nanotube Composites* **2011**, 718-745.

130. Iurilli, P.; Brivio, C.; Wood, V., On the use of electrochemical impedance spectroscopy to characterize and model the aging phenomena of lithium-ion batteries: a critical review. *Journal of Power Sources* **2021,** *505*, 229860. https://doi.org/10.1016/j.jpowsour.2021.229860.

131. Haregewoin, A. M.; Wotango, A. S.; Hwang, B.-J., Electrolyte additives for lithium ion battery electrodes: progress and perspectives. *Energy & Environmental Science* **2016,** *9* (6), 1955-1988. https://doi.org/10.1039/C6EE00123H.

132. Chen, J.; Naveed, A.; Nuli, Y.; Yang, J.; Wang, J., Designing an intrinsically safe organic electrolyte for rechargeable batteries. *Energy Storage Materials* **2020,** *31*, 382-400. https://doi.org/10.1016/j.ensm.2020.06.027.

133. Wong, D. H.; Thelen, J. L.; Fu, Y.; Devaux, D.; Pandya, A. A.; Battaglia, V. S.; Balsara, N. P.; DeSimone, J. M., Nonflammable perfluoropolyether-based electrolytes for lithium batteries. *Proceedings of the National Academy of Sciences of the United States of America* **2014,** *111* (9), 3327-3331. https://doi.org/10.1073/pnas.1314615111.

134. Pan, Y.-T.; Zhang, Z.; Yang, R., The rise of MOFs and their derivatives for flame retardant polymeric materials: A critical review. *Composites Part B: Engineering* **2020,** *199*, 108265. https://doi.org/10.1016/j.compositesb.2020.108265.

135. Sun, C.-C.; Yusuf, A.; Li, S.-W.; Qi, X.-L.; Ma, Y.; Wang, D.-Y., Metal organic frameworks enabled rational design of multifunctional PEO-based solid polymer electrolytes. *Chemical Engineering Journal* **2021,** *414*, 128702. https://doi.org/10.1016/j.cej.2021.128702.

136. Yang, H.; Liu, B.; Bright, J.; Kasani, S.; Yang, J.; Zhang, X.; Wu, N., A single-ion conducting UIO-66 metal–organic framework electrolyte for all-solid-state lithium batteries. *ACS Applied Energy Materials* **2020,** *3* (4), 4007-4013. https://doi.org/10.1021/acsaem.0c00410.

137. Xu, R.; Zhang, S.; Wang, X.; Xia, Y.; Xia, X.; Wu, J.; Gu, C.; Tu, J., Recent developments of all-solid-state lithium secondary batteries with sulfide inorganic electrolytes. *Chemistry A European Journal* **2018,** *24* (23), 6007-6018. https://doi.org/10.1002/chem.201704568.

138. Wang, X.; Zhang, Y.; Zhang, X.; Liu, T.; Lin, Y.-H.; Li, L.; Shen, Y.; Nan, C.-W., Lithium-salt-rich PEO/$Li_{0.3}La_{0.557}TiO_3$ interpenetrating composite electrolyte with three-dimensional ceramic nano-backbone for all-solid-state lithium-ion batteries. *ACS Applied Materials & Interfaces* **2018,** *10* (29), 24791-24798. https://doi.org/10.1021/acsami.8b06658.

139. Fergus, J. W., Ceramic and polymeric solid electrolytes for lithium-ion batteries. *Journal of Power Sources* **2010,** *195* (15), 4554-4569. https://doi.org/10.1016/j.jpowsour.2010.01.076.

140. Zhou, Q.; Ma, J.; Dong, S.; Li, X.; Cui, G., Intermolecular chemistry in solid polymer electrolytes for high-energy-density lithium batteries. *Advanced Materials* **2019,** *31* (50), 1902029. https://doi.org/10.1002/adma.201902029.

141. Zhang, T.; He, W.; Zhang, W.; Wang, T.; Li, P.; Sun, Z.; Yu, X., Designing composite solid-state electrolytes for high performance lithium ion or lithium metal batteries. *Chemical Science* **2020,** *11* (33), 8686-8707. https://doi.org/10.1039/D0SC03121F.

142. Dirican, M.; Yan, C.; Zhu, P.; Zhang, X., Composite solid electrolytes for all-solid-state lithium batteries. *Materials Science and Engineering: R: Reports* **2019,** *136*, 27-46. https://doi.org/10.1016/j.mser.2018.10.004.

143. Cheng, Z.; Liu, T.; Zhao, B.; Shen, F.; Jin, H.; Han, X., Recent advances in organic-inorganic composite solid electrolytes for all-solid-state lithium batteries. *Energy Storage Materials* **2021,** *34*, 388-416. https://doi.org/10.1016/j.ensm.2020.09.016.

144. Zhang, D.; Meng, X.; Hou, W.; Hu, W.; Mo, J.; Yang, T.; Zhang, W.; Fan, Q.; Liu, L.; Jiang, B., Solid polymer electrolytes: Ion conduction mechanisms and enhancement strategies. *Nano Research Energy* **2023,** *2* (2), e9120050. https://doi.org/10.26599/NRE.2023.9120050.

145. Bi, Z.; Guo, X., Solidification for solid-state lithium batteries with high energy density and long cycle life. *Energy Materials* **2022,** *2* (2), 200011. https://doi.org/10.20517/energymater.2022.07.

146. Chen, L.; Li, Y.; Li, S.-P.; Fan, L.-Z.; Nan, C.-W.; Goodenough, J. B., PEO/garnet composite electrolytes for solid-state lithium batteries: From "ceramic-in-polymer" to "polymer-in-ceramic". *Nano Energy* **2018,** *46*, 176-184. https://doi.org/10.1016/j.nanoen.2017.12.037.

147. Huo, H.; Chen, Y.; Luo, J.; Yang, X.; Guo, X.; Sun, X., Rational design of hierarchical "ceramic-in-polymer" and "polymer-in-ceramic" electrolytes for dendrite-free solid-state batteries. *Advanced Energy Materials* **2019,** *9* (17), 1804004. https://doi.org/10.1002/aenm.201804004.

148. Liang, B.; Tang, S.; Jiang, Q.; Chen, C.; Chen, X.; Li, S.; Yan, X., Preparation and characterization of PEO-PMMA polymer composite electrolytes doped with nano-Al_2O_3. *Electrochimica Acta* **2015,** *169*, 334-341. https://doi.org/10.1016/j.electacta.2015.04.039.

149. Othman, L.; Chew, K.; Osman, Z., Impedance spectroscopy studies of poly (methyl methacrylate)-lithium salts polymer electrolyte systems. *Ionics* **2007,** *13*, 337-342. https://doi.org/10.1007/s11581-007-0120-0.

150. Choi, B. N.; Yang, J. H.; Kim, Y. S.; Chung, C.-H., Effect of morphological change of copper-oxide fillers on the performance of solid polymer electrolytes for lithium-metal polymer batteries. *RSC Advances* **2019,** *9* (38), 21760-21770. https://doi.org/10.1039/c9ra03555a.

151. Monroe, C.; Newman, J., The impact of elastic deformation on deposition kinetics at lithium/polymer interfaces. *Journal of The Electrochemical Society* **2005,** *152* (2), A396. https://doi.org/10.1149/1.1850854.

152. Jiang, P.; Du, G.; Shi, Y.; She, F.; Guo, P.; Qian, G.; Lu, X.; Xie, F.; Lu, X., Ultrafast sintering of $Na_3Zr_2Si_2PO_{12}$ solid electrolyte for long lifespan solid-state sodium ion batteries. *Chemical Engineering Journal* **2023,** *451*, 138771. https://doi.org/10.1016/j.cej.2022.138771.

153. Shim, J.; Kim, H. J.; Kim, B. G.; Kim, Y. S.; Kim, D.-G.; Lee, J.-C., 2D boron nitride nanoflakes as a multifunctional additive in gel polymer electrolytes for safe, long cycle life and high rate lithium metal batteries. *Energy & Environmental Science* **2017,** *10* (9), 1911-1916. https://doi.org/10.1039/C7EE01095H.

154. Zhang, Z.; Wang, P.; Wu, J., Dynamic mechanical properties of EVA polymer-modified cement paste at early age. *Physics Procedia* **2012,** *25*, 305-310. https://doi.org/10.1016/j.phpro.2012.03.088.

155. Saba, N.; Jawaid, M.; Alothman, O. Y.; Paridah, M., A review on dynamic mechanical properties of natural fibre reinforced polymer composites. *Construction and Building Materials* **2016,** *106*, 149-159. https://doi.org/10.1016/j.conbuildmat.2015.12.075.

156. Ohashi, A.; Kodama, M.; Horikawa, N.; Hirai, S., Effect of Young's modulus of active materials on ion transport through solid electrolyte in all-solid-state lithium-ion battery. *Journal of Power Sources* **2021,** *483*, 229212. https://doi.org/10.1016/j.jpowsour.2020.229212.

157. Zhuge, J.; Chen, X.; KS, A.; Manica, D. P., Microscale combustion calorimeter-application and limitation. *Fire and Materials* **2016,** *40* (8), 987-998. https://doi.org/10.1002/fam.2358.

158. Nie, K.; Wang, X.; Qiu, J.; Wang, Y.; Yang, Q.; Xu, J.; Yu, X.; Li, H.; Huang, X.; Chen, L., Increasing poly (ethylene oxide) stability to 4.5 V by surface coating of the cathode. *ACS Energy Letters* **2020,** *5* (3), 826-832. https://doi.org/10.1021/acsenergylett.9b02739.

159. Ma, J.; Liu, Z.; Chen, B.; Wang, L.; Yue, L.; Liu, H.; Zhang, J.; Liu, Z.; Cui, G., A strategy to make high voltage $LiCoO_2$ compatible with polyethylene oxide electrolyte in all-solid-state lithium ion batteries. *Journal of The Electrochemical Society* **2017,** *164* (14), A3454. https://doi.org/10.1149/2.0221714jes.

160. DiDomizio, M. J.; Ibrahimli, V.; Weckman, E. J., Testing of liquids with the cone calorimeter. *Fire Safety Journal* **2021,** *126*, 103449. https://doi.org/10.1016/j.firesaf.2021.103449.

161. Xia, X.; Ping, P.; Dahn, J., The reactivity of charged electrode materials with electrolytes containing the flame retardant, triphenyl phosphate. *Journal of The Electrochemical Society* **2012,** *159* (11), A1834. https://doi.org/10.1149/2.059211jes.

162. Morgan, A. B.; Bundy, M., Cone calorimeter analysis of UL-94 V-rated plastics. *Fire and Materials: An International Journal* **2007,** *31* (4), 257-283. https://doi.org/10.1002/fam.937.

163. von Aspern, N.; Röser, S.; Rad, B. R.; Murmann, P.; Streipert, B.; Mönnighoff, X.; Tillmann, S. D.; Shevchuk, M.; Stubbmann-Kazakova, O.; Röschenthaler, G.-V., Phosphorus additives for improving high voltage stability and safety of lithium ion batteries. *Journal of Fluorine Chemistry* **2017,** *198*, 24-33. https://doi.org/10.1016/j.jfluchem.2017.02.005.

164. Gao, D.; Xu, J.; Lin, M.; Xu, Q.; Ma, C.; Xiang, H., Ethylene ethyl phosphate as a multifunctional electrolyte additive for lithium-ion batteries. *RSC Advances* **2015,** *5* (23), 17566-17571. https://doi.org/10.1039/C4RA15899G.

165. Xu, K.; Zhang, S.; Allen, J. L.; Jow, T. R., Nonflammable electrolytes for Li-ion batteries based on a fluorinated phosphate. *Journal of the Electrochemical Society* **2002,** *149* (8), A1079. https://doi.org/10.1149/1.1490356.

166. Dunn, R. P.; Kafle, J.; Krause, F. C.; Hwang, C.; Ratnakumar, B. V.; Smart, M. C.; Lucht, B. L., Electrochemical analysis of Li-ion cells containing triphenyl phosphate. *Journal of the Electrochemical Society* **2012,** *159* (12), A2100. https://doi.org/10.1149/2.081212jes.

167. Wu, B.; Pei, F.; Wu, Y.; Mao, R.; Ai, X.; Yang, H.; Cao, Y., An electrochemically compatible and flame-retardant electrolyte additive for safe lithium ion batteries. *Journal of Power Sources* **2013,** *227*, 106-110. https://doi.org/10.1016/j.jpowsour.2012.11.018.

168. Feng, J.; Lu, L., A novel bifunctional additive for safer lithium ion batteries. *Journal of Power Sources* **2013,** *243*, 29-32. https://doi.org/10.1016/j.jpowsour.2013.05.170.

169. Nilsson, V.; Liu, S.; Battaglia, C.; Kühnel, R.-S., Electrolytes with flame retardant pentafluoro(phenoxy)cyclotriphosphazene for nickel-rich layered oxide/graphite cells. *Electrochimica Acta* **2022,** *427*. https://doi.org/10.1016/j.electacta.2022.140867.

170. Zhou, D.; Li, W.; Tan, C.; Zuo, X.; Huang, Y., Cresyl diphenyl phosphate as flame retardant additive for lithium-ion batteries. *Journal of Power Sources* **2008,** *184* (2), 589-592. https://doi.org/10.1016/j.jpowsour.2008.03.008.

171. Wu, H.-L.; Chong, Y.-H.; Ong, H.-C.; Shu, C.-M., Thermal stability of modified lithium-ion battery electrolyte by flame retardant, tris (2,2,2-trifluoroethyl) phosphite. *Journal of Thermal Analysis and Calorimetry* **2021,** *147* (6), 4245-4252. https://doi.org/10.1007/s10973-021-10824-0.

172. Xia, L.; Xia, Y.; Liu, Z., A novel fluorocyclophosphazene as bifunctional additive for safer lithium-ion batteries. *Journal of Power Sources* **2015,** *278*, 190-196. https://doi.org/10.1016/j.jpowsour.2014.11.140.

173. Hess, S.; Wohlfahrt-Mehrens, M.; Wachtler, M., Flammability of Li-Ion Battery Electrolytes: Flash Point and Self-Extinguishing Time Measurements. *Journal of The Electrochemical Society* **2015,** *162* (2), A3084-A3097. https://doi.org/10.1149/2.0121502jes.

174. Li, Y.; An, Y.; Tian, Y.; Fei, H.; Xiong, S.; Qian, Y.; Feng, J., Stable and Safe Lithium Metal Batteries with Ni-Rich Cathodes Enabled by a High Efficiency Flame Retardant Additive. *Journal of The Electrochemical Society* **2019,** *166* (13), A2736-A2740. https://doi.org/10.1149/2.0081913jes.

175. Yim, T.; Park, M.-S.; Woo, S.-G.; Kwon, H.-K.; Yoo, J.-K.; Jung, Y. S.; Kim, K. J.; Yu, J.-S.; Kim, Y.-J., Self-extinguishing lithium ion batteries based on internally embedded fire-extinguishing microcapsules with temperature-responsiveness. *Nano Letters* **2015,** *15* (8), 5059-5067. https://doi.org/10.1021/acs.nanolett.5b01167.

176. Lei, S.; Zeng, Z.; Wu, Y.; Long, Z.; Li, X.; Liu, M.; Cheng, S.; Xie, J., Cosolvent Engineered Phosphaphenanthrene-Based Self-Extinguishing Electrolyte for Safer Lithium-Ion Batteries. *ACS Applied Energy Materials* **2022,** *5* (9), 10465-10472. https://doi.org/10.1021/acsaem.2c01007.

177. Wu, Z.-H.; Wu, Y.; Tang, Y.; Jiang, J.-C.; Huang, A.-C., Evaluation of composite flame-retardant electrolyte additives improvement on the safety performance of lithium-ion batteries. *Process Safety and Environmental Protection* **2023,** *169*, 285-292. https://doi.org/10.1016/j.psep.2022.11.035.

178. Yang, H.; Zhuang, G. V.; Ross Jr, P. N., Thermal stability of $LiPF_6$ salt and Li-ion battery electrolytes containing $LiPF_6$. *Journal of Power Sources* **2006,** *161* (1), 573-579. https://doi.org/10.1016/j.jpowsour.2006.03.058.

179. Wang, W.; Liao, C.; Liu, L.; Cai, W.; Yuan, Y.; Hou, Y.; Guo, W.; Zhou, X.; Qiu, S.; Song, L.; Kan, Y.; Hu, Y., Comparable investigation of tervalent and pentavalent phosphorus based flame retardants on improving the safety and capacity of lithium-ion

batteries. *Journal of Power Sources* **2019,** *420*, 143-151. https://doi.org/10.1016/j.jpowsour.2019.02.037.

180. Murmann, P.; Mönnighoff, X.; von Aspern, N.; Janssen, P.; Kalinovich, N.; Shevchuk, M.; Kazakova, O.; Röschenthaler, G.-V.; Cekic-Laskovic, I.; Winter, M., Influence of the Fluorination Degree of Organophosphates on Flammability and Electrochemical Performance in Lithium Ion Batteries: Studies on Fluorinated Compounds Deriving from Triethyl Phosphate. *Journal of The Electrochemical Society* **2016,** *163* (5), A751-A757. https://doi.org/10.1149/2.1031605jes.

181. Yao, X. L.; Xie, S.; Chen, C. H.; Wang, Q. S.; Sun, J. H.; Li, Y. L.; Lu, S. X., Comparative study of trimethyl phosphite and trimethyl phosphate as electrolyte additives in lithium ion batteries. *Journal of Power Sources* **2005,** *144* (1), 170-175. https://doi.org/10.1016/j.jpowsour.2004.11.042.

182. Xu, H. Y.; Xie, S.; Wang, Q. Y.; Yao, X. L.; Wang, Q. S.; Chen, C. H., Electrolyte additive trimethyl phosphite for improving electrochemical performance and thermal stability of $LiCoO_2$ cathode. *Electrochimica Acta* **2006,** *52* (2), 636-642. https://doi.org/10.1016/j.electacta.2006.05.043.

183. Shim, E.-G.; Nam, T.-H.; Kim, J.-G.; Kim, H.-S.; Moon, S.-I., Effects of trioctyl phosphate and cresyl diphenyl phosphate as flame-retarding additives for Li-ion battery electrolytes. *Metals and Materials International* **2009,** *15*, 615-621. https://doi.org/10.1007/s12540-009-0615-5.

184. Xiang, H. F.; Xu, H. Y.; Wang, Z. Z.; Chen, C. H., Dimethyl methylphosphonate (DMMP) as an efficient flame retardant additive for the lithium-ion battery electrolytes. *Journal of Power Sources* **2007,** *173* (1), 562-564. https://doi.org/10.1016/j.jpowsour.2007.05.001.

185. Zeng, Z.; Jiang, X.; Wu, B.; Xiao, L.; Ai, X.; Yang, H.; Cao, Y., Bis(2,2,2-trifluoroethyl) methylphosphonate: An Novel Flame-retardant Additive for Safe Lithium-ion Battery. *Electrochimica Acta* **2014,** *129*, 300-304. https://doi.org/10.1016/j.electacta.2014.02.062.

186. Zhu, X.; Jiang, X.; Ai, X.; Yang, H.; Cao, Y., Bis(2,2,2-Trifluoroethyl) Ethylphosphonate as Novel High-efficient Flame Retardant Additive for Safer Lithium-ion Battery. *Electrochimica Acta* **2015,** *165*, 67-71. https://doi.org/10.1016/j.electacta.2015.02.247.

187. Lai, Y.; Ren, C.; Lu, H.; Zhang, Z.; Li, J., Compatibility of Diphenyloctyl Phosphate as Flame-Retardant Additive with $LiNi_{1/3}Co_{1/3}Mn_{1/3}O_2$/Artificial Graphite Cells. *Journal of The Electrochemical Society* **2012,** *159* (8), A1267-A1272. https://doi.org/10.1149/2.058208jes.

188. Ciosek Högström, K.; Lundgren, H.; Wilken, S.; Zavalis, T. G.; Behm, M.; Edström, K.; Jacobsson, P.; Johansson, P.; Lindbergh, G., Impact of the flame retardant additive triphenyl phosphate (TPP) on the performance of graphite/$LiFePO_4$ cells in high power

applications. *Journal of Power Sources* **2014,** *256*, 430-439. https://doi.org/10.1016/j.jpowsour.2014.01.022.

189. Jia, H.; Wang, J.; Lin, F.; Monroe, C. W.; Yang, J.; NuLi, Y., TPPi as a flame retardant for rechargeable lithium batteries with sulfur composite cathodes. *Chemical Communications* **2014,** *50* (53), 7011-3. https://doi.org/10.1039/c4cc01151a.

190. S.SZhang， KXuT.RJow, Tris(2,2,2-trifluoroethyl) phosphite as a co-solvent for nonflammable electrolytes in Li-ion batteries. *Journal of Power Sources* **2003,** *113*, 166-172. https://doi.org/10.1016/S0378-7753(02)00537-2.

191. Pires, J.; Castets, A.; Timperman, L.; Santos-Peña, J.; Dumont, E.; Levasseur, S.; Tessier, C.; Dedryvère, R.; Anouti, M., Tris(2,2,2-trifluoroethyl) phosphite as an electrolyte additive for high-voltage lithium-ion batteries using lithium-rich layered oxide cathode. *Journal of Power Sources* **2015,** *296*, 413-425. https://doi.org/10.1016/j.jpowsour.2015.07.065.

192. Li, X.; Li, W.; Chen, L.; Lu, Y.; Su, Y.; Bao, L.; Wang, J.; Chen, R.; Chen, S.; Wu, F., Ethoxy (pentafluoro) cyclotriphosphazene (PFPN) as a multi-functional flame retardant electrolyte additive for lithium-ion batteries. *Journal of Power Sources* **2018,** *378*, 707-716. https://doi.org/10.1016/j.jpowsour.2017.12.085.

193. Feng, J.; Gao, X.; Ci, L.; Xiong, S., A novel bifunctional additive for 5 V-class, high-voltage lithium ion batteries. *RSC Advances* **2016,** *6* (9), 7224-7228. https://doi.org/10.1039/c5ra22547g.

194. Ramanathan, N.; Sundararajan, K., Hydrogen-bonded complexes of trimethyl phosphate and fluoroform: A matrix isolation infrared and ab initio study. *Journal of Molecular Structure* **2013,** *1034*, 257-264. https://doi.org/10.1016/j.molstruc.2012.10.054.

195. Dobbelaere, T.; Roy, A. K.; Vereecken, P.; Detavernier, C., Atomic Layer Deposition of Aluminum Phosphate Based on the Plasma Polymerization of Trimethyl Phosphate. *Chemistry of Materials* **2014,** *26* (23), 6863-6871. https://doi.org/10.1021/cm503587w.

196. Cataldo, F., Surface interaction and desorption of trimethyl phosphate from ozonized activated carbon fabric. *Fullerenes, Nanotubes and Carbon Nanostructures* **2018,** *26* (6), 379-388. https://doi.org/10.1080/1536383x.2018.1439933.

197. Cuisset, A.; Mouret, G.; Pirali, O.; Roy, P.; Cazier, F.; Nouali, H.; Demaison, J., Gas-phase vibrational spectroscopy and ab initio study of organophosphorous compounds: Discrimination between species and conformers. *The Journal of Physical Chemistry B* **2008,** *112* (39), 12516-12525. https://doi.org/10.1021/jp804665h.

198. Luo, H.; Zhou, F.; Yang, Y.; Cao, X.; Cai, X., Gas–condensed phase flame-retardant mechanisms of tris(3-nitrophenyl) phosphine/triphenyl phosphate/ABS. *Journal of Thermal Analysis and Calorimetry* **2017,** *132* (1), 263-273. https://doi.org/10.1007/s10973-017-6906-z.

199. Shao, L.; Xu, B.; Ma, W.; Wang, J.; Liu, Y.; Qian, L., Flame retardant application of a hypophosphite/cyclotetrasiloxane bigroup compound on polycarbonate. *Journal of Applied Polymer Science* **2019,** *137* (14). https://doi.org/10.1002/app.48699.

200. Jia, H.; Yang, Z.; Xu, Y.; Gao, P.; Zhong, L.; Kautz, D. J.; Wu, D.; Fliegler, B.; Engelhard, M. H.; Matthews, B. E., Is nonflammability of electrolyte overrated in the overall safety performance of lithium ion batteries? A sobering revelation from a completely nonflammable electrolyte. *Advanced Energy Materials* **2023,** *13* (4), 2203144. https://doi.org/10.1002/aenm.202203144.

201. Yang, H.; Guo, C.; Chen, J.; Naveed, A.; Yang, J.; Nuli, Y.; Wang, J., An intrinsic flame-retardant organic electrolyte for safe lithium-sulfur batteries. *Angewandte Chemie International Edition* **2019,** *58* (3), 791-795. https://doi.org/10.1002/anie.201811291.

202. Zhu, G.-R.; Zhang, Q.; Liu, Q.-S.; Bai, Q.-Y.; Quan, Y.-Z.; Gao, Y.; Wu, G.; Wang, Y.-Z., Non-flammable solvent-free liquid polymer electrolyte for lithium metal batteries. *Nature Communications* **2023,** *14* (1), 4617. https://doi.org/10.1038/s41467-023-40394-8.

203. Chen, S.; Zheng, J.; Yu, L.; Ren, X.; Engelhard, M. H.; Niu, C.; Lee, H.; Xu, W.; Xiao, J.; Liu, J., High-efficiency lithium metal batteries with fire-retardant electrolytes. *Joule* **2018,** *2* (8), 1548-1558. https://doi.org/10.1016/j.joule.2018.05.002.

204. Ribière, P.; Grugeon, S.; Morcrette, M.; Boyanov, S.; Laruelle, S.; Marlair, G., Investigation on the fire-induced hazards of Li-ion battery cells by fire calorimetry. *Energy & Environmental Science* **2012,** *5* (1), 5271-5280. https://doi.org/10.1039/C1EE02218K.

205. Zhong, G.; Mao, B.; Wang, C.; Jiang, L.; Xu, K.; Sun, J.; Wang, Q., Thermal runaway and fire behavior investigation of lithium ion batteries using modified cone calorimeter. *Journal of Thermal Analysis and Calorimetry* **2019,** *135*, 2879-2889. https://doi.org/10.1007/s10973-018-7599-7.

206. Schartel, B.; Hull, T. R., Development of fire-retarded materials—interpretation of cone calorimeter data. *Fire and Materials: An International Journal* **2007,** *31* (5), 327-354. https://doi.org/10.1002/fam.949.

207. Shi, X.-H.; Li, X.-L.; Li, Y.-M.; Li, Z.; Wang, D.-Y., Flame-retardant strategy and mechanism of fiber reinforced polymeric composite: a review. *Composites Part B: Engineering* **2022,** *233*, 109663. https://doi.org/10.1016/j.compositesb.2022.109663.

208. Lindholm, J.; Brink, A.; Hupa, M., Cone calorimeter - a tool for measuring heat release rate. *Åbo Akademi Process Chemistry Centre: Turku, Finland* **2009**, 9.

209. Liu, X.; Ren, D.; Hsu, H.; Feng, X.; Xu, G.-L.; Zhuang, M.; Gao, H.; Lu, L.; Han, X.; Chu, Z., Thermal runaway of lithium-ion batteries without internal short circuit. *Joule* **2018,** *2* (10), 2047-2064. https://doi.org/10.1016/j.joule.2018.06.015.

210. Sun, T.; Yan, Y.; Wang, X.; Rasool, G.; Zhang, K.; Li, T., A comprehensive study on heat transfer mechanism and thermal runaway suppression of the lithium-ion battery. *International Journal of Heat and Mass Transfer* **2025,** *245*, 127027. https://doi.org/10.1016/j.ijheatmasstransfer.2025.127027.

211. Hou, J.; Feng, X.; Wang, L.; Liu, X.; Ohma, A.; Lu, L.; Ren, D.; Huang, W.; Li, Y.; Yi, M., Unlocking the self-supported thermal runaway of high-energy lithium-ion batteries. *Energy Storage Materials* **2021,** *39*, 395-402. https://doi.org/10.1016/j.ensm.2021.04.035.

212. Padhi, A. K.; Nanjundaswamy, K. S.; Goodenough, J. B., Phospho-olivines as positive-electrode materials for rechargeable lithium batteries. *Journal of The Electrochemical Society* **1997,** *144* (4), 1188. https://doi.org/10.1149/1.1837571.

213. Zhang, H.; Yang, Y.; Ren, D.; Wang, L.; He, X., Graphite as anode materials: Fundamental mechanism, recent progress and advances. *Energy Storage Materials* **2021,** *36*, 147-170. https://doi.org/10.1016/j.ensm.2020.12.027.

214. Jia, Z.; Qin, P.; Li, Z.; Wei, Z.; Jin, K.; Jiang, L.; Wang, Q., Analysis of gas release during the process of thermal runaway of lithium-ion batteries with three different cathode materials. *Journal of Energy Storage* **2022,** *50*, 104302. https://doi.org/10.1016/j.est.2022.104302.

215. Zhang, M.; Xiao, J.; Tang, W.; He, Y.; Tan, P.; Haranczyk, M.; Wang, D. Y., A Novel Benchmarking Approach to Assess Fire Safety of Liquid Electrolytes in Lithium-Ion Batteries. *Advanced Energy Materials* **2024,** *14* (31), 2401241. https://doi.org/10.1002/aenm.202401241.

216. Dong, Y.; Zhang, N.; Li, C.; Zhang, Y.; Jia, M.; Wang, Y.; Zhao, Y.; Jiao, L.; Cheng, F.; Xu, J., Fire-retardant phosphate-based electrolytes for high-performance lithium metal batteries. *ACS Applied Energy Materials* **2019,** *2* (4), 2708-2716. https://doi.org/10.1021/acsaem.9b00027.

217. Shim, E.-G.; Nam, T.-H.; Kim, J.-G.; Kim, H.-S.; Moon, S.-I., Diphenyloctyl phosphate as a flame-retardant additive in electrolyte for Li-ion batteries. *Journal of Power Sources* **2008,** *175* (1), 533-539. https://doi.org/10.1016/j.jpowsour.2007.08.098.

218. Boublík, T.; Fried, V.; Hála, E., The vapour pressures of pure substances. **1984**.

219. Boethling, R. S.; Cooper, J. C., Environmental fate and effects of triaryl and trialkyl/aryl phosphate esters. In *Residue Reviews: Reviews of Environmental Contamination and Toxicology*, Springer: 1985; 49-99.

220. Howard, P. H., *Handbook of physical properties of organic chemicals*. CRC press: 1996.

221. Qian, X.; Liu, Q.; Li, H.; Zhang, H.; Yan, S., Combining inherent and additive phosphorus-containing flame retardants for enhancing flame retardancy and smoke suppression effects on polyisocyanurate-polyurethane foam. *Polymer Degradation and Stability* **2023,** *213*, 110351. https://doi.org/10.1016/j.polymdegradstab.2023.110351.

222. Ou, M.; Lian, R.; Cui, J.; Guan, H.; Liu, L.; Jiao, C.; Chen, X., Co-curing preparation of flame retardant and smoke-suppressive epoxy resin with a novel phosphorus-containing ionic liquid. *Chemosphere* **2023,** *311*, 137061. https://doi.org/10.1016/j.chemosphere.2022.137061.

223. Park, J.; Park, S. S.; Won, Y. S., In situ XRD study of the structural changes of graphite anodes mixed with SiO_x during lithium insertion and extraction in lithium ion batteries. *Electrochimica Acta* **2013,** *107*, 467-472. https://doi.org/10.1016/j.electacta.2013.06.059.

224. Stephan, A. M., Review on gel polymer electrolytes for lithium batteries. *European Polymer Journal* **2006,** *42* (1), 21-42. https://doi.org/10.1016/j.eurpolymj.2005.09.017.

225. Cheng, X.; Pan, J.; Zhao, Y.; Liao, M.; Peng, H., Gel polymer electrolytes for electrochemical energy storage. *Advanced Energy Materials* **2018,** *8* (7), 1702184. https://doi.org/10.1002/aenm.201702184.

226. Zeng, G.; Xiong, S.; Qian, Y.; Ci, L.; Feng, J., Non-flammable phosphate electrolyte with high salt-to-solvent ratios for safe potassium-ion battery. *Journal of The Electrochemical Society* **2019,** *166* (6), A1217-A1222. https://doi.org/10.1149/2.1171906jes.